The Pennsylvania State University

The Graduate School

Department of Mechanical and Nuclear Engineering

FLOW DYNAMICS AND SCALAR MIXING OF TRANSVERSE JETS INTO CROSSFLOWS

A Dissertation in

Mechanical Engineering

by

Liwei Zhang

Submitted in Partial Fulfillment
of the Requirements
for the Degree of

Doctor of Philosophy

May 2011

The dissertation of Liwei Zhang was reviewed and approved* by the following:

Domenic A. Santavicca
Professor of Mechanical Engineering
Co-Chair of Committee

Vigor Yang
Professor of Mechanical Engineering
Dissertation Advisor
Co-Chair of Committee

Daniel C. Haworth
Professor of Mechanical Engineering

Robert J. Santoro
George L. Guillet Professor of Mechanical Engineering

Robert F. Kunz
Professor of Aerospace Engineering

Karen A. Thole
Department Head of Mechanical and Nuclear Engineering
Professor of Mechanical Engineering

*Signatures are on file in the Graduate School

ABSTRACT

This research focuses on the simulation of turbulent jets into crossflows under both subsonic and supersonic conditions. The primary objectives are: 1) to establish an efficient numerical framework for treatment of flows at moderate and high Mach numbers; 2) to deepen an understanding of the physical mechanism governing the behavior of transverse jets; 3) to explore the mixing processes in such flows; 4) to study the effects of inlet conditions on flow structures; and 5) to investigate the response of flow dynamics and mixing process to external excitations.

The theoretical formulation applied here is based on three-dimensional conservation equations of mass, momentum, energy and species. The turbulence closure is achieved using a large-eddy-simulation technique. A hybrid scheme combining a lower-dissipation central scheme and a shock-capturing upwind scheme is employed for spatial discretization of the convective terms. Temporal integration is achieved using the Runge-Kutta scheme. The finite-volume approach is used to solve governing equations and associated boundary conditions. The density-based in-house code is paralleled by a domain decomposition method in conjunction with the Message Passing Interface library.

The numerical framework is validated by reproducing the mean flow and turbulent statistics in experiments. The coherent structures and shock waves are captured and their dynamic evolutions are examined according to time-accurate calculations. Findings show the jet shear-layer vortices contribute to the crossflow entrainment in the near field. The hanging vortices break down and account for the early formation of the

counter-rotating vortex pair. The deflected crossflow separates and induces upright wake vortices. Spectral and proper-orthogonal-decomposition analyses extract shear-layer instability in the near field and suggest transverse jets with current velocity ratios are globally unstable. External low-amplitude excitations have no apparent influence on the flow and mixing fields; moderate and high magnitudes of variations in the crossflow velocity yield strong vorticity generation and subsequent breakdown. The jet core decreases and the gravity center in the mixing field falls, accompanied by an elongated and narrowed jet plume in any transverse planes downstream. In the case of a sonic ethylene jet into supersonic air crossflow, the salient shock structures are presented in the time-averaged field and further elaborated using instantaneous data. The mixing process is closely related to a stretching-tilting-tearing mechanism of shedding eddies. Results also reveal one low-speed, high-temperature zone ahead of the jet with a flame-holding capability, and one subsonic region in the wake providing a potential pathway for the disturbances downstream to travel back to the near field and impact the injection and mixing processes.

Table of Contents

List of Figures

List of Tables

Nomenclature

A, B, C	Jacobian matrices of convective flux
C_p, C_v	Specific heat, $J{\cdot}Kg^{-1}{\cdot}K^{-1}$
C_R, C_I	Empirical constants
c , a	Speed of sound, m/s
C	Concentration of jet fluid
d	Diameter of jet pipe
D	Van-Driest damping function
e	Specific internal energy, $J{\cdot}Kg^{-1}$
E	Specific total energy, $J{\cdot}Kg^{-1}$
$\mathbf{E}, \mathbf{F}, \mathbf{G}$	Convective flux vector
$\mathbf{E}_v, \mathbf{F}_v, \mathbf{G}_v$	Diffusion flux vector
f	Function or frequency, kHz
$h^0_{f,i}$	Heat of formation of species i at reference condition
k	Turbulent kinetic energy,$m^2{\cdot}s^{-2}$
M	Mach number
N	Total number of species
p	Pressure, Pa
Pr	Prandtl number
r	Jet-to-crossflow velocity ratio
R	Gas constant
Re	Reynolds number
Sc	Schmidt number
St	Strouhal muber
u, v, w , U	Velocity, $m{\cdot}s^{-1}$
V	Volume, m^3

W	Molecular weight of species, or vertical velocity
x, y, z	Spatial coordinate, m
Y	Mass fraction of species
H	Helicity
Y	Mass fraction
y^+	Normalized distance from wall

Greek symbols

μ	Dynamic viscosity, kg/ms
Δ	Forward difference operator or filter width
δ_{ij}	Kronecker delta function
$\varphi_j(\mathbf{x})$	Orthogonal basis function
λ	Thermal conductivity, $W \cdot m^{-1}K^{-1}$
τ_{ij}	Viscous shear stress, N/m^2
ρ	Density, kg/m^3
η	Kolmogorov length scale, m
γ	Ratio of specific heats
ω	Vorticity, $1/s$
Ω	Vorticity magnitude, $1/s$

Subscripts

a	Acoustic property
0	Property of crossflow
J	Property of jet
i, j, k	Spatial coordinate
t	Turbulent property
ξ, η, ζ	Each direction in body fitted coordinate system
F	External excitation/forcing

Superscripts

–	Ensemble averaging
~	Favre averaging
.	Mass flow rate
′	Fluctuation
sgs	Subgrid scale

Acknowledgements

First, I would like to express my deepest gratitude to my thesis advisor, Dr. Vigor Yang. He encouraged me to proceed in this academic area and to conduct scientific research. I have benefitted not only from his knowledge and great insight as an advisor and a scientist, but also from his kindness and patience as a human being. I am especially grateful for his support, guidance and encouragement during the hard times in my second year of graduate life and at all the intermittent desperate moments over the past four-and-a-half years. Working with him, as one of his disciples, has been an inspiring and memorable experience.

Special thanks go to my doctoral committee chair, Dr. Domenic A. Santavicca, for kindly providing me great help in the birth of this thesis and on other important but not obligatory matters. I am also grateful to Dr. Daniel C. Haworth, Dr. Robert F. Kunz, and Dr. Robert J. Santoro for serving as committee members and for providing their expert guidance.

I extend sincere appreciation to Dr. Shanwu Wang, Dr. Tao Liu and Dr. Puneesh Puri for their encouragement and suggestions. I am very thankful to Dr. Dongjun Ma and Professor Jeong-Yeol Choi for their help and valuable discussions.

I would also like to thank people that I had the pleasure of interacting with during the past few years. I thank former and current members of our group, including Dr. Danning You, Dr. Fuhua Ma, Dr. Ying Huang, Dr. Nan Zong, Dr. Yanxing Wang, Dr. Jian Li, Dr. Piyush Thakre, Mr. Hongfa Huo, Mr. Huaguang Li, Dr. Yi Duan, Mr.

Xiaodong Chen, Mr. Prashant Khare, and Mr. Dilip Sundaram for their discussions and comments.

Finally, I thank my family for their constant love and support, which was the ultimate drive for me to complete this thesis. My parents, Xiuying Guo and Mingjun Zhang, and my elder sister, Hongyun Zhang, have always been proud of me, and I am proud of them. To them I dedicate this thesis.

Chapter 1

Introduction

1.1 Background and Motivation

Upcoming environmental constraints have increased the demand for low-emission gas turbine combustors. As fuel-rich combustion leads to more pollutant formations, fuel-lean combustion is one of the most promising candidates to meet the anticipated requirements. However, such designs are often prone to combustion instabilities related to coupling between combustion and acoustics. The unsteady nature of turbulent combustion and/or incomplete fuel/air mixing may result in the formation of inhomogeneous fuel pockets and thus produce oscillatory heat release in a combustion chamber. According to the Rayleigh criterion (Rayleigh, 1945), instabilities can be triggered if the heat-release oscillations are in phase with the pressure oscillations arising from the periodic motions of large-scale flow structures. Further complicating matters, if acoustic resonance occurs, the mechanical constraints imposed on the system can result in mechanical failure, leading to unexpectedly hazardous outcomes. Therefore, both the fuel injection process and the fuel/air mix are of significant importance in the gas turbine combustion system.

The primary motivation of this work is to explore the fundamental physics governing the mixing process of injected fuels in a gas turbine combustor. Figure 1.1 shows the schematic of a model swirl-stabilized gas turbine combustor. By removing the

vagaries within the combustion environment, the fuel injection problem can be simplified by considering the idealized situation of a jet issuing into a crossflow tunnel. Despite any idealization, the jet into crossflow (JICF) is immensely complicated. There are two typical configurations: one in which the jet nozzle is flush with the tunnel wall, and another in which the nozzle protrudes into the uniform region of the tunnel. In each case, the jet (usually under-expanded) is abruptly issuing into the crossflow and undergoing distortion, deformation, and dispersion. The fluid dynamics involved in this process include turbulent shear flow, boundary layer separation, and the creation of diverse vortical structures, among others. After intensive interaction in the initial region, the jet fluid mixes with the crossflow and provides the potential for further micro-scale chemical reactions.

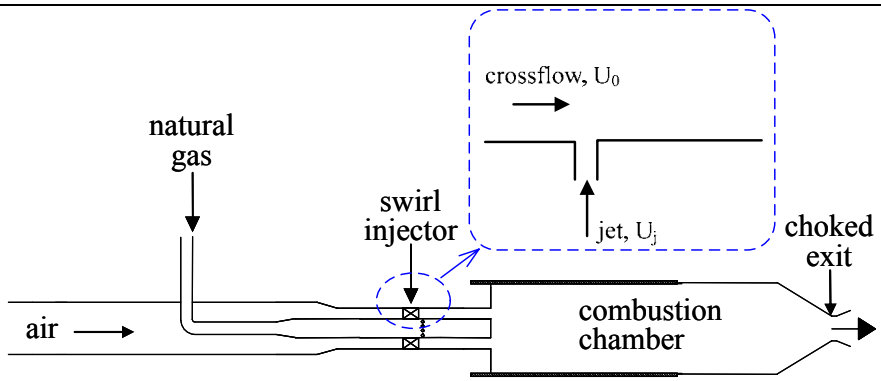

Figure 1.1 Schematic of a model swirl-stabilized gas turbine combustor (after Seo, 1999)

As a model problem, the JICF also has a wide variety of industrial, environmental, and aerospace applications such as turbine blade cooling, dilution air injection in a combustor, volcanic ash drifting, pollutant dispersal, flame stabilization in a supersonic combustor, and vertical and/or short take-off and landing (V/STOL) aircraft

guiding. Numerous studies dealing with jet and ambient flow development under various conditions have been completed since the first investigation of chimney plume dispersal was made in the early 1930s. A comprehensive review of these works was presented by Margason (1993), with a focus on earlier experimental studies. Recent accomplishments in both experimental and numerical work are briefly summarized in Section 2.

1.2 Literature Review

1.2.1 Flow Structures

The ratio of the jet momentum to the crossflow momentum is one of the most important parameters in the context of JICF. It is customary to define the effective velocity ratio r as the square root of the momentum-flux ratio such that

$$r = \sqrt{\frac{\rho_j U_j^2}{\rho_0 U_0^2}} \tag{1.1}$$

where ρ is density, U is velocity, and ' 0 ' and ' j 'are markers for crossflow and jet properties, respectively. In cases of equal-density fluids, $r = U_j / U_0$ is simply referred to as the velocity ratio.

Different flow regimes can be determined based on the velocity ratio r (Schlüter and Schönfeld, 2000). A JICF where $r < 1.0$ is especially important for turbine blade cooling, since the jet flow usually cannot break through the wall boundary layer and instead acts more like an obstacle for the crossflow. Velocity ratios of $1.0 < r < 10.0$ are most common for combustion applications, where the flow field is dominated by free

turbulence characteristics. A JICF where $r > 10.0$ will behave more like a free jet as velocity ratio increases.

In the region where $1.0 < r < 10.0$, furious interactions among the jet, the crossflow and the two wall boundary layers at the jet nozzle and the crossflow tunnel induce complex flow physics which span the range of hydrodynamic stability, turbulence dynamics, and in supersonic cases, aerodynamics.

1.2.1.1 Vortex Systems

In vortex dynamics, the production and evolution of vorticity ($\vec{\omega}$) are described by the equation

$$\frac{D\vec{\omega}}{Dt} = (\vec{\omega} \bullet \nabla)\vec{u} + \vec{\omega}\nabla \bullet \vec{u} + \frac{1}{\rho^2}\nabla\rho \times \nabla p + \nu\nabla^2\vec{\omega} + \nabla \times \vec{f} \qquad (1.2)$$

where $\vec{u}$, p, ρ, ν are the velocity vector, pressure, density, and kinematic viscosity, respectively, and $\vec{f}$ is the body force. The five terms on the right side of the equation represent different dynamic processes; in order, they are 1) stretching or tilting of vorticity due to velocity gradients; 2) the stretching of vorticity due to flow compressibility; 3) the change of vorticity due to the intersection of density and temperature surfaces (the baroclinic term); 4) the diffusion of vorticity due to the viscous effects; and 5) the changes due to body forces. The first and second processes conserve pre-existing circulation as indicated by Kelvin's theorem. Thus, new vorticity (circulation) can only enter a flow through the third and fifth processes, in addition to the imposed inlet conditions.

As the jet enters into the crossflow transversely, mismatches of velocity and pressure at the interface lead to the formation of vortices in the shear layer from the Kelvin-Helmholtz instability, and also induce the distortion and re-organization of the vorticity in the two boundary layers. Four typical coherent structures appear, as commonly accepted: 1) the jet shear-layer vortices; 2) the horseshoe vortices; 3) the counter-rotating vortex pair (CVP); and 4) the wake vortices. Among the four distinct types, CVP is the most dominant structure in the far field. Along with the horseshoe vortices, CVP has mean-flow definition and may also exhibit unsteady behaviors. The shear-layer vortices and the wake vortices are intrinsically unsteady and play important roles in the near field of the jet.

Fric and Roshko (1994) photographed the four types of vortical structures via the smoke-wire flow visualization technique and developed the well-known conceptual schematic as shown in Figure 1.2. They also demonstrated that the wake vortices in JICF were different from those in the rear of a solid cylinder and have their origins in the crossflow boundary layer on the wall from which the jet issues, whereas no analogous shedding of vortices was observed from the jet-crossflow interaction.

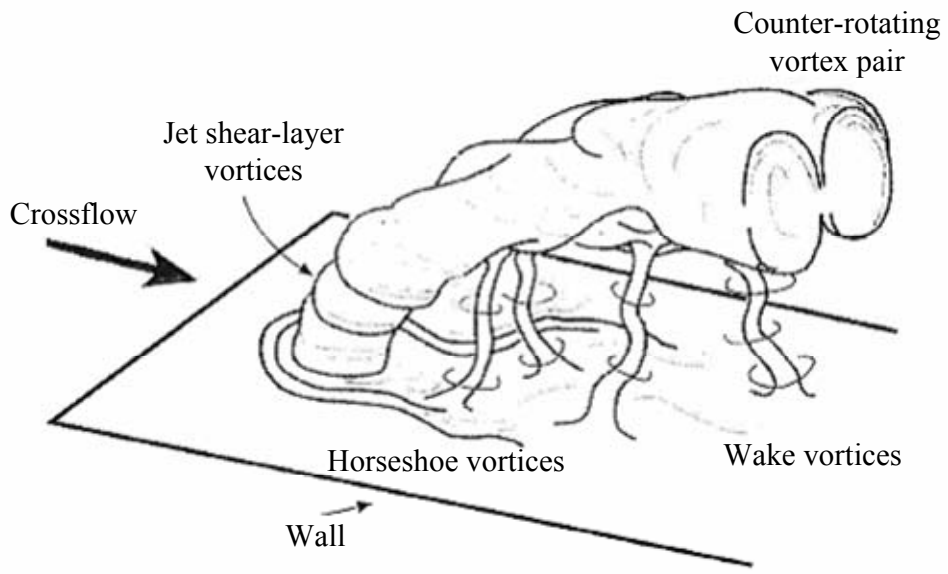

Figure 1.2 Cartoon of vortical structures in the near field of a transverse jet (Fric and Roshko, 1994)

Kelso and Smits (1995) analyzed the horseshoe vortex system and showed it could be steady, oscillating, or coalescing, depending on the flow conditions. Their results also indicated that the wake intermittently became coupled to the horseshoe vortex motions at certain frequencies.

Haven and Kurosaka (1997) performed extensive flow visualization and velocity measurements at the jet exit using laser-induced fluorescence (LIF) and particle image velocimetry (PIV). They proposed that the vorticity around the circumference of the incoming pipe flow was tilted and realigned by the entrainment of crossflow momentum. The tilted vorticity then rolled up into streamwise vortices and formed the nascent CVP.

Kelso, Lim and Perry (1996) employed dye tracers in a water tunnel and flying hot-wires in a wind tunnel to identify JICF's mean topological features. They suggested

that the Kelvin-Helmholtz instability near the jet penetration orifice accounted for the formation of shear-layer vortices, which subsequently rolled up and initiated the CVP through a vortex breakdown mechanism. As the jet evolved farther downstream in the crossflow, the vorticity from the crossflow wall also contributed to the CVP by way of wake vortices entrainment.

Yuan et al. (1999) performed large eddy simulations (LES) to shed further light upon the underlying physics of the JICF flow field. They captured the hanging vortices in the skewed mixing layers on the lateral edges of the jet (which broke down and formed a weak CVP) and the spanwise rollers on the leading and trailing edges of the jet created by Kelvin-Helmholtz instability. They also confirmed that in the wake region, the streamwise-oriented vortices were closely related to the horseshoe vortices, and that the upright vortices formed from the reorientation of streamwise vortices by the strain field could connect the jet body to the wall.

For further investigation, a partial list of the numerous experimental and numerical studies of the vortex system includes the following: Smith and Mungal (1998), Huang and Lan (2005), Denev et al. (2009). At this time, the structural features in JICF are still an intriguing contemporary research topic.

1.2.1.2 Salient Structures of a Sonic Jet into Supersonic Crossflow

In a high-speed propulsion system, the residence time of the flow is extremely short due to the hypersonic/supersonic flight speeds. The efficient mixing of fuel and air is thus a critical requirement to ensure that a combustor is effective. A simple yet

feasible fuel injection configuration is one which can transversely inject the fuel through a wall orifice into the supersonic environment. As the under-expanded fuel jet, sonic at the exit, interacts with the supersonic crossflow, salient structures grow in this flow field as shown in Figure 1.3.

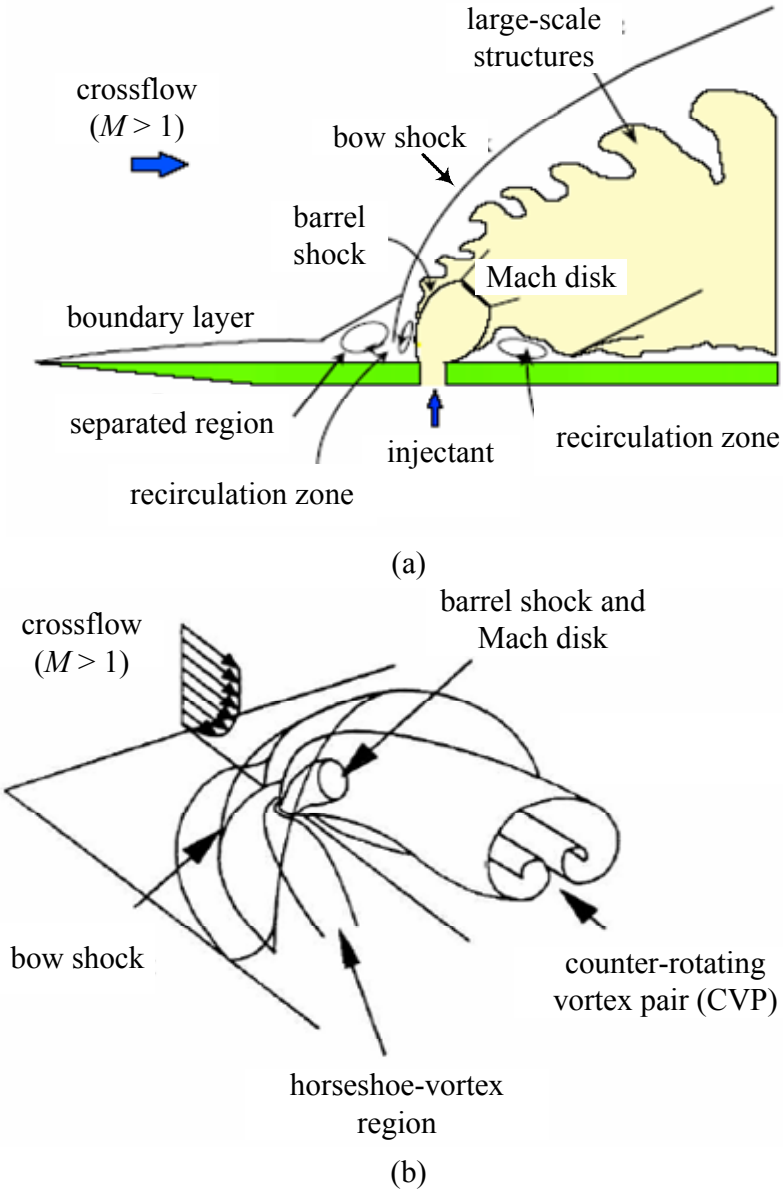

Figure 1.3 Schematic of an under-expanded transverse jet into a supersonic crossflow: (a) 2-D side view of the instantaneous flow field in the center plane (after Ben-Yakar, 2000); and (b) 3-D perspective of the averaged features of the flow field (after Gruber et al., 1995)

As the under-expanded jet enters into the crossflow, it expands three-dimensionally and a rarefaction fan emanates from the orifice. Since the jet interior is out of step with its boundary, it over-expands and the pressure at the boundary pushes the jet back toward the axis, inducing a converging conical shock wave, the barrel shock. This shock is bent by the crossflow, but would otherwise be symmetric for a free jet in a quiescent environment. The pressure difference between the jet and crossflow is typically large. Thus the barrel shock, rather than converging to a point on the axis of the jet, incidents to the axis at a large angle and reflects at the circumference of a Mach disk – a strong shock normal to the flow direction (Norman and Winkler, 1985). Meanwhile, the jet acts as an obstacle to the supersonic crossflow and a three-dimensional bow shock is formed upstream of the injector. The interaction of the bow shock with the turbulent boundary layer induces a separation shock wave and further separates the boundary layer in the near upstream. The separation region confined by the shock wave provides a zone where the boundary layer and the jet fluids mix subsonically, and is particularly important in combustion due to its flame-holding capability (Huber et al., 1979; Parker et al., 1995; Ben-Yakar, 2000).

Santiago and Dutton (1997) generated laser Doppler velocimetry (LDV) measurements of the mean and turbulent velocity fields of a sonic, under-expanded air jet transversely injected into a Mach 1.6 flow. They observed the location of the recirculation region and confirmed its flame-holding capability. Based on the varying distribution of flow unsteadiness in the barrel shock region and the observation of crossflow impingement between the wall and the jet plume on the leeside, they suggested

that mixing could be enhanced by adjusting the orifice configurations, the stagnation-to-effective back pressure ratio, or/and the spanwise separation of the jets.

Ben-Yakar et al. (2006) used a fast-framing-rate (up to 100 MHz) camera to capture the temporal characteristics of hydrogen and ethylene jets into a Mach 3.38 nitrogen crossflow. They observed significant differences in the development of shear-layer vortices for the two injectants, even for similar jet-to-crossflow momentum flux ratio. The larger velocity difference between the ethylene jet and the freestream lead to a quicker dissipation of the shear-layer vortices and a wider eddy-convection-speed distribution. This velocity induced the stretching-tilting-tearing process, further increased both the penetration depth and band thickness of the ethylene jets into the crossflow, and dramatically altered the molecular mixing.

Maddalena et al. (2006) compared the behavior of an angled (30 degree) circular injector with that of an aerodynamic ramp (aeroramp) injector, consisting of an array of two rows with two columns of flush-wall holes. By injecting helium into a Mach 4 air flow, they found the single-hole injectors had a slightly lower mixing efficiency but a somewhat less local total pressure loss. Their numerical analysis concluded that the κ-ω turbulence model could not accurately predict the flow field.

More recent investigations have tried to capture the dynamics of the sonic jet injection into supersonic crossflow by means of advanced numerical simulations. Several featured works will be addressed in Section 2.4.

1.2.2 Mixing Field

Given the significance of the mixing process, increasing emphasis has been given to the study of scalar mixing and closely-related processes such as the modeling of the jet trajectories, as mentioned in the above supersonic cases.

1.2.2.1 Scalar Mixing

The mixing field is usually qualified by the behaviors of a conserved scalar $\varphi(\vec{x},t)$. In the context of JICF, the scalar $\varphi(\vec{x},t)$ is typically chosen to represent the small temperature excess, or the different chemical composition of the jet fluid. Since the momentum equations are not usually mathematically affected by the scalar concentration, a transport equation for a passive scalar must be considered in addition to the Navier-Stokes and energy equations (Denev et al., 2009).

Based on the relation of the maximum centerline scalar concentration decay with the downstream location, the jet fluid penetration depth, and the turbulent flow fields in crossflow, earlier studies of the passive mixing process have proposed several kinds of scaling: 1) self-similarity over a range of momentum ratio r; 2) three different length scales: d, rd, and r^2d (Smith and Mungal, 1998), d is the diameter of the injection orifice; and 3) jet-like scaling in the near field and wake-like scaling in the far field (Su and Mungal, 2004). In addition, Yuan et al (1999), Schlüter and Schönfeld (2000), and Muppidi and Mahesh (2005) also examined numerically the trajectory and entrainment characteristics of JICF using LES and direct numerical simulation (DNS) techniques.

To quantify the mixing efficiency, several parameters have been adopted: 1) the degree of spatial unmixedness – the normalized scalar variance (Liscinsky et al., 1993; Holdeman et al., 1997); 2) the mixing length – the distance downstream of the injection plane after which the flow is considered fully mixed (Muruganandam et al., 2002); 3) the probability density function (PDF) of the mixture fraction (Prière et al., 2004); 4) the temporal mixing deficiency (TMD) and the spatial mixing deficiency (SMD) (Prière et al. 2004). The mathematical details and the physical meanings will be discussed in Chapter 4.

1.2.2.2 Turbulent Mixing Layer

The near-field mixing process plays a crucial role in determining the overall mixing effectiveness of JICF. The details of a turbulent mixing layer are shown in Figure 1.4.

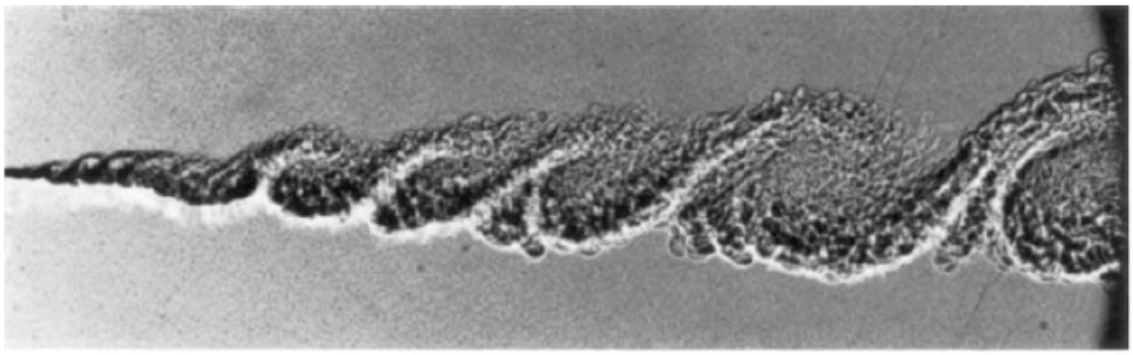

Figure 1.4 A spark shadow graph of a mixing layer between helium (upper) and nitrogen (lower) (Brown and Roshko, 1974)

Brown and Roshko (1974) captured the motions of the distinctive structures in the mixing layer and observed that turbulent mixing occurred over a wide range of scales.

Gutmark et al. (1995) summarized three mixing stages: 1) bulk mixing, in which occurs the merging and entrainment of irrotational fluid into the turbulent shear layer; 2) the "mixing transition", in which the two fluids are stirred and their interface is increased; and 3) the final molecular mixing. The first stage, bulk mixing, is dominated by large-scale structures and leaves the entrained fluid unmixed during the lifetime of the vortices (Dimotakis and Brown, 1976). The second process, the mixing transition, adds nothing to the basic ingestion of fluid, but only to the 'digestion' of the entrained fluid (Brown and Roshko, 1974); it happens during the vortices pairing process or other amalgamation process, when streamwise vortices are developed and interact with the spanwise structures (Bernal and Roshko, 1986), increasing the three-dimensional structures in the shear layer. Interactions among these three-dimensional structures lead to higher-order instabilities and transition to a small-scale dominated flow, in which viscosity and molecular diffusion are important.

In supersonic cases, the mixing layer will be strongly affected by the compressibility effects (Brown and Roshko, 1974). The spreading rate of the shear layer drops as the convective Mach number increases, plausibly because the upstream and crossflow communication paths within the shear layer are suppressed due to the high Mach number (Morkovin, 1987; Papamoschou, 1990). The convection velocity of vortices tends to be asymmetric due to the shock waves (shocklets) generated by the coherent structures on one side of the shear layer (Dimotakis, 1991), while in an incompressible shear layer, vortices are convected at an intermediate velocity between the two freestream velocities. For compressible shear layers subjected to density

gradients, the baroclinic torque $\frac{1}{\rho^2}\nabla\rho\times\nabla p$ emerges and produces vorticity, which is uncommon in incompressible flows (Gutmark et al., 1995). Thus, the compressible mixing layers are highly complicated. An adaption of the convective Mach-number concept to scale the compressibility of transverse jets was developed by Ben-Yakar (2000).

In the JICF mixing process, the convective macro-mixing and the diffusive micro-mixing supplement each other to produce a randomly ordered mixture. Dynamic vortical structures are periodically formed in the near field, which evolve downstream and engulf large quantities of crossflow fluid into the jet shear-layer. The near-field mixing is undoubtedly dominated by the so-called "entrainment-stretching-mixing process" (Ben-Yakar et al., 2006). The shear-layer vortices also stretch the interface between the unmixed fluids, and thus enhance diffusive micro-mixing, as the interfacial area is increased and the local concentration gradient is steepened in the stretching process. The same phenomena also exist along the development of CVP in the far field. In a numerical investigation by Prière et al. (2004), it was found that the entrainments of crossflow and the strength of the mixing process could be enhanced by introducing a mixing device to reinforce the two rotating structures. The vortex stretching-tilting-tearing process in the near field is believed to affect the jet penetration depth and band thickness, even for the same jet-to-crossflow momentum ratio cases with different injectant densities (Ben-Yakar et al., 2006).

1.2.2.3 Mixing vs. Combustion Instabilities

Mixing is a significant factor in combustion and combustor dynamics. The rate of heat production, fuel efficiency, and pollutants formation are all affected by the mixing of fuel and air. According to Lieuwen and Zinn (1998), the reaction rate is highly sensitive to equivalence ratio fluctuations. Their theoretical and numerical modeling on the relations between oscillations in mixing and flame behavior also demonstrated that the oscillatory behavior of mixing, especially at lean regions, could cause combustion instabilities—specifically, periodic pressure oscillations with amplitudes larger than 5% of the mean chamber pressure (Crocco and Cheng, 1956; Weiss, 1966; Sutton and Biblarz, 2000).

Oscillatory mixing, i.e. the equivalence ratio fluctuation, is usually due to the incomplete mixing of air and fuel ahead of the flame front, or the mass flow rate fluctuations at the fuel injection location. The first case is due to the limited space and time available for fuel/air premixing in the combustion inlet system; the second results from excited pressure oscillation. The equivalence ratio fluctuation is one of the major sources of heat release fluctuations. A number of studies have provided strong support, either by direct experimental measurements or by theoretical investigation, for the significance of the correlations between the instability characteristics and the operation conditions.

A theoretical analysis of lean premixed flame response to equivalence ratio oscillations was expounded by Cho and Lieuwen (2005). They calculated flame transfer functions and showed that equivalence ratio perturbations altered heat release by the

superposition of three disturbances: heat of reaction, flame speed, and flame area (Figure 1.5).

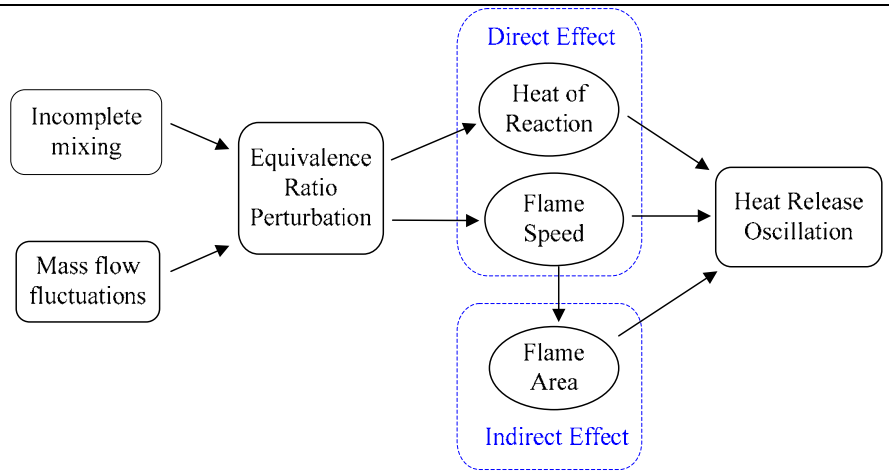

Figure 1.5 Dominant processes generating heat release oscillations caused by equivalence ratio perturbation (after Cho and Lieuwen, 2005)

Lee et al. (2000) presented the first quantitative measures of equivalence ratio fluctuations during unstable combustion in a lean premixed model dump combustor. They estimated the global heat release based on the measured overall equivalence ratio in comparison to the measured global heat release. A strong correlation was revealed by the evidence, indicating that the peaks in the heat release closely coincided with each other, except for a small phase difference which was due simply to the convection time between the location where the equivalence ratio was measured and the location where the fuel was burned.

Employing the idea that equivalence ratio fluctuations play an important role in sustaining the combustion instability, Richards and Janus (1998) were able to suppress pressure oscillations by modulating the fuel flow rate at certain frequencies.

1.2.3 Modulated Jets into Crossflow

1.2.3.1 Controlled Jets

Mixing enhancement has been a critical topic since the earliest JICF investigations in the 1930s. Over the years, the emphasis has largely focused on the modulation of the transverse jet.

Vermeulen et al. (1990) excited the jets using loudspeaker drivers over a range of frequencies and amplitudes. They found that a train of toroidal vortices was developed by the jet motion in a confined crossflow, which changed the mean velocity and the turbulent profiles and enhanced the jet penetration and spread. The mixing process appeared to be optimum at a Strouhal number of 0.22.

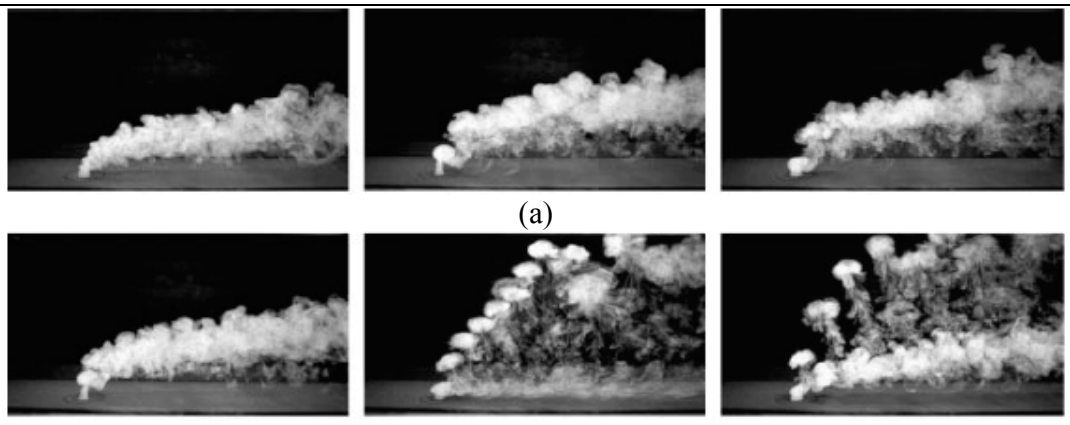

(a)

(b)

Figure 1.6 Smoke images for forced transverse jets with $r = 2.58$, $U_0 = 1.2$ m/s: (a) 'unforced' jet; 'uncompensated' sine wave excitation at 73.5 Hz, and 'compensated' sine wave excitation at 73.5 Hz, (b) 'uncompensated' square-wave excitation at 110 Hz and a duty cycle of 31%, 'compensated' square-wave excitation at 110 Hz and a duty cycle of 31%, and 'compensated' square-wave excitation at 55 Hz and a duty cycle of 15%. (M'Closkey et al., 2002)

M'Closkey et al. (2002) quantified the dynamics of the actuation for a temporally forced round jet and developed a methodology to set a jet compensation system for open-loop jet control. They observed that the optimal jet penetration and spread occurred for square wave excitation at subharmonics of the natural vortex shedding frequency of the jet. Examples of their smoke visualizations are shown in Figure 1.6.

Denev et al. (2009) introduced swirl to the transverse jets. They concluded that although the mixing was intensified near the jet exit as the turbulent kinetic energy and the vorticity of the average flow field increased, the entrainment of the crossflow fluid was attenuated along the CVP as the jet approached the bottom wall and enlarged the wall blocking effect. The overall mixing efficiency remained unchanged in this case.

For additional references on controlled jets, a partial list of relevant works includes Johari et al. (1999), Eroglu and Breidenthal (2001), Narayanan et al. (2003), and Dandois et al. (2006). A recent review paper by Karagozian (2010) covered a broad range of topics in this area, including the reactive jets in crossflow and also the promising future directions for jet control.

1.2.3.2 Unsteady Crossflow

In realistic gas turbine systems, chocked nozzles are practically used for fuel injections, while disturbances from the combustion section in the downstream are free to travel back and influence the fuel/air mixing process. Therefore, transverse jet evolution and dispersion usually happen in the environment of an oscillating crossflow. To date, only limited research has illuminated this area of investigation.

Lam and Xia (2001) and Xia and Lam (2004) investigated the dispersion of a vertical round jet issuing into an unsteady crossflow using both laboratory experiments and numerical analysis. They found that the jet effluent was organized into successive large-scale effluent clouds and that the jet width increased with the incremental rate significantly affected by the crossflow unsteadiness.

Kremer et al. (2007) presented a numerical solution to a steady round jet issuing into an oscillating crossflow with a sinusoidal velocity profile based on FLUENT 6.2 calculations. They found that the jet and scalar concentration trajectories were slightly dependent on the oscillation amplitudes, while both were closely linked to the crossflow oscillation frequencies until the deviation maximum was achieved, bringing them back to the steady scenarios.

1.2.4 Numerical Advancement

1.2.4.1 Turbulent Modeling of JICF

The complexity of flow structures has made JICF a model problem for computational fluid dynamics (CFD). In a flow system with a turbulent shear layer, boundary separation, and coherent structures, turbulent modeling inevitably becomes a long-lasting challenge. In 2005, Muppidi and Mahesh implemented the DNS technique to study the trajectories, mean velocities, turbulent intensities and passive scalar transport of a round jet in a crossflow. However, the heavy computational burden restricts the

DNS application to cases with relatively low Reynolds numbers. The majority of previous works adopt the low-cost turbulent modeling methods.

While early calculations based on the Reynolds-Averaged Navier-Stokes (RANS) equations showed limitations in predicting the highly unsteady behavior of JICF, results from LES shed light onto this area. Yuan et al. (1999) successfully simulated the formation of the CVP, predicted the entrainment of crossflow fluid by the jet, and resolved the turbulent scalar field. Later, Schlüter and Schönfeld (2000) applied an LES approach to a gas turbine burner to obtain detailed information about the momentum field and mixing. Prière et al. (2004) simulated a rectangular channel flow on which five jets were installed on each wall (upper and lower) with mixing devices to obtain detailed information about the mixing quality of gaseous fuels, and confirmed the power of LES to help design actuating devices for flow and mixing control.

To more precisely simulate the scalar mixing process, various subgrid-scale (SGS) mixing models have been proposed. The issue of model adaptability has also been examined. Sun and Su (2004) assessed various scalar-mixing models for LES by computing a correlation coefficient between exact and modeled terms, and found slight differences among the performances of different SGS models.

1.2.4.2 Subgrid-Scale Models

SGS modeling is the core of LES. Several featured models are briefly summarized here, including the algebraic and dynamic Smagorinsky models, the Wall-

Adapting Local Eddy-viscosity (WALE) model, the scale-similar model (mixed model), and the implicit model.

In the algebraic Smagorinsky model, the equilibrium assumption is applied. That is, the small scales are in equilibrium, and entirely and instantaneously dissipate all the energy from the resolved scales. Smagorinsky (1963) developed the model for impressible flows in which

$$\tau_{ij}^{sgs} = -2\nu_t \tilde{S}_{ij} \;,\; \nu_T = (C_s\Delta)^2 \mid \tilde{S} \mid \;,\; \mid \tilde{S} \mid = (2\tilde{S}_{ij}\tilde{S}_{ij})^{1/2} \tag{1.3}$$

where Δ is the filter width, and the coefficient C_s can be determined from the isotropic turbulence decay or a prior test. Later, Erlebacher et al. (1992) extended this model to include the flow compressibility effect by introducing two dimensionless compressible Smagorinsky constants, C_R and C_I:

$$\tau_{ij}^{sgs} = -2\nu_t \bar{\rho}(\tilde{S}_{ij} - \frac{\tilde{S}_{kk}\delta_{ij}}{3}) + \frac{2}{3}\bar{\rho}k^{sgs}\delta_{ij} \;;\; \nu_t = C_R\Delta^2 \mid \tilde{S} \mid \;;\; k^{sgs} = C_I\Delta^2\tilde{S}_{ij}\tilde{S}_{ij} \tag{1.4}$$

The model constants were suggested as $C_R = 0.012$ and $C_I = 0.0066$ by the theoretical approach from a priori investigation (Yoshizawa, 1986) on compressible decaying isotropic turbulence.

The algebraic Smagorinsky model has intrinsic limitations in the laminar/transition regions and does not have the correct limiting behavior near a wall, as noted by Moin et al. (1991). A dynamic model was introduced by Germano et al. (1991) to compute a non-equilibrium flow by adding a coarser test filter and calculating the model coefficients dynamically as a function of position from the information contained

in the resolved velocity field. Based on the least square approach of Lilly (1992) for the momentum SGS stress tensor, C_R and C_I are evaluated as

$$C_R = \frac{< L_{ij} M_{ij} >}{< M_{kl} M_{kl} >} - \frac{1}{3} \frac{< L_{mm} M_{nn} >}{< M_{kl} M_{kl} >} \; ; \quad C_I = \frac{< L_{kk} >}{< \beta - \hat{\alpha} >} \tag{1.5}$$

The forms of L_{ij}, M_{ij} and β are

$$L_{ij} = \widehat{\overline{\rho} \tilde{u}_i \tilde{u}_j} - \hat{\overline{\rho}} \tilde{\tilde{u}}_i \tilde{\tilde{u}}_j = \widehat{\overline{\rho u_i} \overline{\rho u_j} / \overline{\rho}} - \widehat{\overline{\rho u_i}} \, \widehat{\overline{\rho u_j}} / \hat{\overline{\rho}} \tag{1.6}$$

$$M_{ij} = \beta_{ij} - \hat{\alpha}_{ij} \tag{1.7}$$

$$\beta_{ij} = -2 \hat{\Delta}^2 \hat{\overline{\rho}} \, | \tilde{\tilde{S}} | \, (\tilde{\tilde{S}}_{ij} - \frac{\delta_{ij}}{3} \tilde{\tilde{S}}_{kk}) \tag{1.8}$$

$$\beta = 2 \hat{\overline{\rho}} \hat{\Delta}^2 \, | \tilde{\tilde{S}} |^2 \tag{1.9}$$

where over-hat represents the test-filtered variable. A Favre-filtered variable under test-filtering is defined as $\tilde{\tilde{f}} = \widehat{\overline{\rho f}} / \hat{\overline{\rho}}$. The brackets $< \cdot >$ denote an appropriate average to ensure the stability of numerical calculations (Moin et al., 1991; Germano et al., 1991). The average operator can be locally smoothed using the same test filter, as demonstrated by Fureby (1996).

The WALE model proposed by Nicoud and Ducros (1999) is another eddy-viscosity model. It is based on the square of the velocity gradient tensor to account for the effects of both the strain and the rotation rate of the smallest resolved turbulent fluctuations.

$$\nu_t = \left(C_w \Delta \right)^2 \overline{OP}_1 / \overline{OP}_2 \; ; \; C_w^2 = C_s^2 \left\langle \sqrt{2} \left(\tilde{S}_{ij} \tilde{S}_{ij} \right)^{3/2} \right\rangle \Big/ \left\langle \tilde{S}_{ij} \tilde{S}_{ij} \, \overline{OP}_1 / \overline{OP}_2 \right\rangle ; \tag{1.10}$$

$$\overline{OP_1} = \left(\hbar_{ij}^d \hbar_{ij}^d\right)^{3/2}, \quad \overline{OP_2} = \left(\tilde{S}_{ij}\tilde{S}_{ij}\right)^{5/2} + \left(\hbar_{ij}^d \hbar_{ij}^d\right)^{5/4} \tag{1.11}$$

where $\hbar_{ij}^d = \tilde{S}_{ik}\tilde{S}_{kj} + \tilde{\Omega}_{ik}\tilde{\Omega}_{kj} - \delta_{ij}\left[\tilde{S}_{mn}\tilde{S}_{mn} - \tilde{\Omega}_{mn}\tilde{\Omega}_{mn}\right]/3$ is the traceless symmetric part of the square of the velocity gradient tensor. The eddy viscosity goes naturally to zero in the vicinity of wall or in the case of pure shear. Moreover, the WALE model is well suited in complex geometries as it is invariant to any coordinate translation or rotation and only local information is needed in the formulations.

Bardina et al. (1980) proposed a scale-similar model based on the assumption that the most active SGSs are those closer to the cutoff. The coupling effects for the scales far from the cutoff wave number are not as strong as those for the scales immediately above it. This model was found to underestimate the dissipation, making it unsuitable for turbulent flows with large density fluctuations or compressible isotropic turbulence at low Mach numbers (Speziale et al., 1988). In order to overcome these limitations, the scale-similar model was later combined with the eddy-viscosity model to include the effects of Leonard and cross stresses (Erlebacher et al., 1992; Speziale et al., 1988) such that

$$\tau_{ij}^{sgs} - \frac{\delta_{ij}\tau_{kk}^{sgs}}{3} = C_s\alpha_{ij} + A_{ij} - \frac{\delta_{ij}A_{kk}}{3} \tag{1.12}$$

$$\tau_{kk}^{sgs} = C_I\alpha_{kk} + A_{kk} \tag{1.13}$$

where $A_{ij} = \bar{\rho}\left(\widetilde{\tilde{u}_i\tilde{u}_j} - \tilde{\tilde{u}}_i\tilde{\tilde{u}}_j\right)$.

More recently, the coupling between SGS modeling and the truncation error of numerical discretization have been investigated. Ghosal (1996) found that the truncation

error of a fourth-order accurate central-difference discretization could have the same order of magnitude as the SGS stress. This theoretical result was corroborated by Kravchenko and Moin (1997) using numerical simulations. The implicit SGS modeling was thus developed to employ the truncation error into the modeling of the unresolved scales, instead of an explicit computation of the SGS stress tensor. Adams and Franz (2004) and Hickel et al. (2006) proposed and extended the adaptive local deconvolution method (ALDM), representing a full merging of numerical discretization and the SGS model. A comprehensive review of the various ways to approach implicit SGS was presented by Grinstein and Fureby (2007).

1.2.4.3 On the Simulation of Transonic/Supersonic Flows

The sonic jet into a supersonic crossflow is computationally complex, due to the concurrent presence of sharp discontinuities and strong turbulence (as shown in Section 2.1).

To capture a highly discontinuous phenomenon such as a shock, a stable resolution of discontinuities with high accuracy is required. The Godunov-type scheme is a popular shock-capturing method which finds the exact or approximate solution of the local Riemann problem at the cell interface. Among the approximate Riemann solvers, Roe schemes are proven to have good shock-capturing abilities as well as good contact and shear-wave resolving properties, yet a number of problems are encountered in using Roe schemes to solve multi-dimensional flows (Quirk, 1994), including the so-called shock instability in the vicinity of strong shock waves, the nonexistence of a solution for

strong expansion flows, and the entropy violating conditions. As effective cures, combined fluxes (Quirk, 1994), pressure sensing functions (Kim et al., 2010), and entropy fix methods (Lin, 1991; Sanders et al., 1998) have been widely discussed.

A common feature among shock-capturing schemes is that they are generally upwind-biased and very dissipative. This becomes a serious issue when smooth components such as vortices and acoustic waves are also present in the problem. To avoid excessively smearing the discontinuity as well as preserving resolution in the smooth region, schemes with a higher order accuracy which can solve shocks in an essentially nonoscillatory (ENO) fashion have been developed, such as the weighted essentially nonoscillatory (WENO) scheme (Liu et al., 1994; Jiang and Shu, 1996; Borges et al., 2008).

In the context of JICF, recent numerical investigations have adopted one of the aforementioned schemes or an extension of one. Peterson et al. (2006) evaluated the inviscid fluxes using a modified Steger-Warming flux vector splitting method, and a third-order upwind-biased flux reconstruction was used to calculate the fluxes at the cell surface. Boles et al. (2008, 2010) used Edward's low dissipation flux split scheme (LDFSS) and extended it to a higher-order spatial accuracy by using the Piecewise Parabolic Method (PPM) to calculate the inviscid fluxes. Won et al. (2010) formulated the convective fluxes with artificial dissipation using Roe's flux difference splitting method. The primitive variables at the cell interface were extrapolated through the use of the monotone upstream-centered schemes for conservation laws (MUSCL) scheme. Ferrante et al. (2009, 2010) used a hybrid approach, applying tuned centered finite differences (TCD) in smooth flow regions and the WENO scheme around discontinuities

and ghost-fluid boundaries. Génin and Menon (2010) introduced the smoothness parameters and applied the center scheme and MUSCL-type upwind scheme to the smooth and discontinuous regions, respectively.

1.3 Objective and Outline of Thesis

While extensive research has been conducted to capture the flow physics and the scalar mixing process, there remain certain unclear issues such as the energy distribution and transportation within the complex vortex system, and the interaction and connection between the coherent structures and scalar mixing, especially under the conditions of realistic gas turbine combustion. Moreover, much of the previous work has used water or low-speed gases as the working fluids; consequently, the scenarios under realistic gas turbine conditions—that is, relatively high injection speeds with moderate velocity ratios—are rarely discussed. The purpose of the current work is to fill the gap and to remedy the aforementioned deficiencies based on high-fidelity numerical simulation and state-of-the-art data analysis techniques.

The fuel injection processes occur within an unsteady environment. The existing works on the jet into unsteady crossflow, however, are limited. For the rare preceding studies, water was used as the working fluid for both jet and crossflow fluid. In this work, we try to evaluate the acoustic effect within the context of gaseous jet into crossflow by adding external excitations to the crossflow. Multiple sets of forcing frequency/ amplitude are tested to cover a broad range of realistic fluctuations. To capture the peculiar features, the Proper Orthogonal Decomposition (POD) is

implemented to extract the dominant structures in the pressure, velocity, and mixing fields.

Last but not least, the mixing of a sonic jet into supersonic crossflow is investigated. The salient flow structures are clearly captured and carefully analyzed to explore their roles in the compressible mixing layer. The mean scalar field is compared to the experimental counterpart, and the overall mixing efficiency is quantified according to the mixing indices.

The work is organized in seven chapters. In Chapter 2, theoretical formulations are presented, supplemented by the turbulent modeling and the evaluations of thermodynamic and transport properties. Chapter 3 reviews the numerical details, including spatial and temporal discretization, boundary conditions, and parallel implementation. The subsonic mixing cases are discussed in Chapters 4 and 5; specifically, Chapter 4 elaborates on a turbulent gaseous jet into steady crossflow, and Chapter 5 evaluates the effects of the external excitation to the crossflow. In Chapter 6, the supersonic mixing cases are investigated by reproducing Lin et al.'s experimental results (2010). A summary of the work is provided in Chapter 7, and future research opportunities in this field are suggested.

This page intentionally left blank

Chapter 2

Theoretical Formulations

2.1 Governing Equations

The formulation is based on the full conservation equations of mass, momentum, energy and species in Cartesian coordinates such that

$$\frac{\partial \rho}{\partial t} + \frac{\partial \rho u_j}{\partial x_j} = 0 \tag{2.1}$$

$$\frac{\partial \rho u_i}{\partial t} + \frac{\partial (\rho u_i u_j)}{\partial x_j} = -\frac{\partial p}{\partial x_i} + \frac{\partial \tau_{ij}}{\partial x_j} \tag{2.2}$$

$$\frac{\partial \rho E}{\partial t} + \frac{\partial [(\rho E + p) u_i]}{\partial x_i} = -\frac{\partial q_i}{\partial x_i} + \frac{\partial (u_i \tau_{ij})}{\partial x_j} \tag{2.3}$$

$$\frac{\partial \rho Y_k}{\partial t} + \frac{\partial \rho Y_k \left(u_j + U_{k,j}\right)}{\partial x_j} = \dot{\omega}_k, \quad k = 1, \cdots, N \tag{2.4}$$

where $i, j,$ and k are the spatial coordinate index, the dummy index to spatial coordinate, and the species index, respectively; N is the total number of species; and Y_k and $U_{k,j}$ represent the mass fraction and diffusion velocities of species k, respectively. For binary mixture and ordinary diffusion only, Fick's law is used to evaluate the diffusive flux:

$$\rho Y_k U_{k,j} = -\rho D_{AB} \frac{\partial Y_k}{\partial x_j} \tag{2.5}$$

where D_{AB} is the binary mass diffusion coefficient for the two species, A and B.

The viscous tensor τ_{ij} for a Newtonian fluid (with Stokes assumption) and the heat flux vector q_j are defined as:

$$\tau_{ij} = \mu\left(\frac{\partial u_i}{\partial x_j} + \frac{\partial u_j}{\partial x_i} - \frac{2}{3}\delta_{ij}\frac{\partial u_l}{\partial x_l}\right) \tag{2.6}$$

$$q_j = -\lambda\frac{\partial T}{\partial x_j} + \rho\sum_{k=1}^{N} h_k Y_k U_{k,j} \tag{2.7}$$

where μ and λ are the coefficients of viscosity and heat conductivity, respectively. Within the thermodynamic regime of the present concern, μ and λ can be represented by polynomial functions of temperature. The specific total energy E is given by:

$$E = e + \frac{u_i u_i}{2} \tag{2.8}$$

The governing equations are supplemented with the equation of state for an ideal gas. Then the specific internal energy e is obtained as:

$$e = h - \frac{p}{\rho} \tag{2.9}$$

The specific enthalpy of mixture h containing contributions from its constituent species can be written as:

$$h = \sum_{k=1}^{N} Y_k h_k = \sum_{k=1}^{N} Y_k\left(h_{ref,k} + \int_{T_{ref}}^{T} C_{p,k}\,dT\right) \tag{2.10}$$

The species specific heat at constant pressure $C_{p,k}$ can be approximated by a polynomial function of temperature:

$$C_{p,k} = \sum_{p=1}^{M} a_{k,p} T^{p-1} \tag{2.11}$$

The formulation is closed by an equation of state for a perfect mixture:

$$p = \rho R_u T \sum_{k=1}^{N} \frac{Y_k}{W_k} = \rho RT \tag{2.12}$$

where R_u is the universal gas constant and W_k is the molecular weight of species k. $\dot{\omega}_k$ is the net mass production rate of species k by chemical reaction. Since no chemical reaction is involved in this work, $\dot{\omega}_k$ is set to be zero.

2.2 Turbulent Closure: Large Eddy Simulation

One of the characteristics of turbulence flow is that various length scales exist in the global structure, and each length scale functions differently. Large eddies, which are strongly dependent on mean flow and geometry, transfer kinetic energy of the mean flow to turbulent kinetic energy; conversely, small eddies, which tend to be homogenous and universal and less affected by the boundary layer, dissipate turbulent kinetic energy to internal energy. The LES technique, which has demonstrated great capability in many complex scenarios, is implemented in the present work to resolve the large eddies' contribution and to model the effect of the unresolved scales.

2.2.1 Filtering Operations

In a large eddy simulation, the separation of large scales from the small scales is achieved by a filtering operation. A filtered (or resolved, or large-scale) variable is defined as:

$$\bar{f}(\mathbf{x}) = \int_{\infty} f(\mathbf{x}) G_f(\mathbf{x} - \mathbf{x}') d\mathbf{x}' \tag{2.13}$$

where G_f is the filter function and $\int_{\infty} G_f(\mathbf{x}) d\mathbf{x} = 1$. Leonard (1974) indicated that if G_f is only a function of $\mathbf{x} - \mathbf{x}'$, differentiation and the filtering operation could commute with each other.

In a finite-volume method, the cell-averaged variables are defined at each cell as:

$$\bar{f} = \frac{1}{\Delta V} \int_{\Delta V} f(\mathbf{x}) d\mathbf{x} \tag{2.14}$$

This procedure is essentially a top-hat filtering operation. A detailed description of the properties of various filters can be found in text book (Pope, 2000).

2.2.2 Filtered Governing Equations

The Favre-averaging is used here to simplify the governing equations and to account for the variable density effects. Hereafter, any instantaneous variable is defined as the sum of a Favre-averaged filtered scale and a subgrid scale such that:

$$f = \tilde{f} + f'' \tag{2.15}$$

where the Favre-filtered quantity is defined as $\tilde{f} = \overline{\rho f} / \bar{\rho}$.

The Favre-averaged conservation equations of mass, momentum, energy and species can be written as:

$$\frac{\partial \bar{\rho}}{\partial t} + \frac{\partial \bar{\rho} \tilde{u}_j}{\partial x_j} = 0 \tag{2.16}$$

$$\frac{\partial \overline{\rho}\widetilde{u}_i}{\partial t}+\frac{\partial(\overline{\rho}\widetilde{u}_i\widetilde{u}_j+\overline{p}\delta_{ij})}{\partial x_j}=\frac{\partial\left(\widetilde{\tau}_{ij}-\tau_{ij}^{sgs}\right)}{\partial x_j} \tag{2.17}$$

$$\frac{\partial \overline{\rho}\tilde{E}}{\partial t}+\frac{\partial((\overline{\rho}\tilde{E}+\overline{p})\tilde{u}_i)}{\partial x_i}=\frac{\partial}{\partial x_i}(\tilde{u}_j\tilde{\tau}_{ij}+\lambda\frac{\partial\tilde{T}}{\partial x_i}-H_i^{sgs}+\sigma_i^{sgs}) \tag{2.18}$$

$$\frac{\partial \overline{\rho}\tilde{Y}_k}{\partial t}+\frac{\partial\left(\overline{\rho}\tilde{u}_j\tilde{Y}_k\right)}{\partial x_j}=\frac{\partial}{\partial x_j}\left(-\overline{\rho}\tilde{Y}_k\tilde{U}_{k,j}-\Phi_{k,j}^{sgs}-\theta_{k,j}^{sgs}\right)+\overline{\dot{\omega}}_k \tag{2.19}$$

where the unclosed subgrid terms are:

$$\tau_{ij}^{sgs}=(\overline{\rho u_i u_j}-\overline{\rho}\widetilde{u}_i\widetilde{u}_j) \tag{2.20}$$

$$H_i^{sgs}=(\overline{\rho E u_i}-\overline{\rho}\widetilde{E}\widetilde{u}_i)+(\overline{p u_i}-\overline{p}\widetilde{u}_i) \tag{2.21}$$

$$\sigma_{ij}^{sgs}=(\overline{u_j\tau_{ij}}-\widetilde{u}_j\widetilde{\tau}_{ij}) \tag{2.22}$$

$$\Phi_{k,j}^{sgs}=(\overline{\rho Y_k u_j}-\overline{\rho}\widetilde{Y}_k\widetilde{u}_j) \tag{2.23}$$

$$\Theta_{k,j}^{sgs}=(\overline{\rho Y_k U_{k,j}}-\overline{\rho}\widetilde{Y}_k\widetilde{U}_{k,j}) \tag{2.24}$$

Those terms arising from the unresolved scales must be modeled in terms of resolved scales. Because the filter scale of LES falls in the turbulence inertial range, the modeling of the subgrid terms is relatively universal in comparison with the RANS modeling. This apparently is the biggest advantage of LES. The subgrid-scale models will be discussed in detail in the following section.

In addition to the conservation equation, the equation of state also needs to be filtered as:

$$\overline{p}=\overline{\rho}R_u\tilde{T}\sum_{k=1}^{N}\frac{\tilde{Y}_k}{W_k}+\overline{\rho}R_u\sum_{k=1}^{N}\frac{T_k^{sgs}}{W_k} \tag{2.25}$$

where $T_k^{sgs} = \overline{\rho T Y_k} / \bar{\rho} - \tilde{T}\tilde{Y}_k$. For high heat release reacting cases, this correlation might have a discernible effect on the results, but it is disregarded in the current study due to the difficulty and uncertainty in the modeling process (Calhoon and Menon, 1996).

The filtered total energy can be approximated as:

$$\tilde{E} = \tilde{h} - \frac{\tilde{p}}{\bar{\rho}} + \frac{\tilde{u}_k^2}{2} + k^{sgs} = \tilde{\psi} + \int_{T_{ref}}^{\tilde{T}} C_p(T)\,dT - \frac{\tilde{p}}{\bar{\rho}} + \frac{\tilde{u}_k^2}{2} + k^{sgs} \tag{2.26}$$

where $\tilde{\psi} = \sum_{k=1}^{N} \tilde{Y}_k \Delta h_{f,k}^0$ and $k^{sgs} = \tau_{kk}^{sgs} / 2\bar{\rho} = \left(\overline{\rho u_k u_k} / \bar{\rho} - \tilde{u}_k^2 \right) / 2$.

2.2.3 Subgrid-Scale Models

The SGS modeling is the core of LES. Several recent models were reviewed in Chapter 1. An algebraic eddy-viscosity model is elaborated here. This model is based on the assumption that the small scales' motions have much shorter time restraints than the large, energy-carrying eddies. Therefore, they can adjust rapidly to perturbations and recover equilibrium nearly instantaneously. The eddy viscosity is thus obtained algebraically without solving additional equations:

$$\nu_T = (C_s \Delta)^2 \,|\, \tilde{S} \,| \tag{2.27}$$

where Δ is the filter width and $|\, \tilde{S} \,| = (2\tilde{S}_{ij}\tilde{S}_{ij})^{1/2}$. The coefficient C_s can be determined from the isotropic turbulence decay or a priori test.

Erlebacher et al. (1992) extended the above model to include the flow compressibility effect such that

$$\tau_{ij}^{sgs} = -2\nu_t \overline{\rho}(\widetilde{S}_{ij} - \frac{\widetilde{S}_{kk}\delta_{ij}}{3}) + \frac{2}{3}\overline{\rho}k^{sgs}\delta_{ij} \tag{2.28}$$

where

$$\nu_t = C_R \Delta^2 |\widetilde{S}| \tag{2.29}$$

$$k^{sgs} = C_I \Delta^2 \widetilde{S}_{ij}\widetilde{S}_{ij} \tag{2.30}$$

and the dimensionless quantities C_R and C_I represent the compressible Smagorinsky constants. The Van-Driest damping function (D) is used to take into account the inhomogeneities near the surface (Moin and Kim, 1982), and is expressed as

$$D = 1 - \exp\left(1 - (y^+)^3 / 26^3\right) \tag{2.31}$$

where $y^+ = yu_\tau / \nu$ and u_τ is the friction velocity.

The subgrid energy flux term H_j^{sgs} is modeled as

$$H_j^{sgs} = -\overline{\rho}\frac{\nu_t}{Pr_t}\left(\frac{\partial \widetilde{h}}{\partial x_j} + \widetilde{u}_i \frac{\partial \widetilde{u}_i}{\partial x_j} + \frac{1}{2}\frac{\partial k^{sgs}}{\partial x_j}\right) \tag{2.32}$$

where Pr_t represents the turbulent Prandtl number (here a standard value of 0.7).

The convective species flux term is usually approximated as:

$$\Phi_{k,i}^{sgs} = -\overline{\rho}\frac{\nu_t}{Sc_t}\frac{\partial \widetilde{Y}_k}{\partial x_i} \tag{2.33}$$

where Sc_t is the turbulent Schmidt number (a value of 0.9 in this work).

The SGS viscous diffusion term, σ_{ij}^{sgs}, is neglected due to its small contribution to the total energy equation. The SGS species diffusive fluxes ($\Theta_{k,j}^{sgs}$), which come from the correlation of species mass fractions with diffusion velocities, are also overlooked.

As for the dynamic model introduced by Germano et al. (1991), the equilibrium assumption is relaxed and the model coefficients are computed dynamically in a non-equilibrium flow. A detailed introduction can be found in Wang (2002).

Both the algebraic Smagorinsky model and the dynamic Smagorinsky model are considered in the current study and their differences are compared in Chapter 4.

2.3 Evaluation of Thermodynamic and Transport Properties

Following Lin et al.'s experiment (2010) with the sonic jet into supersonic crossflow, the working fluids have a relatively low temperature in contrast to most cases commonly encountered. To precisely represent the thermodynamic and transport properties, the data sources (claimed to be valid in the temperature range of 50-1000 K) in The Properties of Gases and Liquids (Poling et al., 2000) are used to calculate the specific heat as a fourth-order polynomial function of temperature such that

$$c_{pk} = \sum_{i=0}^{4} a_{ik} T^i \tag{2.34}$$

To assess the thermal conductivity and viscosity, the curve-fitting technique is applied to NIST calculations. The curve-fitted algebraic equations are then incorporated into the code with air treated as a mixture of 75.57% N_2, 1.27% Ar, and 23.16% O_2 in mass.

The binary mass diffusion coefficient for species A and species B is calculated based on the Chapman-Enskog theoretical description of the binary mixtures of gases at low to moderate pressures. A simplified equation is given in text book (Turns, 2000):

$$D_{AB} = \frac{0.0266T^{3/2}}{P \cdot MW_{AB}^{1/2} \cdot \sigma_{AB}^{1/2} \cdot \Omega_D} \qquad (2.35)$$

The associated units are: $D_{AB}[=]m^2/s$, $T[=]K$, and $P[=]Pa$. The terms involved are:

Collision integral: $\Omega_D = \frac{A}{(T^*)^B} + \frac{C}{\exp(DT^*)} + \frac{E}{\exp(FT^*)} + \frac{G}{\exp(HT^*)}$

Dimensionless temperature: $T^* = k_B T/\varepsilon_{AB} = k_B T/\sqrt{\varepsilon_A \varepsilon_B}$

Averaged hard-sphere collision diameter: $\sigma_{AB} = (\sigma_A + \sigma_B)/2$

Averaged molecular weight: $MW_{AB} = 2\left[(MW_A)^{-1} + (MW_B)^{-1}\right]^{-1}$

All the Lennard-Jones parameters ($\sigma_A, \sigma_B, \varepsilon_A/k_A, \varepsilon_B/k_B$) and the constants (A-H) are available in Turns (2000).

The properties evaluated in the code agree well with NIST calculation as shown in Figure 2.1.

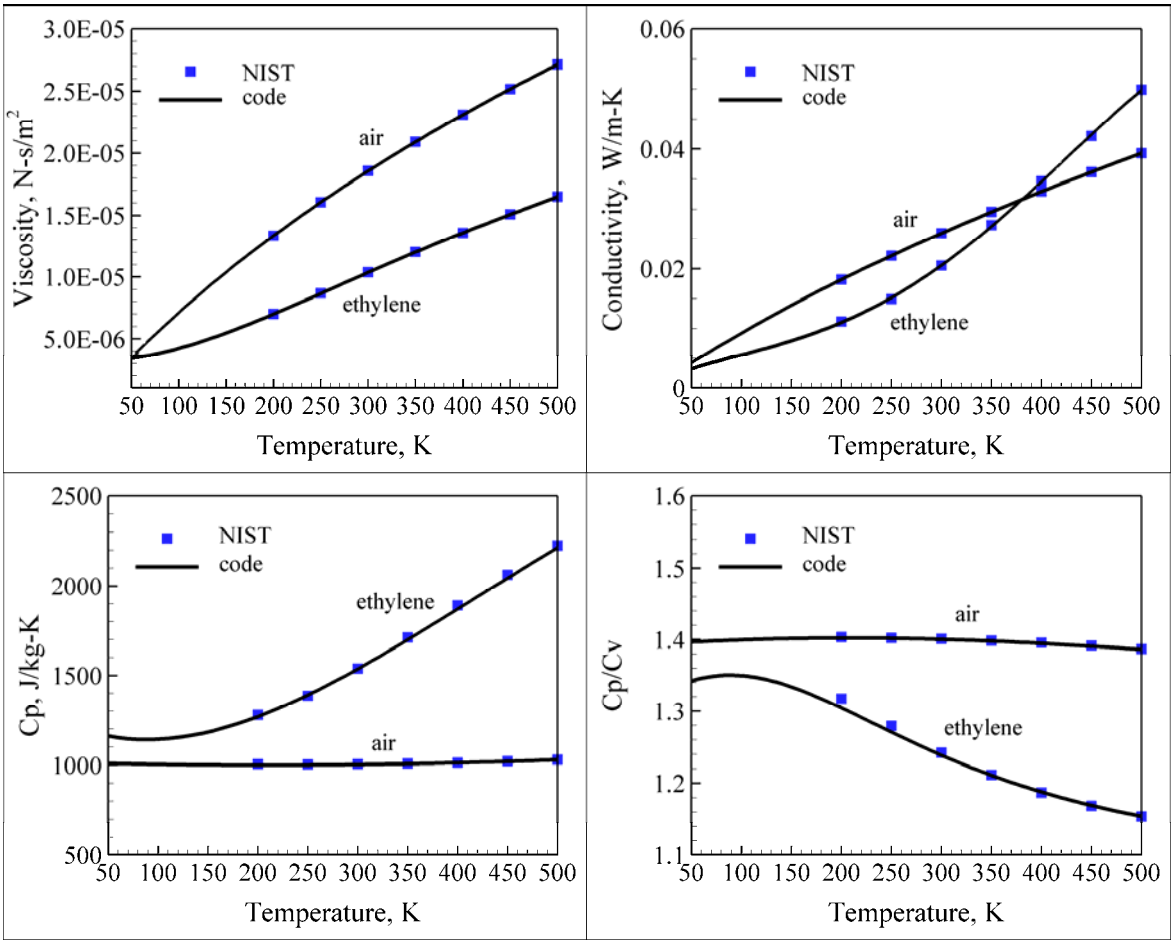

Figure 2.1 Thermodynamic and transport properties for air and ethylene

Chapter 3

Numerical Method

3.1 Mathematical Equations

The three-dimensional, unsteady, density-weighted, Favre-filtered forms of the compressible Navier-Stokes equations and species equation can be expressed as:

$$\frac{\partial \mathbf{Q}}{\partial t}+\frac{\partial(\mathbf{E}-\mathbf{E}_v)}{\partial x}+\frac{\partial(\mathbf{F}-\mathbf{F}_v)}{\partial y}+\frac{\partial(\mathbf{G}-\mathbf{G}_v)}{\partial z}=\mathbf{H} \tag{3.1}$$

where the vectors $\mathbf{Q}, \mathbf{E}, \mathbf{F}, \mathbf{G}, \mathbf{E}_v, \mathbf{F}_v, \mathbf{G}_v$ and $\mathbf{H}$ are defined as:

$$\mathbf{Q}=\left(\bar{\rho}, \overline{\rho u}, \overline{\rho v}, \overline{\rho w}, \overline{\rho E}, \overline{\rho Y_i}\right)^T \tag{3.2}$$

$$\mathbf{E}=\left(\overline{\rho u}, \overline{\rho u}^2+\bar{p}, \overline{\rho u v}, \overline{\rho u w}, \left(\overline{\rho E}+\bar{p}\right)\tilde{u}, \overline{\rho u} \tilde{Y}_i\right)^T \tag{3.3}$$

$$\mathbf{F}=\left(\overline{\rho v}, \overline{\rho u v}, \overline{\rho v}^2+\bar{p}, \overline{\rho v w}, \left(\overline{\rho E}+\bar{p}\right)\tilde{v}, \overline{\rho v} \tilde{Y}_i\right)^T \tag{3.4}$$

$$\mathbf{G}=\left(\overline{\rho w}, \overline{\rho u w}, \overline{\rho v w}, \overline{\rho w}^2+\bar{p}, \left(\overline{\rho E}+\bar{p}\right)\tilde{w}, \overline{\rho w} \tilde{Y}_i\right)^T \tag{3.5}$$

$$\mathbf{E}_v=\left(0, \bar{\tau}_{xx}-\tau_{xx}^{sgs}, \bar{\tau}_{xy}-\tau_{xy}^{sgs}, \bar{\tau}_{xz}-\tau_{xz}^{sgs}, \tilde{u}\bar{\tau}_{xx}+\tilde{v}\bar{\tau}_{xy}+\tilde{w}\bar{\tau}_{xz}+\bar{q}_x-H_x^{sgs}, -\bar{\rho}\tilde{Y}_i\tilde{U}_{i,x}-\Phi_{i,x}^{sgs}\right)^T \tag{3.6}$$

$$\mathbf{F}_v=\left(0, \bar{\tau}_{xy}-\tau_{xy}^{sgs}, \bar{\tau}_{yy}-\tau_{yy}^{sgs}, \bar{\tau}_{yz}-\tau_{yz}^{sgs}, \tilde{u}\bar{\tau}_{xy}+\tilde{v}\bar{\tau}_{yy}+\tilde{w}\bar{\tau}_{yz}+\bar{q}_y-H_y^{sgs}, -\bar{\rho}\tilde{Y}_i\tilde{U}_{i,y}-\Phi_{i,y}^{sgs}\right)^T \tag{3.7}$$

$$\mathbf{G}_v=\left(0, \bar{\tau}_{xz}-\tau_{xz}^{sgs}, \bar{\tau}_{yz}-\tau_{yz}^{sgs}, \bar{\tau}_{zz}-\tau_{zz}^{sgs}, \tilde{u}\bar{\tau}_{xz}+\tilde{v}\bar{\tau}_{yz}+\tilde{w}\bar{\tau}_{zz}+\bar{q}_z-H_z^{sgs}, -\bar{\rho}\tilde{Y}_i\tilde{U}_{i,z}-\Phi_{i,z}^{sgs}\right)^T \tag{3.8}$$

$$\mathbf{H}=\left(0,0,0,0,0,0\right)^T \tag{3.9}$$

Each nomenclature is defined beforehand and the superscript T stands for the transpose of the vector. In the following, all the "-" and "~" are omitted without confusion for simplicity.

A compressible in-house code, *Parallel Multi-Block Flow Solver - Version 2 (PMBFS2)*, is developed to time-accurately solve the governing equations and to capture the unsteady phenomena. The essences of the code are introduced in the rest of this chapter.

3.2 Finite Volume Approach

The finite-volume method is adopted to solve the conservation equations. This method is inherently conservative and allows for the treatment of arbitrary geometry. To utilize the finite-volume approach, the governing equation is integrated over the control volume V enclosed by the surface S in the physical domain as:

$$\iiint_V \left(\frac{\partial \mathbf{Q}}{\partial t} + \frac{\partial (\mathbf{E} - \mathbf{E}_v)}{\partial x} + \frac{\partial (\mathbf{F} - \mathbf{F}_v)}{\partial y} + \frac{\partial (\mathbf{G} - \mathbf{G}_v)}{\partial z} - \mathbf{H} \right) dV = 0 \qquad \textbf{(3.10)}$$

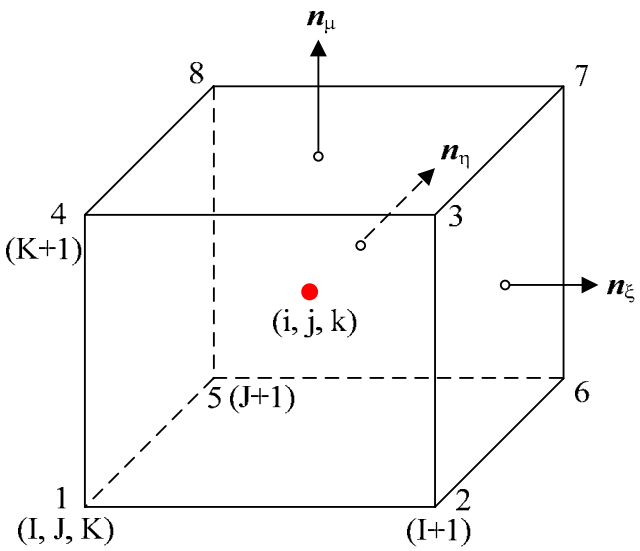

Figure 3.1 Schematic of a finite-volume cell (i, j, k)

Using the Gauss divergence theorem, the integral conservation equation takes the following form for the three-dimensional cell with six surfaces, as shown in Figure 3.1:

$$\iiint_V \frac{\partial \mathrm{Q}}{\partial t} dV + \int_{S_\xi} \vec{W} \bullet \vec{n}_\xi dS_\xi + \int_{S_\eta} \vec{W} \bullet \vec{n}_\eta dS_\eta + \int_{S_\zeta} \vec{W} \bullet \vec{n}_\zeta dS_\zeta = \iiint_V \mathrm{H} dV \tag{3.11}$$

where

$$\vec{W} = (\mathbf{E} - \mathbf{E}_v)\vec{i} + (\mathbf{F} - \mathbf{F}_v)\vec{j} + (\mathbf{G} - \mathbf{G}_v)\vec{k} \tag{3.12}$$

and $\vec{n}_\xi$, $\vec{n}_\eta$ and $\vec{n}_\zeta$ are unit normal vectors to the surface in the ξ-, η-, and ζ-directions, respectively. The unit normal vectors are related to cell surface areas $\vec{S}_\xi$, $\vec{S}_\eta$, and $\vec{S}_\zeta$ as:

$$\begin{aligned} \vec{n}_\xi &= \left(S_{\xi x}\vec{i} + S_{\xi y}\vec{j} + S_{\xi z}\vec{k}\right) / \left|\vec{S}_\xi\right| \\ \vec{n}_\eta &= \left(S_{\eta x}\vec{i} + S_{\eta y}\vec{j} + S_{\eta z}\vec{k}\right) / \left|\vec{S}_\eta\right| \\ \vec{n}_\zeta &= \left(S_{\zeta x}\vec{i} + S_{\zeta y}\vec{j} + S_{\zeta z}\vec{k}\right) / \left|\vec{S}_\zeta\right| \end{aligned} \tag{3.13}$$

The cell surface areas are defined as:

$$\vec{S}_\xi = \frac{1}{2}\left(\vec{r}_{72} \times \vec{r}_{36}\right) = \frac{1}{2}\begin{vmatrix} \vec{i} & \vec{j} & \vec{k} \\ x_2 - x_7 & y_2 - y_7 & z_2 - z_7 \\ x_6 - x_3 & y_6 - y_3 & z_6 - z_3 \end{vmatrix} = S_{\xi x}\vec{i} + S_{\xi y}\vec{j} + S_{\xi z}\vec{k}$$

$$\vec{S}_\eta = \frac{1}{2}\left(\vec{r}_{86} \times \vec{r}_{75}\right) = \frac{1}{2}\begin{vmatrix} \vec{i} & \vec{j} & \vec{k} \\ x_6 - x_8 & y_6 - y_8 & z_6 - z_8 \\ x_5 - x_7 & y_5 - y_7 & z_5 - z_7 \end{vmatrix} = S_{\eta x}\vec{i} + S_{\eta y}\vec{j} + S_{\eta z}\vec{k} \qquad \textbf{(3.14)}$$

$$\vec{S}_\zeta = \frac{1}{2}\left(\vec{r}_{74} \times \vec{r}_{83}\right) = \frac{1}{2}\begin{vmatrix} \vec{i} & \vec{j} & \vec{k} \\ x_4 - x_7 & y_4 - y_7 & z_4 - z_7 \\ x_3 - x_8 & y_3 - y_8 & z_3 - z_8 \end{vmatrix} = S_{\zeta x}\vec{i} + S_{\zeta y}\vec{j} + S_{\zeta z}\vec{k}$$

The magnitude of each surface vector can be obtained by

$$\left|\vec{S}_\xi\right| = \left(S_{\xi x}{}^2 + S_{\xi y}{}^2 + S_{\xi z}{}^2\right)^{1/2}$$

$$\left|\vec{S}_\eta\right| = \left(S_{\eta x}{}^2 + S_{\eta y}{}^2 + S_{\eta z}{}^2\right)^{1/2} \qquad \textbf{(3.15)}$$

$$\left|\vec{S}_\zeta\right| = \left(S_{\zeta x}{}^2 + S_{\zeta y}{}^2 + S_{\zeta z}{}^2\right)^{1/2}$$

The cell volume ΔV associated with each cell can be evaluated using Kordulla and Vinokur's (1983) formula:

$$\Delta V = \frac{1}{2}\vec{r}_{17}\left(\vec{S}_\xi + \vec{S}_\eta + \vec{S}_\zeta\right) \qquad \textbf{(3.16)}$$

Assuming the increments $\Delta\xi=\Delta\eta=\Delta\zeta=1$ in the body-fitted coordinate system and substituting Equations 3.12 and 3.13 into Equation 3.11 yields the following governing equation in the general coordinates:

$$\frac{\Delta \mathbf{Q}}{\Delta t}\cdot\Delta V + \left(\mathbf{E}_\xi - \mathbf{E}_{\xi v}\right)\Big|_{i-1/2,j,k}^{i+1/2,j,k} + \left(\mathbf{F}_\eta - \mathbf{F}_{\eta v}\right)\Big|_{i,j-1/2,k}^{i,j+1/2,k} + \left(\mathbf{G}_\zeta - \mathbf{G}_{\zeta v}\right)\Big|_{i,j,k-1/2}^{i,j,k+1/2} = \mathbf{H}\cdot\Delta V \qquad \textbf{(3.17)}$$

where $\Delta\mathbf{Q}$ is defined as:

$$\Delta\mathbf{Q} = \mathbf{Q}^{n+1} - \mathbf{Q}^{n} \tag{3.18}$$

The inviscid flux terms $\mathbf{E}_{\xi}, \mathbf{F}_{\eta}, \mathbf{G}_{\zeta}$ are:

$$\mathbf{E}_{\xi} = \left(S_{\xi x}\mathbf{E} + S_{\xi y}\mathbf{F} + S_{\xi z}\mathbf{G}\right) = \begin{pmatrix} \rho U \\ \rho u U + S_{\xi x} p \\ \rho v U + S_{\xi y} p \\ \rho w U + S_{\xi z} p \\ (\rho E + p) U \\ \rho Y_k U \end{pmatrix}$$

$$\mathbf{F}_{\eta} = \left(S_{\eta x}\mathbf{E} + S_{\eta y}\mathbf{F} + S_{\eta z}\mathbf{G}\right) = \begin{pmatrix} \rho V \\ \rho u V + S_{\eta x} p \\ \rho v V + S_{\eta y} p \\ \rho w V + S_{\eta z} p \\ (\rho E + p) V \\ \rho Y_k V \end{pmatrix} \tag{3.19}$$

$$\mathbf{G}_{\zeta} = \left(S_{\zeta x}\mathbf{E} + S_{\zeta y}\mathbf{F} + S_{\zeta z}\mathbf{G}\right) = \begin{pmatrix} \rho W \\ \rho u W + S_{\zeta x} p \\ \rho v W + S_{\zeta y} p \\ \rho w W + S_{\zeta z} p \\ (\rho E + p) W \\ \rho Y_k W \end{pmatrix}$$

where the contravariant velocities are given by:

$$\begin{aligned} U &= S_{\xi x}u + S_{\xi y}v + S_{\xi z}w \\ V &= S_{\eta x}u + S_{\eta y}v + S_{\eta z}w \\ W &= S_{\zeta x}u + S_{\zeta y}v + S_{\zeta z}w \end{aligned} \tag{3.20}$$

The viscous flux terms $\mathbf{E}_{\xi v}, \mathbf{F}_{\eta v}, \mathbf{G}_{\zeta v}$ are:

$$\mathbf{E}_{\xi\nu}=\left(S_{\xi x}\mathbf{E}_{\nu}+S_{\xi y}\mathbf{F}_{\nu}+S_{\xi z}\mathbf{G}_{\nu}\right)=\begin{pmatrix}0\\ S_{\xi x}\left(\tau_{xx}-\tau_{xx}^{sgs}\right)+S_{\xi y}\left(\tau_{xy}-\tau_{xy}^{sgs}\right)+S_{\xi z}\left(\tau_{xz}-\tau_{xz}^{sgs}\right)\\ S_{\xi x}\left(\tau_{yx}-\tau_{yx}^{sgs}\right)+S_{\xi y}\left(\tau_{yy}-\tau_{yy}^{sgs}\right)+S_{\xi z}\left(\tau_{yz}-\tau_{yz}^{sgs}\right)\\ S_{\xi x}\left(\tau_{zx}-\tau_{zx}^{sgs}\right)+S_{\xi y}\left(\tau_{zy}-\tau_{zy}^{sgs}\right)+S_{\xi z}\left(\tau_{zz}-\tau_{zz}^{sgs}\right)\\ S_{\xi x}b_x+S_{\xi y}b_y+S_{\xi z}b_z\\ S_{\xi x}c_x+S_{\xi y}c_y+S_{\xi z}c_z\end{pmatrix}$$

$$\mathbf{F}_{\eta\nu}=\left(S_{\eta x}\mathbf{E}_{\nu}+S_{\eta y}\mathbf{F}_{\nu}+S_{\eta z}\mathbf{G}_{\nu}\right)=\begin{pmatrix}0\\ S_{\eta x}\left(\tau_{xx}-\tau_{xx}^{sgs}\right)+S_{\eta y}\left(\tau_{xy}-\tau_{xy}^{sgs}\right)+S_{\eta z}\left(\tau_{xz}-\tau_{xz}^{sgs}\right)\\ S_{\eta x}\left(\tau_{yx}-\tau_{yx}^{sgs}\right)+S_{\eta y}\left(\tau_{yy}-\tau_{yy}^{sgs}\right)+S_{\eta z}\left(\tau_{yz}-\tau_{yz}^{sgs}\right)\\ S_{\eta x}\left(\tau_{zx}-\tau_{zx}^{sgs}\right)+S_{\eta y}\left(\tau_{zy}-\tau_{zy}^{sgs}\right)+S_{\eta z}\left(\tau_{zz}-\tau_{zz}^{sgs}\right)\\ S_{\eta x}b_x+S_{\eta y}b_y+S_{\eta z}b_z\\ S_{\eta x}c_x+S_{\eta y}c_y+S_{\eta z}c_z\end{pmatrix} \tag{3.21}$$

$$\mathbf{G}_{\zeta\nu}=\left(S_{\zeta x}\mathbf{E}_{\nu}+S_{\zeta y}\mathbf{F}_{\nu}+S_{\zeta z}\mathbf{G}_{\nu}\right)=\begin{pmatrix}0\\ S_{\zeta x}\left(\tau_{xx}-\tau_{xx}^{sgs}\right)+S_{\zeta y}\left(\tau_{xy}-\tau_{xy}^{sgs}\right)+S_{\zeta z}\left(\tau_{xz}-\tau_{xz}^{sgs}\right)\\ S_{\zeta x}\left(\tau_{yx}-\tau_{yx}^{sgs}\right)+S_{\zeta y}\left(\tau_{yy}-\tau_{yy}^{sgs}\right)+S_{\zeta z}\left(\tau_{yz}-\tau_{yz}^{sgs}\right)\\ S_{\zeta x}\left(\tau_{zx}-\tau_{zx}^{sgs}\right)+S_{\zeta y}\left(\tau_{zy}-\tau_{zy}^{sgs}\right)+S_{\zeta z}\left(\tau_{zz}-\tau_{zz}^{sgs}\right)\\ S_{\zeta x}b_x+S_{\zeta y}b_y+S_{\zeta z}b_z\\ S_{\zeta x}c_x+S_{\zeta y}c_y+S_{\zeta z}c_z\end{pmatrix}$$

where

$$\begin{aligned} b_x&=u\tau_{xx}+v\tau_{xy}+w\tau_{xz}+q_x-H_x^{sgs}; \quad c_x=-\rho Y_i U_{i,x}-\Phi_{i,x}^{sgs}\\ b_y&=u\tau_{yx}+v\tau_{yy}+w\tau_{yz}+q_y-H_y^{sgs}; \quad c_y=-\rho Y_i U_{i,y}-\Phi_{i,y}^{sgs}\\ b_z&=u\tau_{zx}+v\tau_{zy}+w\tau_{zz}+q_z-H_z^{sgs}; \quad c_z=-\rho Y_i U_{i,z}-\Phi_{i,z}^{sgs}\end{aligned} \tag{3.22}$$

The quantities $\mathbf{E}_{\xi,i\pm1/2,j,k}$, $\mathbf{E}_{\xi\nu,i\pm1/2,j,k}$, $\mathbf{F}_{\eta,i,j\pm1/2,k}$, $\mathbf{F}_{\eta\nu,i,j\pm1/2,j,k}$, $\mathbf{G}_{\zeta,i,j,k\pm1/2}$ and $\mathbf{G}_{\zeta\nu,i,j,k\pm1/2}$ represent the numerical fluxes associated with each cell interface (see Figure 3.1).

In fact, the above analysis describes the transformation of a hexahedral cell with a volume ΔV in *x*-*y*-*z* coordinates to a cubic cell with unit volume in the general coordinate (i.e., ξ-η-ζ coordinates).

The maximum time increment Δt of each cell can be evaluated by:

$$\Delta t = \frac{\Delta t_\xi \, \Delta t_\eta \, \Delta t_\zeta}{\Delta t_\xi \, \Delta t_\eta + \Delta t_\eta \, \Delta t_\zeta + \Delta t_\zeta \, \Delta t_\xi} \tag{3.23}$$

where

$$\begin{aligned} \Delta t_\xi &= \frac{CFL \cdot \Delta V}{\left| uS_{\xi x} + vS_{\xi y} + wS_{\xi z} \right| + c \left| \vec{S}_\xi \right|} \\ \Delta t_\eta &= \frac{CFL \cdot \Delta V}{\left| uS_{\eta x} + vS_{\eta y} + wS_{\eta z} \right| + c \left| \vec{S}_\eta \right|} \\ \Delta t_\zeta &= \frac{CFL \cdot \Delta V}{\left| uS_{\zeta x} + vS_{\zeta y} + wS_{\zeta z} \right| + c \left| \vec{S}_\zeta \right|} \end{aligned} \tag{3.24}$$

and $c = \sqrt{\gamma R T}$ is the local speed of sound.

In time-accurate calculations, the predefined constant time step is always chosen to be less than the maximum time increment calculated in Equation 3.23.

3.3 Evaluation of Inviscid Fluxes

Different approaches used for evaluating the numerical fluxes at the cell interfaces lead to different schemes with disparate numerical characteristics. In this work, the central-difference scheme and the upwind scheme are considered.

3.3.1 Central Scheme and Artificial Dissipations

For the central-difference scheme, the convective fluxes at any cell face in the ξ-direction can be written as:

$$\hat{\mathbf{E}}_{\xi,i+1/2,j,k} = \frac{1}{2}\left[\mathbf{E}_{\xi}(\mathbf{Q}^{L}) + \mathbf{E}_{\xi}(\mathbf{Q}^{R})\right] \tag{3.25}$$

where the left (L) and right (R) stencils are used to ensure desired accuracy.

Depending on the manner in which these terms are evaluated, a wide variety of central schemes can be obtained. In the present work, the methodology proposed by Rai and Chakravarthy (1993) is used. Accordingly the numerical flux is computed as:

$$\hat{\hat{\mathbf{E}}}_{\xi,i+1/2,j,k} = \hat{\mathbf{E}}_{\xi,i+1/2,j,k} - \varphi^{(4)}\left(\frac{\hat{\mathbf{E}}_{\xi,i+3/2,j,k} - 2\hat{\mathbf{E}}_{\xi,i+1/2,j,k} + \hat{\mathbf{E}}_{\xi,i-1/2,j,k}}{24}\right) \tag{3.26}$$

where $\phi^{(4)}$ is the flux limiter. This term switches the truncation error associated with the flux difference from fourth-order accuracy when $\phi^{(4)} = 1$ to second-order accuracy when $\phi^{(4)} = 0$.

To evaluate to the desired accuracy, the left and right state terms in Equation 3.25 must be computed using the same or higher order accuracy. These terms are written as follows to facilitate easy switching and ensure the scheme has total-variation-diminishing (TVD) feature.

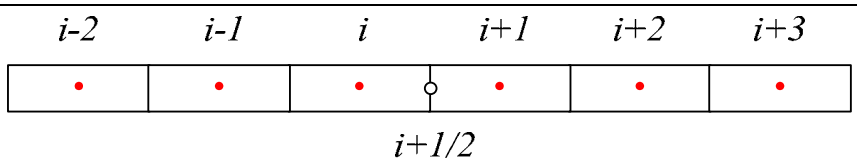

Left: $(i-2,\ i-1,\ i,\ i+1,\ i+2)$; Right: $(i-1,\ i,\ i+1,\ i+2,\ i+3)$

Figure 3.2 Schematic of the stencils used in the construction of $Q_{i+1/2}$ in ξ-direction

$$\mathbf{Q}^{L}_{i+1/2,j,k} = \mathbf{Q}_{i,j,k} + \varphi^{(3)}\left(\frac{3\nabla\mathbf{Q}_{i+1,j,k} + \nabla\mathbf{Q}_{i,j,k}}{8}\right) + \varphi^{(5)}\left(\frac{-5\nabla\mathbf{Q}_{i+2,j,k} + 7\nabla\mathbf{Q}_{i+1,j,k} + \nabla\mathbf{Q}_{i,j,k} - 3\nabla\mathbf{Q}_{i-1,j,k}}{128}\right) \quad \textbf{(3.27)}$$

$$\mathbf{Q}^{R}_{i+1/2,j,k} = \mathbf{Q}_{i+1,j,k} - \varphi^{(3)}\left(\frac{\nabla\mathbf{Q}_{i+2,j,k} + 3\nabla\mathbf{Q}_{i+1,j,k}}{8}\right) + \varphi^{(5)}\left(\frac{3\nabla\mathbf{Q}_{i+3,j,k} - \nabla\mathbf{Q}_{i+2,j,k} - 7\nabla\mathbf{Q}_{i+1,j,k} + 5\nabla\mathbf{Q}_{i,j,k}}{128}\right) \quad \textbf{(3.28)}$$

$$\nabla\mathbf{Q}_{i,j} = \mathbf{Q}_{i,j} - \mathbf{Q}_{i-1,j} \quad \textbf{(3.29)}$$

The stencils illustrated in Figure 3.2 can be used to get fifth-order accuracy ($\varphi^{(5)}=1, \varphi^{(3)}=1$), third-order accuracy ($\varphi^{(5)}=0, \varphi^{(3)}=1$), and first-order accuracy ($\varphi^{(5)}=0, \varphi^{(3)}=0$), respectively. The present work utilizes second-order overall accuracy for the spatial discretization, except close to the physical boundaries; hence, the third-order accurate evaluation of the left and right states is employed. The fluxes in η-, and ζ-directions can be computed in a similar fashion to that shown above.

To ensure the numerical stability of the central scheme, artificial dissipation must be supplemented. The form of the artificial dissipation terms depends on the order of accuracy of the numerical scheme, and must be higher-order accurate to keep its magnitude to the minimal. For the present case, the numerical differentiation of the flux vectors is second-order accurate in the core region of the computational domain. Accordingly, the artificial dissipation is fourth-order accurate. The order of accuracy of the numerical scheme decreases near the physical boundary, and the artificial dissipation terms also shift to a lower order.

In the present schemes, the form of numerical dissipation used is quite often a blending of second- and fourth-order dissipation terms. The second-order terms are used to prevent oscillations near shock waves and in flame zones to prevent spurious oscillations within such thin regions, while the fourth-order terms are important for stability and convergence. To reasonably produce the numerical dissipation, the matrix dissipation model constructed by Swanson and Turkel (1992) and by Jorgenson and Turkel (1993) is used here. In their model,

$$\begin{aligned} \mathrm{AD} &= \text{artificial dissipation} \\ &= \mathbf{d}_{i+1/2,j,k} - \mathbf{d}_{i-1/2,j,k} \end{aligned} \tag{3.30}$$

where

$$\mathbf{d}_{i\pm1/2,j,k} = \varepsilon^{(2)}_{i\pm1/2,j,k} \left|\hat{\mathrm{A}}\right|_{i\pm1/2,j,k} \left.\frac{\partial \mathbf{Q}}{\partial \xi}\right|_{i+\pm1/2,j,k} - \varepsilon^{(4)}_{i\pm1/2,j,k} \left|\hat{\mathrm{A}}\right|_{i\pm1/2,j,k} \left.\frac{\partial^3 \mathbf{Q}}{\partial \xi^3}\right|_{i\pm1/2,j,k} \tag{3.31}$$

with

$$\left|\hat{\mathbf{A}}\right| = \mathbf{M}_\xi \left|\hat{\mathbf{\Lambda}}_\xi\right| \mathbf{M}_\xi^{-1} \tag{3.32}$$

$$\varepsilon^{(2)}_{i+1/2,j,k} = \kappa^{(2)} \max(\nu_{i-1,j,k}, \nu_{i,j,k}, \nu_{i+1,j,k}, \nu_{i+2,j,k}) \tag{3.33}$$

$$\nu_{i,j,k} = \left|\frac{p_{i-1,j,k} - 2p_{i,j,k} + p_{i+2,j,k}}{p_{i-1,j,k} + 2p_{i,j,k} + p_{i+1,j,k}}\right| \tag{3.34}$$

$$\varepsilon^{(4)}_{i+1/2,j,k} = \max\left(0, (\kappa^{(4)} - \varepsilon^{(2)}_{i+1/2,j,k}\right) \tag{3.35}$$

$$\kappa^{(2)} = \frac{1}{4} \sim \frac{1}{2}, \quad \kappa^{(4)} = \frac{1}{64} \sim \frac{1}{32} \tag{3.36}$$

The matrix dissipation model makes the central-difference scheme closely resemble an upwind scheme near flow discontinuities and has the TVD property, which

prevents the occurrence of spurious oscillations. The terms $\mathbf{M}_\xi$ and $\mathbf{M}_\xi^{-1}$ are the right and left eigenvectors matrices, which diagonalize $\mathbf{A}$, where $\mathbf{A} = \partial \mathbf{E}_\xi / \partial \mathbf{Q}$. The eigenvalues of the flux Jacobian matrix $\mathbf{A}$ are:

$$\lambda_1 = \lambda_2 = \lambda_3 = \lambda_6 = U$$
$$\lambda_{4,5} = U \pm C \tag{3.37}$$

where $U = S_{\xi x}u + S_{\xi y}v + S_{\xi z}w$ and $C = c\left|\vec{S}_\xi\right|$. The term $\hat{\mathbf{\Lambda}}_\xi$ in Equation 3.32 represents the modified diagonal matrix of eigenvalues $\hat{\mathbf{\Lambda}}_\xi = diag(\tilde{\lambda}_1, \tilde{\lambda}_2, \tilde{\lambda}_3, \tilde{\lambda}_4, \tilde{\lambda}_5, \tilde{\lambda}_6)$ to avoid zero eigenvalues, and the modified eigenvalues are:

$$\tilde{\lambda}_1 = \tilde{\lambda}_2 = \tilde{\lambda}_3 = \tilde{\lambda}_6 = \max(|\lambda_1|, V_l\sigma)$$
$$\tilde{\lambda}_{4,5} = \max(|\lambda_{4,5}|, V_n\sigma) \tag{3.38}$$

where σ is the spectral radius of the flux Jacobian matrix $\mathbf{A}$. We use $V_l = 0.025$ and $V_n = 0.25$ (Zingg et al., 2000) for the present study.

Scalar dissipation model developed by Jameson et al. (1981) is a simpler version of the matrix dissipation model. In the scalar dissipation model, the modified eigenvalues are given as:

$$\tilde{\lambda}_1 = \tilde{\lambda}_2 = \tilde{\lambda}_3 = \tilde{\lambda}_4 = \tilde{\lambda}_5 = \tilde{\lambda}_6 = \sigma \tag{3.39}$$

Then Equation 3.31 can be written as:

$$\mathbf{d}_{i+1/2,j,k} = \varepsilon^{(2)}_{i+1/2,j,k}\,\sigma_{i+1/2,j,k}\left.\frac{\partial \mathbf{Q}}{\partial \xi}\right|_{i+1/2,j,k} - \varepsilon^{(4)}_{i+1/2,j,k}\sigma_{i+1/2,j,k}\left.\frac{\partial^3 \mathbf{Q}}{\partial \xi^3}\right|_{i+1/2,j,k} \tag{3.40}$$

The matrix dissipation model is more generalized and accurate, although the computation of these matrices at every grid-cell requires more computational time and memory.

The second-order dissipation term given in Equations 3.31 and 3.40 is nonlinear and its purpose is to introduce an entropy-like condition and to suppress oscillations in the neighborhood of shock discontinuities; this term is small in the smooth portion of the flow field, thus the switch $\nu_{i,j,k}$ is important in locating the discontinuities where pressure gradients vary greatly. The fourth-order term is basically linear and is included to damp high-frequency modes and allow the scheme to approach a steady state; only this term affects the linear stability of the scheme, and near discontinuities it is reduced to zero.

3.3.2 Upwind Scheme and Entropy Fix

In the flux-difference splitting (FDS) method of Roe, the interface flux is calculated:

$$\mathbf{E}_{\xi,i+1/2,j,k} = \frac{1}{2}\left[\mathbf{E}_{\xi}(\mathbf{Q}^L) + \mathbf{E}_{\xi}(\mathbf{Q}^R) - \left|\bar{\mathbf{A}}\left(\mathbf{Q}^L,\mathbf{Q}^R\right)\right|\left(\mathbf{Q}^R - \mathbf{Q}^L\right)\right] \tag{3.41}$$

where $\bar{\mathbf{A}}$ is the inviscid Jacobian evaluated with Roe-averaged variables.

The Roe matrix has the following properties:

i) $\bar{\mathbf{A}}(\mathbf{Q},\mathbf{Q}) = \bar{\mathbf{A}}(\mathbf{Q})$

ii) $\bar{\mathbf{A}}\left(\mathbf{Q}^L,\mathbf{Q}^R\right)$ has a complete set of real eigenvalues and eigenvectors.

iii) $\bar{\mathbf{A}}\left(\mathbf{Q}^L,\mathbf{Q}^R\right)\cdot\left(\mathbf{Q}^R-\mathbf{Q}^L\right)=\mathbf{E}_\xi(\mathbf{Q}^R)-\mathbf{E}_\xi(\mathbf{Q}^L)$

The construction of this matrix is based on Roe's approximate Riemann solver. The Roe matrix is obtained when the following average values are used for the calculation of its eigenvalues and eigenvectors:

$$\bar{\rho}=\sqrt{\rho_L\rho_R}\;;\quad \bar{f}=\frac{\left(f\sqrt{\rho}\right)_L+\left(f\sqrt{\rho}\right)_R}{\sqrt{\rho_L}+\sqrt{\rho_R}} \tag{3.42}$$

f could be any one of $\{u,\ v,\ w,\ H\}$

The matrix $\left|\bar{\mathbf{A}}\right|$ is then calculated by

$$\left|\bar{\mathbf{A}}\right|=\bar{\mathbf{T}}\left|\bar{\Lambda}\right|\bar{\mathbf{T}}^{-1} \tag{3.43}$$

where $\bar{\mathbf{T}}$ and $\bar{\mathbf{T}}^{-1}$ are the right and left eigenvector matrices of $\left|\bar{\mathbf{A}}\right|$.

The absolute eigenvalues $\left|\lambda_k\right|$ of the Roe matrix are redefined in order to avoid violation of entropy condition in the region of expansion shocks:

$$\left|\lambda_k\right|=\begin{cases}\left|\lambda_k\right|, & \text{if } \left|\lambda_k\right|\geq\varepsilon\\ \dfrac{\lambda_k^2+\varepsilon^2}{2\varepsilon}, & \text{if } \left|\lambda_k\right|\leq\varepsilon\end{cases} \tag{3.44}$$

where ε is a small number. Special care has to be taken when the entropy fix is applied to the eigenvalues which correspond to the linear characteristic fields. In Euler flows, these fields are associated with contact discontinuities. The entropy correction modifies the modulus of the near-zero eigenvalues and therefore falsifies the upwind terms in Equation 3.41. This becomes particularly important for Navier-Stokes calculations since an incorrect representation of the eigenvalues can result in an artificial boundary layer

(too much artificial dissipation is added). Therefore for all calculations ε is set to zero for the linear fields.

3.3.3 Hybrid Scheme

In the supersonic mixing case, strong discontinuities and fine intermittent structures present at the same time. While low-dissipation schemes tend to create unphysical oscillations in regions of high gradients, the inherent dissipation in the shock-capturing schemes would smooth the turbulent structures. A hybrid scheme is thus required to cope with the two kinds of schemes and resolve the flow behavior. Two smoothness parameters are introduced for pressure and density, respectively:

$$S_{p,i} = \begin{cases} \dfrac{\left|p_{i+1} - 2p_i + p_{i-1}\right|}{\left|p_{i+1} - p_i\right| + \left|p_i - p_{i+1}\right|} - 0.5 & if \left|p_{i+1} - 2p_i + p_{i-1}\right| \geq 0.05 p_i \\ -1 & otherwise \end{cases} \tag{3.45}$$

$$S_{\rho,i} = \begin{cases} \dfrac{\left|\rho_{i+1} - 2\rho_i + \rho_{i-1}\right|}{\left|\rho_{i+1} - \rho_i\right| + \left|\rho_i - \rho_{i+1}\right|} - 0.25 & if \left|\rho_{i+1} - 2\rho_i + \rho_{i-1}\right| \geq 0.1 \rho_i \\ -1 & otherwise \end{cases} \tag{3.46}$$

The inviscid flux evaluation is given by

$$\mathbf{E}_{\xi,i+1/2,j,k} = \begin{cases} \mathbf{E}^c_{\xi,i+1/2,j,k} & if \max\left(S_{p,i}, S_{p,i+1}, S_{\rho,i} S_{\rho,i+1}\right) \leq 0 \\ \mathbf{E}^u_{\xi,i+1/2,j,k} & otherwise \end{cases} \tag{3.47}$$

where $\mathbf{E}^c$ is the flux obtained by a central scheme adapted to resolve the turbulent structures, and $\mathbf{E}^u$ is evaluated by an upwind scheme adapted to capture the contact discontinuity.

3.4 Evaluation of Viscous Fluxes

A three-dimensional auxiliary cell is shown schematically by the blue lines in Figure 3.3. The viscous fluxes need to be evaluated at the center of the cell faces, i.e., $(i+1/2, j, k)$ for the viscous flux in the axial direction. Using the Gauss divergence theorem and applying it to a small control volume ΔV, the viscous fluxes can be approximated as:

$$\nabla \cdot \vec{f} = \frac{1}{\Delta V} \oint_S \vec{f} \cdot \vec{n} dS \tag{3.48}$$

Applying the above formulation to the auxiliary cell at $(i+1/2, j, k)$ gives:

$$\left(\frac{\partial f}{\partial x}\right)_{i+1/2,j,k} = \frac{1}{\Delta V_{i+1/2,j,k}} \left[f S_{\xi x}\Big|_{i+1,j,k} - f S_{\xi x}\Big|_{i,j,k} + f S_{\eta x}\Big|_{i+1/2,j+1/2,k} - f S_{\eta x}\Big|_{i+1/2,j-1/2,k} + f S_{\zeta x}\Big|_{i+1/2,j,k+1/2} - f S_{\zeta x}\Big|_{i+1/2,j,k-1/2} \right] \tag{3.49}$$

Similarly,

$$\left(\frac{\partial f}{\partial y}\right)_{i+1/2,j,k} = \frac{1}{\Delta V_{i+1/2,j,k}} \left[f S_{\xi y}\Big|_{i+1,j,k} - f S_{\xi y}\Big|_{i,j,k} + f S_{\eta y}\Big|_{i+1/2,j+1/2,k} - f S_{\eta y}\Big|_{i+1/2,j-1/2,k} + f S_{\zeta y}\Big|_{i+1/2,j,k+1/2} - f S_{\zeta y}\Big|_{i+1/2,j,k-1/2} \right] \tag{3.50}$$

$$\left(\frac{\partial f}{\partial z}\right)_{i+1/2,j,k} = \frac{1}{\Delta V_{i+1/2,j,k}} \left[f S_{\xi z}\Big|_{i+1,j,k} - f S_{\xi z}\Big|_{i,j,k} + f S_{\eta z}\Big|_{i+1/2,j+1/2,k} - f S_{\eta z}\Big|_{i+1/2,j-1/2,k} + f S_{\zeta z}\Big|_{i+1/2,j,k+1/2} - f S_{\zeta z}\Big|_{i+1/2,j,k-1/2} \right] \tag{3.51}$$

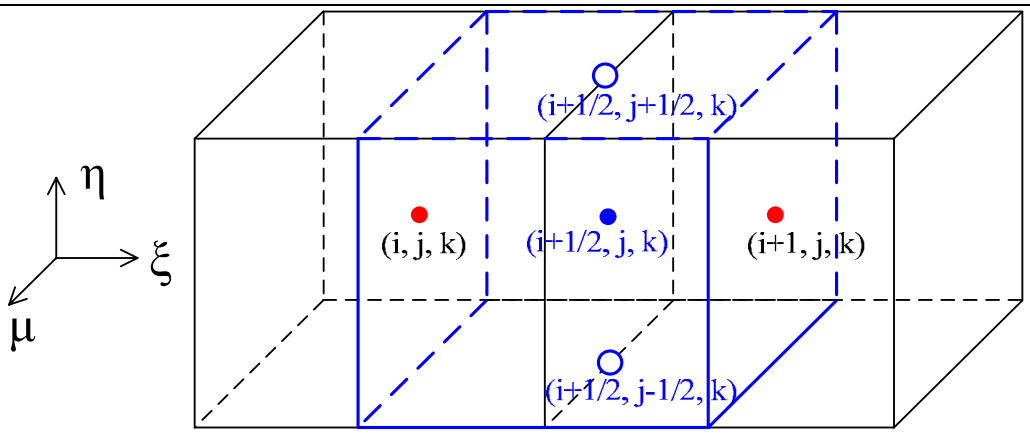

Figure 3.3 Schematic diagram of three-dimensional auxiliary cells

Note that all factors f in the above equations are elements of the viscous flux vectors $\mathbf{E}_{\xi v}, \mathbf{F}_{\eta v}$ or $\mathbf{G}_{\zeta v}$. Physical variables with one-half indices (the blue hollow dots) need to be interpolated from the quantities at the neighboring cell centers (the red dots) and are given as

$$f_{i+1/2,j\pm1/2,k} = \frac{1}{4}(f_{i,j,k} + f_{i+1,j,k} + f_{i+1,j\pm1,k} + f_{i,j\pm1,k})$$
$$f_{i+1/2,j,k\pm1/2} = \frac{1}{4}(f_{i,j,k} + f_{i+1,j,k} + f_{i+1,j,k\pm1} + f_{i,j,k\pm1}) \qquad \textbf{(3.52)}$$

The evaluation of SGS fluxes follows a similar procedure as for the viscous and diffusive fluxes.

All the flux evaluations above are valid for the uniform Cartesian grids as shown in Figure 3.4(a). In our code, a curvilinear coordinate transformation is accomplished in the implementation of the finite volume approach; the irregular computational mesh (Figures 3.4(b) and (c)) in the *x-y-z* coordinates is reshaped into an evenly spaced mesh

with unit volume in the general coordinate (i.e., ξ-η-ζ coordinates). However, the violations might happen in the reconstruction process of the state terms where the cell-averaged values are used directly without any weighting parameters to incorporate the grid information. Since the size and the shape of the grids vary slowly and smoothly, the impact is believed to be quite small, yet compact schemes accommodating mesh stretching and deformation will be considered in the future to eliminate this deficiency.

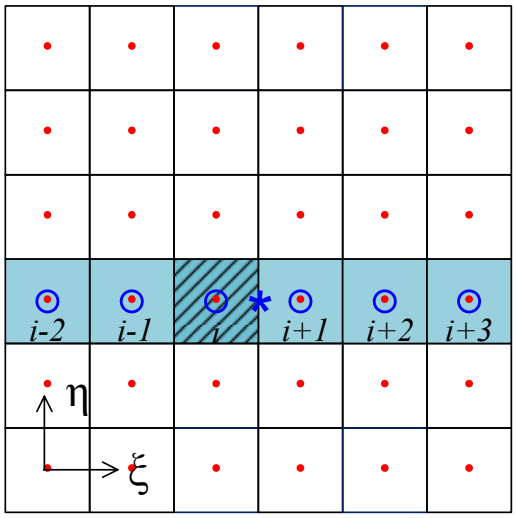

(a)

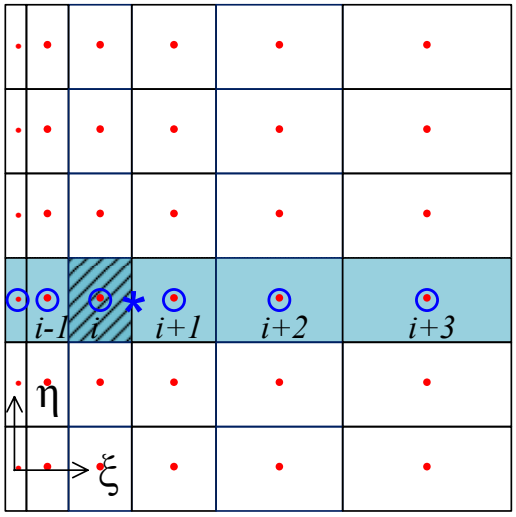

(b)

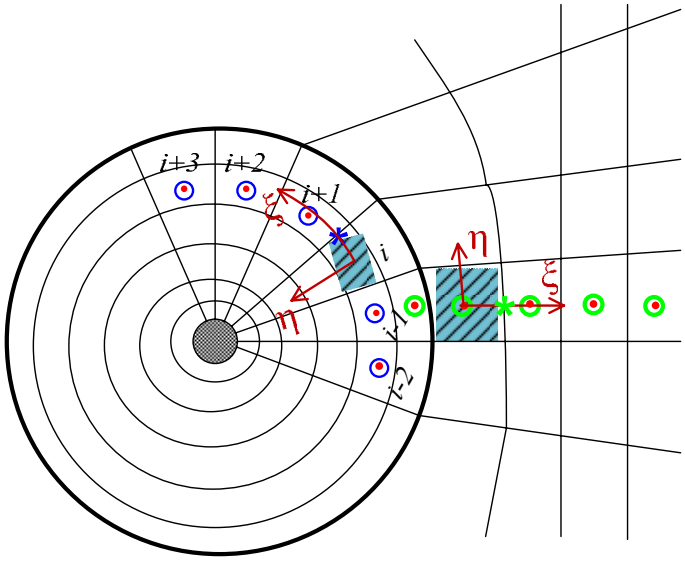

(c)

Figure 3.4 Schematics of two-dimensional grid distribution

3.5 Temporal Integration: Runge-Kutta Scheme

A fourth-order Runge-Kutta (RK4) scheme is used to solve the governing equations due to its higher temporal accuracy and relatively larger CFL number (i.e. $2\sqrt{2}$

for Euler calculation using RK4). Using the standard four-stage Runge-Kutta scheme (Jameson, 1983), each temporal-integration is completed through four consecutive intermediate steps, as given below.

$$\begin{aligned}
\mathbf{Q}_0 &= \mathbf{Q}^n \\
\mathbf{Q}_1 &= \mathbf{Q}_0 + \frac{1}{4}\Delta t.\mathbf{R}(\mathbf{Q}_0)\Big/\Delta V \\
\mathbf{Q}_2 &= \mathbf{Q}_0 + \frac{1}{3}\Delta t.\mathbf{R}(\mathbf{Q}_1)\Big/\Delta V \\
\mathbf{Q}_3 &= \mathbf{Q}_0 + \frac{1}{2}\Delta t.\mathbf{R}(\mathbf{Q}_2)\Big/\Delta V \\
\mathbf{Q}^{n+1} &= \mathbf{Q}_0 + \Delta t.\mathbf{R}(\mathbf{Q}_3)/\Delta V
\end{aligned} \tag{3.53}$$

where

$$\mathbf{R}(\mathbf{Q}) = \mathbf{H} - [\left(\mathbf{E}_\xi - \mathbf{E}_{\xi v}\right)\Big|_{i-1/2,j,k}^{i+1/2,j,k} + \left(\mathbf{F}_\eta - \mathbf{F}_{\eta v}\right)\Big|_{i,j-1/2,k}^{i,j+1/2,k} + \left(\mathbf{G}_\zeta - \mathbf{G}_{\zeta v}\right)\Big|_{i,j,k-1/2}^{i,j,k+1/2}] \tag{3.54}$$

Superscripts 'n' and '$n+1$' stand for the solution at the 'n^{th}' and '$(n+1)^{\text{th}}$' time steps, respectively.

3.6 Boundary Conditions

At the outlet of the computational domain, care must be taken when specifying the numerical boundary conditions. One has to ensure that the unphysical spurious wave reflections are avoided at the boundary and the flow is capable of relaxing to ambient conditions in prescribed ways. In the current work, the zero-gradient condition on all flow variables (Yuan, 1997) is applied at the outlet such that

$$\frac{\partial \phi}{\partial x} = 0 \tag{3.55}$$

where ϕ represents any flow variables.

As a benchmark, an inviscid duct flow is tested. Periodical oscillations are added to the inlet velocity:

$$u(t) = U\left(1.0 + 0.1\sin(\omega t)\right)$$
$$U = 40.0\ m/s,\ \omega = 2\pi f,\ f = 1000\ Hz \tag{3.56}$$

The duct has a length of 0.4 m. Three probes are placed on the centerline with axial locations of: $x_1 = 0.01\ m$, $x_2 = 0.19\ m$, $x_3 = 0.39\ m$. The histories of the axial velocity and pressure are recorded in Figures 3.5 and 3.6. Apparent shape consistency is observed at the three locations with advection time lags. Both the fluctuating frequency and amplitude are spatially and temporally well-maintained, suggesting that a noise-free environment has been ensured by the non-reflective boundaries; the spectral analysis in Figure 3.7 further confirms this message.

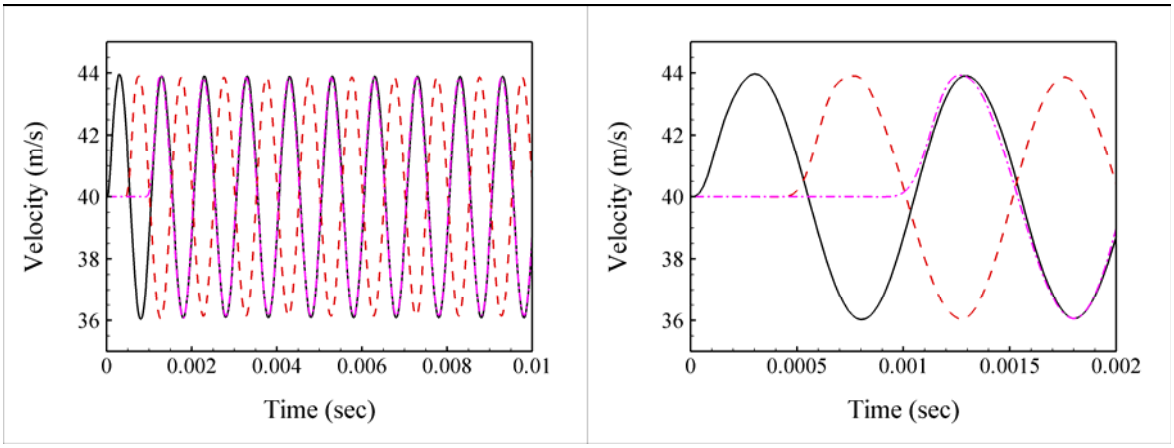

Figure 3.5 Temporal evolutions of the axial velocity
(solid lines: probe1; dashed lines: probe2; dash-dotted lines: probe3)

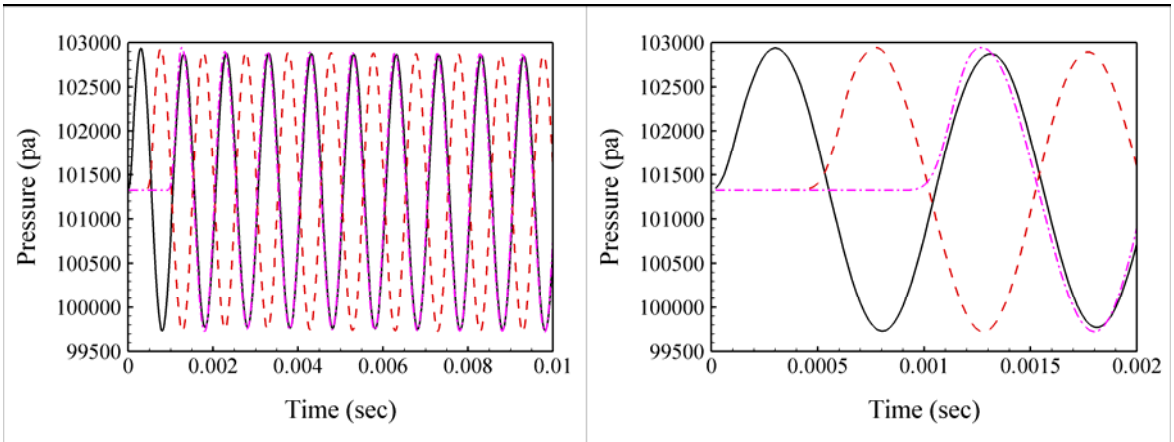

Figure 3.6 Temporal evolutions of the pressure
(solid lines: probe1; dashed lines: probe2; dash-dotted lines: probe3)

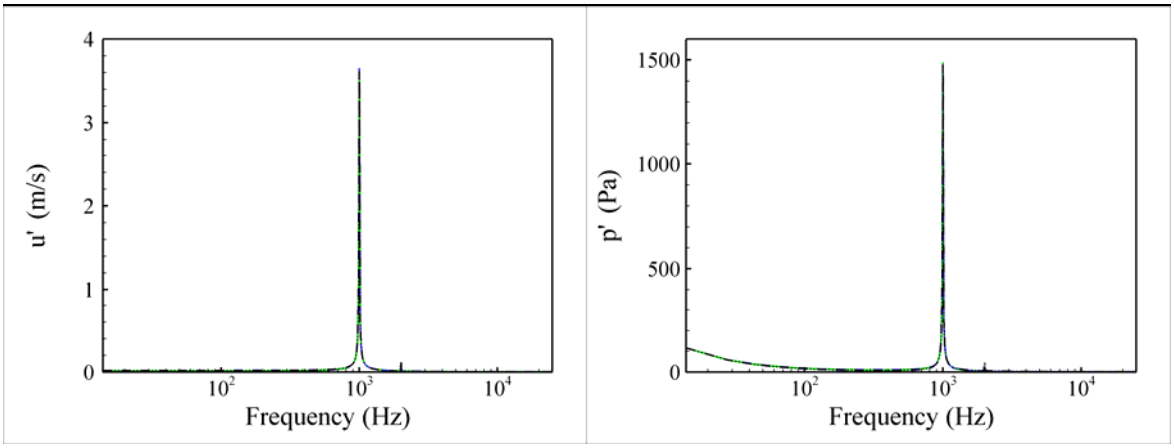

Figure 3.7 Spectral analysis of the axial velocity and the pressure
(solid lines: probe1; dashed lines: probe2; dash-dotted lines: probe3)

3.7 Parallel Implementation - Domain Decomposition

To utilize the merit of parallel computing, a domain decomposition technique is adopted here. In the field of CFD, it is generally referred to as mesh partitioning, where the physical domain is divided into several subdomains based on the geometric

substructure of the computational domain. Variables in each cell are updated to the next time step simultaneously.

Because the explicit time stepping numerical scheme (RK4) is applied in the current study, only the neighboring data (instead of the data from the whole computational domain) is accessed during the calculations in each cell. At the subdomain boundaries, ghost cells are introduced. Figure 3.7 shows an example of a two dimensional subdomain with ghost cells.

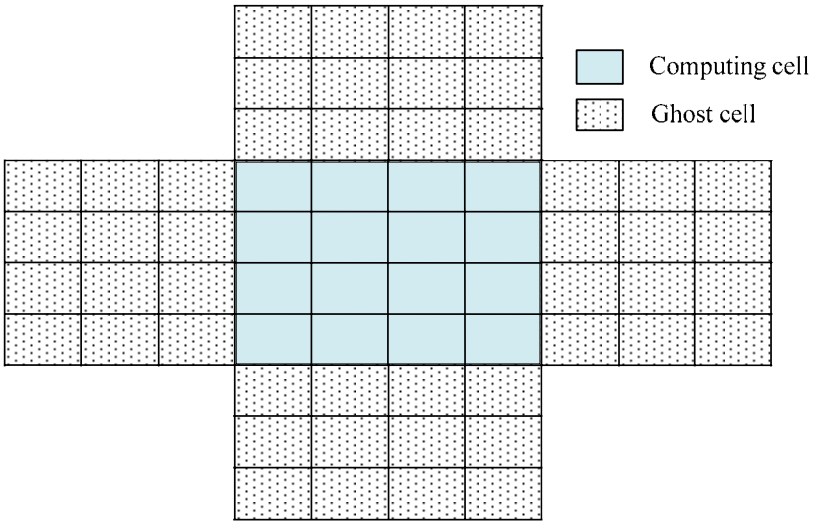

Figure 3.8 Schematic of a two-dimensional subdomain with ghost cells

Because the variables in the ghost cells are updated in another subdomain, the message passing interface (MPI) technique is implemented to synchronize data between neighboring subdomains. The communication overhead is directly proportional to the volume-to-surface ratio of the grid systems in the subdomains; therefore, higher parallel efficiency can be expected by increasing the computation-to-communication ratio. A detailed discussion on the inter-processor communication was presented by Wang (2002).

Chapter 4

Flow Dynamics and Scalar Mixing of a Turbulent Gaseous Jet into Stationary Crossflow

In this chapter, a turbulent gaseous jet into steady crossflow as shown schematically in Figure 4.1 is investigated. This study has several objectives: 1) to achieve a better understanding of the JICF flow characteristics under relatively realistic gas turbine conditions; 2) to assess the velocity ratio effect on the jet evolution; and 3) to explore the scalar mixing process and its coupling with the movements of the coherent flow structures.

First, a validation case is presented by reproducing Su and Mungal's experimental data (2004). The static and dynamic Smagorinsky SGS models are compared with each other to evaluate their effect on the performance of the LES technique. The flow structures and mixing phenomena are then elaborated in computational cases with higher velocities and larger Reynolds numbers.

4.1 Validation Case

4.1.1 Physical Model and Boundary Conditions

By matching the experiment setup designed by Su and Mungal (2004), ambient air is applied to both crossflow and jet fluids. The jet fluid is seeded with acetone vapor to 10% by volume as the scalar for mixing consideration. The crossflow velocity U_0 is

2.95 m/s and the jet velocity U_j is 16.9 m/s, resulting in a momentum ratio $r = 5.7$. Providing the jet orifice diameter $d = 4.53$ mm is the characteristic length, the Reynolds number measures approximately 5000 at the jet exit. Since the experimental flow velocity is too small to be implemented in our compressible in-house code, a FLUENT framework is adopted while maintaining the same LES implementation.

The flow configuration and mesh topology are as shown in Figure 4.2. The origin of Cartesian coordinates is fixed at the center of the jet orifice. The computational domain extends $48d \times 36d \times 36d$ in the crossflow streamwise (x), spanwise (y) and transverse (vertical) (z) directions, respectively. Previous work (Muppidi and Mahesh, 2005) confirmed that a domain of this size did not constrain the jet, and boundaries did not have any confinement effect on the crossflow. Since the early jet/crossflow interaction has a strong dependence on the jet exit velocity profile, a circular pipe having diameter d and length $20d$ is included in the computational domain to ensure a fully developed turbulent pipe flow at the jet exit. The distance between the crossflow inlet plane and the jet exit is $12d$; thus, a boundary layer is generated for the crossflow before it meets the jet. For a meaningful LES calculation, fine mesh is required to ensure the grid-filters act within the inertial range of scales. In the current study, high grid resolution is applied to the near field and the wall boundaries. A total of 1.3 million cells are employed to provide detailed information about the mean flow properties, turbulence statistics, and scalar mixing.

The boundary conditions are specified as follows: 1) at the crossflow inlet plane, the velocities are specified as a function of z such that the laminar boundary layer has

the desired thickness at the jet orifice, in the absence of the jet; 2) at the pipe inlet, a mean turbulent velocity profile is specified as a function of the radial distance from the pipe center; 3) at the top boundary, a freestream velocity of U_0 is prescribed; 4) at the spanwise boundaries and the outlet plane, the zero-gradient boundary condition is used; and 5) viscous wall boundary conditions are applied to the crossflow tunnel wall and the pipe inner surface.

4.1.2 Results and Discussion

According to Smith and Mungal (1998), the trajectory and physical dimensions of the jet display *rd*-scaling in both the near and far fields. Su and Mungal (2004) adopted this scaling in their work, and it is used here to maintain consistency with the original data presentation.

Figure 4.3 presents the profiles of the mean velocity magnitude in the spanwise center plane ($y = 0$ plane) along the lines of fixed z and fixed x for both the static and dynamic SGS model cases, together with to the experimental results. A turbulent pipe flow velocity profile is captured in the $z = 0.1rd$ plot, with a trough upstream of the jet. This is because the jet serves as an obstacle and retards the crossflow fluid by creating a high-pressure region in the upstream. The $<|\vec{u} - U_0\vec{e}_x|>$ profile at location $x = 0.5rd$ departs from symmetry due to the existence of the wake region and shows a bell-shaped peak coinciding roughly with the center streamline. As the flow evolves downstream, the two peaks merge and the magnitude decreases.

Figure 4.4 presents profiles of the mean acetone concentration $< C >$ in the center plane. For locations where $z < 1.0rd$, the fixed-*z* profiles are symmetric around the position of peak concentration, except for a slight elevation in the tails on the downstream location, representing jet fluid that has been advected into the wake region on the lee side of the jet. The entrainment of the crossflow fluid is more clearly shown in the $z = 1.0rd$ plot, in which the shape of $< C >$ is highly asymmetric with a long tail on the wake side. The fixed-*x* profiles depart noticeably from the corresponding mean velocity profiles in Figure 4.3 within the region close to the jet exit. Specifically, at the $x = 0.5rd$ location, only one peak is observed.

Figure 4.5 shows a comparison of the turbulence quantities based on fluctuating velocities. Fair agreements are observed, except for locations near the jet exit ($z = 0.1rd$) where the numerical results are visibly smaller than those of the experiment, suggesting that attention be paid to the inlet turbulences and grid distribution. At $z = 0.1rd$, the averaged normal stress component $< w'^2 >$ shows peaks on both the windward and wake sides of the jet, reflecting the dominance of the jet shear layer instability in the near field; while at $z = 1.0rd$, shear layer vortices on the windward and wake side of the jet plume merge, producing a single peak in the $< w'^2 >$ profile. The shear layer instability in the near field also accounts for the negative turbulent shear stress $< u'w' >$ on the windward side and positive values on the wake side at all constant-z locations.

Although the results of the dynamic SGS model are slightly different from those of the static SGS model in the near field, adequate conformity with the experimental data

is observed for both simulations. To avoid the computational burden required by the dynamic model, the static model is applied in this work.

4.2 Background and Computational Case Description

Under realistic gas turbine conditions, the velocities of the gaseous jet and crossflow are much higher than those in experimental research. Prière et al. (2004) used measurements of $U_0 = 60$ m/s and $U_j = 195$ m/s in their attempt to assess the performance of mixing devices in a Siemens PG combustion chamber. Considering the capability of our in-house code to resolve the compressible flows and a reasonable gas turbine velocity range, crossflow velocities of 80 m/s and 40 m/s were chosen for the two focus cases ($r = 2$ and $r = 4$), respectively. Correspondingly, the jet velocity was maintained at 160 m/s through this work.

The schematic of flow configuration is shown in Figure 4.1. The computational domain extends to $[-5d,\ 16d]$, $[-5d,\ 5d]$ and $[0,\ 11d]$ in the streamwise, spanwise and transverse directions, respectively, for the crossflow duct. $d = 1.27$ mm is the diameter of the jet orifice. The boundary layer thickness of the crossflow is $\delta_{0.95} \approx 0.1d$, calculated at a location $2.0d$ ahead of the jet orifice. To ensure the jet flow is fully developed before entering the crossflow, the length of the jet pipe is set at $20d$. The mean turbulent velocity profile based on the results of turbulent channel flow in Eggels et al. (1994) is applied at the pipe entrance, supplemented by broadband fluctuations with turbulence intensity $u_i' u_i' / U^2$ equal to 0.01. A separate pipe flow calculation was adopted by

Muppidi and Mahesh (2008) and by Denev et al. (2009) to produce the turbulent inflow condition for the jet flow; however, in order to avoid data storage difficulty and to maintain realistic operating conditions, the pipe flow is calculated simultaneously in this work, and provides the instantaneous flow information directly to the jet/crossflow interaction region. The boundary layer thicknesses of the jet flow, $\delta_{0.95}$, is about $0.25d$ at the location $2.0d$ beneath the wall orifice.

Air at ambient conditions (1 atm, 300 K) was chosen as the working fluids for both jet and crossflow. The mass fraction of the jet fluid is set as the scalar under investigation. The Reynolds number based on the bulk velocity and diameter of the jet is then fixed at 1.3×10^4. The turbulent kinetic energy spectrum in Figure 4.7, calculated on the coarse grid set at a distance of $2.0d$ from the jet orifice in the pipe, reveals the Kolmogorov-Obukhov spectrum ($-5/3$ law) as expected and confirms a fully developed turbulent flow field. Correspondingly, the turbulent Prandtl and Schmidt numbers, 0.9 and 0.7, respectively, are used in this work.

No-slip viscous conditions are applied to the inner surface of the jet pipe and the wall of the crossflow tunnel. The subsonic inlet conditions, accommodating the characteristics of Riemann problems, are enforced at the two inlets. All the spanwise boundaries utilize the slip wall condition to best mimic the flow development in a relatively large space, and zero-gradient outflow conditions are applied at the outlet plane.

4.3 Grid System and Grid Independence Study

With $\mathrm{Re}_j = 1.3\times10^4$, the Kolmogorov and Taylor micro-scales (Pope, 2000) are estimated as

$$\eta \approx d \cdot \mathrm{Re}_d^{-3/4} = 0.001mm$$
$$\lambda \approx d \cdot \mathrm{Re}_d^{-1/2} = 0.011mm \quad \textbf{(4.1)}$$

Special attention must be paid to the grid resolution to fully utilize the merit of LES within the constraints of computation. Figure 4.6 shows the grid distribution and the block assignment. With mesh refinements in the mixing and near wall regions, three sets of structured grids with similar topology are generated at total mesh sizes of 2.8 million, 8.9 million, and 29.7 million. Accordingly, the computing cores used are 67, 72, and 262, respectively, to maintain a fair computational efficiency. The mean grid sizes are comparable to those in the Taylor scale, satisfying the grid resolution requirement for LES calculations. For all the grid sets, the near-wall cell sizes are maintained at $y^+ \approx 3$ to manage the boundary flows. Table 4.1 summarizes the grid information.

All the three grids are used for the $r = 2$ case to conduct a grid independence study as well as to capture the details in the flow field. Unless specifically indicated, the following discussions are based on the $r = 2$ case.

4.4 Mean Field and Turbulent Properties

4.4.1 Mean and RMS Velocity and Scalar Profiles

The mean and root-mean-square (RMS) data is collected for over five flow-through times, after washing out the transient conditions of the initial setups. The mean velocity (normalized by U_0) and scalar in the spanwise center plane are compared among all grid resolutions.

Figure 4.8 shows the *x*-profiles at the stations $z/d = 1.0$, $z/d = 2.0$ and $z/d = 5.0$. A trough is observed on the windward side of the jet at $z/d = 1.0$ for $< u > /U_0$, while no jet fluid is detected as $< C >$ remains at zero value there, indicating the blockage effect of the transverse jet on the crossflow. On the lee side of the jet, $< u > /U_0$ recovers to unity at $z/d = 1.0$ and further exceeds unity at $z/d = 2.0$ as the transverse motion $< w > /U_0$ decreases and contributes to the streamwise momentum. The $< w > /U_0$ profile at $z/d = 1.0$ is nearly symmetric around the position of peak velocity, except for a trough in the tails on the lee side, which is also observed in the $< u > /U_0$ profile, representing a local recirculation flow. The $< C >$ profile departs noticeably from the corresponding velocity profile by showing a broad elevated tail on the positive-x side, indicating that jet fluid has been advected into the wake region on the lee side of the jet. The variation of velocity profiles and the rapid decrease of scalar concentration occur in the region $-2 < x/d < 5$ (the near field), which encompasses the most dynamic processes in the jet/crossflow interactions and is further analyzed in

Section 4.5. As indicated by the RMS profiles, the fluctuations of velocities and scalar tend to be more synchronized and the variations are only observed around the shear-layer locations in the early jet plume.

Figure 4.9 shows the z-profiles at the stations $x/d = 1.0$, $x/d = 2.0$, $x/d = 5.0$ and $x/d = 10.0$. Close to the crossflow tunnel wall ($z/d \approx 0$), the streamwise and transverse velocities approach zero as a result of the no-slip boundary conditions. The scalar does not vanish there, however, indicating that the jet fluid has the potential to reach and pile up at the tunnel wall. Right above the crossflow boundary layer ($0.5 < z/d < 1.0$), a negative value is observed for $< u > /U_0$ at $x/d = 1.0$, coinciding with a nearly-zero $< w > /U_0$, suggesting a weak recirculation flow. Two peaks appear in the $< w > /U_0$ profile at $x/d = 2.0$: the upper one is on the jet penetration path, and the lower one is in the weak region, resulting from the "hanging vortices." The profiles of $< C >$ maintain broad bandwidth and one peak located between the two $< w > /U_0$ maximums.

The flow structures are represented by the two-dimensional crossflow streamlines in Figure 4.10, colored by the jet fluid concentration. The results from the $r = 4$ calculation are also included here for comparison. In the close-up views of the region near the jet exit, stagnation points exist and a weak horseshoe vortex, with a clearer view in the $r = 4$ case, presents upstream of the jet and close to the wall at $x/d \approx -1.0$. A few streamlines penetrate into the jet pipe due to the crossflow entrainment and form another vortex pattern near the jet exit; this was termed "a hovering vortex" in Kelso and Smits (1995). The hovering vortices were detected at velocity ratios $r = 2.3$ (Kelso and Smits) and $r = 1.52$ (Muppidi and Mahesh, 2005), but are not seen in high velocity ratio cases

such as this $r = 4$ simulation. The existence of a node with a positive divergence at $x/d \approx 1.2$ is the featured phenomenon downstream of the jet. This has also been noted by Kelso et al. (1996), Hasselbrink and Mungal (2001), Muppidi and Mahesh (2005) and others.

4.4.2 Jet Trajectory

Jet trajectory has been defined in several ways, such as the local velocity maxima (Kamotani and Greber 1972), the local scalar concentration maxima (Smith and Mungal, 1998), and the streamline originating from the center of the jet exit on the center plane (Muppidi and Mahesh, 2005). Both the center streamlines in the symmetry plane and the loci of the local jet fluid maxima are plotted in Figure 4.11, together with the boundaries of the plume at a jet fluid concentration of no less than 0.05.

Since part of the jet fluid on the lateral sides is swept downstream before penetrating deeper into the crossflow near the jet exit or is "trapped" below the jet plume as a result of a velocity trough (Muppidi and Mahesh, 2006), the loci of the local jet fluid maximum is slightly lower than that of the center streamline in the near field, as observed by Fearn and Westton (1974), Yuan and Street (1998), and Su and Mungal (2004). As the trajectories evolve in the downstream direction, most the jet fluid returns to its original trend as a result of the boundary layer separation or/and mass transport from the vortical structures. Thus, both kinds of trajectories collapse with each other in the far field. Comparing the plumes of the two cases, the boundaries of $r = 2$ show no symmetry between the loci of the local maximum and the lower boundary almost collides

with the crossflow wall, while in the $r = 4$ case the trajectories penetrate deeply into the crossflow and a discernable symmetry presents itself. However, the two plumes have comparable widths throughout the mixing fields.

4.4.3 Turbulent Statistics Profiles

The turbulent scalar flux terms, defined as the product of the scalar fluctuation and the components of the velocity fluctuations, $< u_i' C' >$, appear in the Reynolds-averaged scalar transport equation (here in non-dimensional form)

$$\langle u_i \rangle \frac{\partial \langle C \rangle}{\partial x_i} - \frac{1}{\mathrm{Re}\, Sc} \frac{\partial^2 \langle C \rangle}{\partial x_i \partial x_i} = - \frac{\partial \langle u_i' C' \rangle}{\partial x_i} \qquad (4.2)$$

where Re is the Reynolds number, Sc is the Schmidt number, $\langle u_i' \rangle = \overline{u}_i - \langle u_i \rangle$, $\overline{u}_i$ is the resolved velocity, and $< u_i >$ is the mean value of the resolved velocity. Figure 4.12 shows profiles of the scalar flux components $< u' C' >$ and $< w' C' >$ in the center plane. Though slight discrepancies exist among the three grids, all the results show positive $< w' C' >$ and positive/negative-switching modes for $< u' C' >$. A simple interpretation of the observation is as follows. The jet, which is composed of discrete parcels of vortical jet fluid carrying a scalar concentration, moves downstream into the path of crossflow fluid. Since the mean scalar concentration is computed from a mix of crossflow and jet fluid, the concentration within the jet plume will be higher than that within the clean crossflow, creating a negative C' for the entrained crossflow. On the windward side of the jet, the entrained crossflow has a negative w' and a positive u',

thus $\langle u'C' \rangle < 0$ and $\langle w'C' \rangle > 0$. On the leeward side, as a result of the deceasing transverse momentum (as shown in Figure 4.8), the jet plume has an excess of crossflow streamwise velocity. Therefore, the entrained crossflow has a negative w' and u', leading to $\langle u'C' \rangle > 0$ and $\langle w'C' \rangle > 0$. Close to the jet exit, high values of $< w'C' >$ are observed, indicating a strong turbulent transport of scalar in the transverse direction. As the jet plume evolves in the crossflow, the flux in the positive direction decays and approaches zero in the far field. The same phenomena were also reported by Andreopoulos (1983), Yuan (1997), and Su and Mungal (2004).

A slight negative $< w'C' >$ can be discerned in the region $x/d = 2.0, z/d \approx 1.5$. This may be explained using the hypothesis that the CVP produce an updraft velocity at the center in the lower region of the crossflow tunnel (Yuan, 1997). This updraft would carry clean crossflow into the jet plume, and thus induce a negative fluctuation in the scalar concentration and a positive fluctuation in vertical velocity, yielding a negative $< w'C' >$.

Figure 4.13 shows the profiles of turbulent shear stress $< u'w' >$, with high negative values on the windward side and positive values on the leeward side of the jet in the near field. These observations can be accounted by the jet shear-layer instability. As the jet plume develops in the downstream, the dominant mechanism in generating $< u'w' >$ becomes the shear between the jet and crossflow fluid, which diminishes in the far field.

4.5 Flow Dynamics

4.5.1 Vortex System and Crossflow Entrainment in the Near Field

The vortical structures in the JICF flow field are commonly categorized into four groups: the horseshoe vortices wrapped around the windward half of the jet orifice close to the crossflow boundary layer; the jet shear-layer vortices in the early mixing region immediately after the injection; the fingerlike, roller-structured wake vortices rooted in the crossflow boundary underneath the main jet plume; and the counter-rotating vortex pair (CVP) along the jet trajectory path, which encompasses the entire jet plume in the far field.

Figure 4.14 shows the iso-surfaces of vorticity magnitude |Ω| at 125,000 ($\approx U_j/d$) in the instantaneous flow fields for $r = 2$ and $r = 4$ based on grid B. By modulating the brightness in Tecplot360, the vorticity in the crossflow boundary layer is veiled in order to highlight the mixing region. Close to the jet exit, spanwise rollers appear regularly on the windward of the jet plume, visualizing the shear-layer vortices in the initial jet bending region. These strong, energetic structures evolve downstream and define the upper boundary of the jet plume. On the lateral sides of the jet, the uniformly formed vortex ring is not obvious, as the nature of the Kelvin-Helmholtz instability changes as one moves azimuthally around the jet. As the crossflow deflects around the jet body, it accelerates on the lateral sides and induces a skewed mixing layer, which produces the "hanging vortex" in the direction of the mean convective velocity ($\vec{U}_{mean} = \vec{U}_0 + \vec{U}_j$) (Yuan, 1997). The jet fluid carried by the hanging vortex gains

horizontal momentum and merges into the lower half of the jet plume as shown in Figure 4.20. Both the spanwise rollers and the hanging vortices lose regularity and gradually disappear after passing through the near field, and the whole field becomes chaotic and assumes a turbulent appearance, which constitutes the CVP that could be manifested in the mean flow field. While both cases have similar appearances, the $r = 4$ case shows a much broader plume and finer structures in the far field, indicating a stronger vorticity generation close to the jet exit and more intensive transportation along the jet trajectory. Wake vortices, which play an important role in the scalar fluid entrainment and the transport of vorticity from the crossflow tunnel wall to the CVP, are hidden beneath the plume and are depicted by the iso-surfaces of helicity in Figure 4.15.

The spanwise rollers as shown in Figure 4.14 are the most apparent structures in the early evolution of the jet plume. They are produced as a result of Kelvin-Helmholtz instability. On the windward of the jet, an adverse vertical pressure gradient forms as a result of the velocity gradient in the crossflow boundary layer; therefore, as the shear layer enters the crossflow, it quickly becomes unstable and rolls up into vortices. Meanwhile, on the leeward of the jet the shear layer encounters a favorable pressure gradient, which enhances its stability and delays the vortex roll-up.

As proposed by Fric and Roshko (1994), the wake vortices have their origins in the laminar boundary layer of the wall from which the jet issues. The crossflow boundary layer sweeps around the jet and encounters an adverse pressure gradient on the lee side, inducing boundary layer separation in the early wake region. The separation occurrence on the crossflow wall forms a tornado-like vortex which has its base in the wall boundary layer, while its other end may connect to the jet plume. As these vortices

convect downstream, a new vorticity is continually generated at the wall and fed into the wake structures. The structures of the wake in the near field are demonstrated by the iso-surfaces of helicity at $H = 250,000$, presented in Figure 4.15 and colored by the jet flow concentration. In both cases, the crossflow boundary layer comes up as a source that produces and provides helicity for the entire flow field. Whereas in the $r = 2$ case the jet flow plume mingles with the crossflow boundary layer and never actually separates from the wall, a deep penetration of helicity in the mixing region is found in the $r = 4$ case and the tornado-like structures are clearly identifiable. Since helicity represents the rotation about an axis in the direction of motion, it is also an indication of mass transportation. The absence of the jet fluid in the vertical rollers illustrates a strong entrainment of the crossflow toward the jet trajectory, as confirmed and discussed in the experimental work of Fric and Roshko.

The horseshoe vortices are generated by the separation of the crossflow boundary layer on the windward side of the jet. Since the jet constitutes an obstacle for the approaching crossflow, an adverse pressure-gradient region is formed ahead of the jet, accounting for the boundary separation and reattachment as well as a recirculation flow. As the horseshoe vortices are present at a large distance from the jet exit and are very weak in the compressible gaseous jet/crossflow mixing cases, they are demonstrated only by the two-dimensional streamlines in Figure 4.10. Fric and Roshko (1994) captured this vortex structure by means of smoke streaklines in a water tunnel. Kelso and Smits (1995) found that the horseshoe vortex system may be steady, oscillating, or coalescing, depending on the flow conditions, and also noted a connection between the oscillations in the horseshoe vortices and oscillations in the wake behind the jet.

Figure 4.19 shows a sequential mapping of the instantaneous scalar concentration in the symmetry plane for the two cases. Where $r = 2$, counterclockwise-rotating vortices, corresponding to the spanwise rollers, are formed on the windward of the jet plume close to its exit. These vortices are referred to as the "backward-rolling vortices" by Huang and Lan (2005), and typically occur in low velocity ratio cases. Notice that the gaps between the vortices provide an import mechanism for the crossflow to be entrained by the jet fluid. The potential core in this case is less than $2.0d$ and the spacing between the rolling vortices is maintained at around $1.5d$ before they disappear in a downstream position where $x/d \approx 4.0$. The jet plume has a thick brush in the wake region and shows a high possibility of reaching the crossflow tunnel wall. Where $r = 4$, the shear-layer vortices more closely resemble "jet-like vortices", which intermittently appear on the windward side of the jet plume and disappear sometimes without periodicity (Huang and Lan, 2005). The spacing between the vortices is shortened to less than $1.0d$. The rare shear-layer vortices on the leeward surface of the jet have more irregularity and higher vertical locations. The jet potential core extends to the $z/d = 2.5$, after which the shear-layer vortices disappear and the jet fluid loses continuity and sheds into the crossflow. Furious motions exist in the region $0.5 < x/d < 3.0$, $2.5 < z/d < 5.0$ where the jet fluid pocket first rolls up, then elongates, and finally detaches from its potential core. Correspondingly, the crossflow entrainment visually manifests its existence and magnifies its significance in the mixing process, as demonstrated by the breakdown of the jet fluid pockets. This area is recognized as the ending of the near field. Further downstream in the crossflow tunnel, though zones with relatively higher jet fluid

concentration exist, the jet fluid is dispersed into the crossflow. The jet/crossflow mixing tends to be massive but gentle.

The jet plume evolutions can be better visualized by observing a sequence of vorticity evolutions as shown in Figure 4.16 and Figure 4.17, based on grid B. Figure 4.16 shows the iso-surfaces of vorticity magnitude |Ω| at 250, 000 for the $r = 2$ case. Spatially periodical vortical structures are observed in the near field, while the chaotic dispersion of the small rollers prevails in the far field. The same observation applies when $r = 4$ in Figure 4.17, where the iso-surfaces of vorticity magnitude |Ω| at 125, 000 are presented. The reason for a smaller vorticity magnitude is simply that the jet plume is farther from the crossflow tunnel wall in the higher velocity ratio case; high vorticity might not always appear in the wake region, which may make the visualizations ambiguous and misleading. Compared to the $r = 2$ case, the turbulent rollers appear to be much smaller and more condensed in a higher jet plume, even for the same magnitude vorticity, as shown in the lower enlarged plot.

The mesh size has an influence on the vorticity visualizations, but the effect is minor and tolerable. Comparisons among the three grid sets assess the effect of grid resolution on extracting the vortex structures in Figure 4.18, where the iso-surfaces of vorticity magnitude |Ω| at 250, 000 for $r = 2$ are presented at the same time (the count starts as the jet first enters the crossflow). Although more vortical structures appear as the grid resolution is refined, the dominant large-scale structures in the near field show no difference among the three data sets. In the far field, the flow field becomes more chaotic, the mixing relies more on the diffusive effect, and the predictions of the overall mixing efficiency are not much affected by the grid size (as shown in Section 4.6).

4.5.2 CVP Development

The trajectory of the jet is composed of two elements – the motion carrying it further from the wall in its original transverse direction, and the motion carrying it in the crossflow direction. The CVP aligned with the jet trajectory is essentially a manifestation of the mean flow field induced by the impulse of the transverse jet and is investigated here based on the mean flow quantities. Three-dimensional streamlines based on the average velocities are presented in Figure 4.20, together with the contours of the jet fluid concentration at several downstream locations. A total of six streamlines originating from within the jet are tested in the $y \geq 0$ region. Their traces in the $z/d \geq -2$ plane are as shown in the schematic diagram: one streamline passes directly through the center of the pipe, and the other five penetrate through a circumferential line $0.05d$ from the pipe wall, azimuthally $\pi/4$ apart from each other. Clearly, the three streamlines on the symmetry plane follow their original trends and penetrate deeply into the crossflow as part of the main jet plume. The three streamlines on the lateral side, however, are bent to the crossflow direction and twisted around the jet plume, contributing to the tails of the kidney-shaped profiles. This observation can be explained by the "path downstream for the jet fluid" provided by the hanging vortices (Yuan, 1997). On the lateral sides of the jet, skewed mixing layers are formed as the crossflow deflects around the jet body. The vortical structures formed in these layers grow in the direction of the mean convective velocity and carry a strong axial flow (Lu, 1995). The hanging vortices encounter an adverse pressure gradient as they move downstream and thus undergo the vortex breakdown, initializing the nascent CVP (mainly in the lower part). Notice where $r = 2$,

no apparent kidney-shape is exhibited in the jet fluid concentration contours, likely because the jet plume never actually separates from the crossflow boundary, and typical JICF structures are not developed here.

Figure 4.21 gives the spatial evolutions of the jet fluid concentration together with two-dimensional streamlines for the $r = 4$ case. The CVP is clearly manifested by the streamline spirals centered at the tails of the kidney-shaped profiles. It is the dominant motion in the far field and accounts for most of the scalar transport by way of large-scale momentum transportation as demonstrated in the plots. By carrying the crossflow in the wake region into the jet plume, the CVP widens the gap between the tails. The fluid in the jet plume is vertically drifted and then dispersed spanwise across a broad region in the main duct. The interaction occurs all the way downstream with decreasing intensity. The streamlines also reveal a pair of vortices close to the crossflow tunnel wall, known as "the secondary vortex" (Denev et al., 2009).

In Figure 4.22, a sequence of slices is extracted along the center streamline of the mean flow field to provide a close-up view of the CVP evolution for the $r = 4$ case. Starting from the coordinate origin (the center of the jet exit plane), the first slice is $0.5d$ away from the jet exit. Both the jet fluid concentration and the vertical velocity contours show the images of a horseshoe-shaped potential core. The tails of the horseshoes reveal that immediately after injection, a small portion of the jet fluid, mostly at the lateral sides, has been blown downstream and twisted in the leeside of the main jet plume. The second slice is about $2.5d$ away from the jet exit, where the potential core almost disappears and the deformation of the jet plume increases, yielding a much larger kidney-shaped profile. In the transverse velocity contour, two peak zones approximately

$2.0d$ away from each other are observed: one in the jet plume, and the other in the wake region. The latter is recognized as the second flow and its location coincides with the gap in the kidney-shaped jet fluid concentration contour. It is consistent with the node observed in Figure 4.10 and is likely formed when the crossflow bypassing the jet blockage breaks down in the low-pressure region and gains vertical momentum in the rear side of the jet. The third slice (about $5.0d$ away from the jet exit) and the remaining ones follow the trend, except that the size of the jet plume increases while the jet fluid concentration and vertical velocity decrease in the downstream direction.

4.5.3 Spectral Analysis

The flow fields were probed to extract their intrinsic flow instabilities. Figure 4.23 shows the temporal evolutions of the pressure and the scalar at three locations within the jet plume:

$$\begin{aligned} &\text{Probe07: } (0.54d,\ 0,\ 2.04d) \\ &\text{Probe20: } (4.93d,\ 0,\ 4.95d) \\ &\text{Probe34: } (12.03d,\ 0,\ 6.67d) \end{aligned} \tag{4.3}$$

All the data was recorded after the transient period had been completed and the statistically steady state had been achieved. The data recording period elapsed at $38d/U_0$, (i.e.)0.6 *ms* and 1.2 *ms* for the $r = 2$ and $r = 4$ cases, respectively, covering more than two flow-through times. Comparison of the probes shows that the fluctuation magnitudes decrease and the high-frequency intermittencies disappear as the jet evolves

in the downstream direction. Additionally, the $r = 4$ case maintains larger fluctuation magnitudes and finer intermittent phenomena than does the $r = 2$ case.

The Fast Fourier transformation (FFT) technique was performed to determine the frequency spectra for the above quantities, as shown in Figure 4.24. Since the jet has a relatively large velocity and small diameter, the characteristic frequencies are considerably high, to the order of 10 kHz. Looking at the pressure oscillations, one spike may be observed in the low frequency region and is believed to be the computational boundary effect, not relevant to the flow dynamics. Two peaks are found in each case: both exhibit one at 14.5 kHz, corresponding to a Strouhal number ($St = fd/U_j$) 0.12, while the other has a broad distribution in the domain of 60-80 kHz where $r = 2$ and in the domain of 80 kHz to 100 kHz where $r = 4$. The first peak diminishes in the downstream and is likely related to the near-field phenomena. The latter peak also appears in the scalar concentration fluctuations and will be addressed carefully in Chapter 5. No spikes are observed in the far field.

4.6 Mixing Quantifications

Though perfect mixing is desired for the combustion system, the reality is that mixing efficiency is always affected by unsteady flow characteristics. This section involves measuring the mixing field quantitatively through statistical analysis.

4.6.1 Decay of Maximum Mean Scalar Concentration and Velocity

A log-log plot is shown in Figure 4.25 to give a sense of mixing efficiency explicitly by tracking the spatial evolutions of the local jet flow concentration and the vertical velocity maxima. For both $r = 2$ and $r = 4$, the two properties do not converge with each other although they do maintain the same slopes in certain regions. Near the jet exit, a classic jet potential core exists just prior to a decrease with a slope of $k \approx -0.37$ beginning at $x/d \approx 0.8$. Irregularity happens in the region $1.0 < x/d < 4.0$ corresponding to the areas where the jet fluid pockets shed into the crossflow. Starting from the position where $x/d \approx 5.0$, all the curves converge to a decreasing rate of $k \approx -0.77$, exhibiting a homogeneous mixing in the far field.

4.6.2 Point Probability Density Functions

To extract the spatial mixing characteristics at a specific location, the point probability density function (PDF) is examined. The PDF at point x is defined as:

$$f(\xi;\, x_i) = \{\text{probability that the event } \alpha_{ik} = \xi \text{ occurs}\} \tag{4.4}$$

where ξ is the statistical representation of α and x_i is the point under observation. Each function $f(\xi;\, x_i)$ is constructed from the time series α_{ik} (i is fixed for a given location, k is the index for the time series) so that mean temporal quantities are obtained by integration such that:

$$\langle \alpha_i \rangle = \int_{-\infty}^{+\infty} \xi f(\xi; x_i) d\xi \tag{4.5}$$

Figure 4.26 shows the PDF at the probe points noted earlier for both cases. Since Probe07 is located in the jet potential core, its PDF rises significantly approaching $C = 1.0$. The PDFs disperse for both of the other probes around their average value and give a sense of temporal homogeneity at their corresponding locations. For Probe20, which is located $x/d \approx 5.0$ downstream of the jet exit, the $r = 4$ case shows a flatter profile, exhibiting larger inhomogeneity. The profiles for Probe34, located $x/d \approx 12.0$ downstream of the jet exit, however, show a more centralized distribution and demonstrate a more homogeneous mixing in the far field.

4.6.3 Spatial Mixing Deficiency and Temporal Mixing Deficiency

Two mixing indices, the spatial mixing deficiency (SMD) and the temporal mixing deficiency (TMD) are investigated in the downstream locations where $x/d =$ 0, 1, 2, 5, 8, 10, 12, and 15. The SMD index represents a planar average and measures the spatial heterogeneity of the mixture (a zero SMD value indicates perfect mixing in this plane). The TMD index gives a planar average of the temporal fluctuations and tends to quantify the temporal heterogeneity of the mixture. Both indices are calculated based upon instantaneous scalar concentration C. Over n snapshots, the SMD and TMD at point i are calculated as

$$SMD = \frac{RMS_{plane}\left(\langle C_i \rangle\right)}{Avg_{plane}\left(\langle C_i \rangle\right)} \qquad (4.6)$$

$$TMD = Avg_{plane}\left(\frac{RMS_i}{\langle C_i \rangle}\right) \tag{4.7}$$

where

$$\langle C_i \rangle = \frac{1}{n}\sum_{k=1}^{n} C_{i,k}$$

$$RMS_i = \sqrt{\frac{1}{n-1}\sum_{k=1}^{n}\left(\langle C_i \rangle - C_{i,k}\right)^2} \tag{4.8}$$

$$Avg_{plane}\left(\langle C_i \rangle\right) = \frac{1}{m}\sum_{i=1}^{m}\langle C_i \rangle$$

$$RMS_{plane}\left(\langle C_i \rangle\right) = \sqrt{\frac{1}{m-1}\sum_{i=1}^{m}\left(\langle C_i \rangle - Avg_{plane}\left(\langle C_i \rangle\right)\right)^2}$$

The calculations are carried out only in the regions where the jet fluid concentration is not zero. The regions in the YZ planes extend to $[-3.0d,\ 3.0d]\times[0,\ 6.0d]$ and $[-4.0d,\ 4.0d]\times[0,\ 10.0d]$ for the $r = 2$ and $r = 4$ cases, respectively. Figure 4.27 shows the spatial evolution of the two indices as percentages. For the same velocity ratios, no significant difference is observed between the grid sets. As a result of the nature of complex flow, high spatial heterogeneity exists in both cases and provides a large SMD at all locations, though it diminishes all the way downstream. As for the TMD, the descending trend only applies to locations where $x/d > 5.0$, demonstrating high oscillatory movement in the near field. The two indices maintain smaller values at all locations for the $r = 4$ case, indicating that the mixing field is less heterogeneous and has larger velocity ratios.

4.7 Conclusion

Large eddy simulations (LES) have been conducted to investigate the flow dynamics and mixing processes for a turbulent gaseous jet into stationary crossflow. Two velocity ratios were considered: $r = 2$ and $r = 4$. Major results are summarized here:

1. Vortical structures are identified: a) the horseshoe vortices are detected ahead of the jet body, and their strength is quite small compared to the other vortices; b) the spanwise rollers (jet shear-layer vortices) appear on both the windward and leeward sides of the jet in the near field, and play an important role in defining the boundary of the jet plume; c) the wake vortices present tornado-like structures and provide a possible connection between the jet plume and the crossflow boundary layer; d) the counter-rotating vortex pair (CVP) can be manifested by the mean flow properties and its early formation is closely related to the hanging vortices produced in the skewed mixing layer. The strength and structures of the vortices are affected by the velocity ratio, with a tendency to indicate that a higher velocity ratio generates more apparent visualizations.

2. Scalar mixing is discussed in relation to several processes: a) the entrainment of the crossflow by the jet can be accounted for by the gaps between the rolling vortices on the surface of the jet plume; b) for a low jet trajectory, the upright wake vortices have a high intermittency in transporting the crossflow fluid into the main jet body; c) turbulent scalar flux is created primarily by the coherent vortical structures.

3. Mixing efficiency is quantified as follows: a) the decay rate of the scalar concentration is closely related to the flow dynamics; b) the probability density function

(PDF) is an effective method for testing the local mixing characteristics; c) the spatial mixing deficiency (SMD) and temporal mixing deficiency (TMD) have a strong dependence on the velocity ratio and are less heterogeneous in the $r = 4$ case.

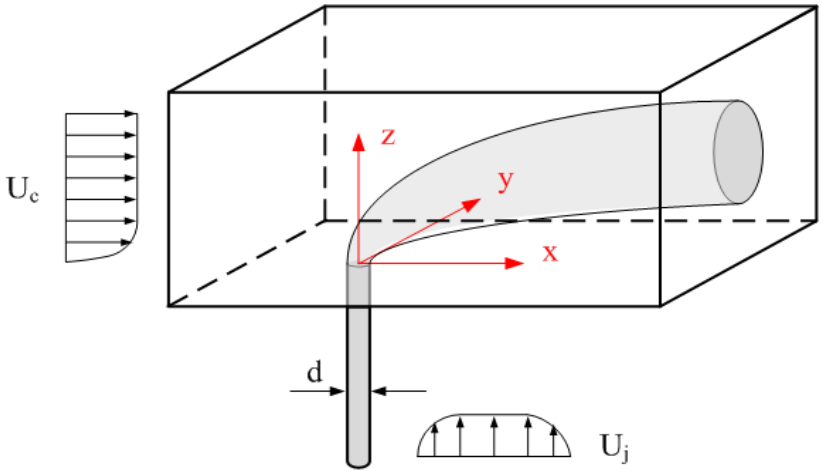

Figure 4.1 Schematic of a jet into crossflow

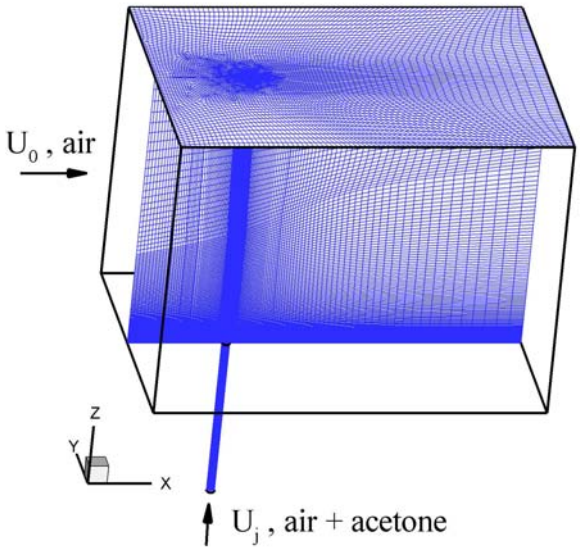

Figure 4.2 Flow configuration and mesh topology for the validation case

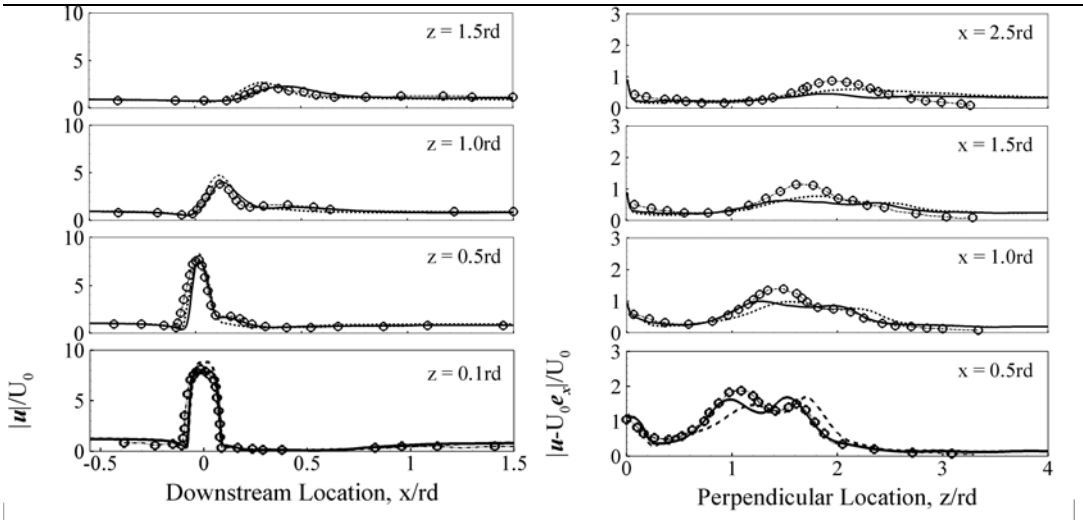

Figure 4.3 Averaged velocity magnitude profiles in the jet center plane. Solid lines: Dynamic SGS model; Dashed lines: Static SGS model; Symbols: Experiments.

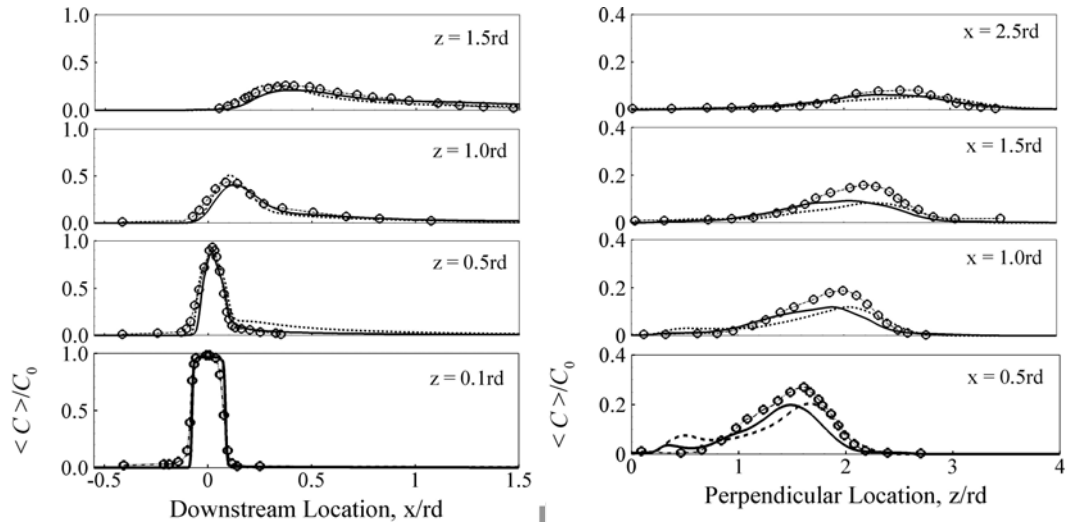

Figure 4.4 Averaged scalar field profiles in the jet center plane. Solid lines: Dynamic SGS model; Dashed lines: Static SGS model; Symbols: Experiments.

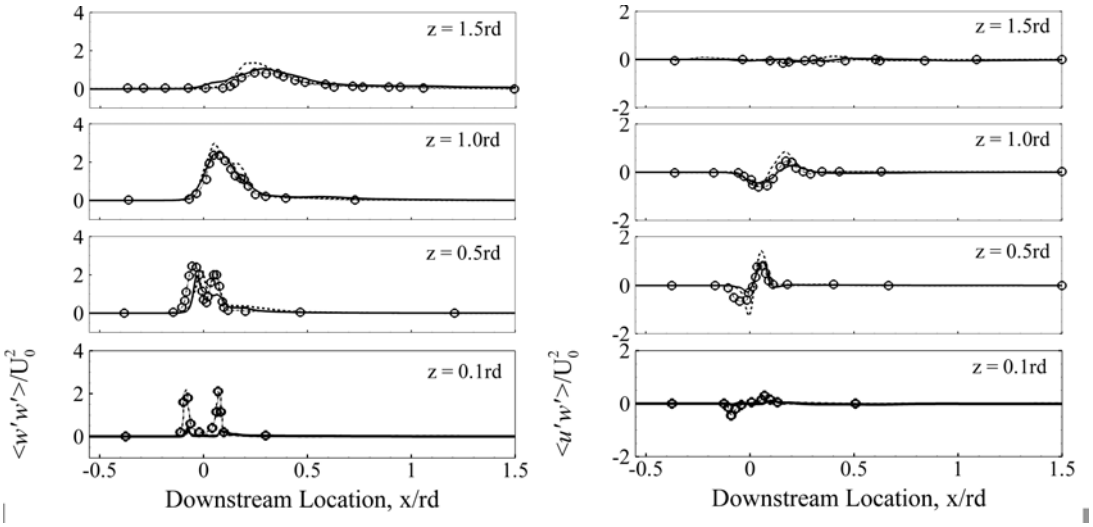

Figure 4.5 Stress profiles in the jet center plane. Solid lines: Dynamic SGS model; Dashed lines: Static SGS model; Symbols: Experiments.

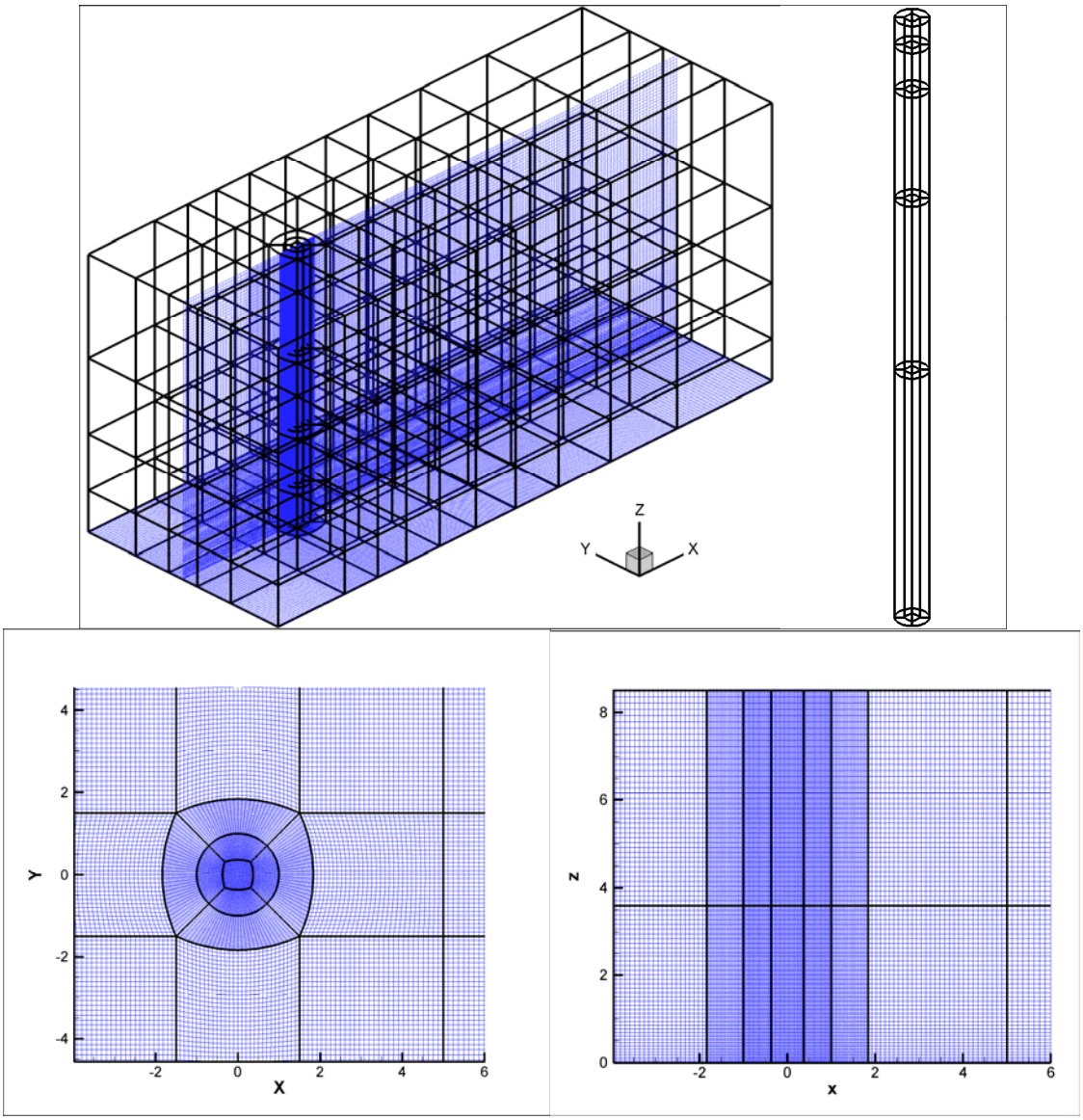

Figure 4.6 Grid distributions and block assignment

Table 4.1 Grid systems

	Total grid size	Average mesh size	Near wall resolution	CPU cores
Grid A	2.8 million	0.15mm	$y^+ \approx 3$	67
Grid B	8.9 million	0.09mm	$y^+ \approx 3$	72
Grid C	29.7 million	0.06mm	$y^+ \approx 3$	262

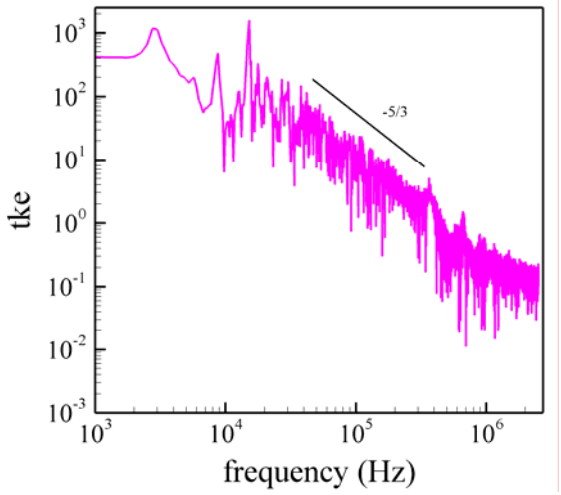

Figure 4.7 Turbulent kinetic energy spectrums at a probe in the jet pipe

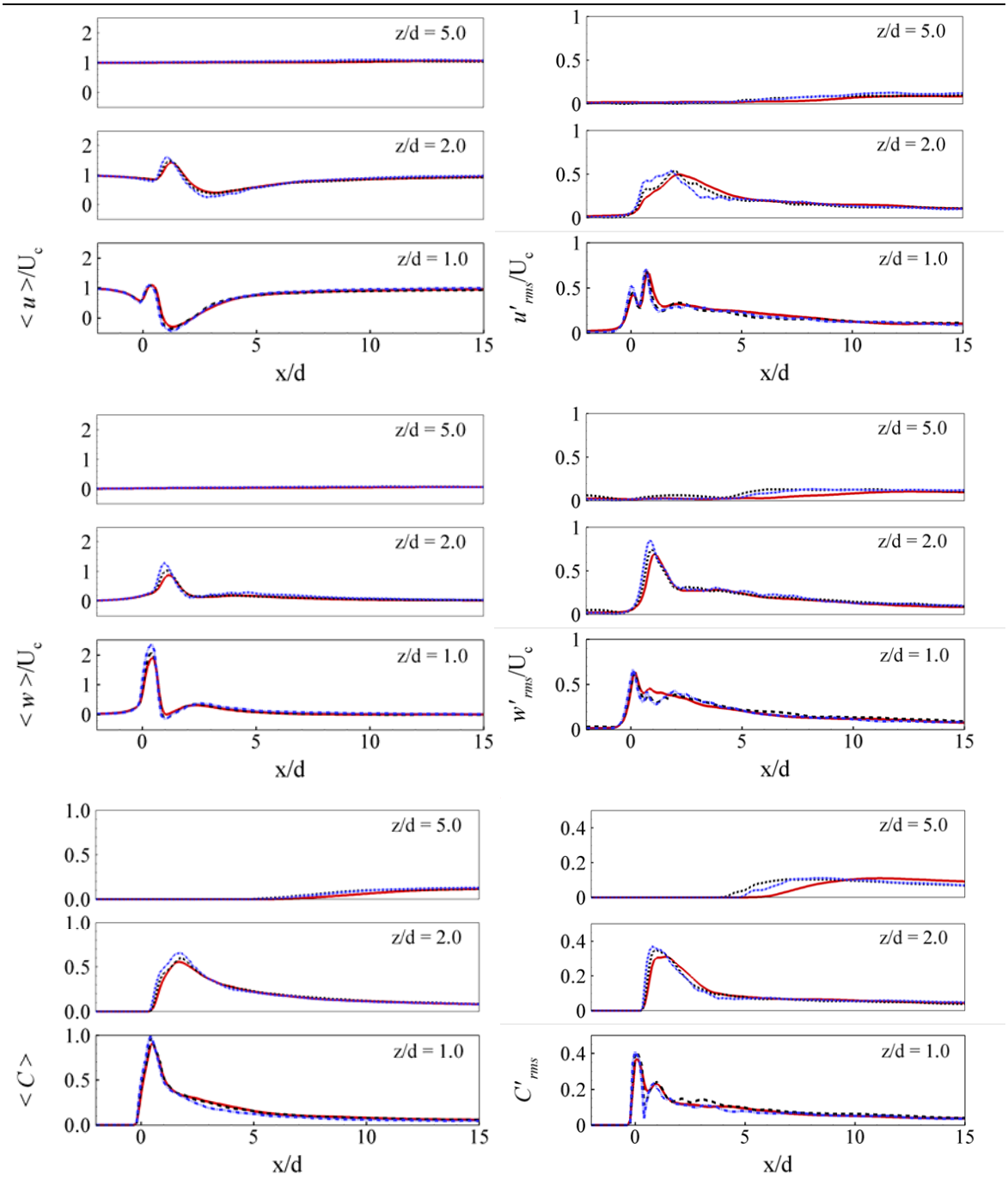

Figure 4.8 Mean and RMS (a) streamwise velocity, (b) vertical velocity and (c) scalar concentration in the center plane at vertical locations
(Red solid: grid A; Black dashed: grid B; Blue dashdotdot: grid C)

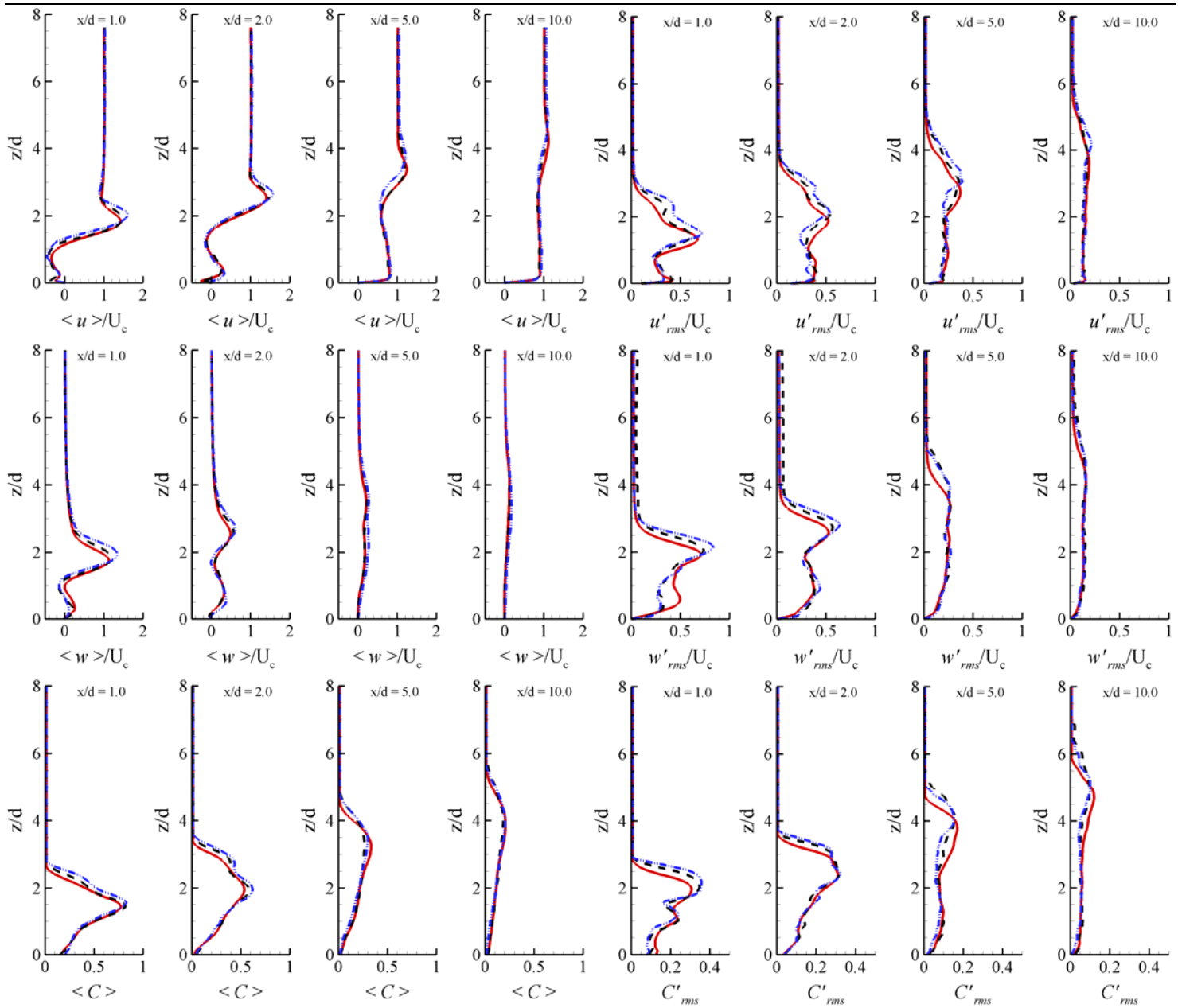

Figure 4.9 Mean and RMS (a) streamwise velocity, (b) vertical velocity and (c) scalar concentration in the center plane at downstream locations (Red solid: grid A; Black dashed: grid B; Blue dashdotdot: grid C)

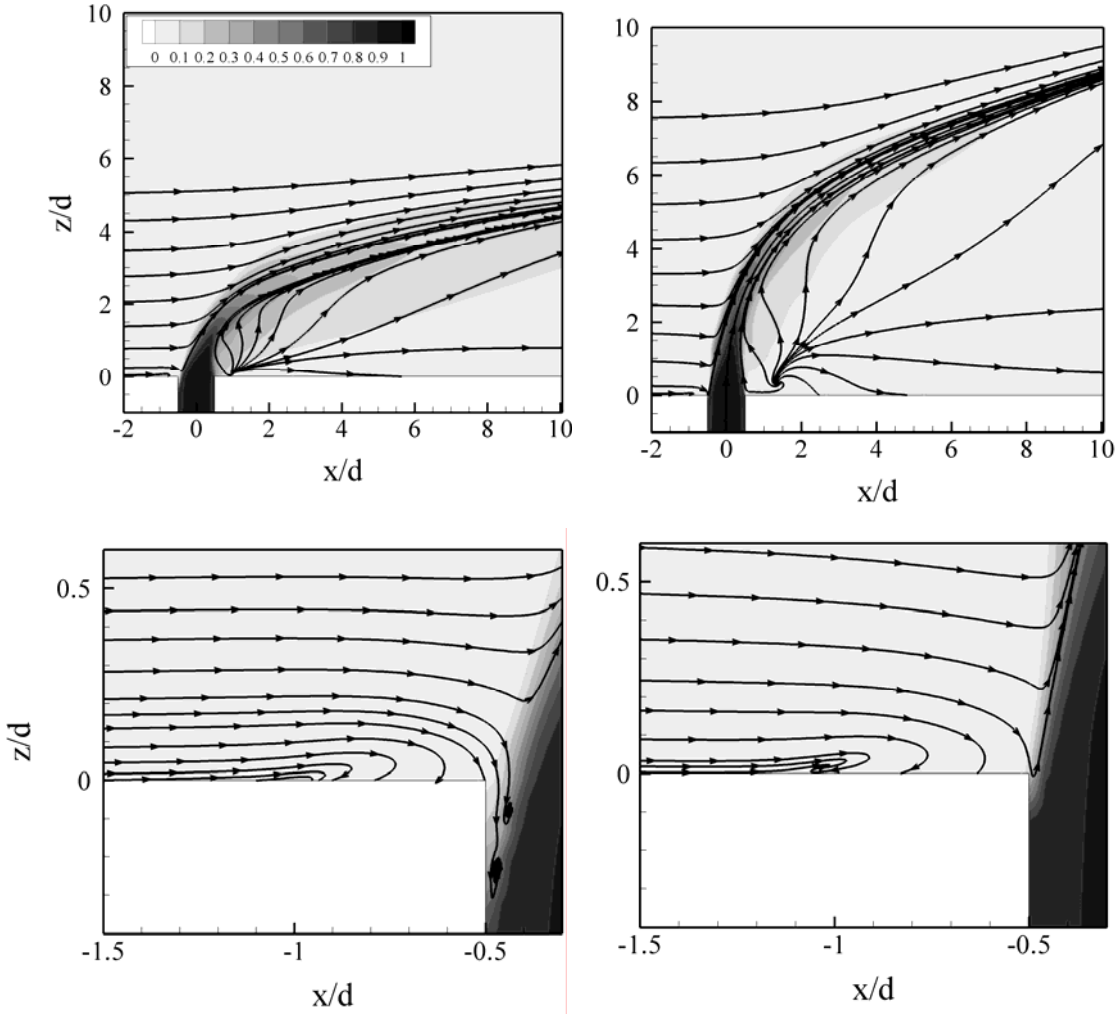

Figure 4.10 Two-dimensional streamlines of the average flow in the center plane: a) $r = 2$ and b) $r = 4$

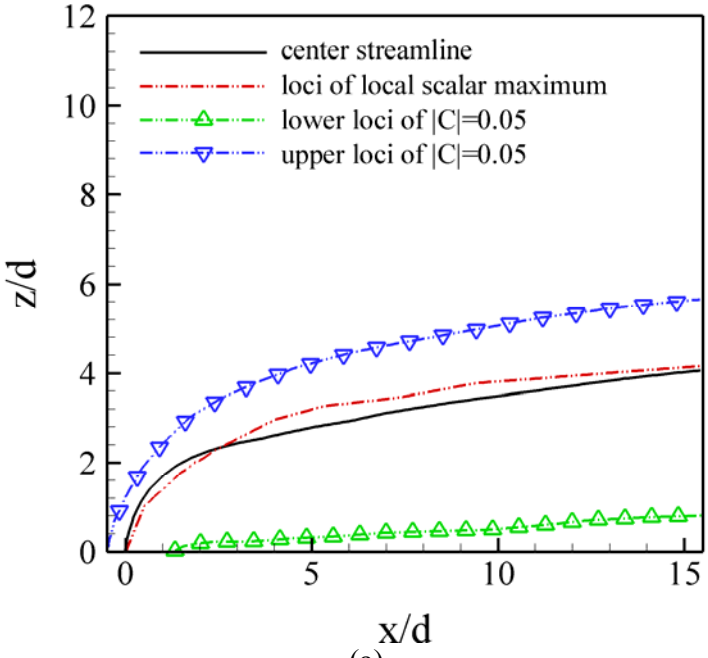

(a)

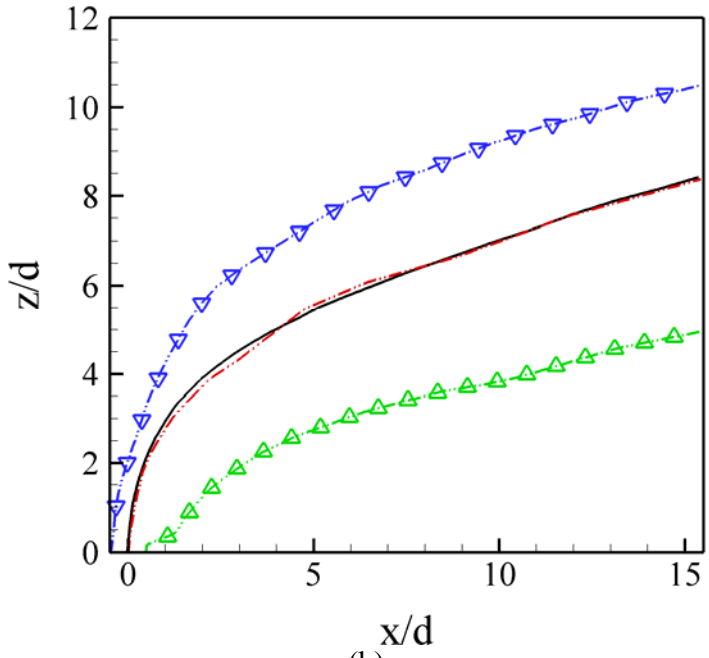

(b)

Figure 4.11 Jet trajectories in the center plane: a) $r = 2$ and b) $r = 4$

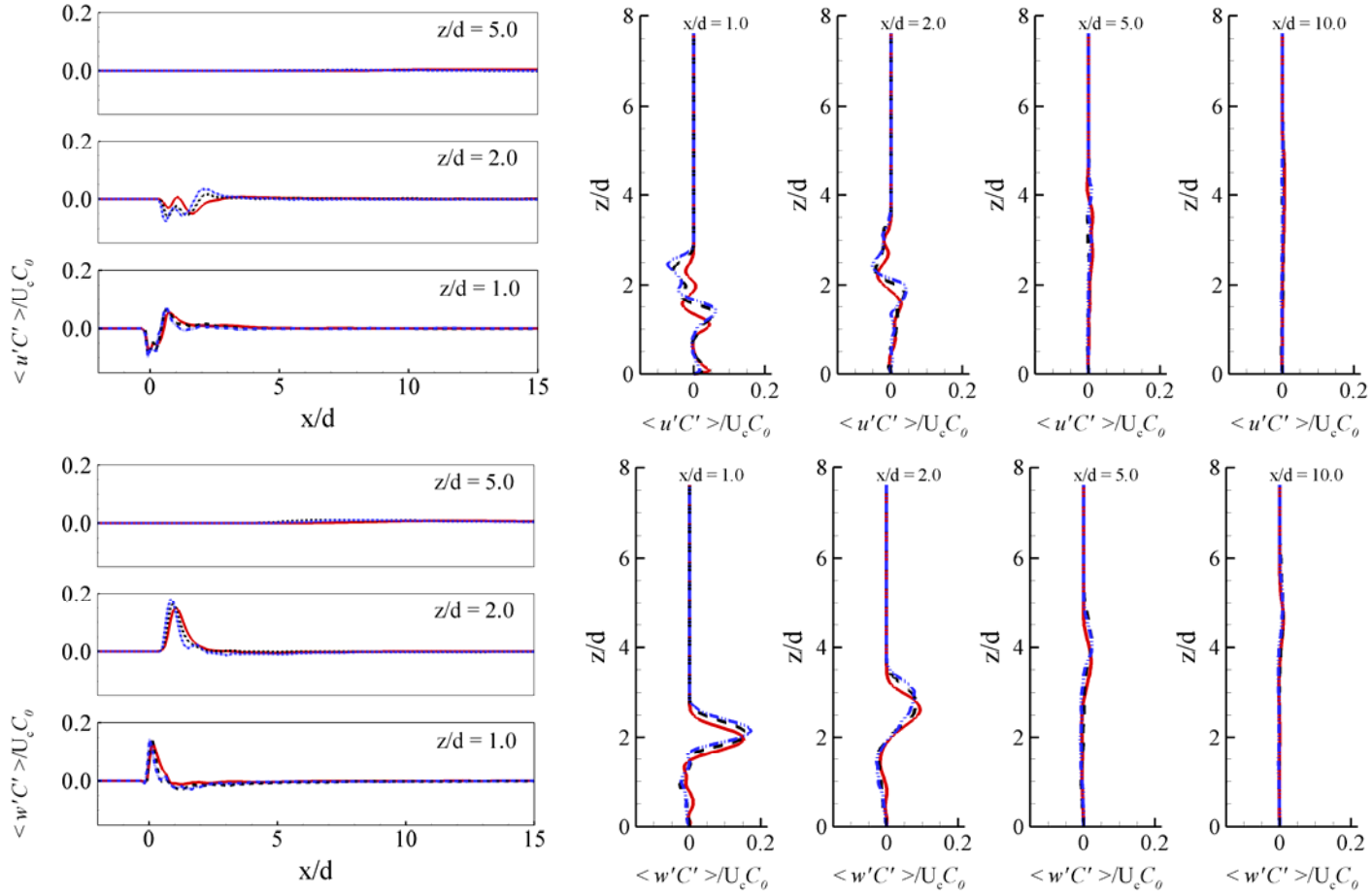

Figure 4.12 Turbulent scalar fluxes in the center plane at downstream locations
(Red solid: grid A; Black dashed: grid B; Blue dashdotdot: grid C)

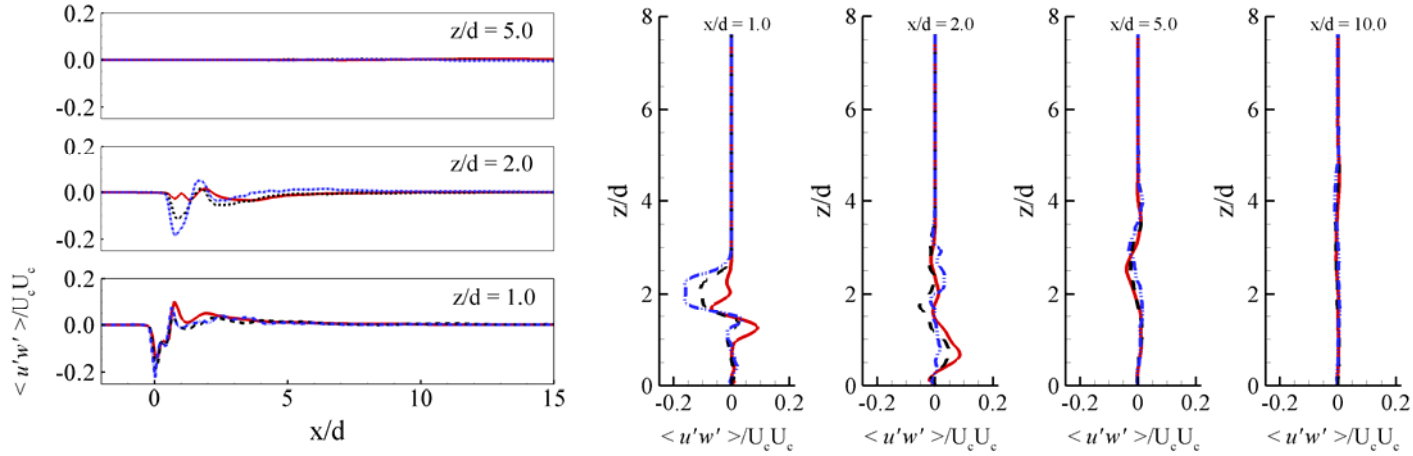

Figure 4.13 Turbulent stresses in the center plane at downstream locations
(Red solid: grid A; Black dashed: grid B; Blue dashdotdot: grid C)

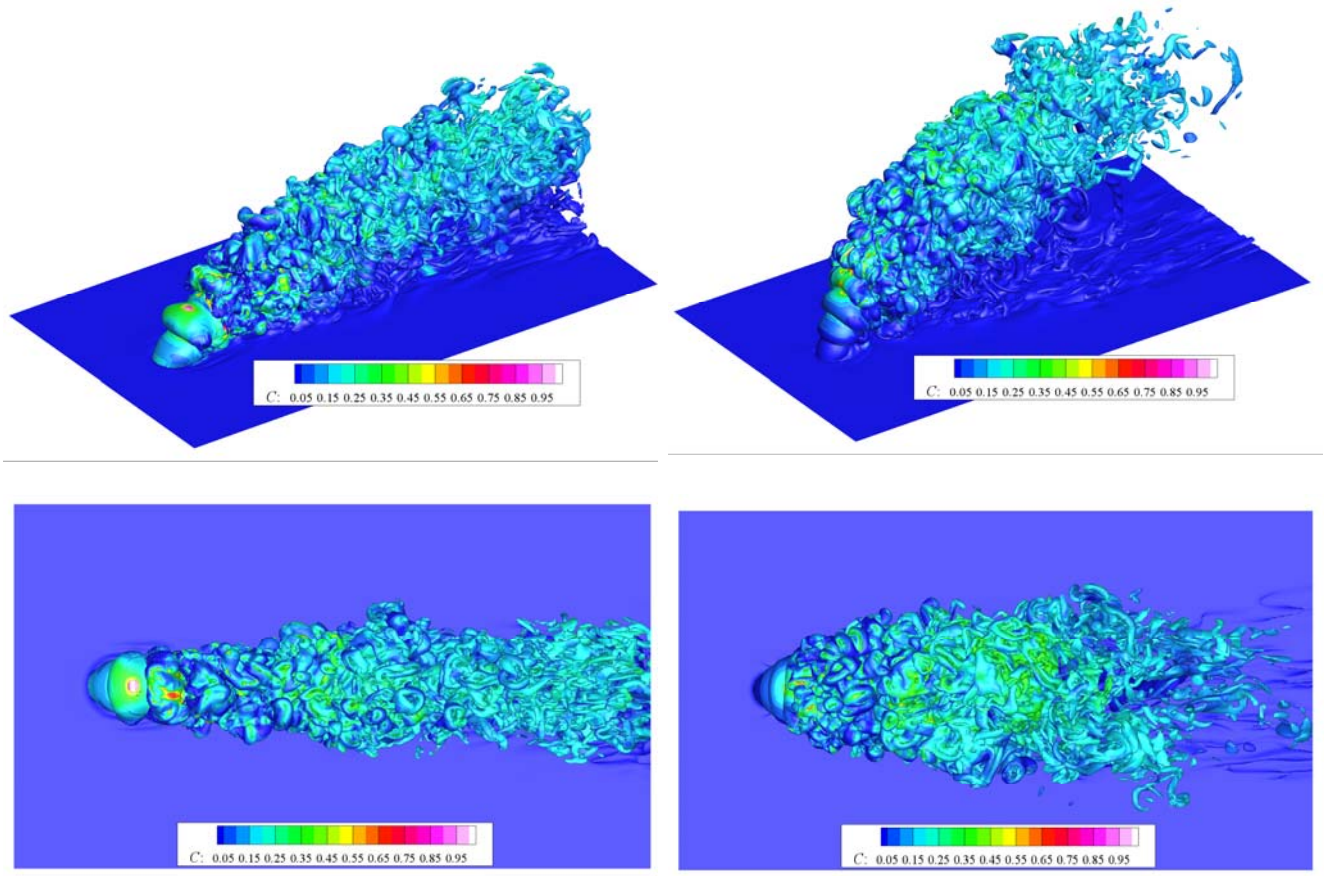

(a) (b)

Figure 4.14 Instantaneous vorticity: Iso-surface of vorticity magnitude $|\Omega| = 125,000$ colored by scalar concentration: (a) $r = 2$ and (b) $r = 4$ (Grid B)

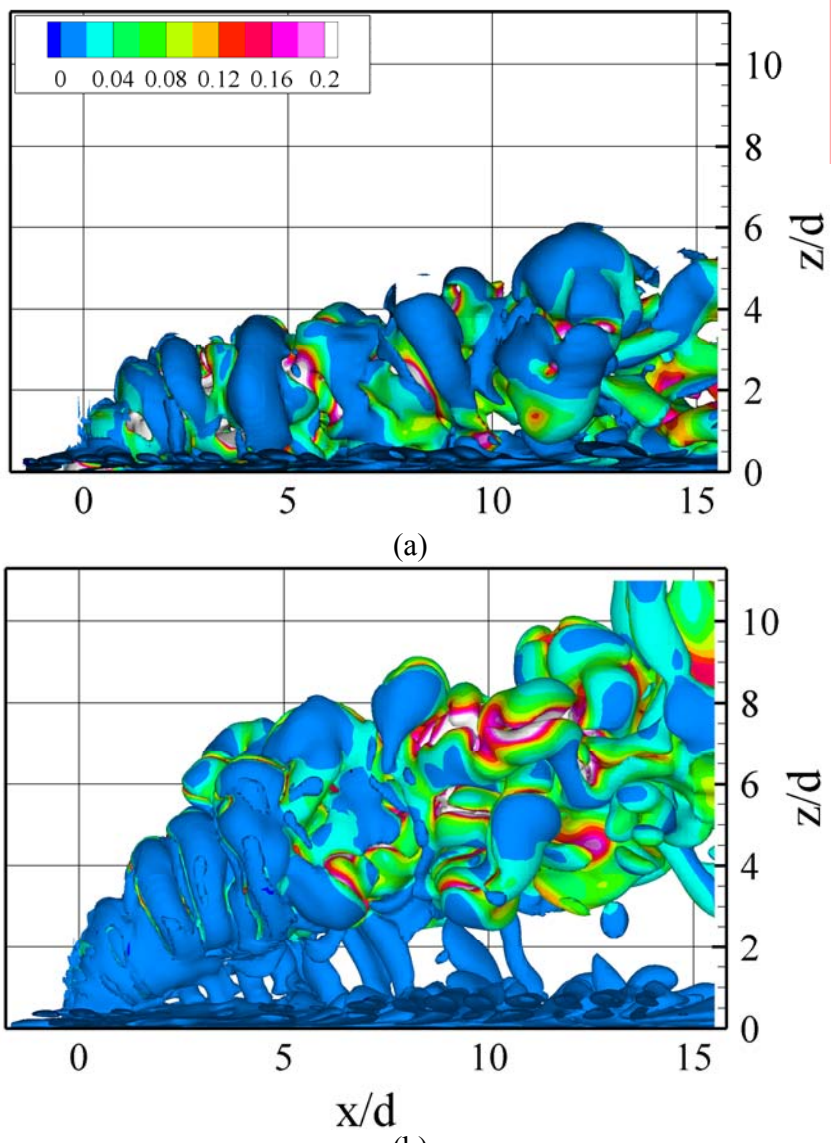

Figure 4.15 Instantaneous helicity: Iso-surface of $H = 250,000$ colored by scalar concentration: (a) $r = 2$ and (b) $r = 4$ (Grid A)

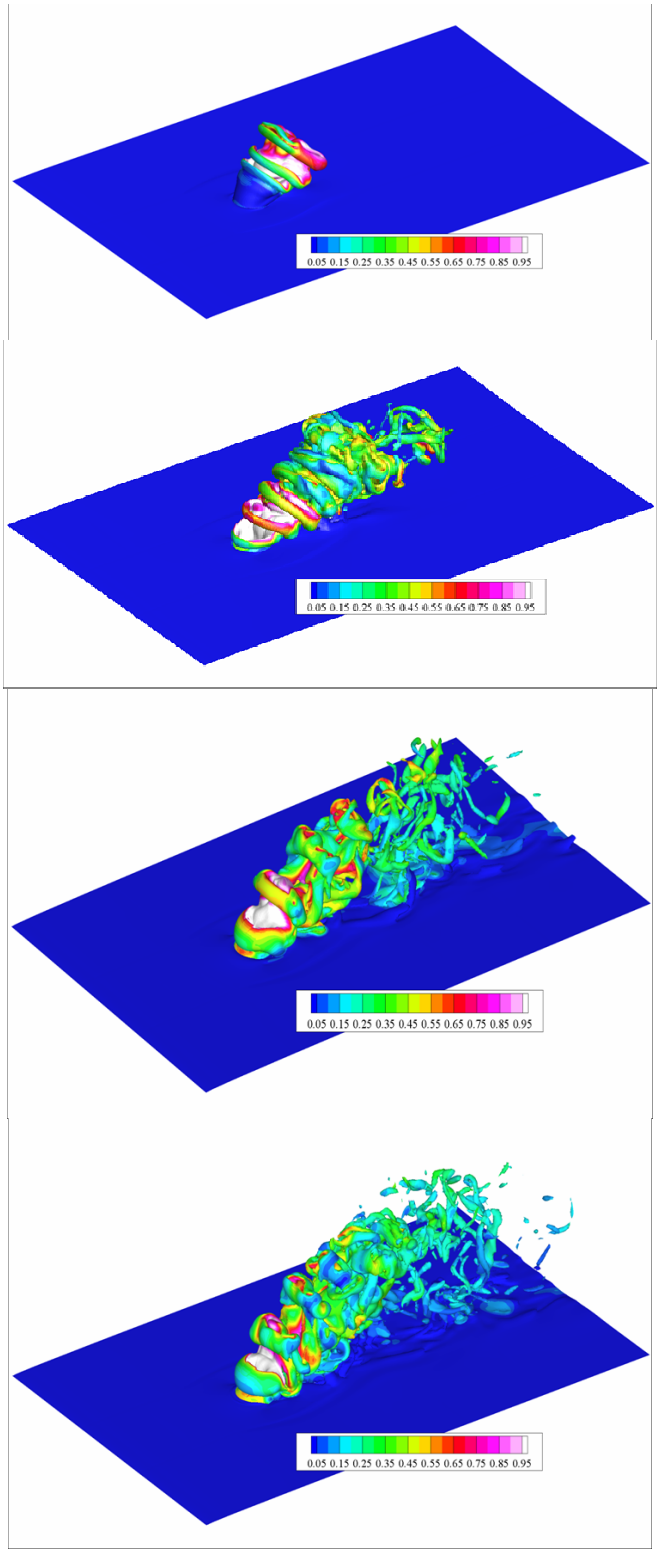

Figure 4.16 Iso-surfaces of |Ω|=250, 000 colored by scalar concentration on Grid B ($r = 2$)

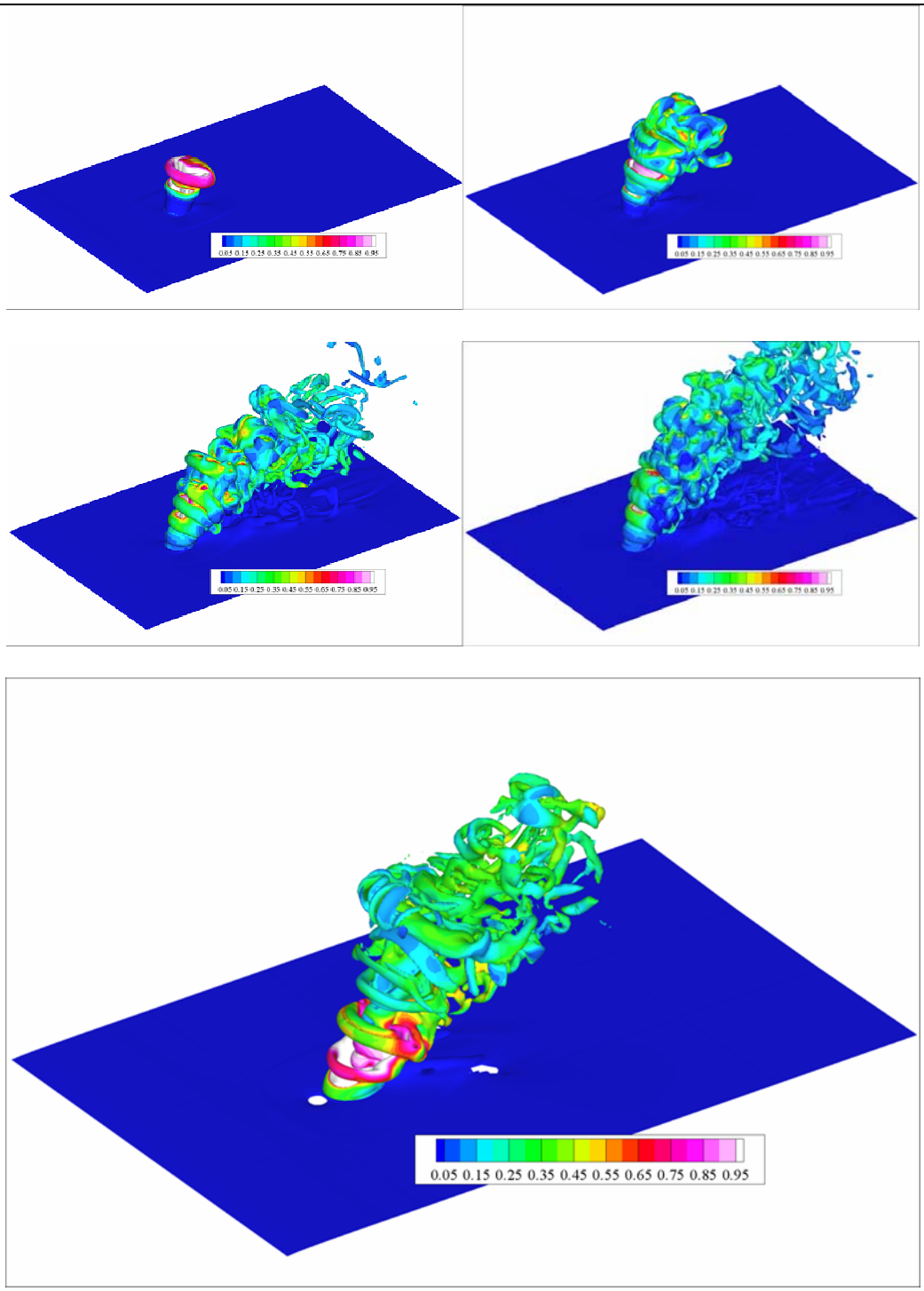

Figure 4.17 Iso-surfaces of |Ω|=125, 000 colored by scalar concentration on Grid B ($r = 4$)

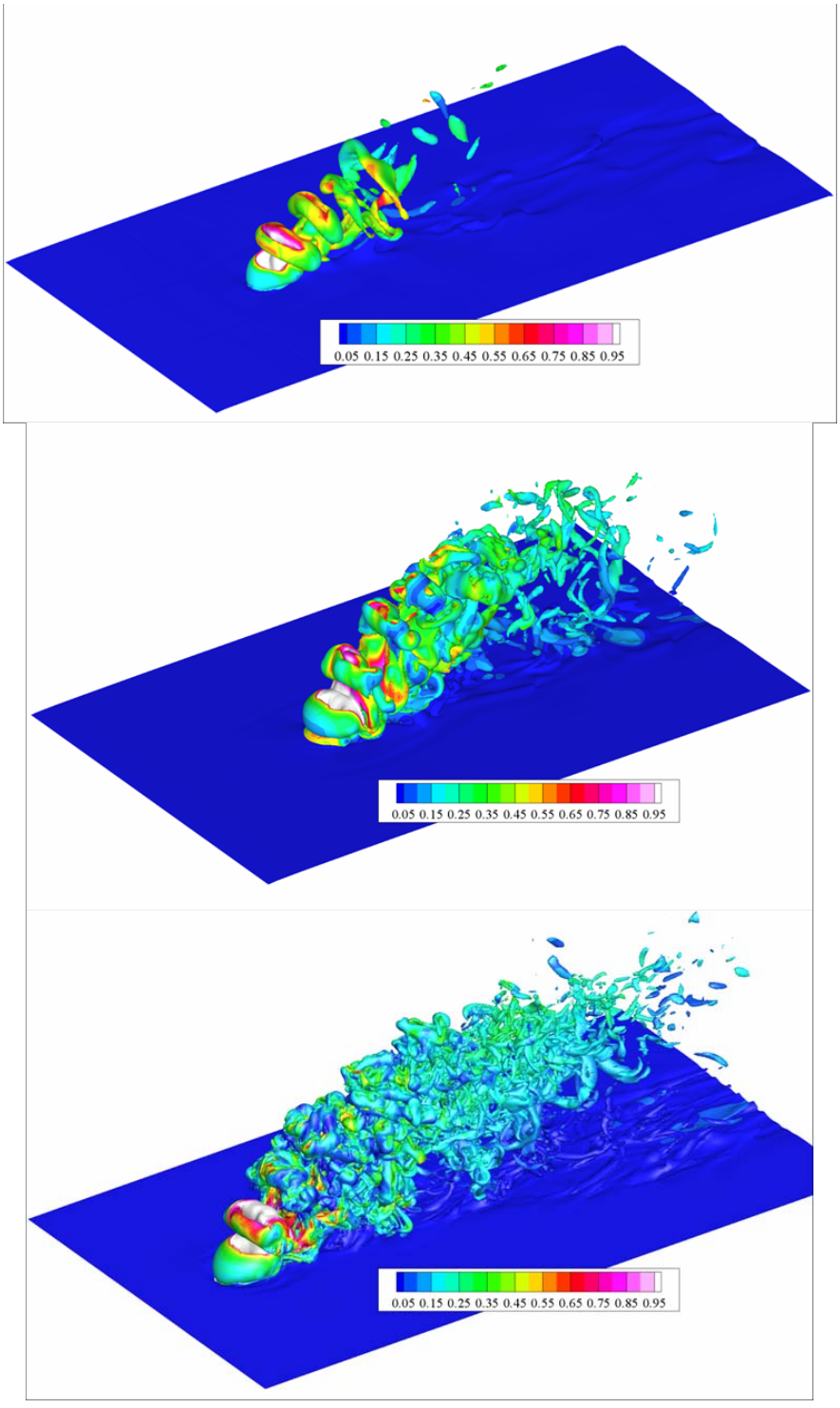

Figure 4.18 Iso-surfaces of |Ω|=250, 000 colored by scalar concentration at 0.8ms on three grids ($r = 2$)

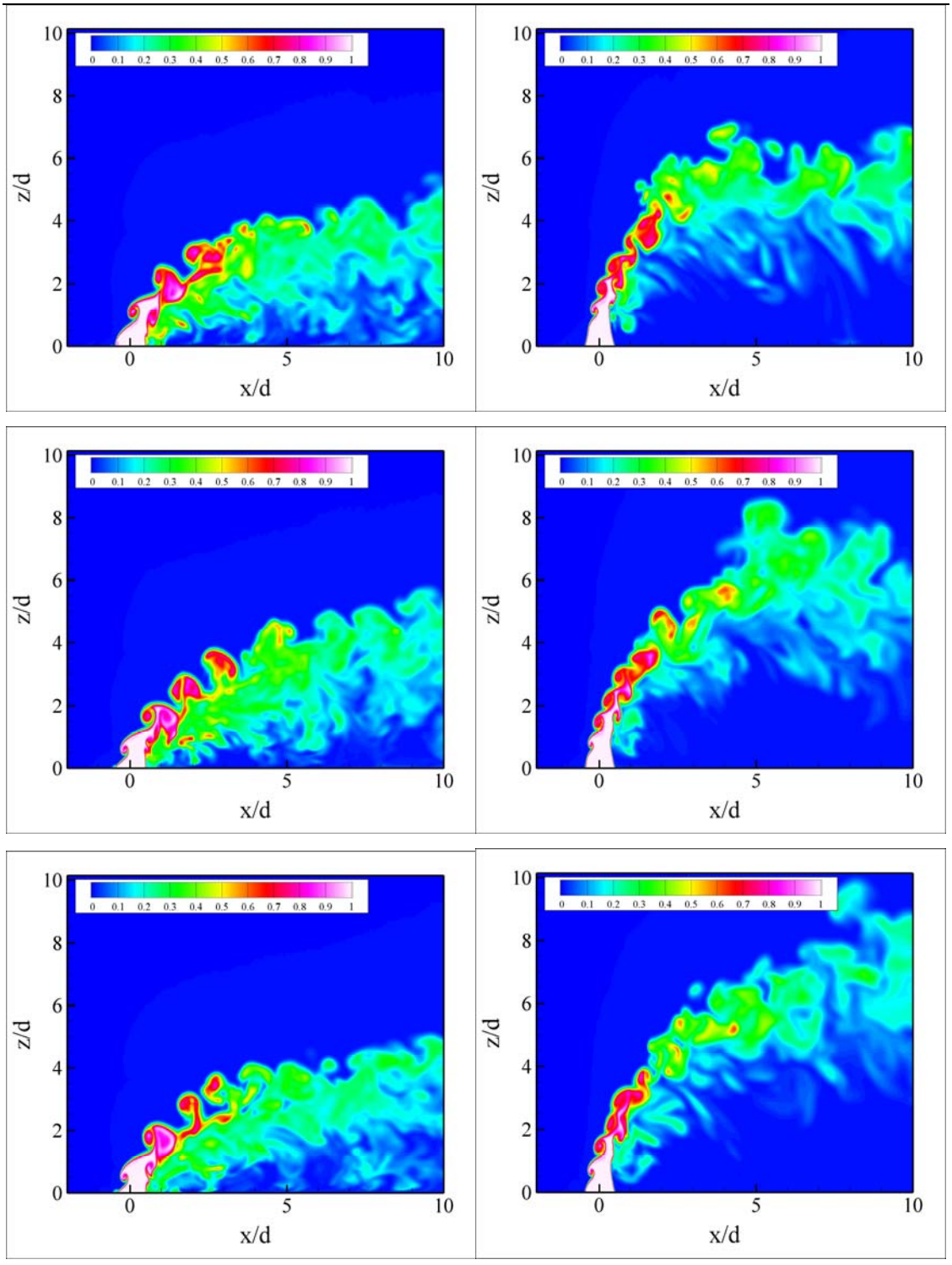

Figure 4.19 Temporal evolutions of scalar concentration in the center plane on Grid B (Left: $r = 2$, Right: $r = 4$)

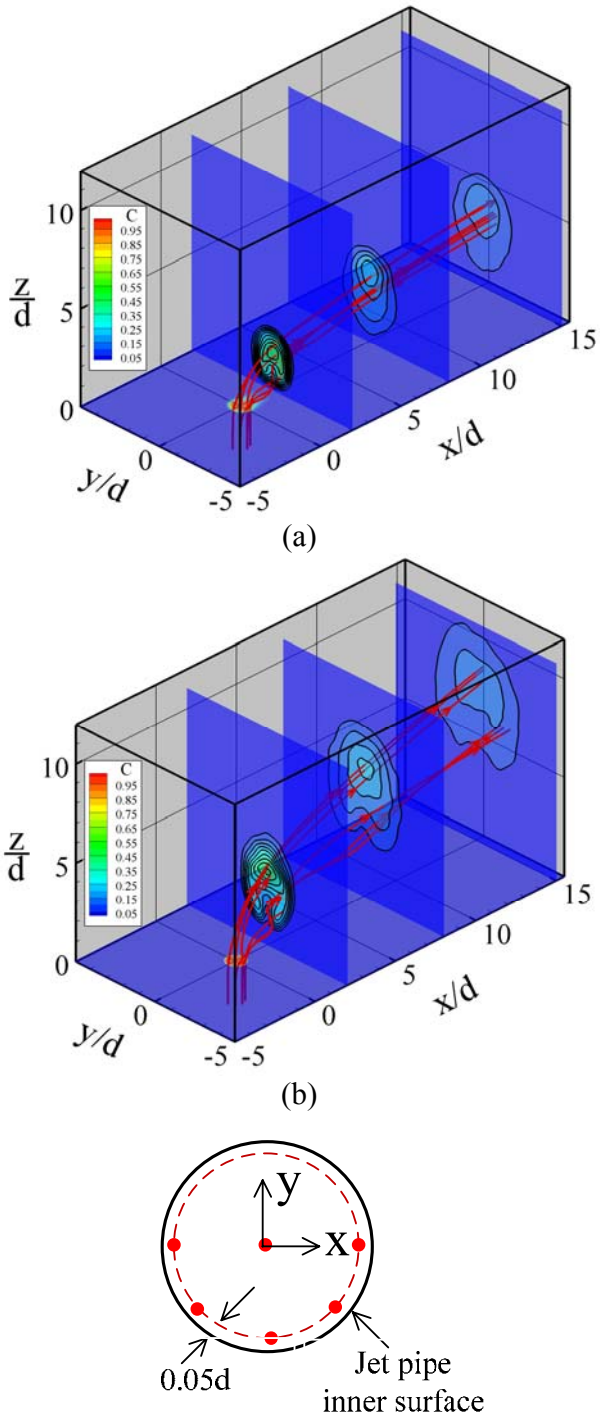

Figure 4.20 Three-dimensional streamlines of the average flow: a) $r = 2$, b) $r = 4$ and c) streamline traces in the $z/d = -2$ plane

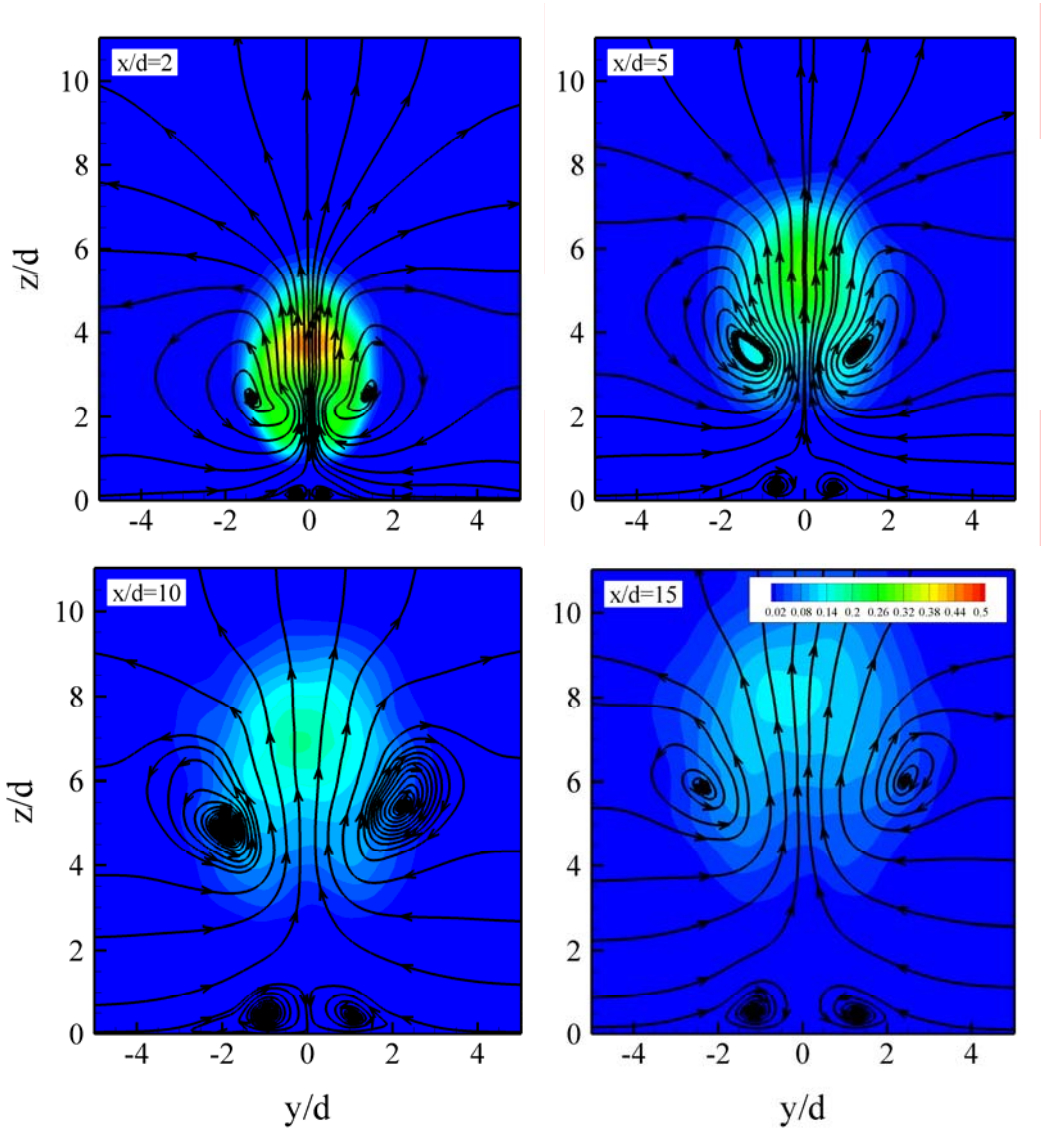

Figure 4.21 Spatial evolutions of the jet fluid concentration with two-dimensional streamlines ($r = 4$)

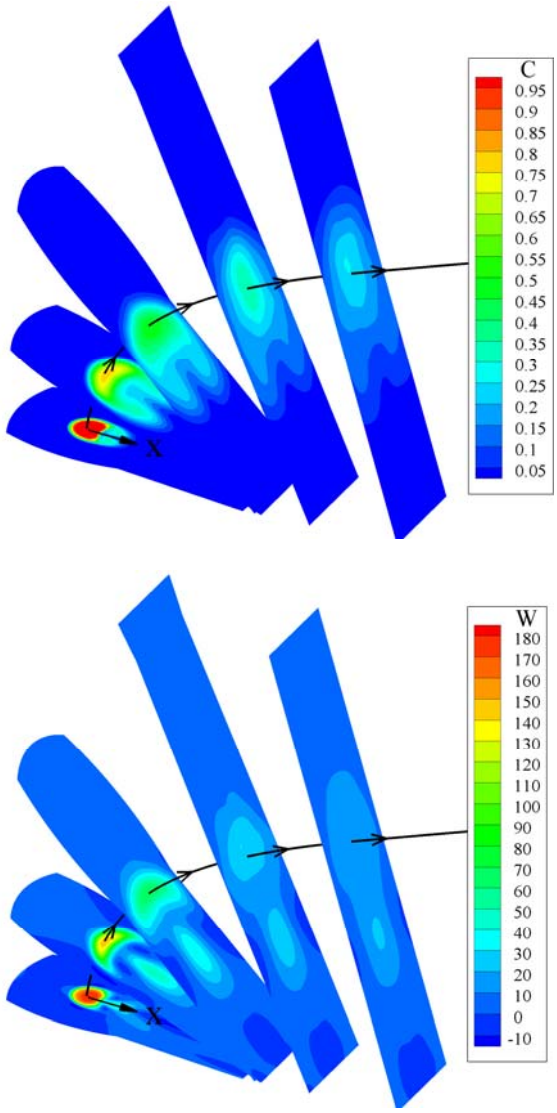

Figure 4.22 Spatial evolutions of the average flow field along the center streamlines ($r = 4$)

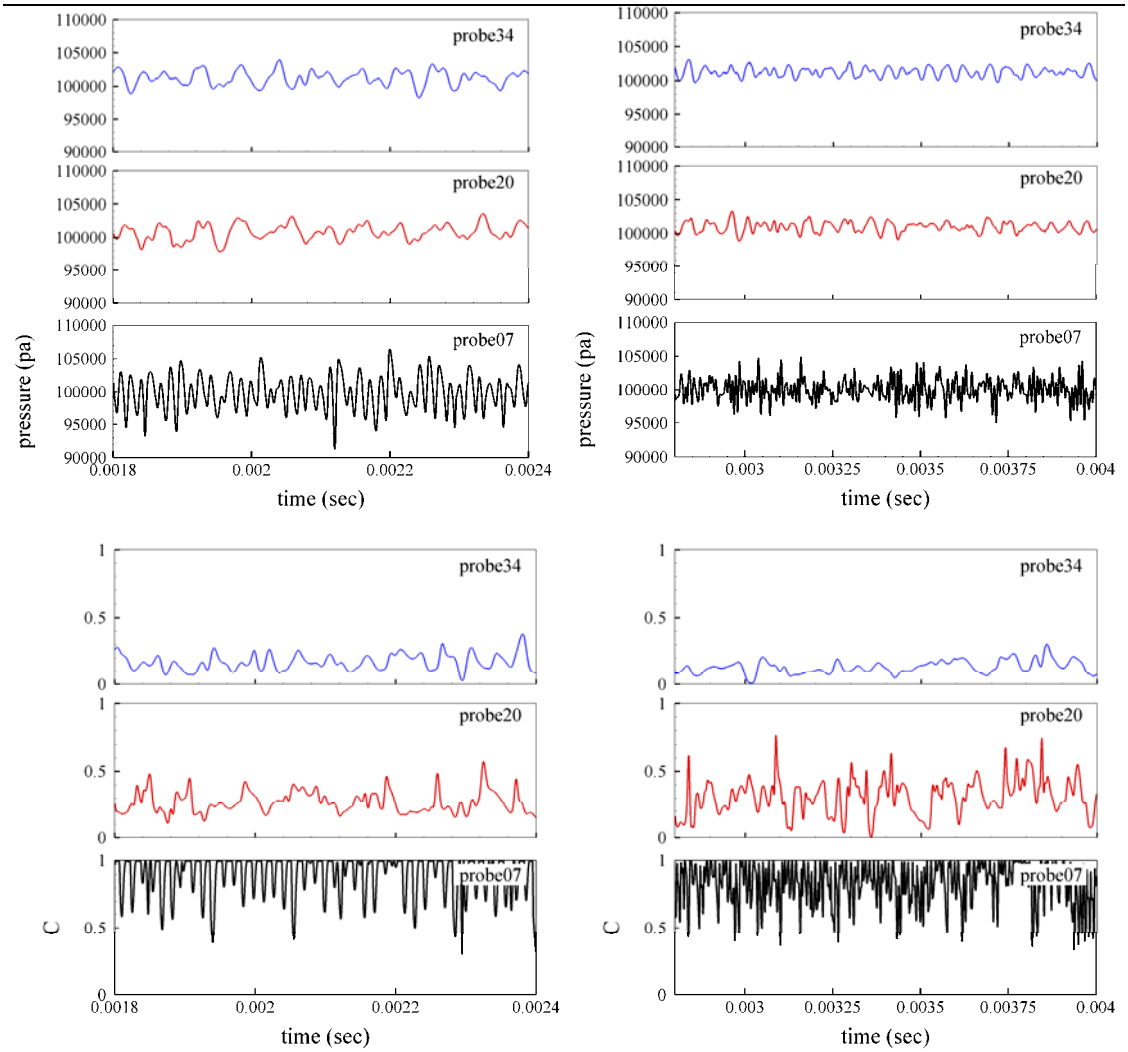

Figure 4.23 Time evolutions of pressure and scalar concentration at probe locations (Left: $r = 2$, Right: $r = 4$)

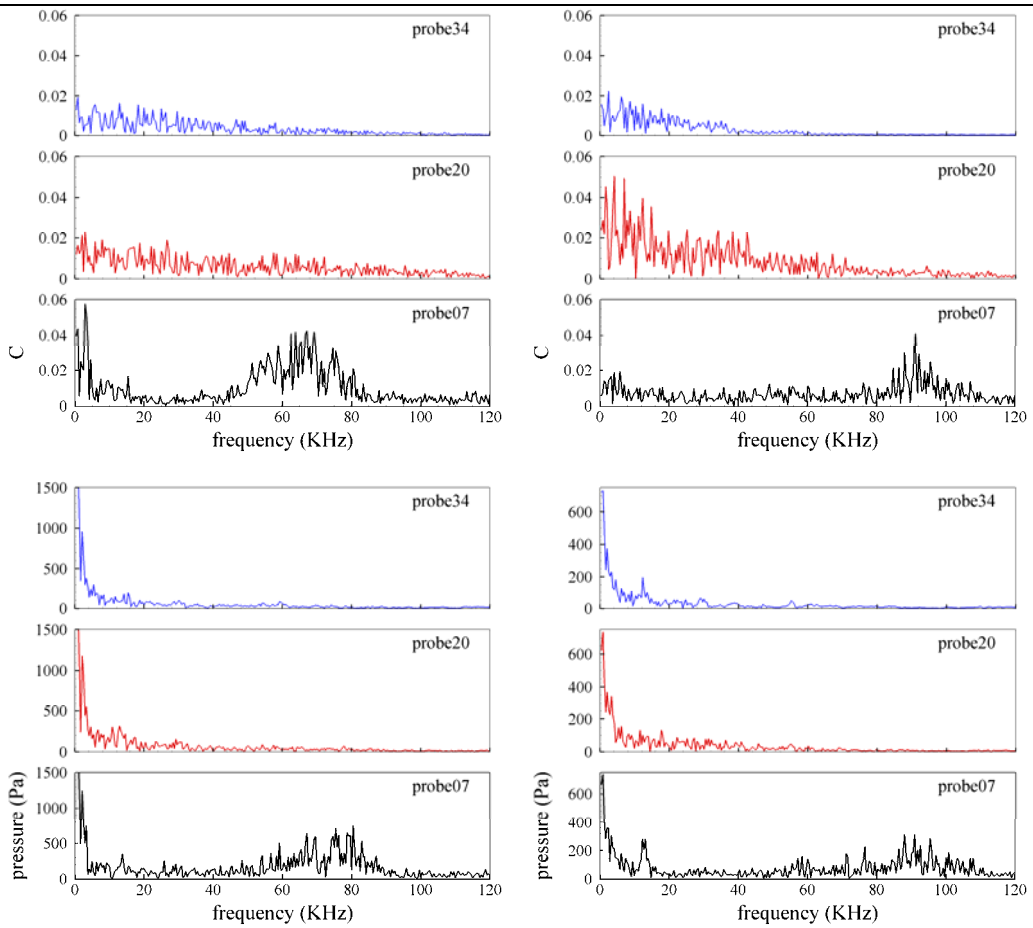

Figure 4.24 Power spectral analysis of pressure and scalar concentration at probe locations (Left: $r = 2$, Right: $r = 4$)

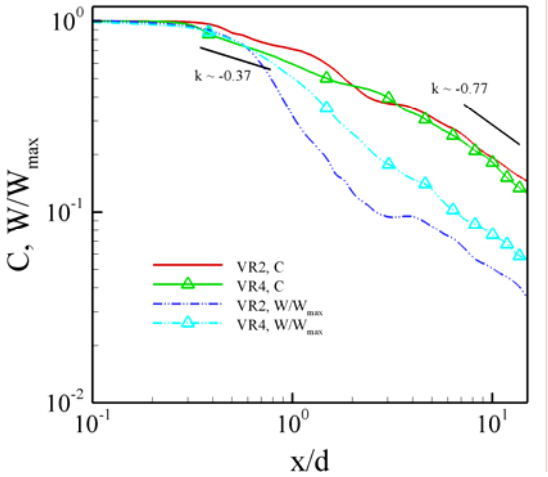

Figure 4.25 Decays of local maxima of scalar concentration and normalized vertical velocity

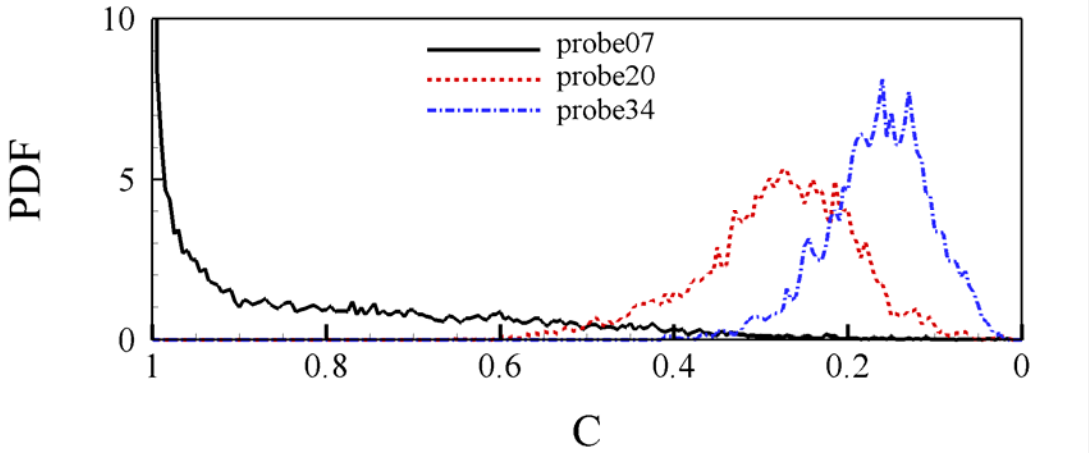

(a)

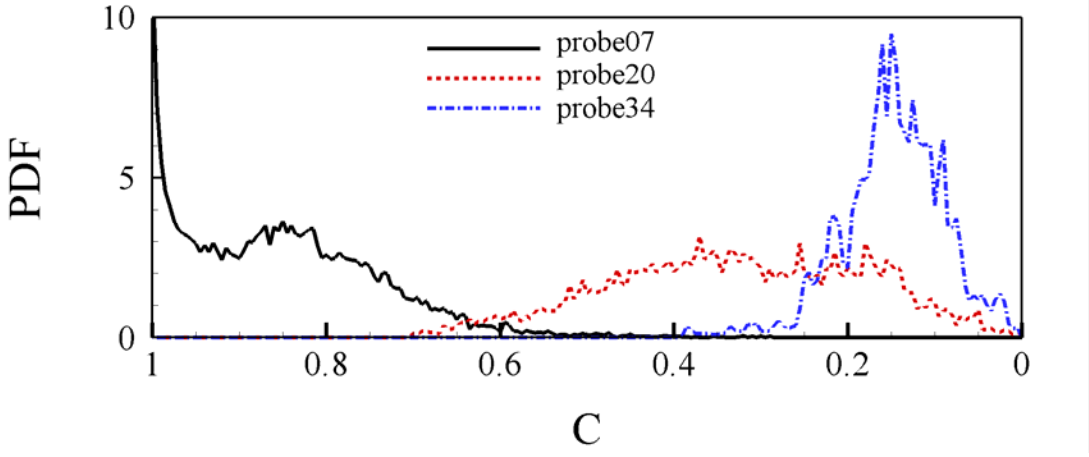

(b)

Figure 4.26 Point PDF of scalar concentration: a) $r = 2$, b) $r = 4$

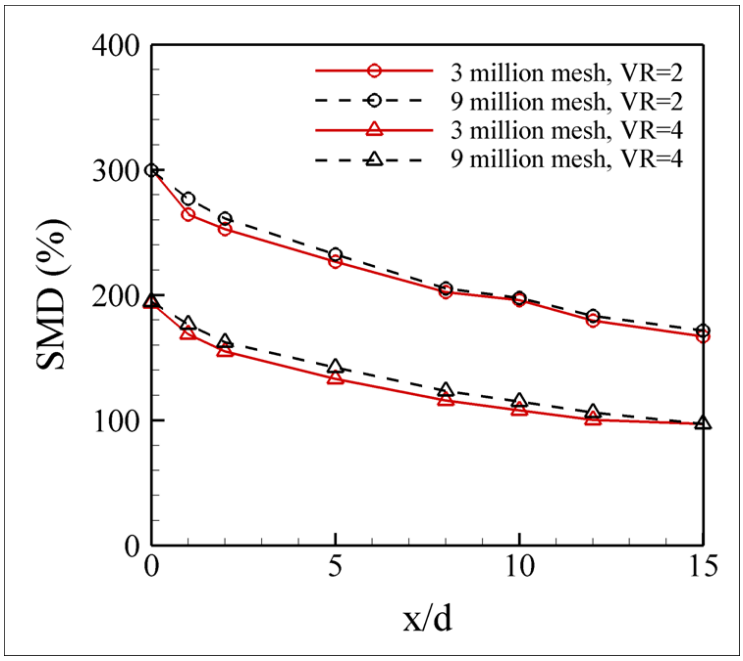

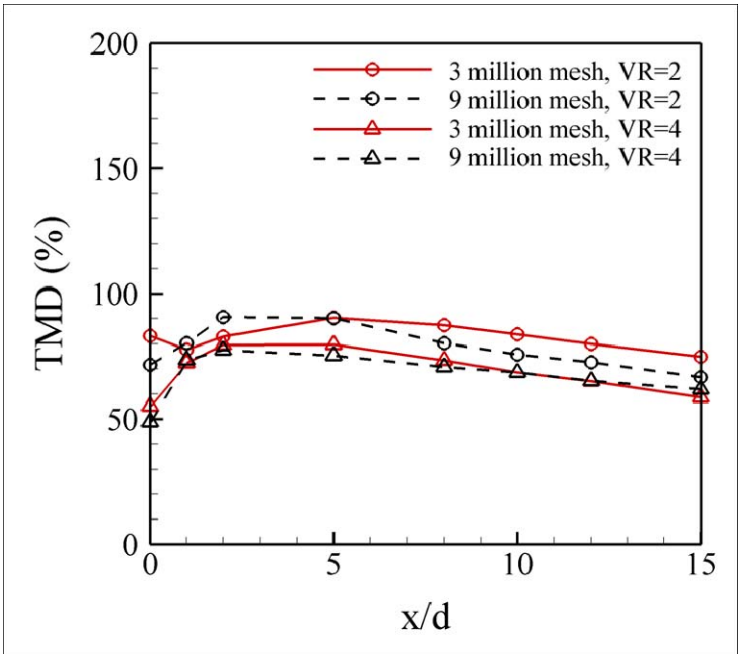

Figure 4.27 SMD and TMD

This page intentionally left blank

Chapter 5

Flow Dynamics and Scalar Mixing of a Turbulent Gaseous Jet into Oscillating Crossflow

5.1 Introduction

External excitations are frequently used in the analysis of system dynamics. In 1984, Ho and Huerre published their classic work on perturbed (forced) free shear layers. They found that monochromatic excitation could suppress broadband background noise and lead to well-organized vortical structures. In addition, they noted that the appearance of other discrete frequency components observed in free forcing flows could be delayed by single-frequency forcing.

Recent studies have investigated the use of forced oscillations to simulate combustion-generated fluctuating environments. It has been shown that external excitations at certain frequencies are able to effectively organize the flow structure, amplify the instability, and modify the whole flow field. Apte and Yang (2002) studied unsteady flow dynamics in a porous-wall chamber using impressed periodic excitations. They found these excitations led to earlier laminar-to-turbulent transitions than those observed in a stationary flow, and that the coupling between the turbulent and acoustic motions resulted in significant changes in the unsteady flow dynamics. Wang and Yang (2005) analyzed the acoustic response of a gas-turbine swirl-stabilized injector to broadband externally imposed excitations. They observed that dynamic behaviors were

significantly modulated in both the spatial and spectral domains, while the flow dynamics under forcing was highly frequency-dependent. Because of the broadband nature of the injector flow field, the mean flow properties appeared to be marginally changed, except in regions where the characteristic frequencies of the flow motion matched the forcing frequency.

In the context of jet in crossflow, acoustically modulated jets have been widely investigated as a means to enhance the jet/crossflow mix. However, only limited work (using water as the working fluid) has focused on a jet into an unsteady crossflow, even though the jet injection processes in realistic gas turbine systems occur in the environment of an oscillating crossflow. In this work, we try to evaluate the acoustic effect on the evolution and mixing of a gaseous jet into crossflow by imposing periodic oscillations to the crossflow. First, the intrinsic instabilities within the flow field are reviewed and extracted using Proper Orthogonal Decomposition (POD) analysis. Then, multiple sets of acoustic frequency/amplitude are considered, mimicking a broad range of fluctuations. Their induced flow structures are indicated and analyzed across the pressure, velocity and mixing fields.

5.2 Stability Analysis of a Jet into Crossflow

5.2.1 Global Stability of a Jet into Crossflow

The flow structure and mixing properties of the JICF are dominated by a set of complex, inter-related vortex systems as shown in Figure 1.2. An accurate description of

the relevant fundamental dynamics is a prerequisite to understanding flow response to external perturbations.

Bagheri et al. (2009) carried out a global stability analysis of a JICF with $r = 3$ based on a steady solution to the incompressible Navier-Stokes equations. They observed two groups of global modes: the wake modes having low frequencies associated with the vortical structures in the wake region, and the shear-layer modes with high frequencies and larger amplitudes ("growth rates") located on the CVP. Megerian et al. (2007) provided a detailed experimental exploration of the shear-layer instabilities for $1 \le r \le 10$ and $r \to \infty$ with jet Reynolds numbers of 2000 and 3000. They reported the JICF went through a transition from the convectively unstable flow at higher values of r to a globally or absolutely unstable flow at lower values of r and suggested different forcing strategies to control the JICF systems: where $r > 3.5$ in flush jet cases, relatively low-level excitation (Narayanan et al., 2003) can be employed to promote mixing by excitation of the convective instability; where $r < 4.0$, when the jet may already be self-excited, the imposition of stronger forcing, especially with a distinct, externally imposed time scale (M'Closkey et al., 2002), may be required to impact jet penetration and spread.

In addition to the frequency detections in Chapter 4, the Proper Orthogonal Decomposition (POD) is adopted in this work to extract the dominant structures of the pressure and mixing fields and to capture their dynamic characteristics.

5.2.2 Proper Orthogonal Decomposition Analysis of JICF

The POD analysis is an effective and elegant technique used to extract hidden information buried in massive experimental and numerical data, especially effective for working with complex turbulent flows which usually feature and are dominated by energetic coherent structures. The main intent of the POD is to find a set of ordered orthogonal basis functions, $\varphi_j(\mathbf{x}), j = 1, 2, \cdots$, for a given flow property, $f(\mathbf{x},t)$, so that the samples of $f(\mathbf{x},t)$ can be expressed optimally using the first n basis functions; that is, the projection of $f(\mathbf{x},t)$ onto the first n basis (Holmes et al., 1998), as such,

$$\hat{f}(\mathbf{x},t) = \overline{f}(\mathbf{x}) + \sum_{j=1}^{n} a_j(t)\varphi_j(\mathbf{x}) \qquad (5.1)$$

has the smallest error, defined as $E\left(\left\|f - \hat{f}\right\|^2\right)$. Here, $a_j(t)$ is the temporal variation of the jth mode. $E(\cdot)$ and $\|\cdot\|$ represent the time average and a norm in the L^2 space, respectively (Rowley et al. 2000). A detailed description of the realization may be found in Wang (2002).

The applicability of POD in the context of JICF has been demonstrated in several works. Guan (2005) applied POD analysis to parametric numerical studies and obtained the energy possessions and evolution processes of selected bases. Meyer et al. (2007) analyzed experimental data using POD and reported that in the $r = 3.3$ case, wake vortices are the dominant dynamic flow structures and they interact strongly with the jet core, while in the $r = 1.3$ case, jet shear-layer vortices are more dominant. A POD analysis of experimental snapshots has also captured the most dynamic structures of near-

field unforced liquid jets into gas crossflow at different momentum ratios (Arienti et al., 2009). In this current work, a two-dimensional POD analysis is conducted at two perpendicular slices located in the near field and far field where 1) $y = 0$ plane and 2) $x/d = 10$ plane, respectively. Only the $r = 4$ case is presented here. The procedures are validated by the flow reconstruction (not shown here) and the frequencies of the instabilities are usually quantified in terms of a jet Strouhal number, $St = fd/U_j$, where f is the corresponding frequency.

Figure 5.1 presents the POD results describing the fluctuating pressure field in the $y = 0$ plane: the energy possessions of the most energetic modes, the Fast Fourier Transformation (FFT) of the first five modes, and the mode shapes of the first three modes. Since POD analysis is sensitive to the focus area, the computing region is confined to $-2 \le x/d \le 6$ and $-2 \le z/d \le 8$. (Note that $z/d < 0$ region is not plotted here.) This area covers the early jet development region, where the jet/cross interactions are most intense. As expected, the fluctuating pressure field is dominated by the shear-layer vortices with total energy possessions up to 80% for the first two modes. Their corresponding frequencies, $f \approx 92KHz$ and $St = 0.73$), are quite high due to the small jet orifice diameter and high penetration velocity. The first two modes have almost the same structure and are distinct from each other only in a 180-degree phase difference. Two modes with a "phase-shift" are needed to show that vortices are moving in the direction of the jet trajectory (Meyer et al., 2007). The third mode with 10% energy possession shows high-pressure regions piled up close to the crossflow tunnel wall and can be interpreted as the compressing effect of jet penetration on the crossflow. The frequency

of the third mode ($f \approx 14kHz$ and $St \approx 0.12$) was detected in Chapter 4 and found to be weak in the far field.

The frequency of the shear-layer modes ($f \approx 92kHz$, $St = 0.73$) is consistent with the broad peak in the domain of 80-100 kHz, as shown in Figure 4.24. The jet shear-layer instability is prone to be affected by the operating conditions, and a wide range of Strouhal numbers has been documented in literature, as shown in Table 5.1. The studies by Rudman (1996), Camussi et al. (2002), Narayanan et al. (2003) and Megerian et al. (2007) provided spectra data; others have presented estimated values or images from which roll-up frequencies may be roughly estimated. Megerian and Karagozian (2005) found that for a fixed jet Reynolds number, different r values correspond to different skewings of the jet's velocity profile near the jet exit, which alter the jet's momentum thickness and result in a change in the frequency as well as the amplitude of the most unstable modes (Alves et al., 2007). Megerian et al. (2007) provided spectra data for cases with $1 \le r \le 10$ and $r \to \infty$. They observed the early "shear-layer mode" immediately at the jet exit with $St \approx 0.7$ and the "preferred mode" downstream with $St \approx 0.5$ for the free jet. As the crossflow velocity was increased from zero (r is decreased from infinity), multiple modes or peaks appeared in the range of $0.5 \le St \le 0.7$ and moved successively closer to the jet exit. When r was reduced to less than 3.5 to 4, the flush jet exhibited a strong distinct fundamental mode very close to the jet exit. This dramatic change in its spectral character suggested the presence of a globally unstable mode, assessed by Bagheri et al. (2009) at a value of $r = 3.0$.

Figure 5.2 shows the POD results describing the fluctuating scalar field in the $y = 0$ plane. Comparing to the results of the pressure field, a fine qualitative uniformity is present in the mode distributions: the first two modes show the shear-layer vortices structures have an unambiguous high frequency of $92KHz$ and take the greatest share (more than 35%) of the energy. The third mode shows regions of alternating positive and negative scalar fluctuations along the jet trajectory and also has a high-value zone on the leeward side of the jet plume. It combines the responses from the mixing field to the delayed roll-ups of the shear-layer on the jet's leeward side and the vorticity breakdown at the end of the near-field. Quantitatively, the energy distribution is more even for the scalar field than that in the pressure field, indicating that scalar mixing can occur more equitably.

Figure 5.3 shows POD results for the pressure oscillation on a transverse plane at $x/d = 10$ (in the far field). The focus region extends to $-5 \le y/d \le 5$ and $0 \le z/d \le 11$. An overwhelmingly dominant mode with an energy share of more than 80% is detected and the corresponding frequency is 12.5 kHz, very close to that of the third mode (13.5 kHz) in Figure 5.1 which has been interpreted as the compressing effect of jet penetration on the crossflow. Here in Figure 5.3, the mode shape yields undisturbed pressure iso-lines and manifests itself as vertical movements; that is, the jet plume flaps up and down in the far field. Mode 2 and Mode 3 represent the spanwise movements and share only a small portion of energy. Figure 5.4 shows the POD results describing the fluctuating scalar field in the $x/d = 10$ plane. No distinct peak appears in the first mode (which shows high scalar variations in the jet plume region and marks the locations of the CVP)

and broad peaks are observed for the other lower energy-possessed modes. Although the first mode takes a larger portion of the energy, it does not play a predominant role in the system.

5.3 A Jet into Oscillating Crossflow

The CVP is the dominant structure in the JICF system, especially in the far field; its development, sustenance, and eventual breakdown are closely related the mixing processes (Karagozian, 1986; Margason, 1993). As also indicated by Megerian et al. (2007), the vorticity generation and breakdown in the near field may be critical to mixing for low velocity ratio cases (Megerian et al. suggested $r \le 4$). In our attempt to study mixing enhancement at $r = 4$, we impose moderate to strong oscillations on the crossflow to modulate the vorticity production and dispersion.

5.3.1 Case Description

A simplified schematic of the boundary setups is given in Figure 5.5. All the calculations are conducted on grid B with total grid size 8.9 million. The grid resolutions were tested in Chapter 4 and found not to be an issue. Before implementing external excitation, a stationary case was calculated until the steady state was attained; the results were then used as the initial conditions for the acoustic cases.

Throughout the work, we impose the excitation by periodically varying the crossflow velocity at the crossflow inlet such that

$$U_0(t) = U_0\left(1.0 + \alpha \sin\left(2\pi f_F t\right)\right) \tag{5.2}$$

where $U_0 = 40ms^{-1}$ is the mean crossflow velocity and f and α denote the forcing frequency and the relative amplitude, respectively. A total of five oscillation conditions, summarized in Table 5.2, are investigated. The frequency dependency is revealed by the comparison between Cases I, II, and III. The amplitude effect is elaborated in Case II, II-1, and II-2.

At the jet inlet, a rigid boundary condition, i.e. perfect reflection with $\beta = 1.0$, is applied to maintain a pressure peak (velocity node) and to force the acoustics to bounce back to the computational domain, which implies: $P^+ = P^-$, where P^+ and P^- are the complex amplitudes of the incoming and reflected waves. According to the linear acoustics theory, the acoustic pressure $p_j^a(x,t)$ and velocity $u_j^a(x,t)$ are:

$$p^a(x,t) = P^-\left(e^{ikx} + e^{-ikx}\right)e^{-i(\omega t + Mkx)} \tag{5.3}$$

$$u^a(x,t) = \frac{P^-}{\bar{\rho}\bar{a}}\left(e^{ikx} - e^{-ikx}\right)e^{-i(\omega t + Mkx)} \tag{5.4}$$

where $\omega = 2\pi f$ is the wave frequency, and k is the modified wave number defined as: $k = \dfrac{\omega/\bar{a}}{1-\bar{M}^2}$. $\bar{a}$ and $\bar{M} = \bar{U}/\bar{a}$ are the sound speed and Mach number for the mean field. The collaborative pressure $P_j(x,t)$ and velocity $U_j(x,t)$ are:

$$P_j(x,t) = \bar{P}_j(x) + p_j^a(x,t) \tag{5.5}$$

$$U_j(x,t) = \bar{U}_j(x) + u_j^a(x,t) \tag{5.6}$$

where $\bar{P}_j(x)$ and $\bar{U}_j(x)$ are the pressure and velocity at stationary crossflow conditions.

Notice that $p' \sim \bar{\rho}\bar{a}u'$, thus:

$$\frac{p'}{\bar{p}} \sim \frac{\bar{\rho}\bar{a}u'}{\bar{\rho}RT} = \frac{\bar{a}u'}{\bar{a}^2/\gamma} = \gamma\frac{u'}{\bar{a}} \qquad (5.7)$$

Even when a 50% velocity oscillation is applied, the acoustic pressure induced is still at a minor level compared to the mean pressure. The last column in Table 1 provides the relative acoustic pressure magnitudes.

No-slip wall conditions are applied to the crossflow tunnel and the inner surface of the jet pipe. For the crossflow spanwise as well as the upper and outlet boundaries, a zero-gradient condition is maintained as it was in the steady case (non-reflective characteristics were assessed and confirmed in Chapter 3). Though the unexpected artificial acoustic wave reflection is negligible, a buffer region is introduced to the crossflow tunnel at its downstream outlet to completely rule out wave reflection.

5.3.2 Response of the Instantaneous Flow/Scalar Field

As a rough estimate, given the speed of sound as $a = 340$ m/s, the wave lengths ($\lambda = a/f$) corresponding to the external excitations ($f = 2$ kHz, 5 kHz, and 10 kHz) are 17.0 *cm*, 6.8 *cm*, and 3.4 *cm*, respectively. The diameter of the jet (1.27 *mm*), however, is much smaller and the dimensions of the computational domain are much shorter than the acoustic wave length; thus the computational zone is acoustically compact, and acoustic-induced variations are expected to be spatially indiscernible. Therefore, the visualization of the acoustic effect is only presented based on the temporal evolutions of the flow field.

Three series of snapshots indicating iso-vorticity surfaces colored by scalar concentration are shown in Figure 5.6: a stationary case, a case involving 10% crossflow velocity oscillation at 5 kHz (Case II), and a case involving 50% crossflow velocity oscillation at 5 kHz (Case II-2). The total time span depicted is 0.2 *ms*, corresponding to one period of oscillation. Each series of five snapshots is based on an extraction according to this time sequence: t_0 (equal to 0.08 *ms* here), t_0+0.05 *m*s, t_0+0.10 *ms*, t_0+0.15 *ms*, t_0+0.20 *ms*. The initial measure of t_0 was recorded as the excitations were turned on. Wrinkled surfaces (spanwise vortices) in the early jet shear layer regions and fine structures in the far fields can be observed in all three cases. In the stationary case, the vorticity plume evolves continuously in the downstream direction and shows no apparent time-dependency, while in the 10% oscillation case, the plume deforms and twists, inducing a time-evolving upper edge and non-uniform vorticity region in the far field. The oscillatory phenomenon manifests itself more clearly in the 50% oscillation case, in which the vorticity plume reveals temporal spatial discontinuity. The whole plume flaps in the oscillating crossflow at the excitation frequency. The vorticity periodically generated in the shortened shear-layer vortices region expands spatially, breaks down from the core region, and ultimately disperses into the crossflow in the far field.

To further visualize the flapping of the jet plume in oscillating cases, Figure 5.7 shows the temporal evolution of scalar concentration on the symmetry plane, corresponding to the time sequence in Figure 5.6. The shear-layer vortices are presented in all the figures, but their structures diminish as the forcing magnitude increases. The length of the jet potential core varies sharply in one forcing cycle for the 50% oscillation

case, where the jet plume resonates with the crossflow and swings in the streamwise direction, causing the bulk of the jet fluid to break from the potential core and disperse into the crossflow tunnel. The size of the detached jet pocket is much larger than that in the stationary case and tends to increase the spatial inhomogeneity.

To calibrate the acoustic-induced variations, the time histories of pressure are recorded at different locations – close to the rigid jet-inlet boundary (z/d = -39.0), near the jet-exit orifice (z/d = 2.0), and in the far field (x/d = 10.0). Fast Fourier Transformation (FFT) was used to extract the oscillation frequencies and magnitudes as shown in Figure 5.8. The left three plots show the results of the 10% velocity oscillation cases at three frequencies. The right plots present the cases with different oscillation amplitudes (10%, 20% and 50%) at the same excitation frequency (5 kHz). For all cases, the forcing frequencies may be observed at all three locations with varying amplitudes. Since the perfect reflection is imposed at the jet inlet (z/d = -40.0), a pressure peak is expected there and is confirmed by the relatively higher peaks at location z/d = -39 for f = 2 kHz and 5 kHz. In the case of f =10 kHz, however, the excitation seems to resonate with the intrinsic instability near the jet orifice and results in a strong pressure oscillation at z/d = -2.0.

5.3.3 Proper Orthogonal Decomposition Analysis

Though the acoustic-induced instabilities can be visualized in the direct observations of the flow structure, the underlying reasons are yet to be retrieved. The POD analysis is thus applied to the unsteady crossflow cases.

Figure 5.9 illustrates the POD results based on the fluctuating pressure field for Case II in the $y = 0$ plane. Compared to the stationary case in Figure 5.1, the modes of the shear-layer vortices (Mode 2 and Mode 3) are suppressed, with a total energy share lowered to 30%. Meanwhile, the distinctive peak in the frequency domain is smoothed and transformed to a broad plateau with a relatively lower magnitude. A new mode (Mode 1) appears and consumes more than 50% of the energy, demonstrating its significance in composing the fluctuating pressure field. Positive and negative pressure zones alternate in the jet plume, the wake region, and the end of the jet core. Mode 1 represents the combined effect of the flapping of the jet in the streamwise direction and the bulk breakdown along the jet trajectory. Since the jet flow resonates with the crossflow, the frequency of this mode complies with external excitation indicated by an unambiguous peak at 5 kHz. The external excitation amplifies its influence more clearly in Case II-2 shown in Figure 5.10. The first "flapping/detaching" mode takes almost 90% of the energy. The second mode with around 10% energy also represents a flapping movement inconsistent with the oscillatory environment. The shear-layer vortices modes phase out in this case and all the dominant modes obtain the external excitation frequency or its subharmonic (10 kHz in Mode 3). It is worth noting that even at a pressure oscillation that is only 6% of ambient pressure (corresponding to 50% velocity oscillation in Case II-3), a high possibility exists that the flow structures will be substantially changed by the external excitation.

Figure 5.11 shows the POD results of the fluctuating scalar field in the $y = 0$ plane. As observed in the fluctuating pressure field, the flapping/detaching mode at the forcing frequency becomes the dominant structure with 17% of the energy share. The

shear-layer modes degenerate to minor roles and their distinct frequencies are replaced by broad peaks. The dominance of the flapping/detaching modes (or their subharmonics) is more clearly visualized in Figure 5.12 for Case II-2. As the forcing amplitude increases, the negative/positive scalar zones enlarge in size and strengthen in magnitude. Since the shear-layer vortices play an important role in entraining the crossflow, the prevalence of the flapping modes in the jet-core region may hinder the engulfing (bulk mixing) of the crossflow in the near field.

The POD results on a transverse plane at the downstream location $x/d = 10$ are shown in Figure 5.13 and Figure 5.14. Only Case II-2 is considered here for purposes of clarity and briefness. The computing region covers $-5 \le y/d \le 5$ and $0 \le z/d \le 11$. Although the modes representing the vertical (Mode 2) and spanwise (Mode 3) movements appear as the second and third most dominant structures, the first mode with a frequency of 5 kHz consumes almost all the energy and its mode shape does not comply with any modes observed in the stationary case. Two relatively high pressure zones are found above the jet plume region, while in the scalar analysis (Figure 5.14), two high scalar zones appear in the jet plume region and resemble the counter-rotating vortex pair.

The phenomena observed in the POD analyses are consistent with what was found in the instantaneous vorticity and scalar fields (Figure 5.6 and Figure 5.7). The oscillating crossflow not only induces the bulk shedding of vorticity, but also makes the jet plume swing and flap at the exactly the forcing frequency. Similar observations were also derived (although not shown here) for other forcing cases with frequencies of 2 kHz or 10 kHz.

5.3.4 Responses of Mean Flow/Scalar Field

5.3.4.1 Jet Trajectory

Figure 5.15 illustrates the jet trajectories based on the center streamline and on the boundaries of the plume at a jet fluid concentration of no less than 0.05. All five unsteady cases and the baseline stationary case are compiled for direct comparison. The three low-amplitude forcing cases show almost identical jet trajectories and plume sizes as those in the stationary case. This observation is consistent with the Megerian et al. (2007) experimental studies showing that for the $r \leq 4$ cases, the transverse jet may already be self-excited and the imposition of weak-to-moderate sinusoidal excitation has little effect on jet penetration or spread (Shapiro et al., 2006); additionally, the imposition of stronger forcing, especially with a distinct, externally imposed time scale such as that created by square-wave excitation with a prescribed temporal pulse-width, may be required to impact jet penetration and excitation (M'Closkey et al., 2002). The jet trajectory in the strong oscillation case (Case II-2) deviates significantly from the stationary case immediately after the jet-core region by showing a center streamline about $1.0d$ lower, a condition also observed by Kremer et al. (2007). The jet plume increases by presenting a lower bottom edge and a higher upper edge in the symmetry plane. More clear visualizations of the jet penetration are shown in Figure 5.16.

5.3.4.2 Mean Scalar Field

The mean scalar fields are shown in the center plane and several transverse planes ($x/d = 2$, 5 and 10) in Figure 5.16. The low excitation case (Case II) shows no discernable difference from the stationary case, while the jet-core decreases significantly in the strong excitation case (Case II-2) with a much broader plume in the center plane. The jet plume is substantially elongated in the transverse direction as depicted in the transverse planes. The intrinsically asymmetric behavior of CVP accounts for the spanwise asymmetry in the scalar distribution for the stationary case and Case II; nonetheless, the kidney-shape structures are developed and strengthened in the downstream. In Case II-2, the flapping mode extracted in the POD analysis enhances the jet dispersion in the transverse direction while the spanwise development is suppressed, leading to a long and narrow mixing zone in a transverse plane with a lower "center of gravity" of the scalar field (Denev et al., 2009).

5.3.4.3 RMS Properties and Turbulent Fluxes

Figure 5.17 shows the *z*-profiles of RMS velocities and scalar concentration, together with the turbulent scalar fluxes in the symmetry plane at the stations $x/d = 1.0$, 2.0, 5.0, and 10.0. The variations are apparent in Case II-2 but not in the other forcing cases. Strong excitations primarily alter the fluctuating properties by creating an unsteady zone on the upper surface of the jet plume and in the near-field wake region. The most distinct feature is observed in the C' profiles at $x/d = 1.0$ where the two-ripple

structure corresponding to the upper and lower mixing layers is replaced by a flattened structure, indicating that the jet-core has ends and the mixing field does not exactly follow the flow field under strong excitation conditions.

5.3.4.4 Mixing Indices

The mixing indices (i.e. spatial mixing deficiency (SMD) and temporal mixing deficiency (TMD), described in Chapter 4), are calculated at various downstream locations for all six cases. As shown in Figure 5.18, the excitation frequency variation does not affect the SMD, and all three forcing cases (I, II and III) at 10% velocity oscillations remain comparable to the stationary case. As for the TMD, although all the results increase with excitation, Cases I, II and III almost converge with each other and no frequency dependency is observed. On the other hand, both the SMD and the TMD undergo discernable variations as the excitation magnitude increases from 10% to 50% velocity oscillation. The size of the jet plume expands, inducing a lower SMD in the strong excitation case, while the flapping and detaching phenomena are enhanced, yielding a much higher TMD. Notice that the values of the mixing indices are sensitive to the focus area and that the calculations in the current work are carried out only in the regions where the jet fluid concentration is not zero-valued ($-4.0 < y/d < 4.0$ and $0 < z/d < 10.0$).

5.4 Conclusion

The stability of a jet into crossflow at $r = 4$ has been examined in this chapter. The shear-layer instability, transverse and spanwise motions have been reviewed and extracted in both the fluctuating pressure and scalar fields by applying Proper Orthogonal Decomposition (POD) analysis. The mode frequencies are consistent with previous work in the existing literature and with the probe detections in Chapter 4.

The second part of this chapter investigated the acoustic response of a jet into crossflow system to external excitations. The stationary $r = 4$ case was used for the baseline flow condition. The crossflow velocity was imposed with sinusoidal oscillations at different frequencies and amplitudes. The results confirm that:

1. low-level excitations have little impact on the jet penetration and evolution at the critical velocity ratio $r = 4$ (which may mark the transition from convective instability to the absolute instability in the JICF system);

2. at moderate and high excitations, the behavior of the jet plume is affected by the oscillations in the crossflow. The strong vorticity generation and breakdown leads to a much shorter jet-core and a significant loss in plume contiguity. POD analysis reveals that flapping and detaching motions at the forcing frequencies (and their subharmonics) play predominant roles in the jet evolution, yielding to a lower jet trajectory and a broader plume in the transverse direction;

3. the imposition of velocity oscillation in the crossflow stream influences the development of the counter-rotating vortex pair (CVP). The strengthened transverse

movement and the suppressed spanwise movement result in a longer and narrower jet plume in any transverse plane and a lower "center of gravity" within the scalar field; and

4. the spatial mixing deficiency (SMD) and the temporal mixing deficiency (TMD) show fine uniformity among the cases with different forcing frequencies and low-level amplitudes. At a fixed forcing frequency, as the excitation magnitude increases, the SMD decreases and the TMD increases, resulting from the enlarged plume size and weakened plume contiguity.

Table 5.1 Approximate values of Strouhal numbers associated with the jet near-field shear layer

	Re	r	St
Fric and Roshko (1994)	7700	2	1.70 (approximate)
Camussi et al. (2002)	220	2.2	0.30
Kelso et al. (1996)	13600	2.2	0.30
Megerian et al. (2007)	2000	4.1	0.80
Megerian et al. (2007)	3000	4.1	0.95
Rudman (1996)	2000	5	0.7-0.75
Narayanan et al. (2003)	5000	6	0.10 (broad peak)

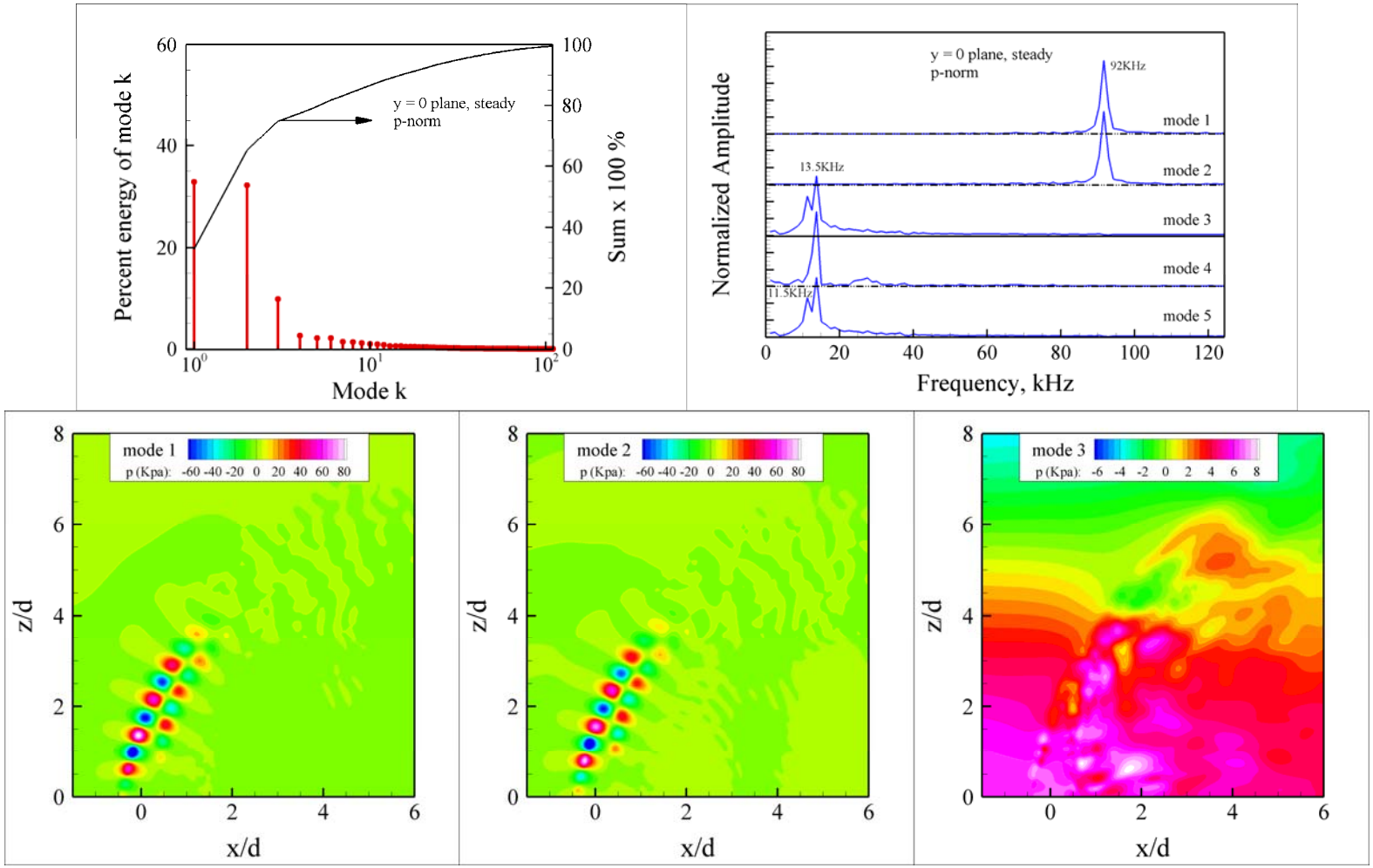

Figure 5.1 2D-POD in $y = 0$ plane (p-norm)

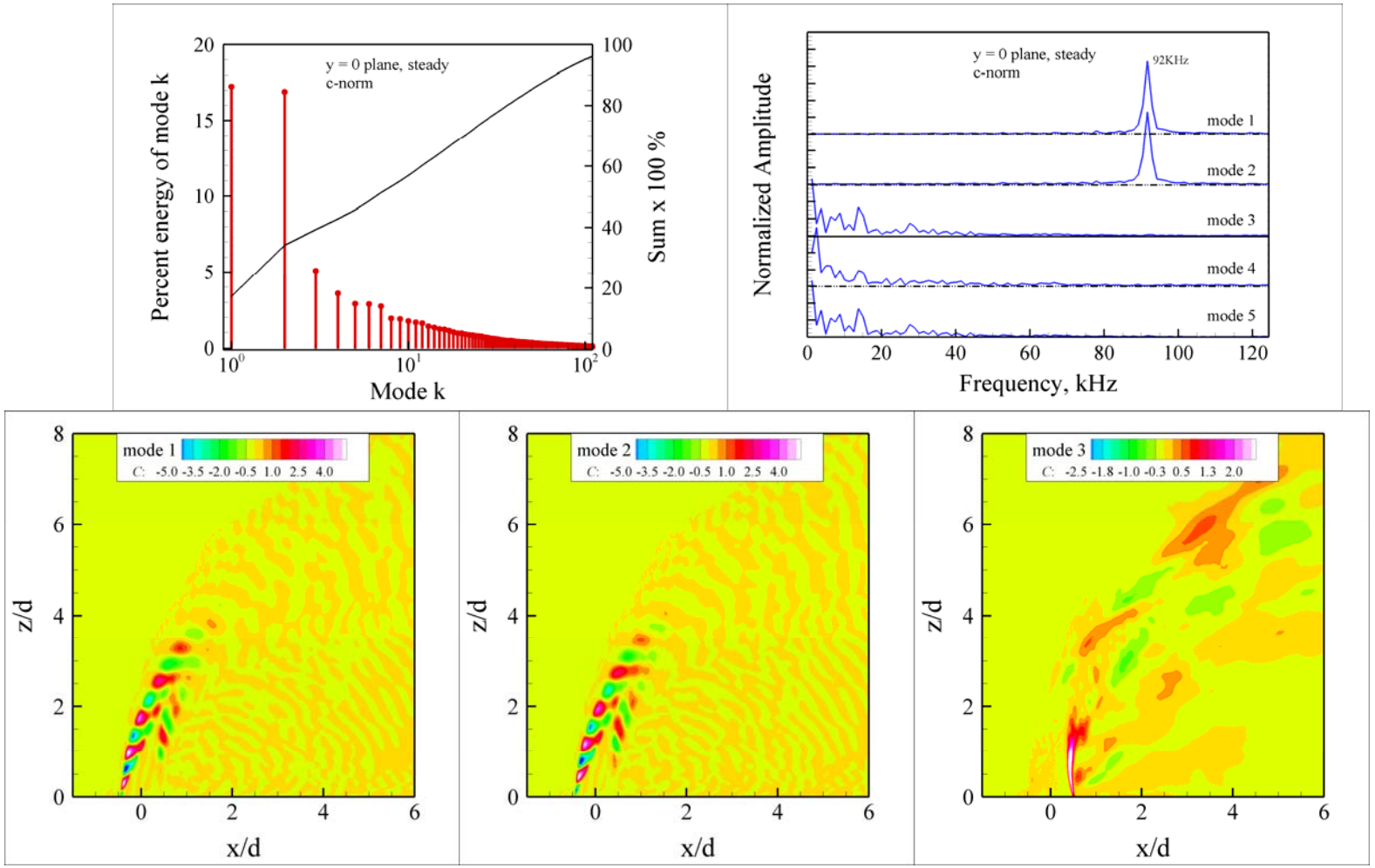

Figure 5.2 2D-POD in $y = 0$ plane (c-norm)

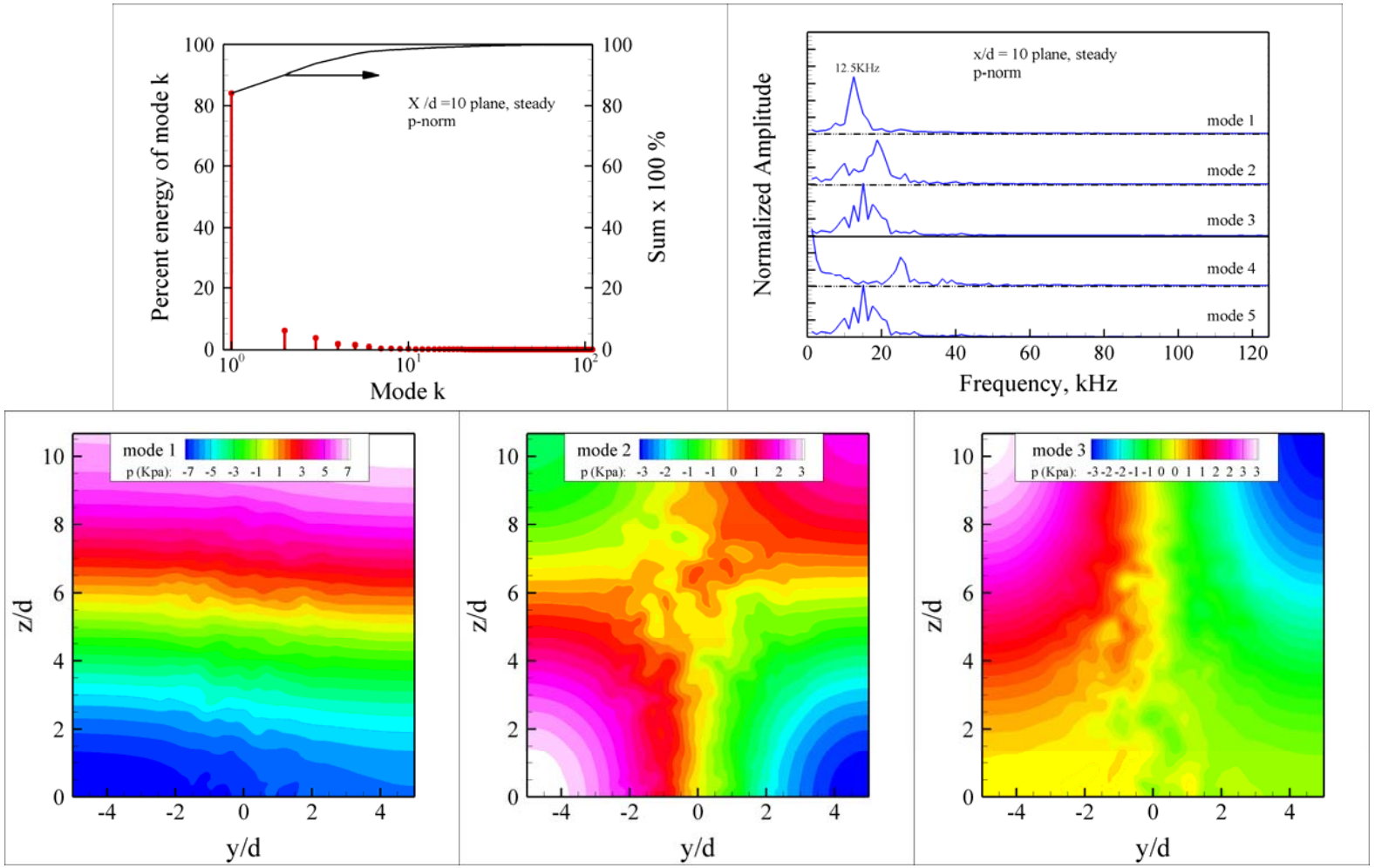

Figure 5.3 2D-POD in $x/d = 10$ plane (p-norm)

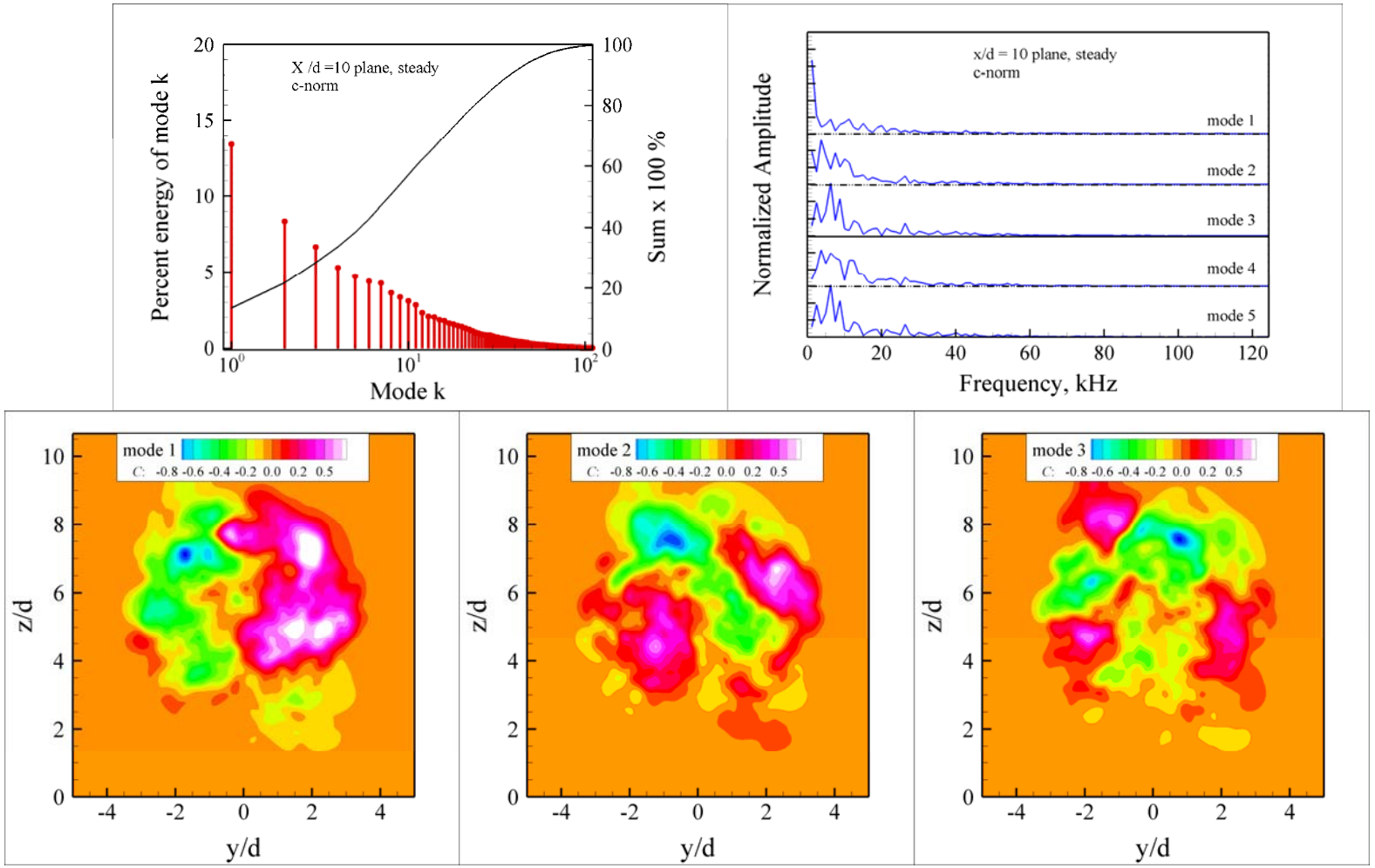

Figure 5.4 2D-POD in $x/d = 10$ plane (c-norm)

Table 5.2 Case conditions for oscillating crossflow

	Forcing frequency (f)	Strouhal number ($S_t = fd/U_j$)	Forcing amplitude ($\alpha = u'/U_0$)	Forcing amplitude (p'/P_0)
Case I	2 kHz	0.06350	10%	1.61%
Case II	5 kHz	0.15875	10%	1.61%
Case III	10 kHz	0.31750	10%	1.61%
Case II-1	5 kHz	0.15875	20%	3.22%
Case II-2	5 kHz	0.15875	50%	8.10%

$p' \sim \bar{\rho}\bar{a}u'$: provided $\bar{\rho} = 1.2\,kg/m^3$ and $\bar{a} = 340\,m/s$

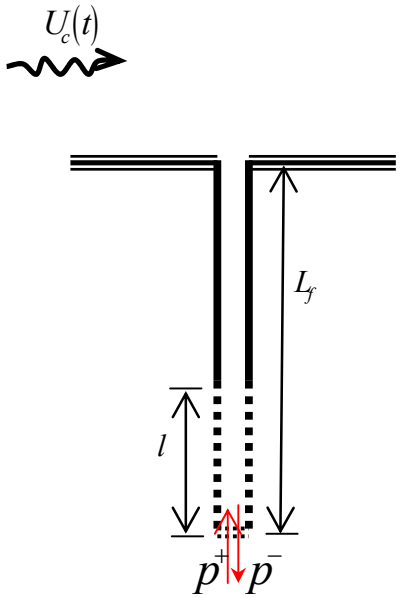

Figure 5.5 Schematic of boundary setups for a jet into oscillating crossflow

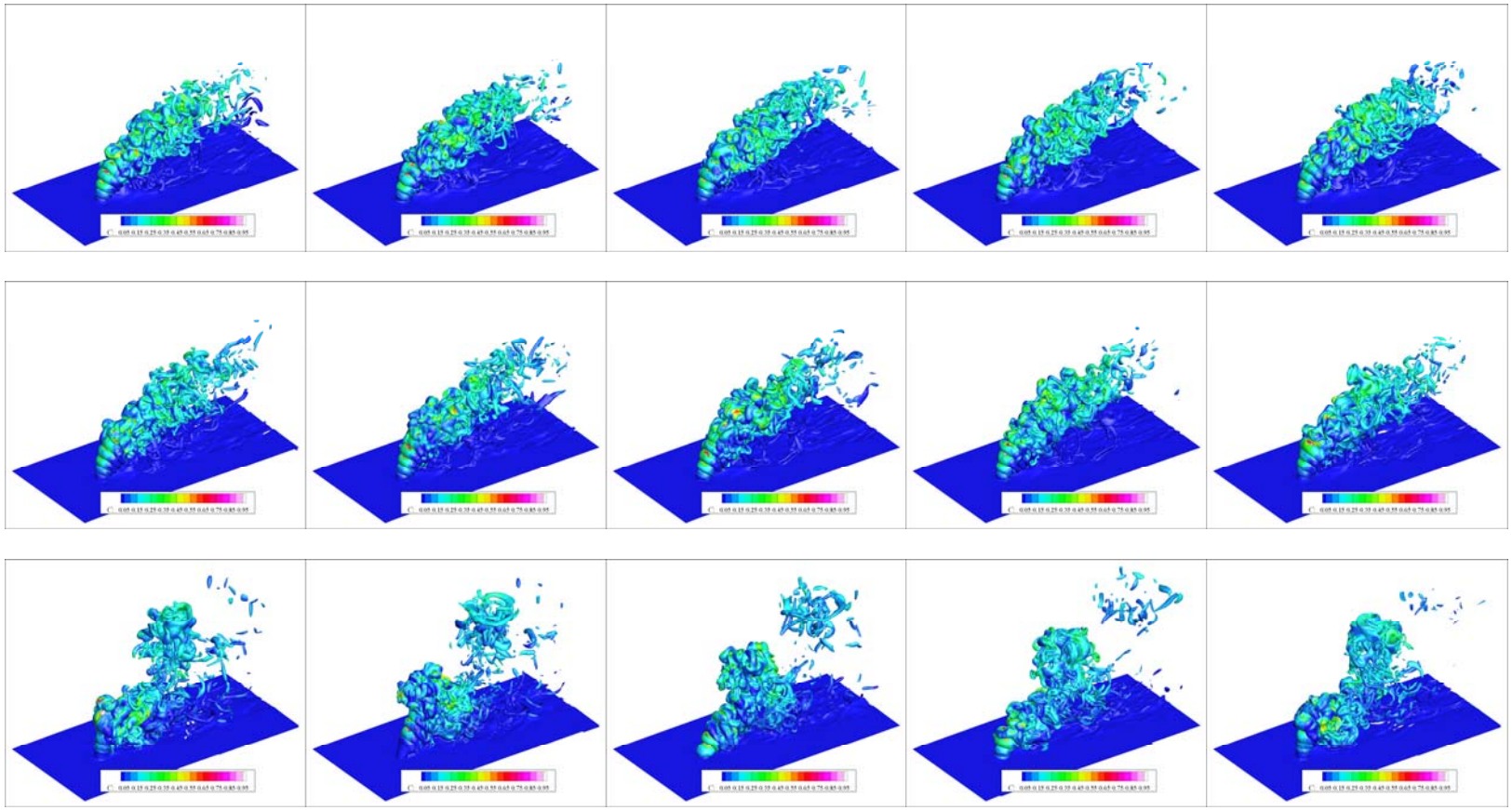

Figure 5.6 Snapshots of iso-vorticity (|Ω|=100, 000/s) surface colored by jet fluid concentration

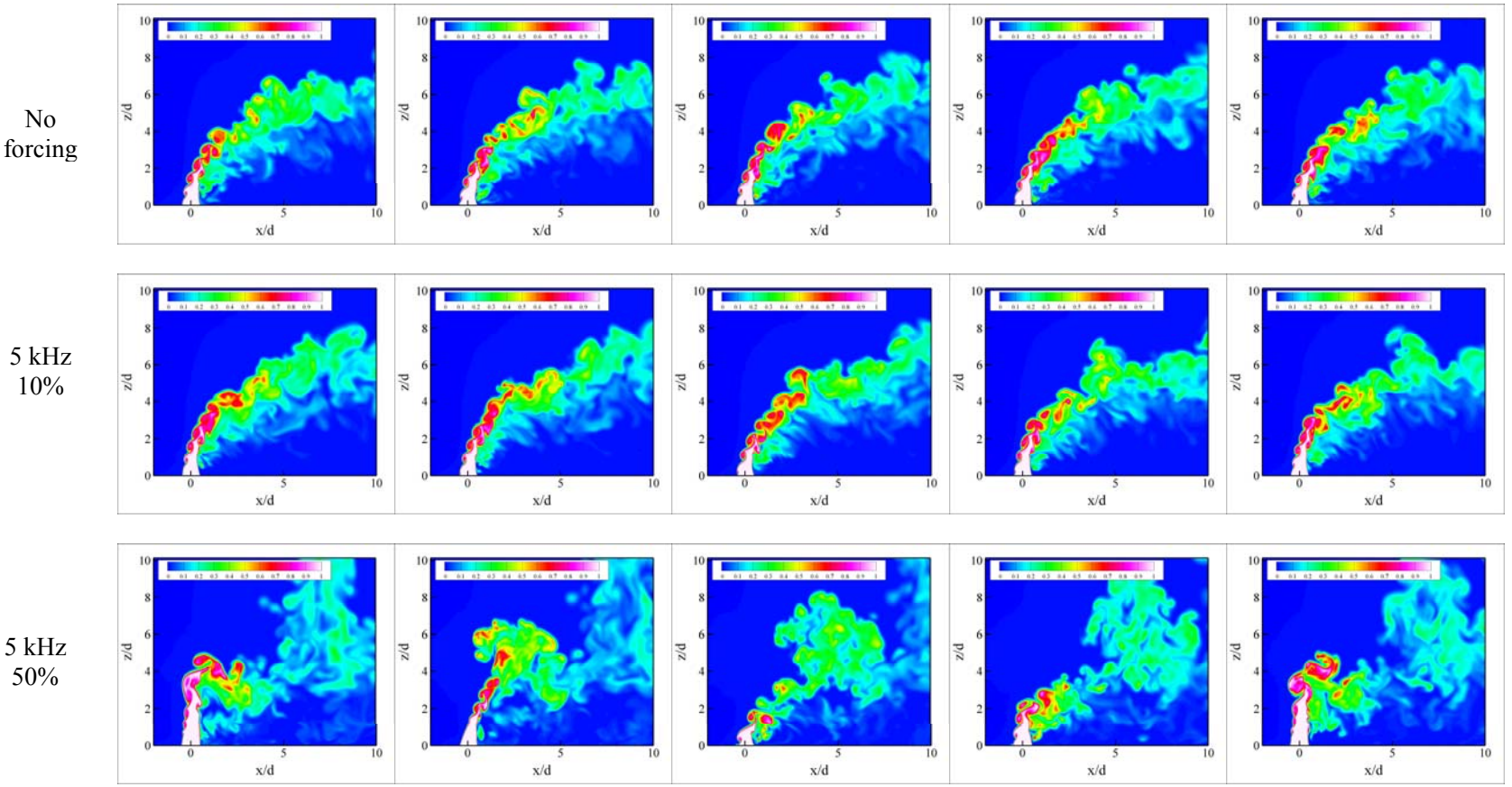

Figure 5.7 Snapshots of jet fluid concentration

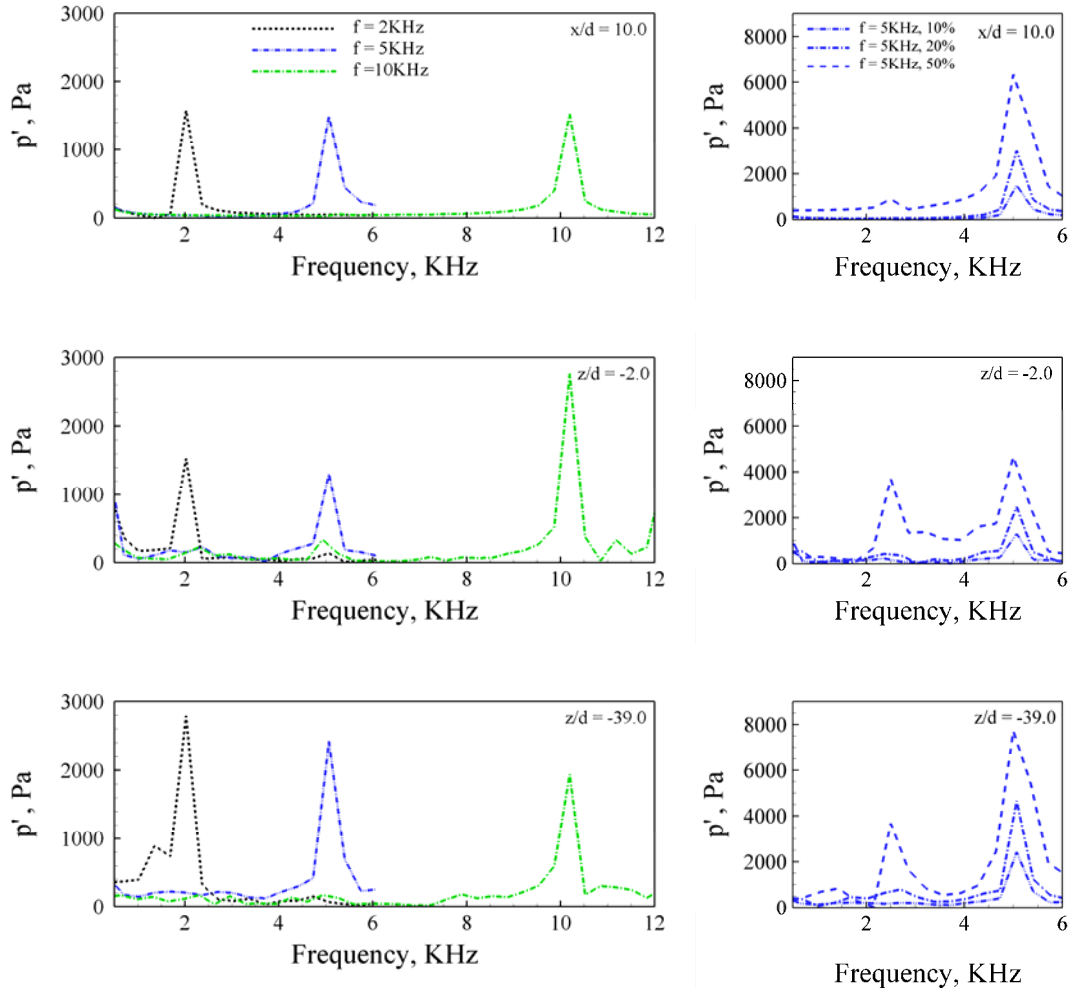

Figure 5.8 PSD of pressure oscillations

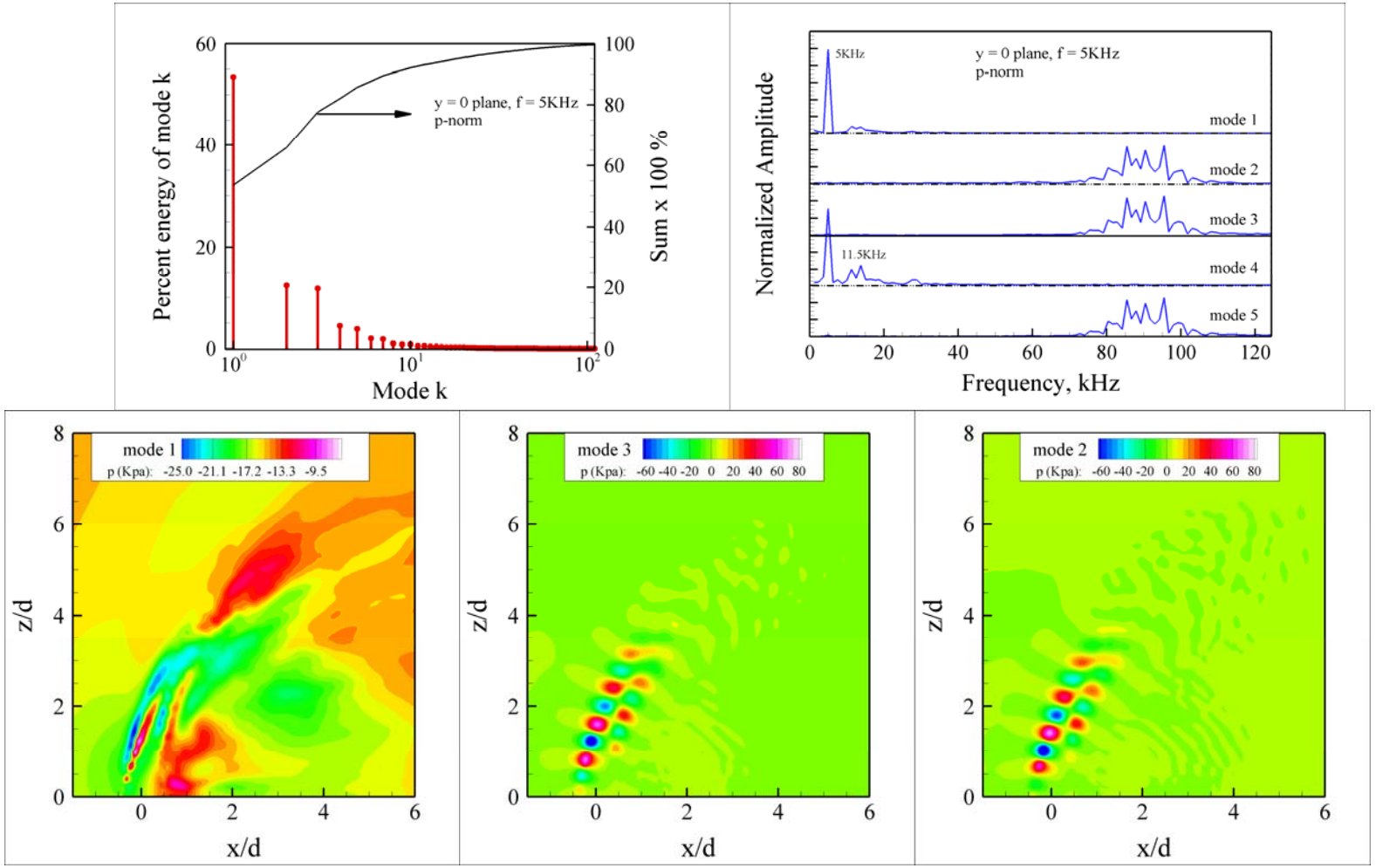

Figure 5.9 2D-POD in $y = 0$ plane (p-norm, case II)

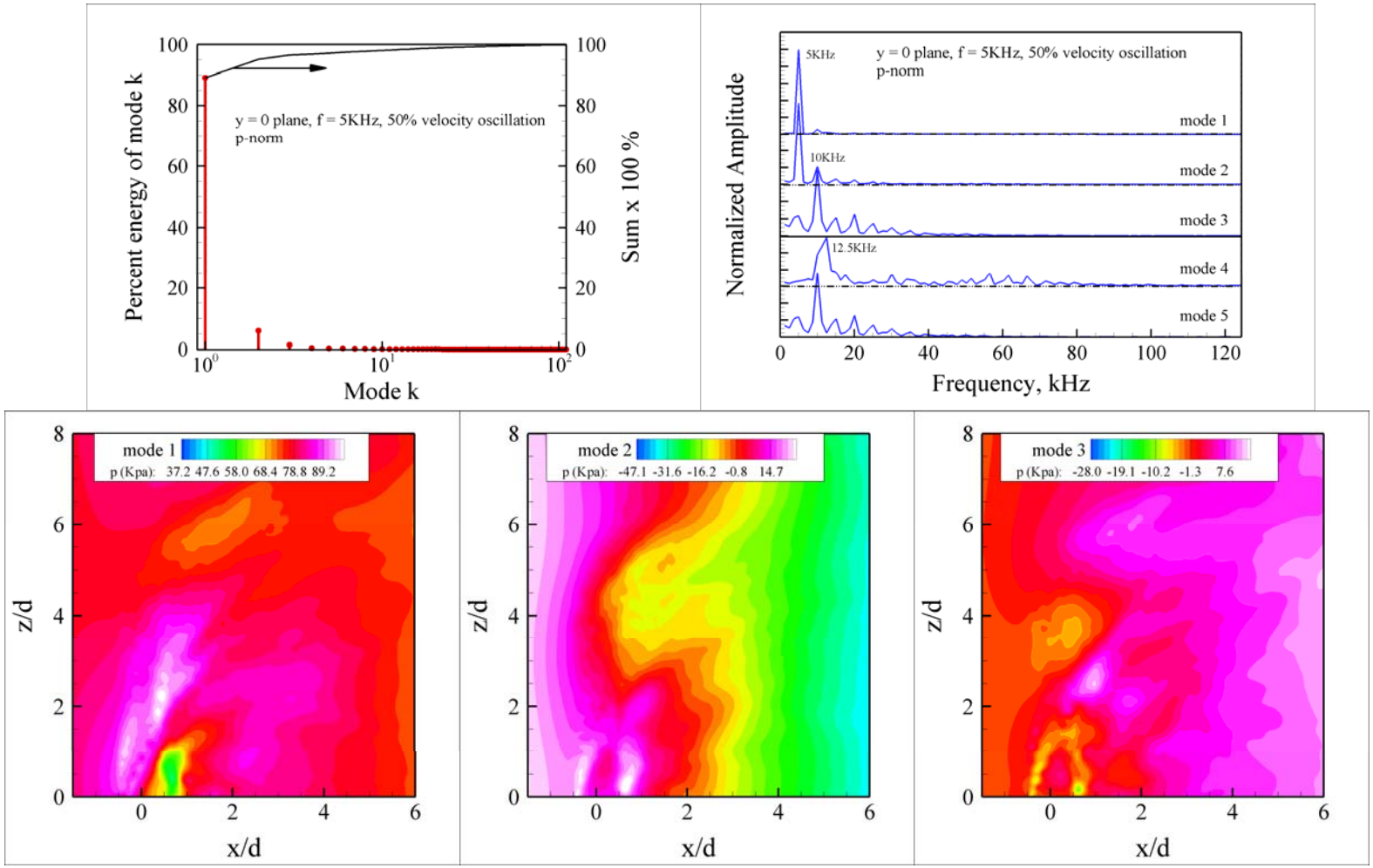

Figure 5.10 2D-POD in $y = 0$ plane (p-norm, case II-2)

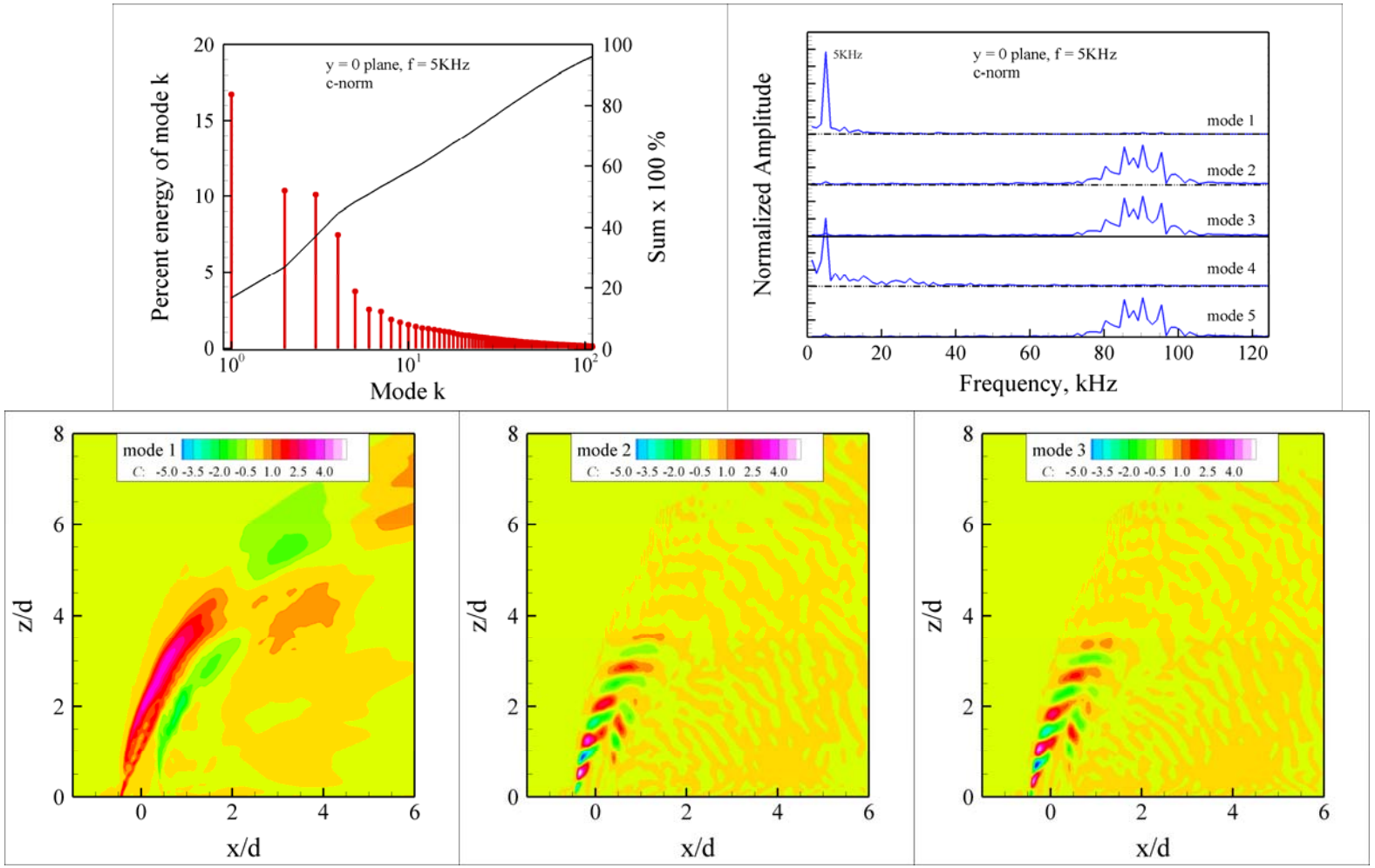

Figure 5.11 2D-POD in $y = 0$ plane (c-norm, case II)

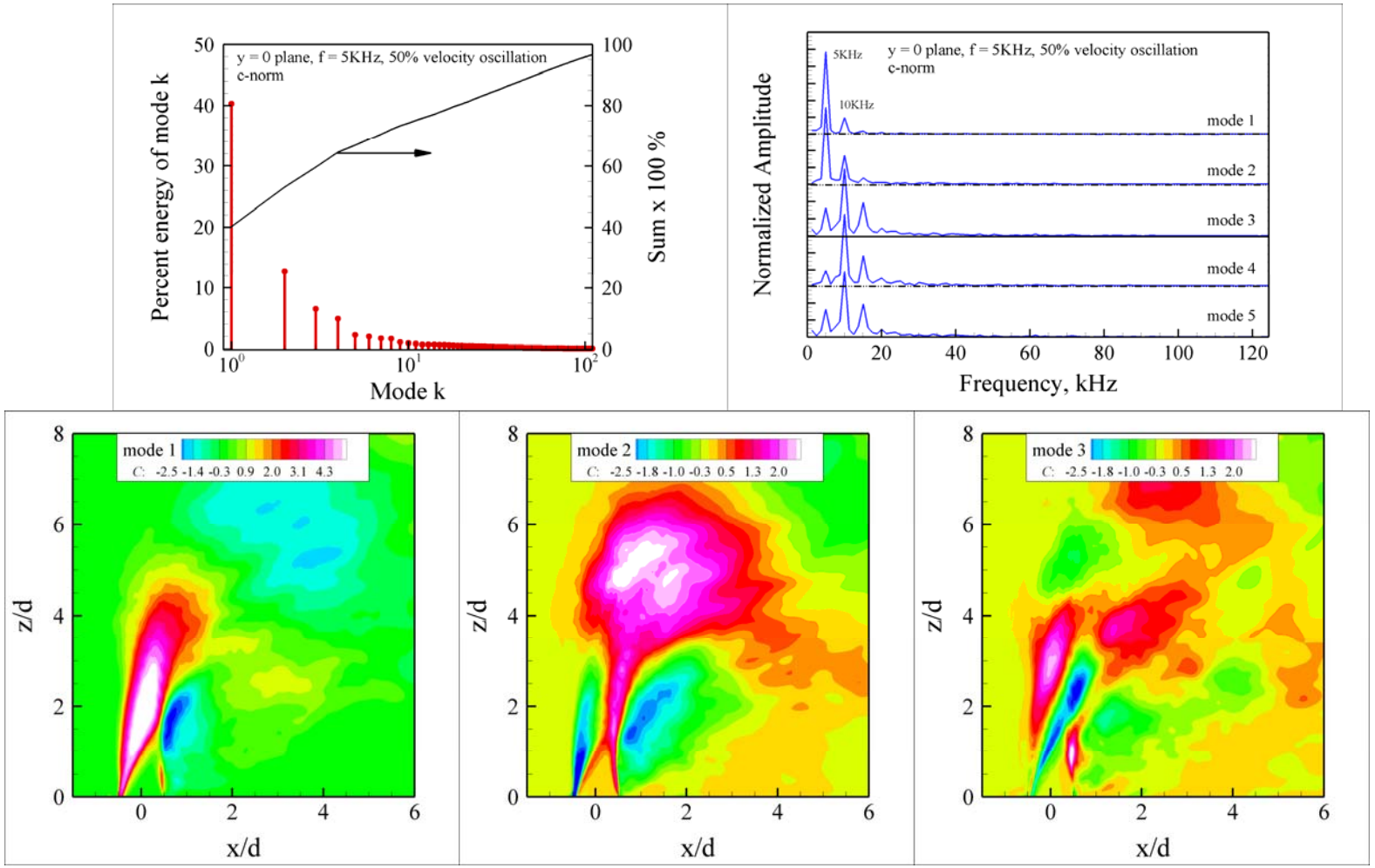

Figure 5.12 2D-POD in $y = 0$ plane (c-norm, case II-2)

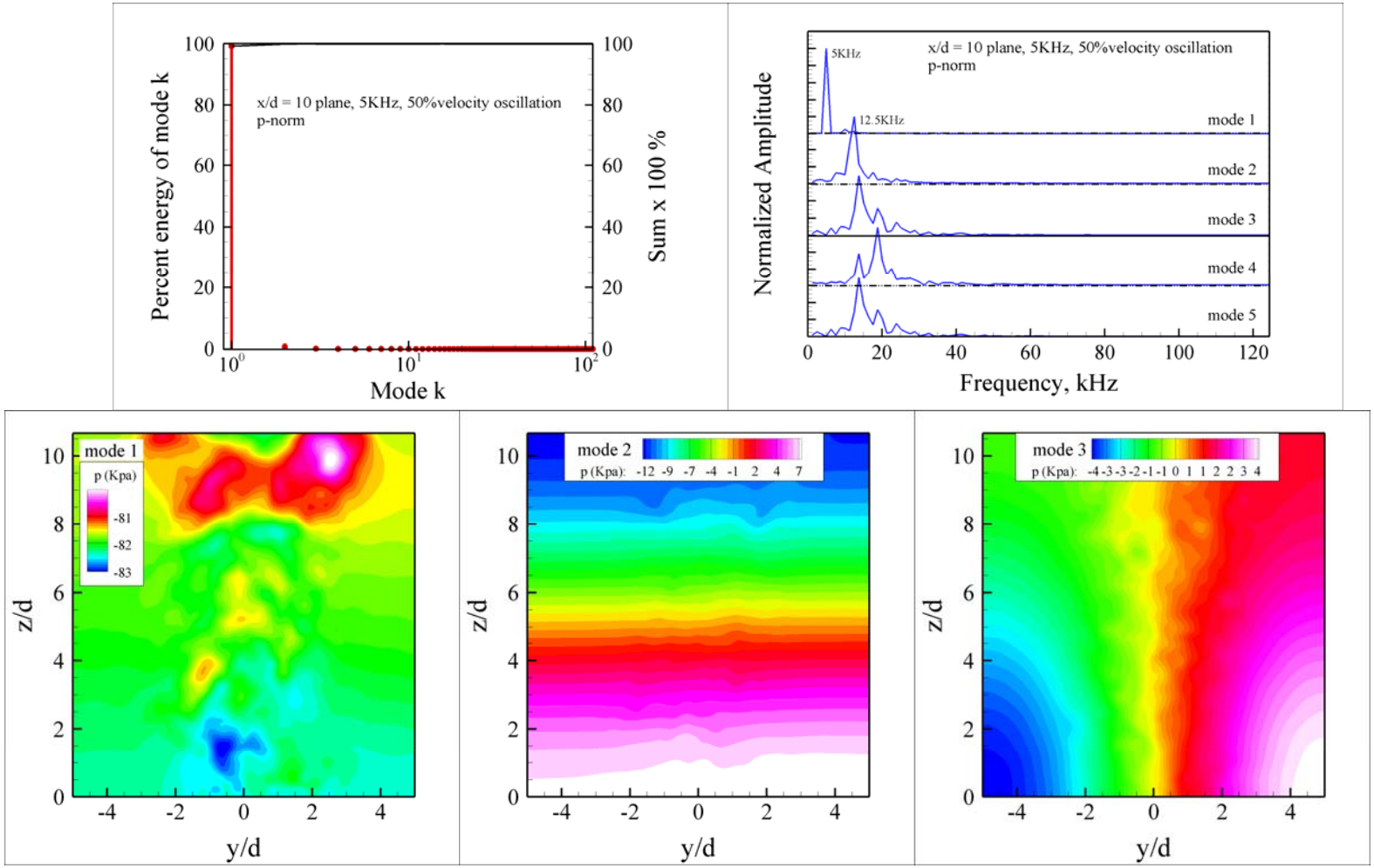

Figure 5.13 2D-POD in $x/d = 10$ plane (p-norm, case II-2)

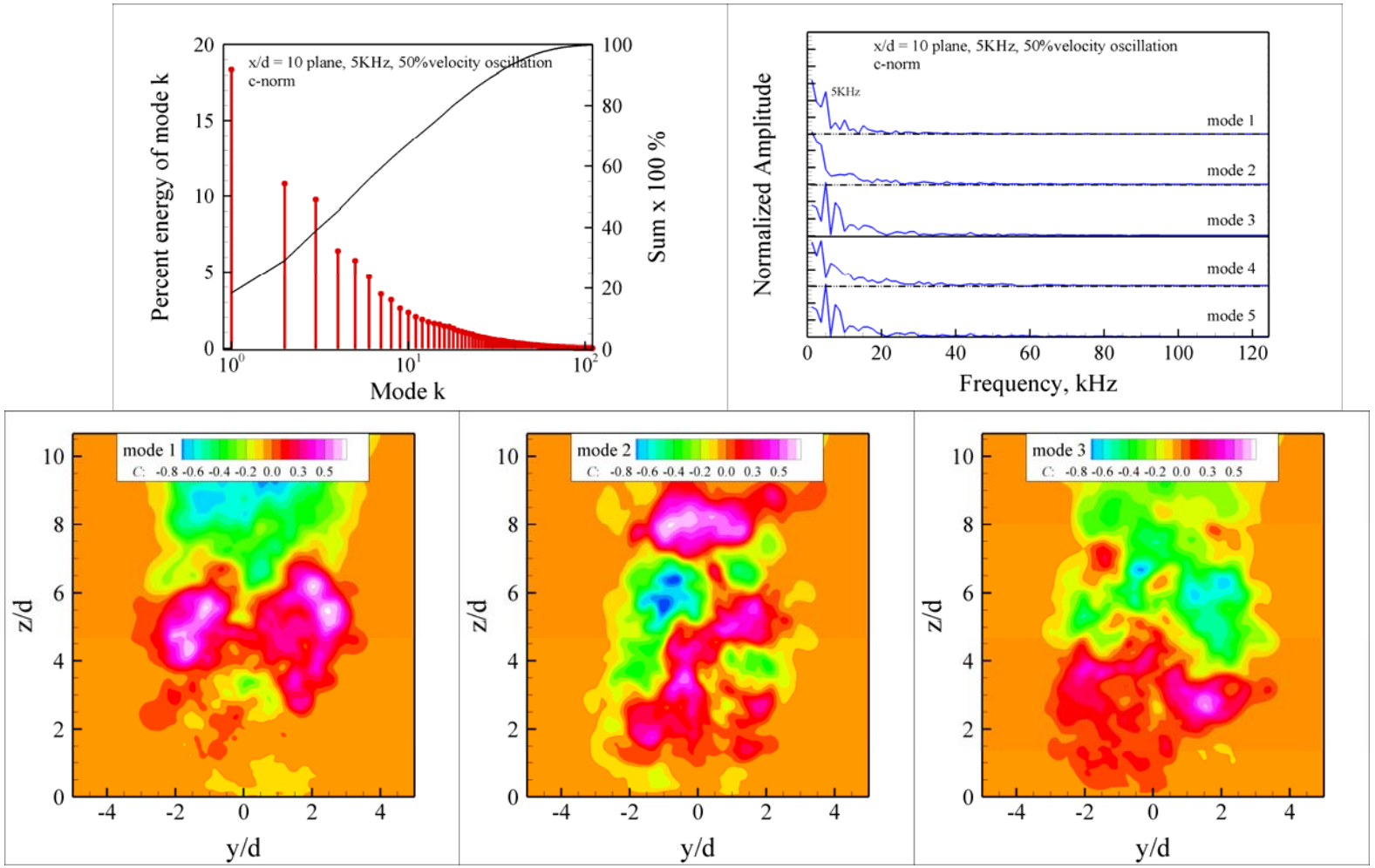

Figure 5.14 2D-POD in $x/d = 10$ plane (c-norm, case II-2)

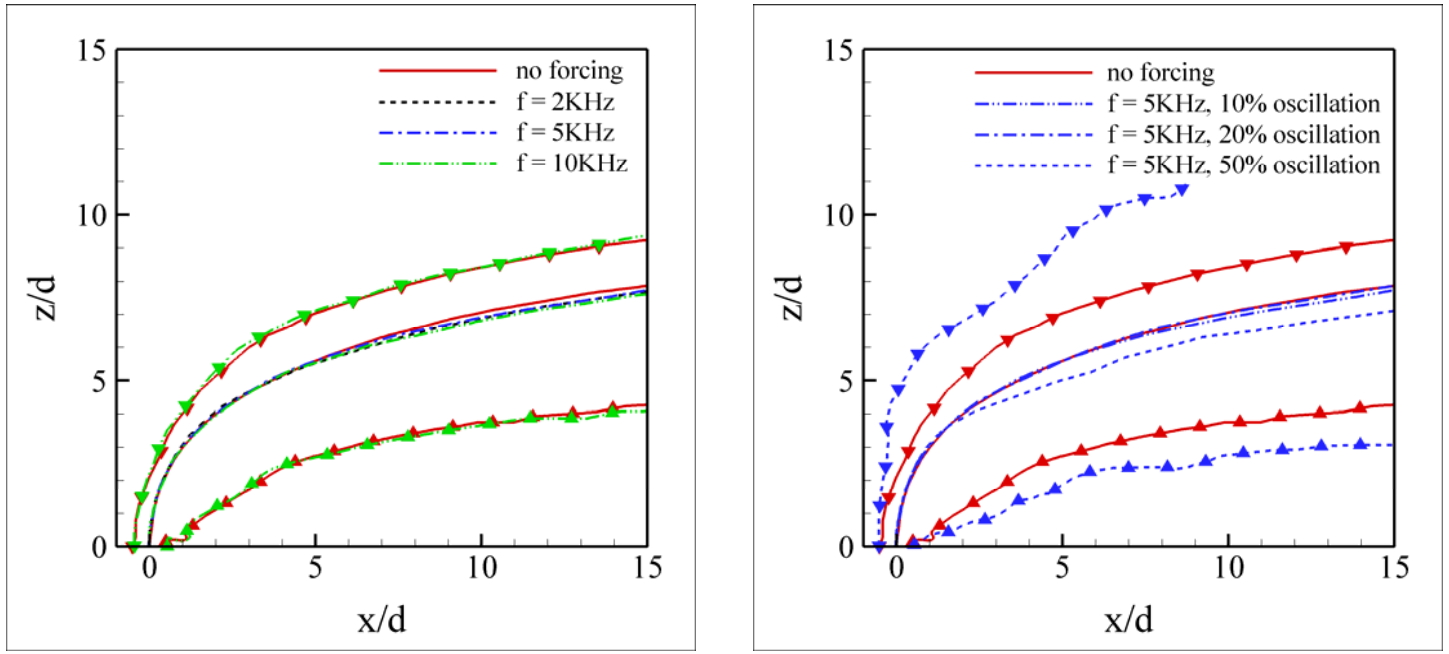

Figure 5.15 Jet trajectories

No forcing

5 kHz 10%

5 kHz 50%

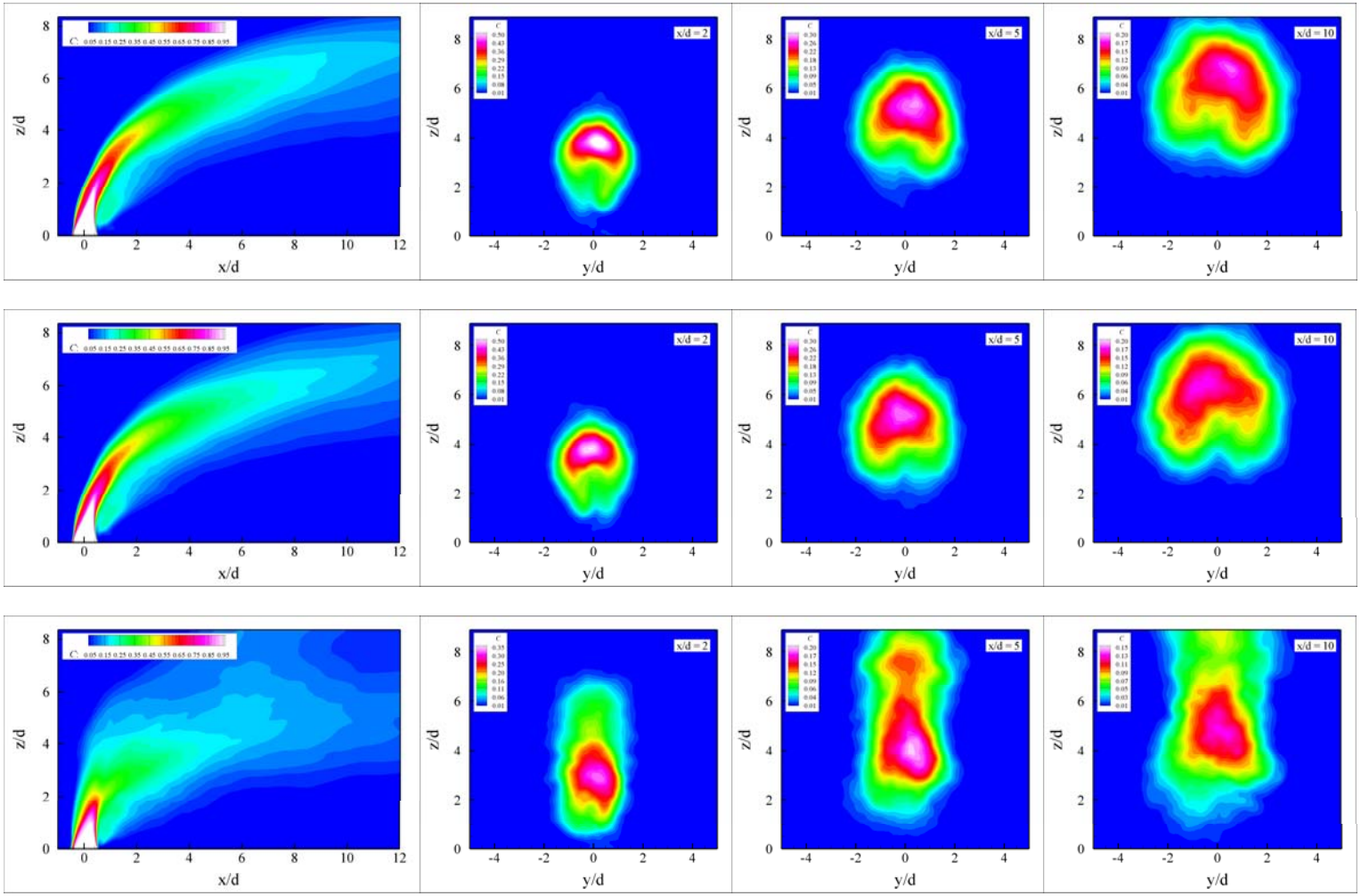

Figure 5.16 Contours of mean jet fluid concentration

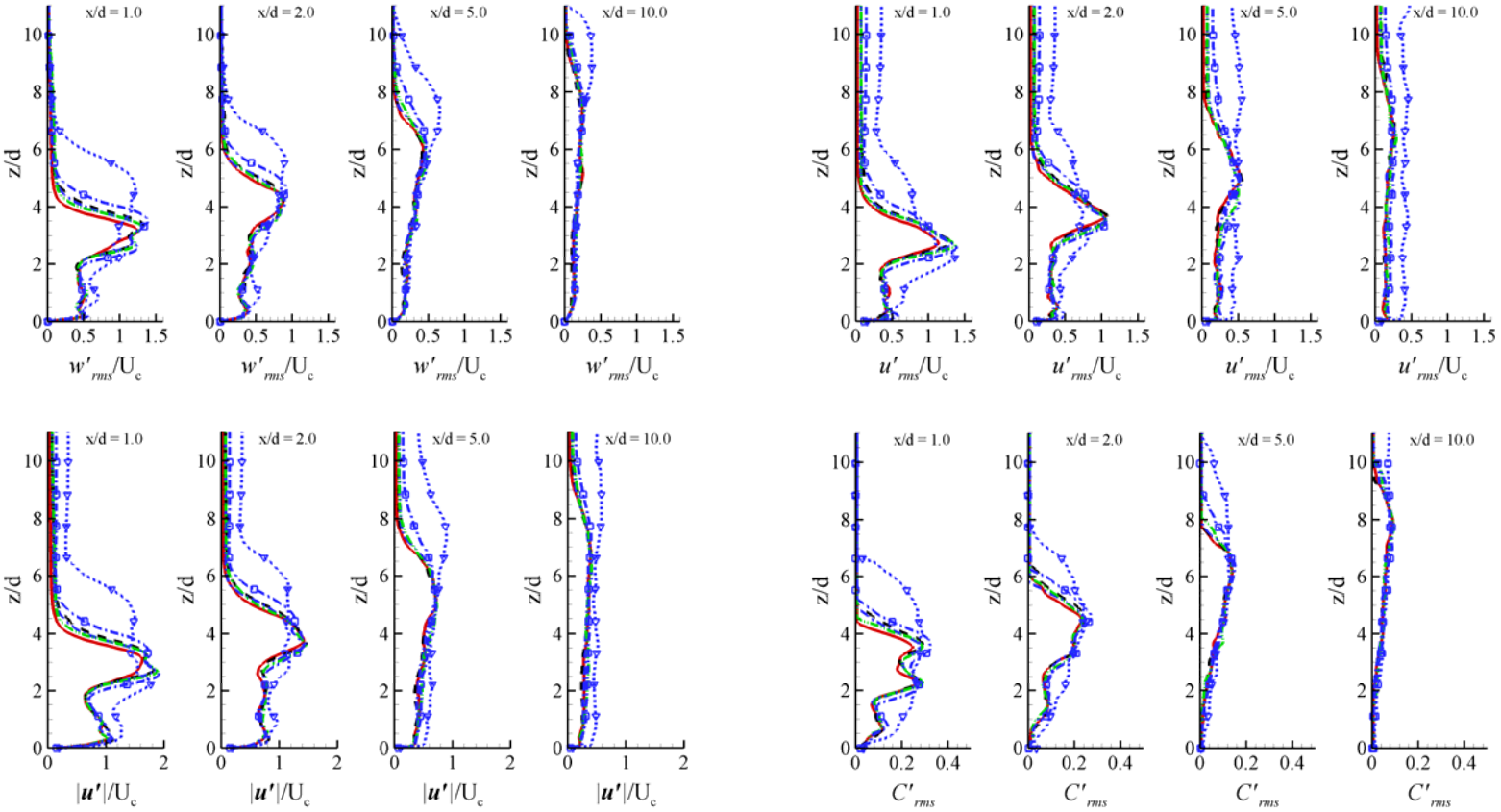

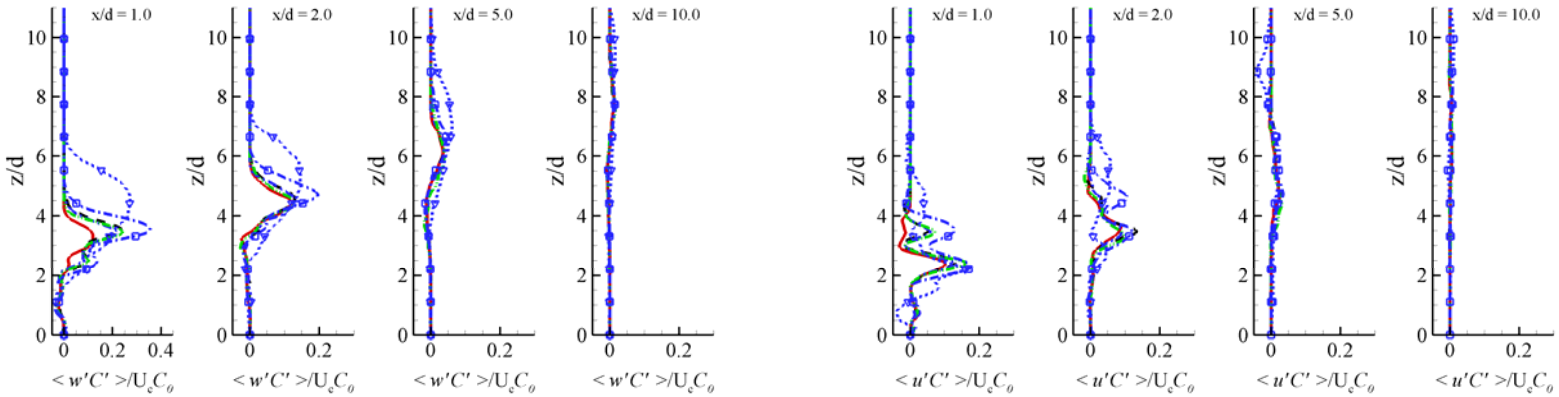

Figure 5.17 RMS properties and turbulent fluxes

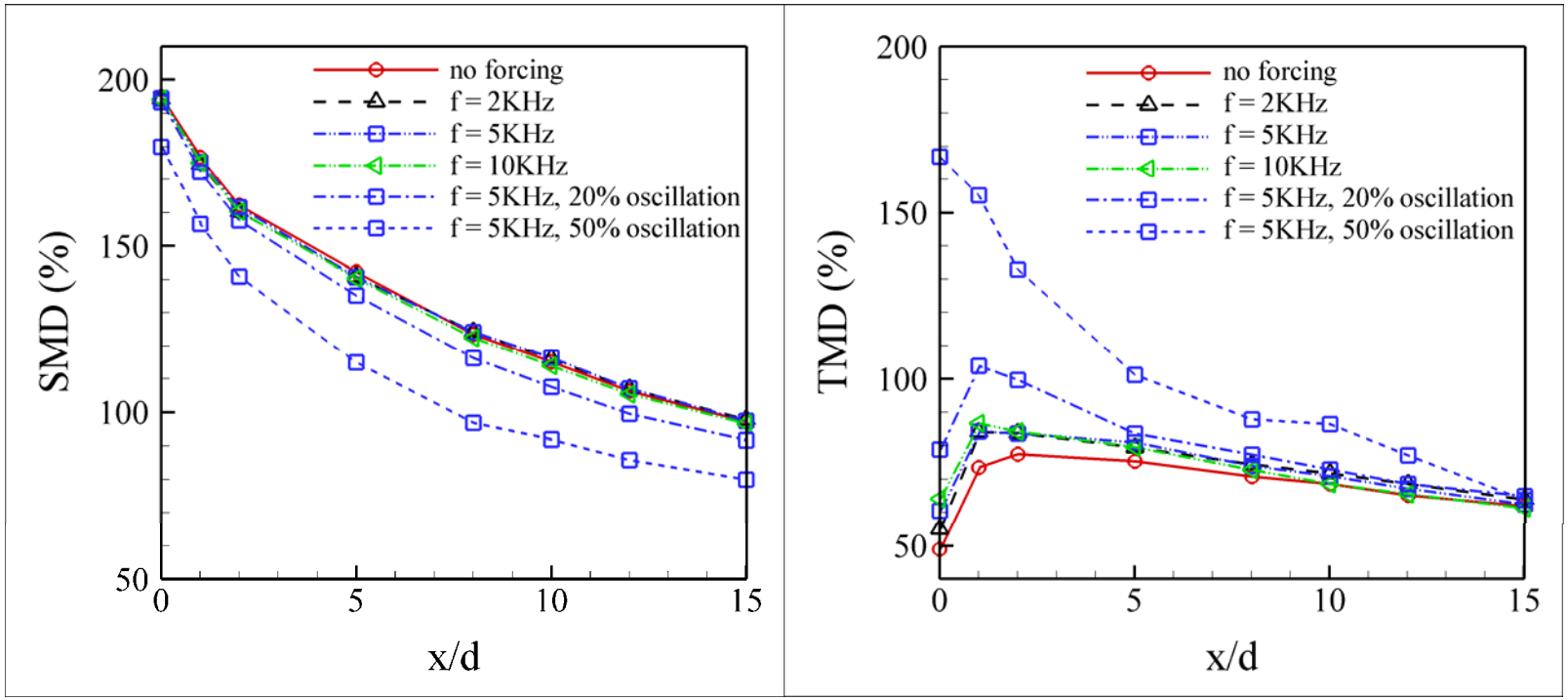

Figure 5.18 SMD and TMD

Chapter 6

Flow Dynamics and Scalar Mixing of a Sonic Jet into Supersonic Crossflow

The fast and efficient mixing of fuel and oxidizer is a requirement for ensuring a useful scramjet combustor. Among various injector designs, the transverse injection of fuel through a wall orifice into the supersonic environment is one of the simplest yet most effective configurations. Aside from the complex vortical and turbulent structures in lower-speed flows, the JICF in a supersonic environment has the salient highly-discontinuous structures as shown in Figure 1.3. The mixing properties are closely related to these flow phenomena.

In this chapter, a sonic ethylene jet into supersonic air crossflow is investigated numerically. The study has two objectives: 1) to assess the numerical strength and weakness of the current in-house code for solving the high-speed flows; and 2) to achieve better understanding of the flow field and the mixing process of an under-expanded transverse jet in the supersonic environment.

6.1 Case Description

The present computational case is designed to match the experimental work of Lin et al. (2010). In that experimental study, sonic ethylene jets were injected into a Mach 2 supersonic air crossflow with different injector angles, diameters, and momentum flux ratios. The study's purpose was to examine the effects of different types of flush

wall injectors on the jet plume size, penetration height and fuel concentration. Only one of the cases is simulated in the current work. The chosen case employs a $d = 3''/16$ (4.8 mm) injector at an angle of $90°$ and a momentum flux ratio of 1.52. The flow conditions are given in Table 6.1.

In the current work, a hybrid scheme is adopted for the spatial discretization to resolve the turbulence and strong discontinuities simultaneously. Upon the introduction of the smoothness parameters (Chapter 3), the dissipative upwind scheme is mainly used in the jet expansion region and in the areas with a high density gradient, $\nabla\rho$, and a high pressure gradient, ∇p. It has been confirmed (although corresponding visualizations are not shown here) that only a small portion of the flow field is resolved by the upwind scheme, and the larger part engages the low-dissipative center scheme. The thermodynamic and transport properties of air and ethylene are evaluated according to the discussion in Chapter 2.

6.2 Grid System and Boundary Conditions

The origin of the coordinate system is located at the center of the injector orifice. The computational domain extends to $[-5d,\ 15d]$, $[-8d,\ 8d]$ and $[0,\ 12d]$ in the streamwise, spanwise and transverse directions, respectively, for the crossflow duct. The spanwise and transverse boundaries are far enough away from the wall orifice that the leading shock generated at the crossflow inlet and the reflected shocks will not cross the jet plume within the domain. The outflow boundary conditions are further employed at these boundaries, as well as at the crossflow outlet, so as not to artificially constrain the

flow. The grids extend $5d$ into the injector chamber to provide the instantaneous flow information directly to the jet/crossflow interaction region.

Since the Reynolds number in this case ($\mathrm{Re}_j = 1.84 \times 10^5$) is substantially greater than those for the subsonic cases in Chapter 4 and Chapter 5, new sets of grids are generated to ensure proper resolution, especially in the key areas of the flow field. The grids are stretched at the walls and the injector exit to resolve the boundary layer and the jet breakdown in the immediate near field. The flow field contains 35^3 cells per d^3 on average and 60^3 cells per d^3 in the core regions. The grid distributions and block assignment are similar to those shown in Figure 4.6.

6.3 Mean Flow/Scalar Field

6.3.1 Flow Structures

The salient time-averaged structures of an under-expanded jet into supersonic crossflow were reviewed in Chapter 1 and are reiterated here for the current simulation.

Since the jet has a larger pressure than the environment it enters (and so is called "under-expanded"), it soon expands far enough to reduce the exit pressure to that of its surroundings. Meanwhile, as the jet penetrates the crossflow boundary layers, typical JICF coherent structures tend to appear. Figure 6.1 shows the contours of the mean velocity magnitude ($|\boldsymbol{u}|$) and pressure with two-dimensional streamlines on the center plane, as well as the mean ethylene concentration overlapped by the isolines of time-averaged temperature. A Prandtl-Meyer expansion fan emanates immediately at the jet

exit, creating a region with decreasing pressure and flow slowdown. As the jet passes the expansion fan, it develops a supersonic core which cannot sense the information at the outer area; therefore, the jet over-expands and the pressure of the surrounding flow pushes the jet back toward its axis (which is bent for the transverse injection), leading to the formation of a converging conical shock—the barrel shock. Note that the barrel shock has a strong effect in slowing down the flow and $|\boldsymbol{u}|$ drops sharply as the flow passes through it. Since the pressure mismatch between the jet and the crossflow is large, the barrel shock reflects at the perimeter of a Mach disk - a strong shock normal to the flow direction. The reflected shock is not apparent in the time-averaged pressure contour, but it can be detected by the clustering of the temperature isolines at the tip of the Mach disk; it envelopes a low-velocity, high-temperature region. Immediately after the Mach reflection, the reflected shock encounters the jet boundary; it pushes the boundary outward, creating a new rarefaction fan which can be discerned from the enlarged distribution of the jet fluid (ethylene) starting at $x/d \approx 2.0$, $z/d \approx 1.3$ in Figure 6.1c.

Schematic diagrams are shown in Figure 6.2 which delineate the Mach reflection in a simpler case – idealized free jet expansion. As the under-expanded jet enters the quiescent environment, it immediately expands and induces a converging conical shock. If P_j is only slightly larger than the ambient pressure, the converging shock incidents to the jet axis at a small angle, reaching the jet axis and undergoing a regular reflection: that is, it forms a diverging shock.; while for the cases $P_j >> P_a$, the angle between the incident shock and the jet axis is larger than the one that yields a sonic relative velocity

for the flow downstream of the shock; therefore the Mach reflection ensues in which a normal shock occurs in the middle of the jet and the conical incident shock is reflected on its perimeter. Since the thermodynamic pathway through both the incident and reflected shocks does not equal the pathway through the Mach disk, a slip discontinuity concurrently emerges from the shock trip point (the location where the incident shock, reflected shock and Mach disk meet). Across this contact surface, the pressure and flow direction do not vary, while the velocity magnitude, density and temperature are discontinuous. Notice that in reality, the supersonic jet does not have a sharp, stable boundary but rather a turbulent boundary where the jet and ambient gases mix; moreover, the mixing layer grows as a result of Kelvin-Helmholtz instabilities and progressively eats its way into the core of the jet, leading to a flow susceptible to twisting and bending motions, as will be observed in Section 6.4.

The distance (H_M) between the injection nozzle and the Mach disk is not sensitive to the gas species and can be estimated by an empirical correlation (Ashkenas and Sherman, 1966) as a function of jet stagnation pressure ($p_{tot,jet}$) to effective back pressure ($p_{b,eff}$) ratio such that:

$$\frac{H_M}{d} = 0.67\sqrt{\frac{p_{tot,jet}}{p_{b,eff}}} \tag{6.1}$$

Discrepancy exists for the selection of the effective back pressure in the context of JICF. Among the earlier studies, Schetz and Billig (1966) estimated $p_{b,eff} = 0.8 p_0$, Billig et al. (1971) used $p_{b,eff} = 0.67 p_{0,tot}$, and Everett et al. (1998) reported $p_{b,eff} \approx 0.35 p_0$ for the cases where the jet-to-crossflow momentum ratio was $J < 1.5$.

Ben-Yakar et al. (2006) suggested that the discrepancy was due to the larger momentum ratios used in the early works; they adopted $p_{b,eff} \approx 0.35 p_0$ for their $J = 1.4$ cases and achieved a fine comparison between the empirical estimation and experimental results. In the current work, $J = 1.52$; using the back pressure value of Everett, the calculation from Equation 6.1 gives $H_M \approx 3.9d$, while using the back pressure value of Schetz and Billig gives $H_M \approx 2.6d$. As implied in Figure 6.1, the current work produces a Mach disk location in-between these two estimations, possibly due to the mismatch of the boundary conditions and the jet-to-crossflow momentum ratio.

The jet acts as a blockage to the crossflow and retards the incoming flow ahead of it, leading to the formation of a primary shock wave—the bow shock and the separation of the boundary layer. Due to the subsequent thickening of the boundary layer, a weak λ-structure shock is also created in the lower region close to the wall (as shown by the $|\boldsymbol{u}|$ variation around $x/d \approx -0.7$, $z/d \approx 0.5$). Two vortex structures are formed ahead of the jet: the larger is centered at $x/d \approx -1.4$, $z/d \approx 0.2$ with a long and narrow clockwise- recirculating zone; the smaller one is counterclockwise-rotating and is located in the immediate-outer region of the expansion wave. The first is created by the separation of the crossflow boundary layer, and the latter is due to the roll-up of the jet shear layer. These recirculation regions resemble those in the subsonic case (Chapter 4) and were also observed in the experimental work of Santiago et al. (1997) and the numerical simulation of Génin and Menon (2010). Notice that the low-speed and high-temperature (as shown in Figure 6.3) region ahead of the jet plays a significant role in the

ignition and stabilization of supersonic combustion, which is further addressed in Section 6.4.

Due to the low ambient pressure on the leeward side of the jet, the leeward part of the jet flow expands more drastically and induces a stronger converging shock—the leeward barrel shock. As shown by the streamlines in Figures 6.1a and 6.1b as well as the ethylene concentration in Figure 6.1c, most of the jet fluid passes through the windward (and lateral, visualized in Figure 6.5) barrel shock and the Mach disk. Only a small amount of jet fluid passes through the leeward barrel shock. In the leeward of the jet, a weak shock is also detected in the lower region close to the jet exit; this is induced by the lower portion of the leeward over-expanded jet flow and is generated from the reattachment point at the wall. A node with a weak and positive divergence at $x/d \approx 2.0$, $z/d \approx 0.2$ is also observable on the leeside of the jet, consistent with the subsonic case in Chapter 4.

Figure 6.3a shows the contour of the mean temperature on the center plane overlapped by the two-dimensional streamlines. The shock waves discussed above predominantly account for the temperature variations. As shown by the purple lines, the isoline of $T = 220K$ in the near field marks the locations of the crossflow boundary layer, the bow shock, the expansion fan, the windward barrel shock and its reflected shock, the Mach disk, the weak shock at the jet-leeward reattachment point. The iso-surface of $T = 220K$ is thus presented in Figure 6.3b to trace the three-dimensional features of the shock waves. The circumference of the jet orifice on the crossflow wall is denoted by a thick red line. The crossflow boundary layer shows a slight elevation ahead

of the jet as a consequence of its separation. A vertical-plate structure is most obvious, showing the spatial extension of the bow shock. The tails which connect to the foot of the bow shock deflect around the jet body and extend all the way to the crossflow downstream. At the jet exit, a hemisphere structure is identifiable, displaying the topology of the Prandtl-Meyer expansion wave. A small structure is also observed in the leeward of the jet, corresponding to the weak wave generated from the reattachment point. The barrel shock and Mach disk are buried in the high-temperature region after the bow shock and above the expansion fan. In the far field, the iso-surface of $T = 220K$ shows two inter-connected hollowed tubes, suggesting a sense of the CVP structure along the jet trajectory.

The mean temperature contour on the $z/d = 0.5$ plane is shown in Figure 6.3c to extract the information close to the wall. The thick-dashed-black circle marks the vertical projection of the jet orifice. The two high-temperature regions ahead of the jet correspond to the crossflow boundary separation and the weak λ-structure shock. In the leeward of the jet, a low-temperature belt with temperature troughs at its tips is detected, corresponding to the low-pressure and high-velocity region as shown in Figures 6.4a and 6.4b; it is accounted for by the over-expanded jet flow close to the leeward barrel shock, as confirmed by the high ethylene concentration enveloped by the clustered isolines of temperature in Figure 6.4c. Farther in the leeward of the jet, two zonal regions with low temperature, low pressure and high velocity magnitudes exist, created by the deflected crossflow which expands in the wake region. Notice that discernable asymmetry of the flow structures is observed in the leeward of the jet, suggesting that the time span for collecting the mean data is not long enough.

6.3.2 Mixing Field

To expose the mixing field in the current simulation, contours of ethylene concentration are shown on several z-planes, i.e. $z/d = 0.5, 1.0, 1.5$, and 2.0 in Figures 6.4c, 6.5a, 6.5b, and 6.5c, respectively. All the contours are overlapped by the isolines of mean temperature to mark the locations of shock waves, and the vertical projection of the jet orifice is marked by the thick-dashed-black circle. In the lower two planes, a high-concentration region is enveloped by the tilted and deformed barrel shock. Immediately adjacent to the crossflow wall (on the $z/d = 0.5$ plane), non-zero ethylene concentration is observed, suggesting that the jet fluid has a strong possibility of being swept downstream by the crossflow boundary flow. Two symmetric zonal regions appear in the $z/d = 1.0$ plane as we move upward to the jet plume. Since the tilted Mach disk passes the $z/d = 1.5$ plane, a small shock wave is observed and the jet fluid that penetrates through the windward barrel shock disperses into the crossflow and creates a fuzzy windward periphery of the jet plume; two tails present in the leeward, generated by the jet fluid across the lateral barrel shock. The fuzzy periphery of the jet plume is more obvious as we leave the barrel shock region (shown in the $z/d = 2.0$ plane).

The contours of ethylene concentration are also shown on several downstream planes, i.e. $x/d = 1.0$, 2.0, 5.0, and 10.0 in Figure 6.6, overlapped by the two-dimensional streamlines; on the slices, the contours of mean pressure overlapped by the isolines of vertical velocity are presented to display the influence of the flow structures The $x/d = 1.0$ plane traverses the near-field shock region and shows a fuzzy and

zigzagging upper boundary of the jet plume due to the flow deflection across the barrel shock. On the lower lateral edges, hanging vortices are observed; they are created by the skewed mixing layer as the crossflow deflects around the jet body. Since little jet fluid passes the leeward barrel shock, the jet plume loses its orbicularity and evolves into a winglike structure in the $x/d = 2.0$ plane. The hanging vortices also contribute to the jet deformation as they travel downstream in the direction of the mean convective velocity $\vec{U}_{mean} = \vec{U}_0 + \vec{U}_j$. In the $x/d = 5.0$ plane, the near-field shock has a minor effect, and regions with negative vertical velocity are detected on the "shoulders" of the jet plume, which connect with the diminished hanging vortices, yielding the distinctive counter-rotating vortex pair (CVP). Two secondary counter-rotating vortices are also observed close to the wall. In the far field (as shown in the $x/d = 10.0$ plane), CVP becomes the predominant structure and subsequently accounts for the two large lateral zones with negative vertical velocity; the jet fluid mixes with the crossflow and shows a nearly even ethylene distribution.

Lin et al. (2010) collected Raman scattering data at a transverse plane $x/d = 5.0$ (as shown in Figure 6.7). Numerical results in the current simulation are presented for the same focus region. The two contours exhibit similar structure and plume size, yet the results seem to under-predict the mixing and show a larger maximum. In our work, we found the mixing realization in this compressible mixing layer was closely related to the capture of the fine turbulent structures as observed in Chapter 1; thus, the grid resolution and spatial discretization scheme play crucial roles in the simulation. Further complicating matters, the unsteadiness of the incoming crossflow boundary has a

significant effect on the breakdown of the jet plume in the near field (Peterson and Candler, 2010) and subsequently affects the mixing realization. To eliminate any concern about the simulation conditions, the mass flow rate is calculated for mean field and for a random snapshot at various spatial locations both inside the injection pipe and in the crossflow duct. Good mass conservation is obtained and the mass flow rate is consistent with the experimental setup.

6.4 Instantaneous Flow Structures

The unsteady features of the complex flow dynamics and the mixing process discussed above are explored using the instantaneous data in this section.

Figure 6.8 provides a random snapshot showing the contours of Mach number (with its isoline $M = 1.0$), ethylene concentration (with isolines of temperature), magnitude of the pressure gradient ($|\nabla p|$), and magnitude of the density gradient ($|\nabla \rho|$) on the center plane. The over-expansion of the sonic jet is demonstrated by the high Mach number region enveloped by the barrel shock and Mach disk; in the leeward part of the jet body and close to the Mach disk, the local Mach number even exceeds 4.0, suggesting a normal shock is needed to match this over-expanded region with the conditions downstream. An evident subsonic (and high-temperature, as shown in Figure 6.3) zone exists ahead of the jet in the separation region and in the lower region behind the bow shock, providing an important site for the crossflow and jet fluids to mix thoroughly with a relatively long residence time; it thus contributes substantially to the ignition and sustaining of the supersonic combustion (Ben-Yakar, 2000; Won et al.,

2010). In the leeside of the jet, a subsonic region is also arising behind the barrel shock and close to the wall in the wake; it provides a pathway for the information in the far field to travel back to the near-field shock zone, suggesting that the disturbance generated downstream has the capacity to affect and modulate the fuel injection and consequently the mixing and combustion process.

The strong shock waves in this supersonic case have a powerful impact on jet evolution in the near field as discussed in Section 6.3; the small shock waves (shocklets) in a relatively farther field also have a critical impact on the spreading of the mixing layer (Morkovin, 1987; Papamoschou, 1990) and the convection of the shear-layer vortices (Dimotakis, 1991). As shown by the instantaneous ethylene concentration in Figure 6.8, in the early jet development the shear-layer vortices are observable only in the windward surface, while in the leeward, they are suppressed partially due to the stronger barrel shock (as well as by the inverse-sign borne by the pressure gradient, as discussed in Chapter 4). After the jet bends downstream, fine vortex structures appear on both the windward (upper) and the leeward (bottom) shear layers—the latter having discernable clusters of temperature isolines and intermittent subsonic spots, suggesting the existence of the shocklets.

A shock front can be identified by a sharp gradient in the pressure field and in the density field, but it must be differentiated from contact discontinuities. In the contours of $|\nabla p|$ and $|\nabla \rho|$ in Figure 6.8, the bow shock, expansion fan, barrel shock, Mach disk and weak reflected shocks are clearly presented; distinctive structures appear immediately ahead of the leeward barrel shock, and for the $|\nabla \rho|$ contour, local peak regions emanate

on the periphery of the jet plume downstream of the Mach disk. Since the distinctive structures near the leeward barrel shock correspond to the low Mach number ($M \leq 1.0$) regions, they cannot be identified as shock fronts; while in the lower periphery of the jet plume and in the early wake region, shocklets appear and account for the spots of local peak values.

Time series of $|\nabla p|$ and $|\nabla \rho|$ at a sequence of $t = 0.14\ ms$, $0.16\ ms$, and $0.18\ ms$, are presented in Figure 6.9 and Figure 6.10, respectively. A weak shocklet created by the boundary separation appears at the foot of the bow shock at $t = 0.14\ ms$ and emerges to the bow shock at $t = 0.16\ ms$, yielding to a varying shock front in the lower part of the bow shock. A traveling compression wave generated at the lower windward jet boundary was captured by Génin and Menon (2010) at a time interval of $8\ \mu s$; this shock wave is not apparent in the current work, probably because of a much larger time interval, yet the kink (created by the reconnection of the traveling wave to the barrel shock (Génin and Menon)) is observed on the windward barrel shock. The size of the Mach disk also varies, showing a discernable larger one at $0.16\ ms$, while its location is marginally changed. The distinctively high $|\nabla p|$ and $|\nabla \rho|$ spots close to and connected to the windward barrel shock (these are the spatially evolving shear-layer vortices shown in Figure 6.13) travel downstream and interact with the weak reflected shock, yielding to large-scale vortices as evident in $|\nabla \rho|$ series.

Figure 6.11 shows the temporal evolution of ethylene concentration on the center plane and on the $x/d = 5.0$ plane at the same time sequence as listed above. The overlapping isolines of temperature confirm the shock and vortex identification and

differentiation from Figure 6.9 and Figure 6.10. The shear-layer vortices on the windward and later on the leeward of the jet periphery have great capacity to engulf the crossflow ("macro-scale mixing" as coined by Ben-Yakar in 2000). Vortices pairing or amalgamating as they travel downstream contribute to the dispersion ("digestion" as termed by Brown and Roshko in 1974) of the engulfed crossflow; it is the second stage or intermediate of mixing ("mixing transition" as classified by Gutmark et al. in 1995). The molecular diffusion ("micro-scale mixing" as noted by Ben-Yakar in 2000) appears last but not least, creating a mixture for the chemical reactions to occur at the molecular level. Notice that the jet plumes are highly unsteady and asymmetric in the $x/d = 5.0$ plane, accounting for the asymmetry observed in the average mixing field as shown in Figure 6.7.

Since the evolution of the shear-layer vortices is one of the primary controlling parameters in the near-field mixing, the temporal behavior of vorticity field is thus examined here. Figure 6.12 shows contours of vorticity magnitude (Ω) and the three components of vorticity (ω_x, ω_y, and ω_z) at $t = 0.18\ ms$ on the center plane. The vorticity is observed to be mainly distributed on the jet periphery and in the early wake region. On the shear layer at the jet boundary, the y-component (ω_y) is the major contributor; hence a time sequence of ω_y is recorded in Figure 6.13. Negative ω_y is generated at and shed from the immediate upstream of the jet, forming the periodically detached eddies (in consistency with the local high $|\nabla p|$ and $|\nabla \rho|$ spots in Figure 6.9 and 6.10); the velocity gradients between the crossflow behind the bow shock and the jet affect the tilting and stretching of eddies. These eddies persist for long distances

downstream and are stretched and enlarged in the traveling process, as more clearly indicated by the expanded $|\nabla\rho|$ spots in Figure 6.10. These traveling eddies account for the fuzzy structures on the windward of the jet plume and evidently impact the mixing at the jet shear layer. Ben-Yakar et al. (2006) experimentally explored the velocity-induced stetching-tilting-tearing mechanism and detected the periodically shedding of counter-rotating vortices for the ethylene and hydrogen jets into nitrogen crossflow (Mach number equal to 3.38) at momentum ratio of 1.4. Won et al. (2010) reproduced the experimental data; they found the period of shedding one positive eddy and one negative eddy was $5\ \mu s$. Since the flow conditions and time interval are quite different in the current study, the eddies with positive ω_y are not apparent, yet the positive ω_y regions appear intermittently between the eddies with negative ω_y as shown in Figure 6.13. Iso-surfaces of $\Omega = 9.6\times10^5\, s^{-1}$ (colored by the ethylene concentration) and $|\omega_y| = 4.8\times10^5\, s^{-1}$ are shown in Figure 6.14 to display the spatial distributions of the vorticity in the mixing field. In consistency with Figure 6.13, the vorticity condenses in the boundary layer and the near-field jet shear layer; in the far field, the vorticity scatters in the enlarged jet plume, and fine vortex structures appear and prevail in the flow field.

6.5 Conclusion

In this chapter, the evolution and mixing of a sonic ethylene jet into supersonic air crossflow was investigated. The flow conditions followed the experimental setup of Lin

et al. (2010); the mean mixing field was reproduced in the current simulation and achieved qualitative consistence. The major conclusions are:

(1) the salient shock structures can be captured in the time-averaged flow field: the bow shock, separation shock, Prandtl-Meyer expansion fan, tilted barrel shock, Mach disk and reflected shocks; the formation of Mach disk can be described in terms of an idealized free jet expansion; the distance between the injection orifice and Mach disk converges to the empirical estimation;

(2) the unsteady features of shock waves can be observed in the snapshots of the Mach number, pressure gradient magnitude ($|\nabla p|$), density gradient magnitude ($|\nabla \rho|$); the existence of a lower-speed and high-temperature region ahead of the jet confirms the flame-holding capability of JICF; the possibility of disturbances downstream traveling back to the injection near field is proposed in the subsonic lower wake region; and

(3) the mixing process was examined according to the instantaneous contours of ethylene concentration; the engulf of crossflow at the mixing layer is connected to the periodically shedding of eddies; the stretching-tilting-tearing mechanism was revisited here and related to the mixing details.

Table 6.1 Flow conditions of the sonic ethylene jet into supersonic air crossflow

	Crossflow	Jet
Fluid	air	ethylene
Mach number	1.99	1.0
Total pressure	244 kPa	380 kPa
Total temperature	300 K	320 K
Static pressure	31.5 kPa	211.4 kPa
Static temperature	165 K	285.46 K
Velocity	515 m/s	327.83 m/s
Density	0.665 kg/m^3	2.495 kg/m^3

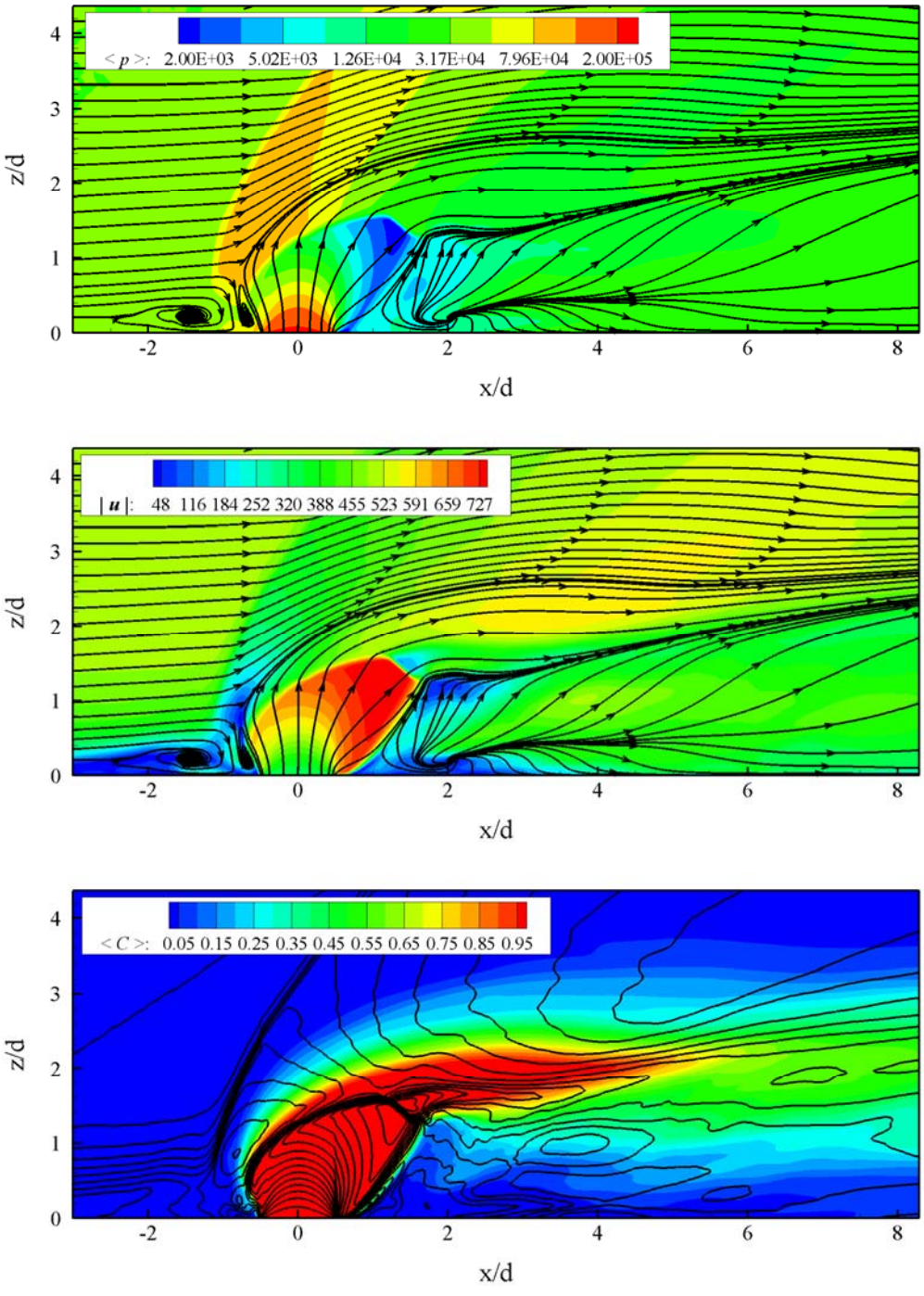

Figure 6.1 Contours of time-averaged (a) velocity magnitude with 2D streamlines, (b) pressure with 2D streamlines, and (c) ethylene concentration with isolines of temperature on the center plane

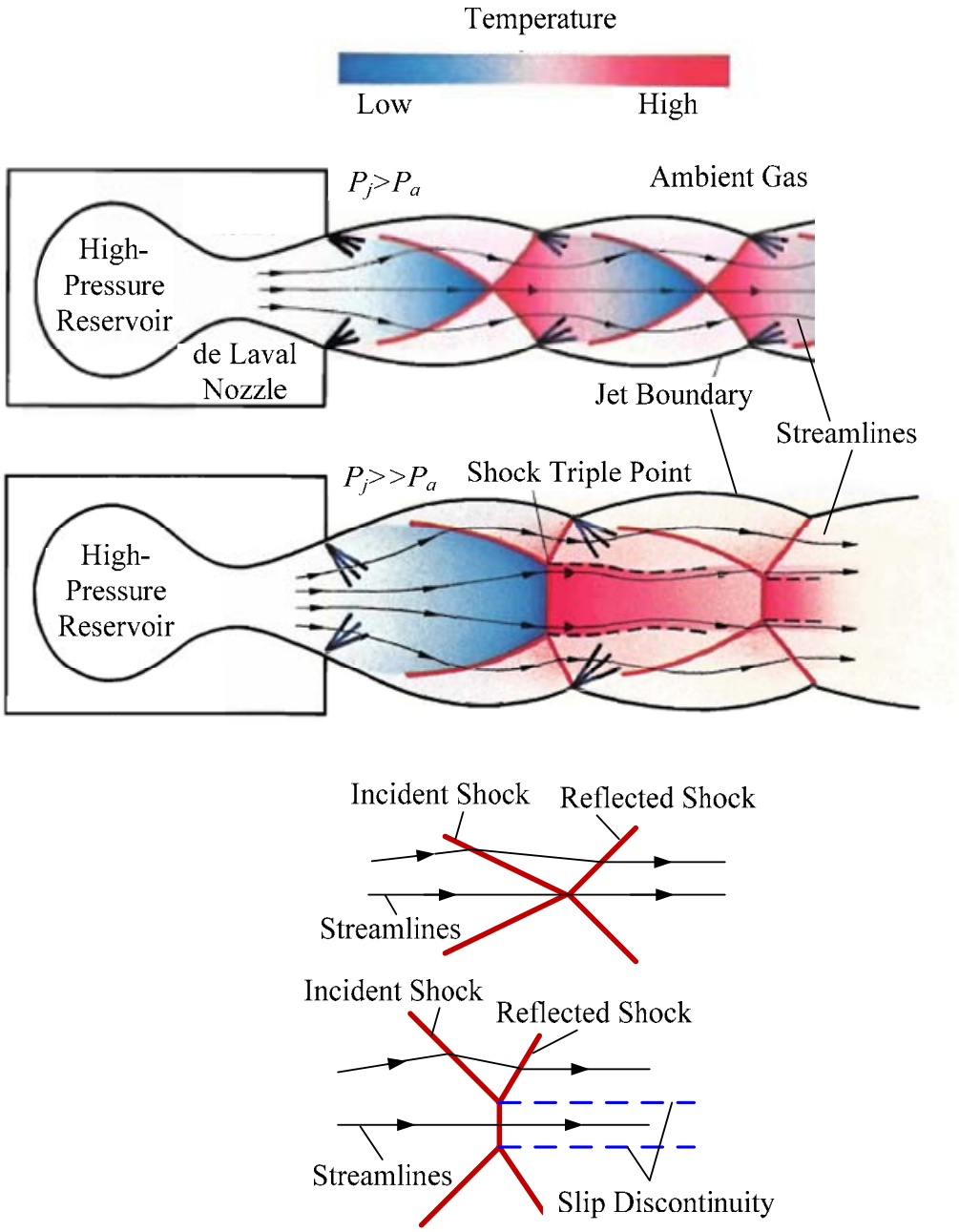

Figure 6.2 (a) Idealized steady-state structure of an under-expanded jet (after Narman and Winkler, 1985) and (b) regular reflection vs. Mach reflection

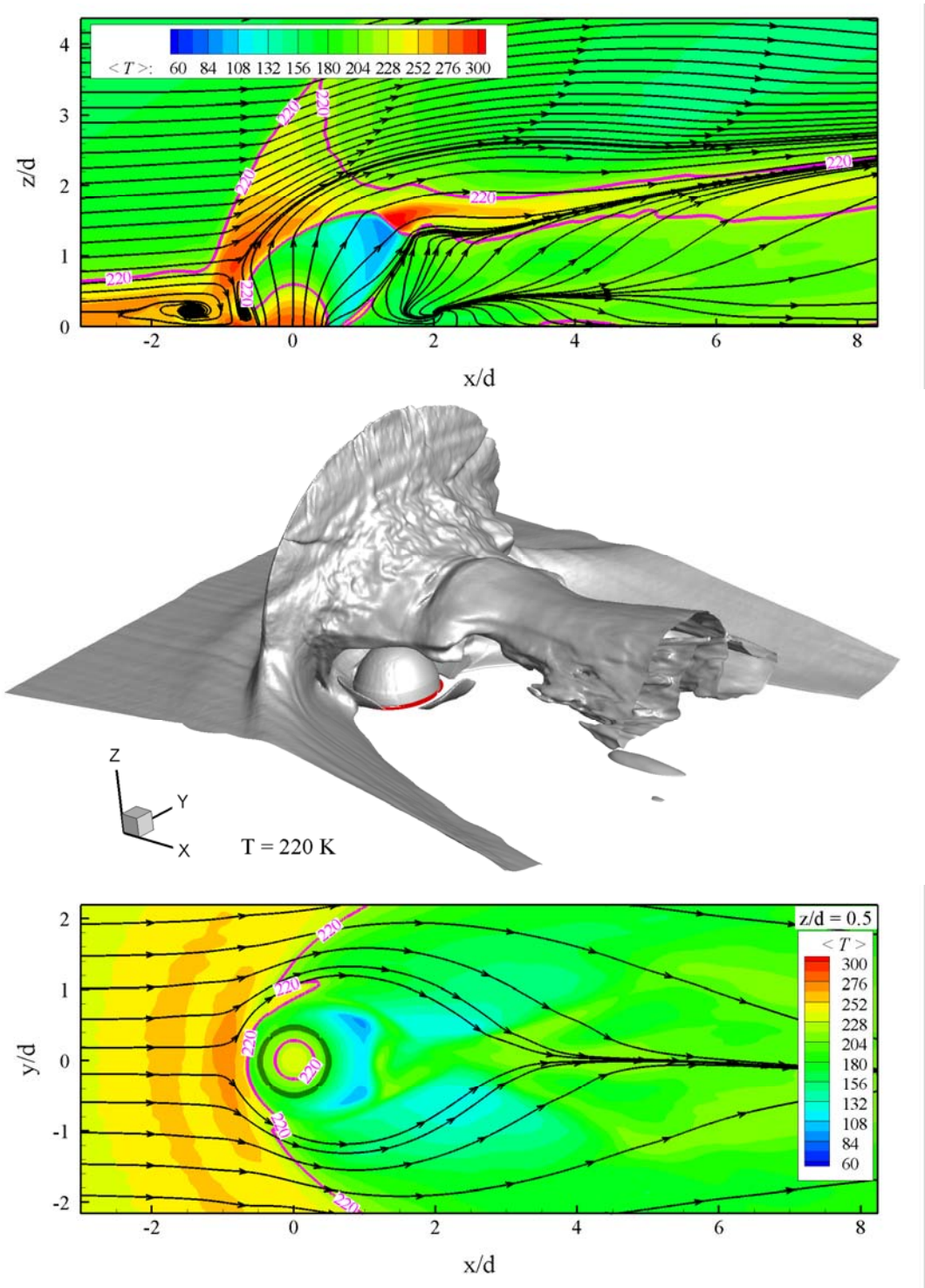

Figure 6.3 (a) Contour of mean temperature with 2D streamlines on the center plane, (b) Iso-surface of mean temperature at 220K, and(a) Contour of mean temperature with 2D streamlines on the z/d=0.5 plane

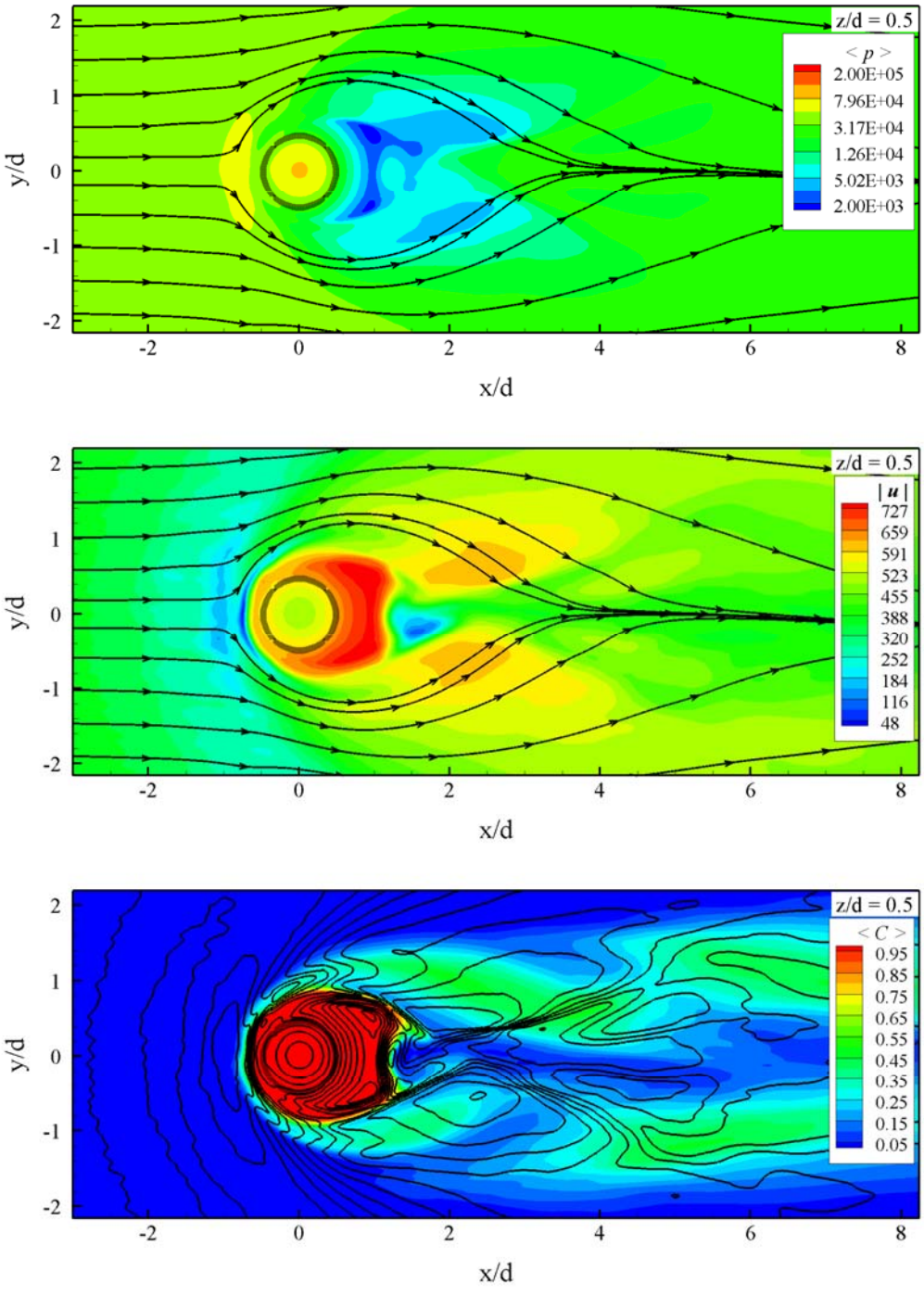

Figure 6.4 Contours of time-averaged (a) velocity magnitude with 2D streamlines, (b) temperature with 2D streamlines, and (c) ethylene concentration with isolines of temperature on the z/d = 0.5 plane

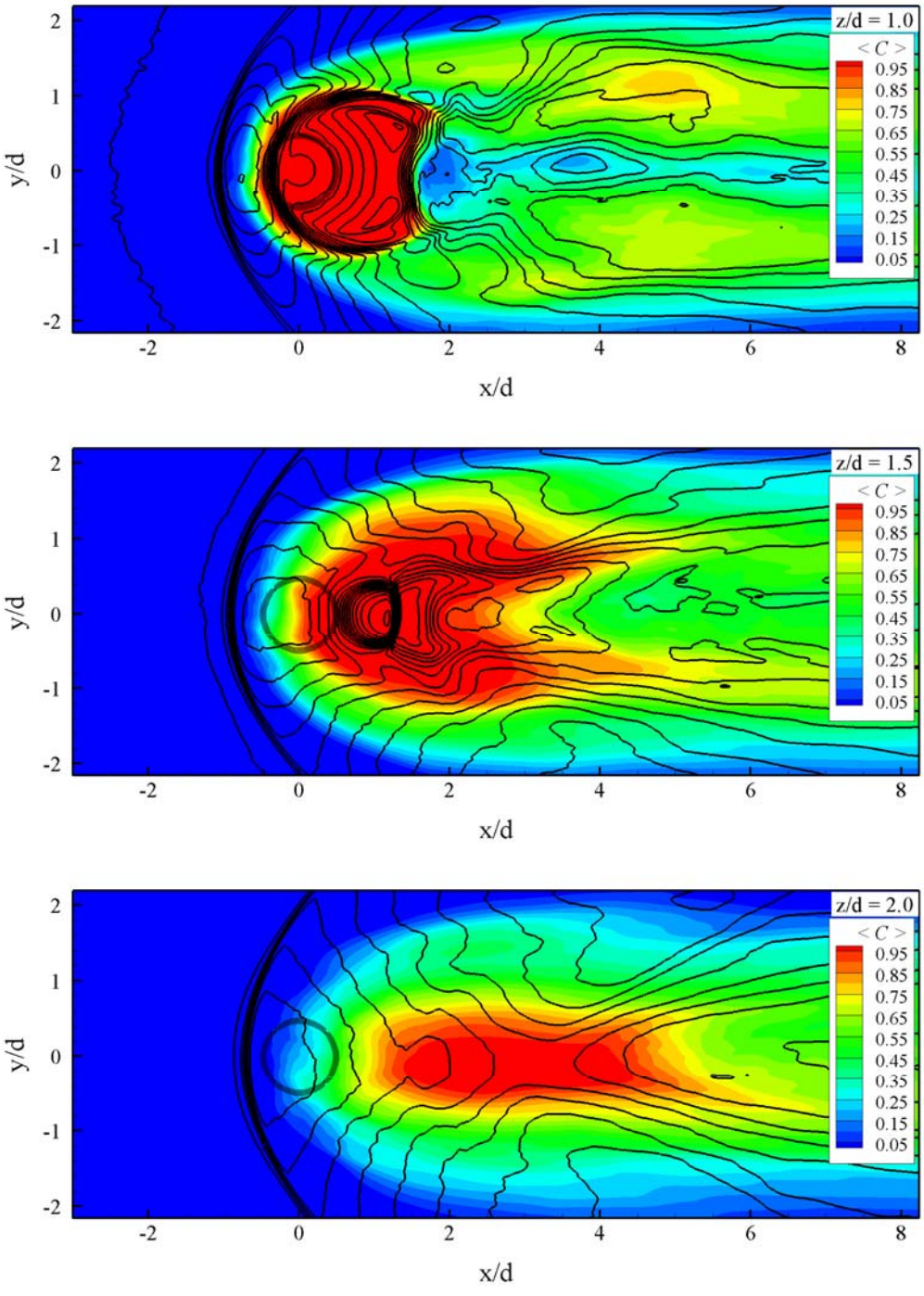

Figure 6.5 Contours of mean ethylene concentration with isolines of temperature on z-planes

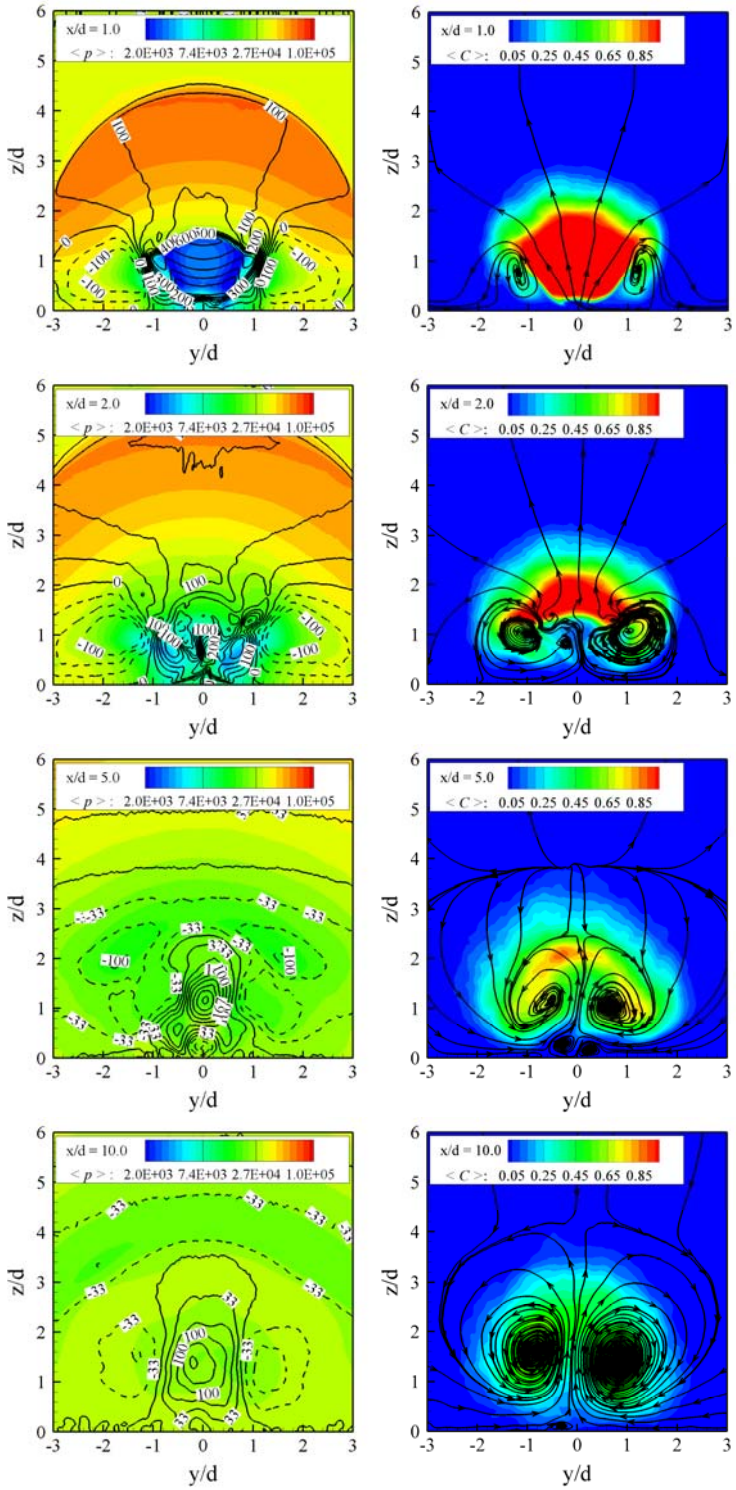

Figure 6.6 Contours of mean pressure overlapped by isolines of transverse velocity (left) and mean ethylene concentration with 2D streamlines (right) on x-planes

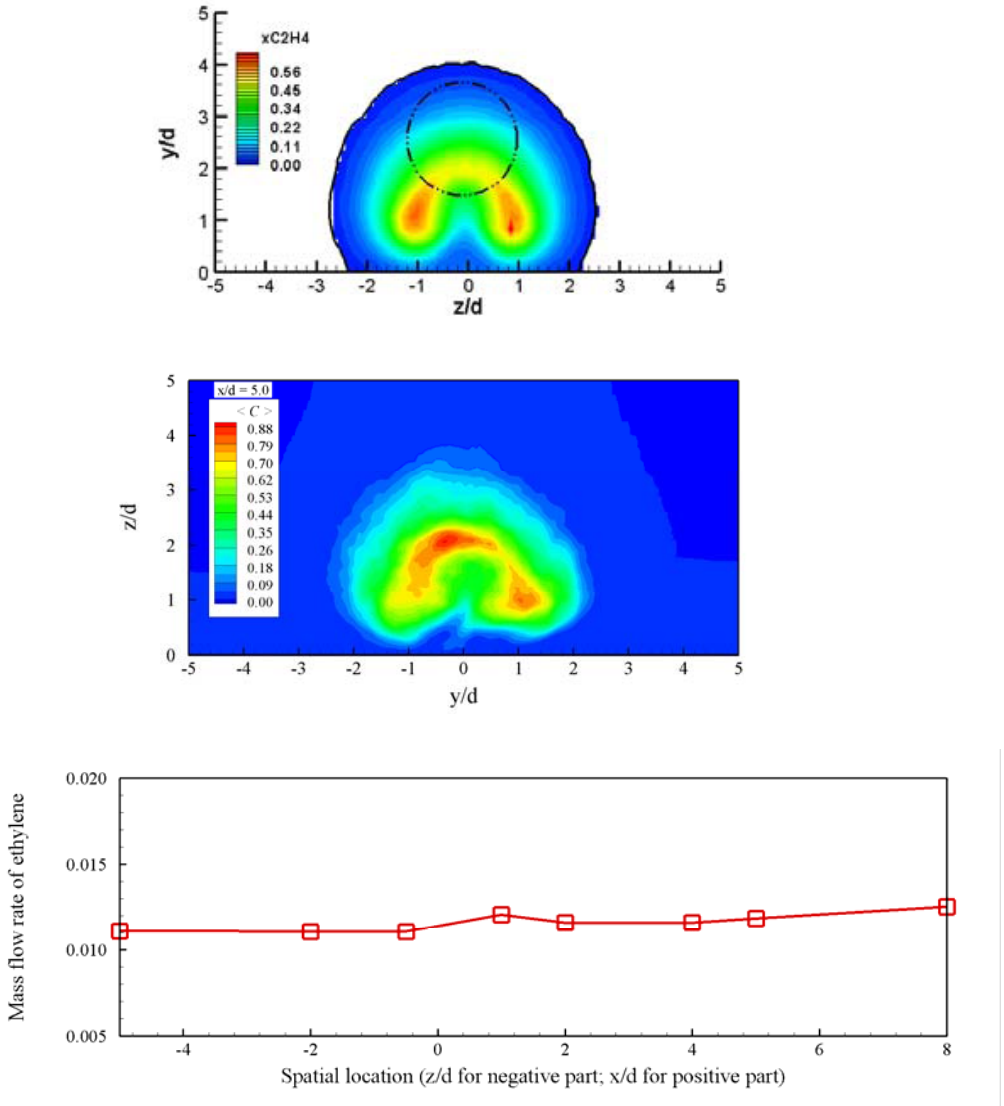

Figure 6.7 Contours of ethylene concentration in the x/d =5.0 plane: experimental (top) and numerical results (middle), and spatial evolution of mass flow rate for jet fluid at a random snapshot (bottom)

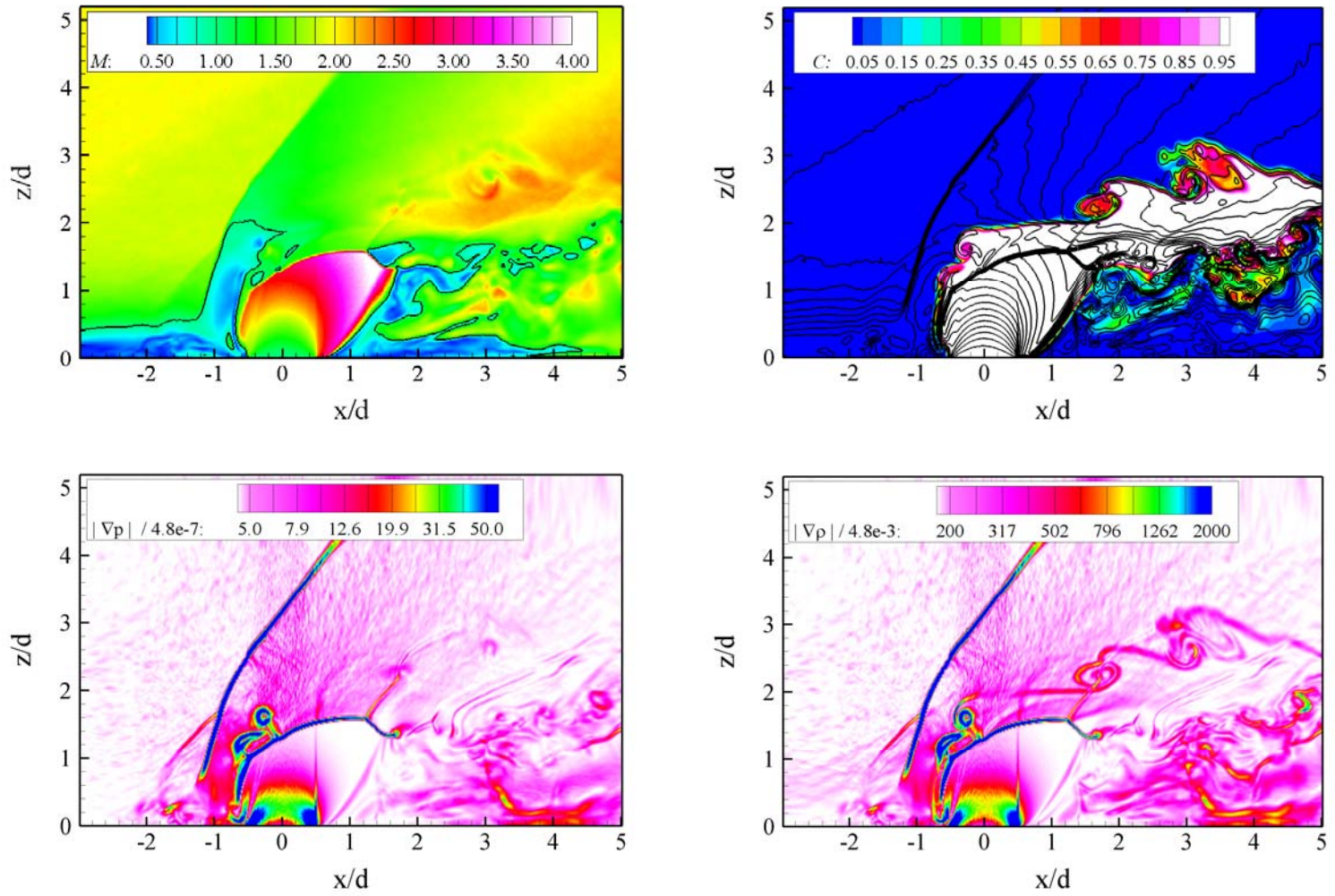

Figure 6.8 Contours of instantaneous (a) Mach number, (b) ethylene concentration (overlapped by isolines of temperature), (c) pressure gradient, and (d) density gradient in the center plane

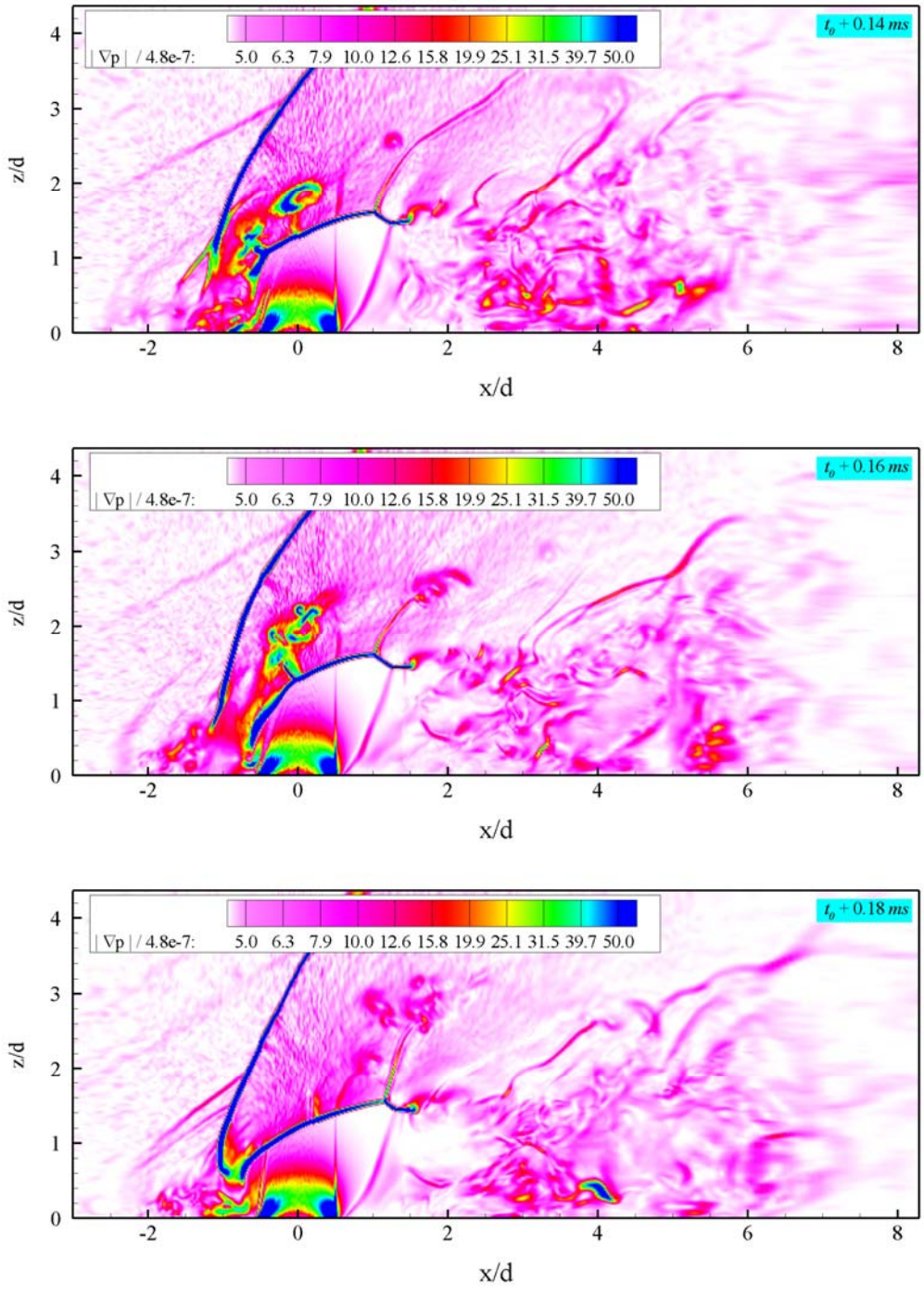

Figure 6.9 Temporal evolution of pressure gradient in the center plane

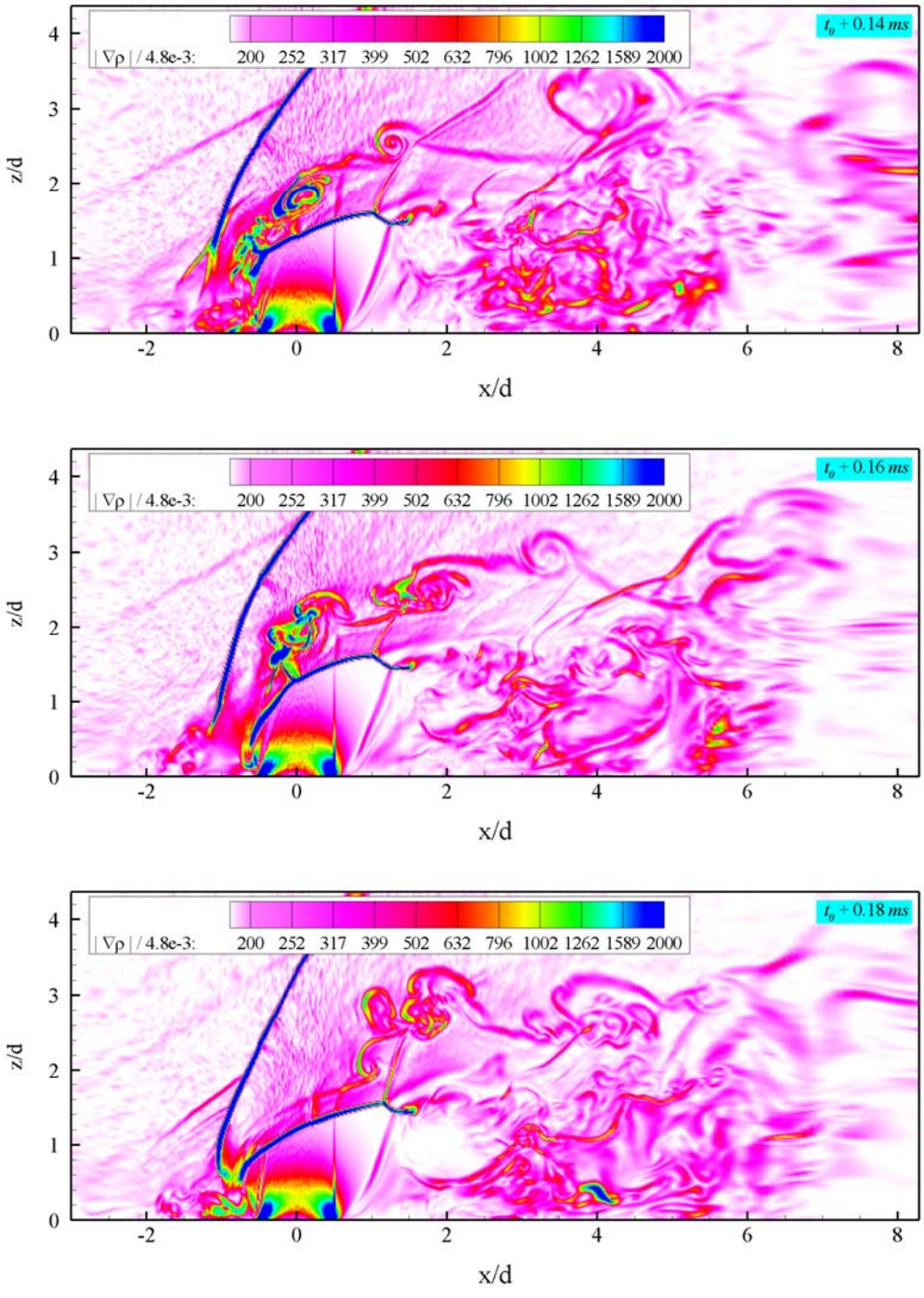

Figure 6.10 Temporal evolution of density gradient in the center plane

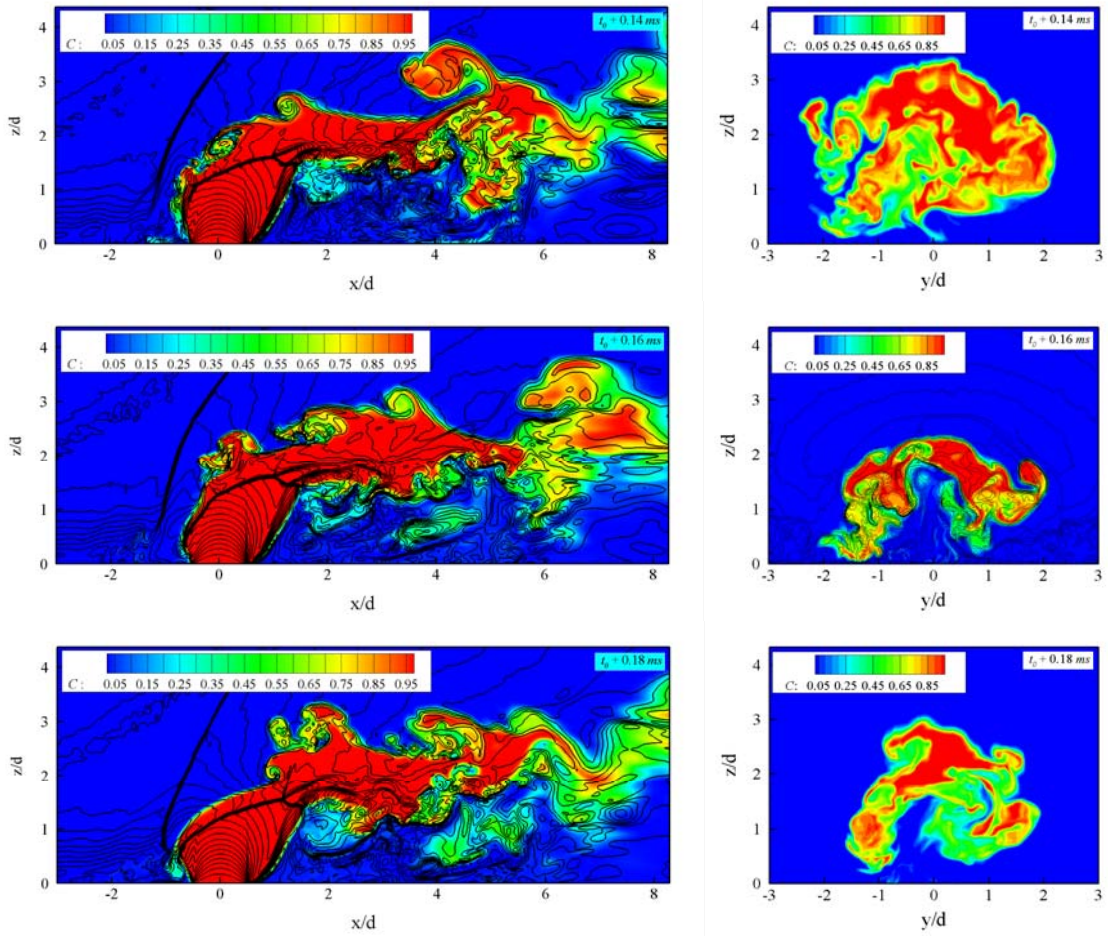

Figure 6.11 Temporal evolutions of ethylene concentration in the center plane (with isolines of temperature) and in the x/d = 5.0 plane

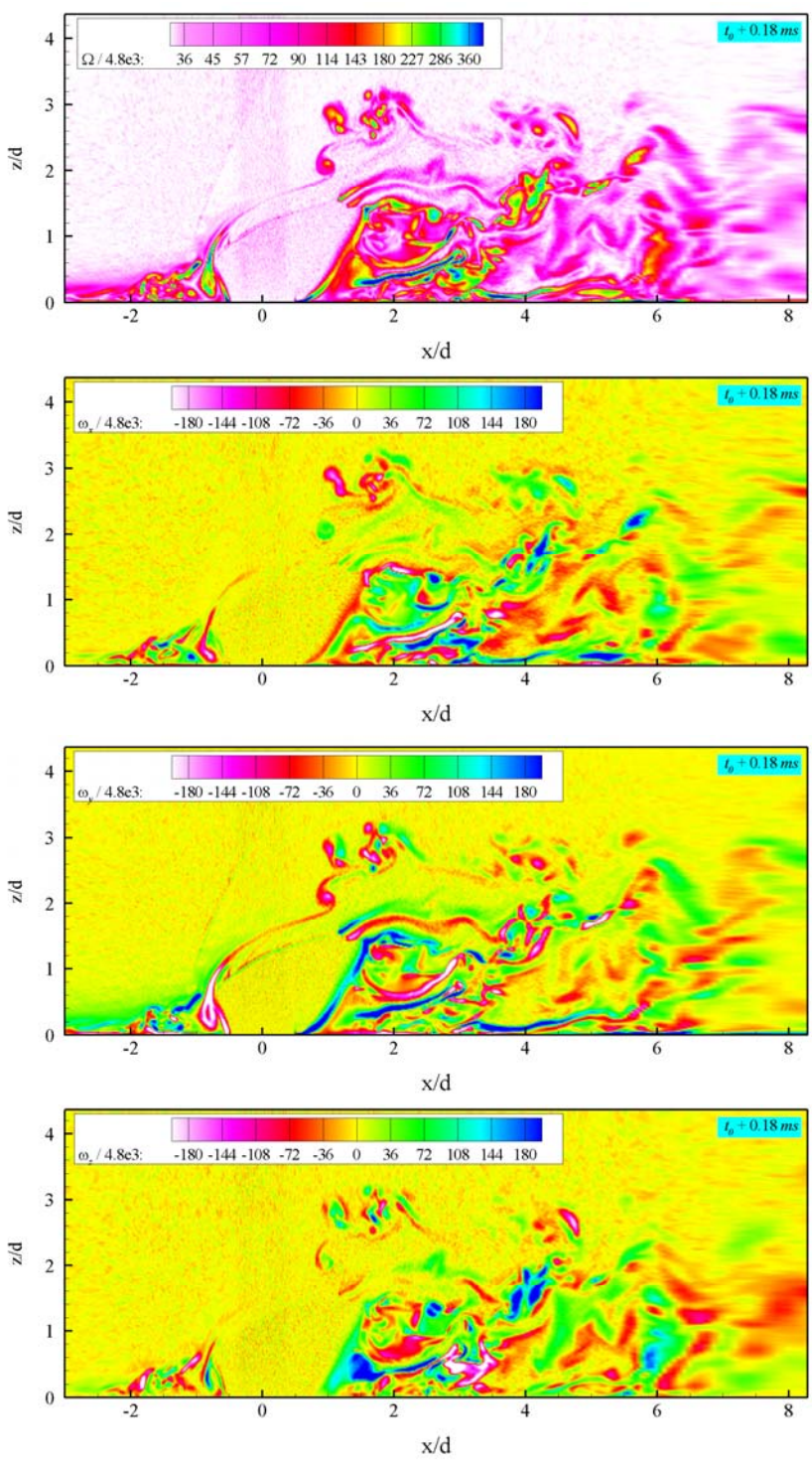

Figure 6.12 Instantaneous vorticity distributions in the center plane

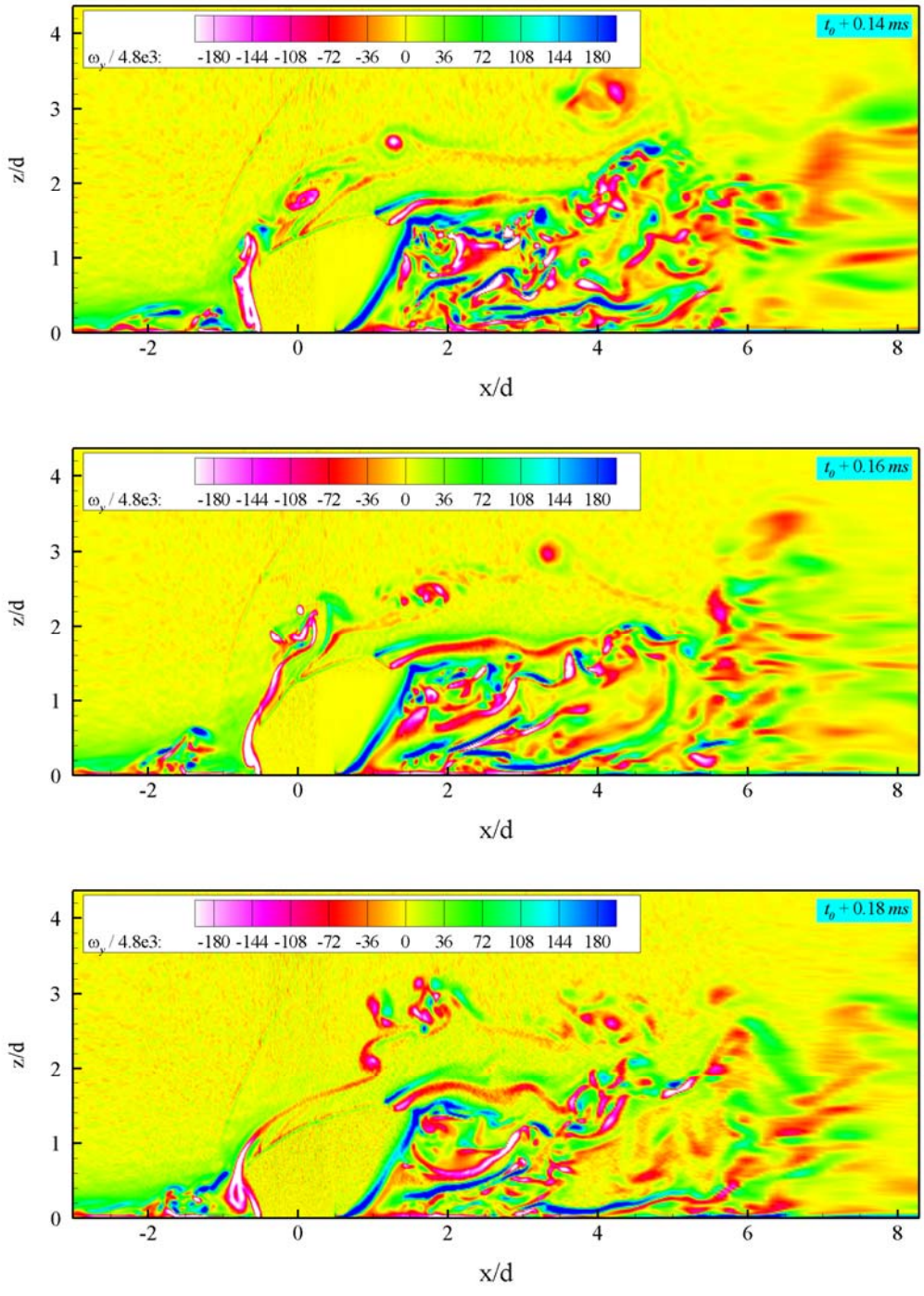

Figure 6.13 Temporal evolution of y-component vorticity ω_y in the center plane

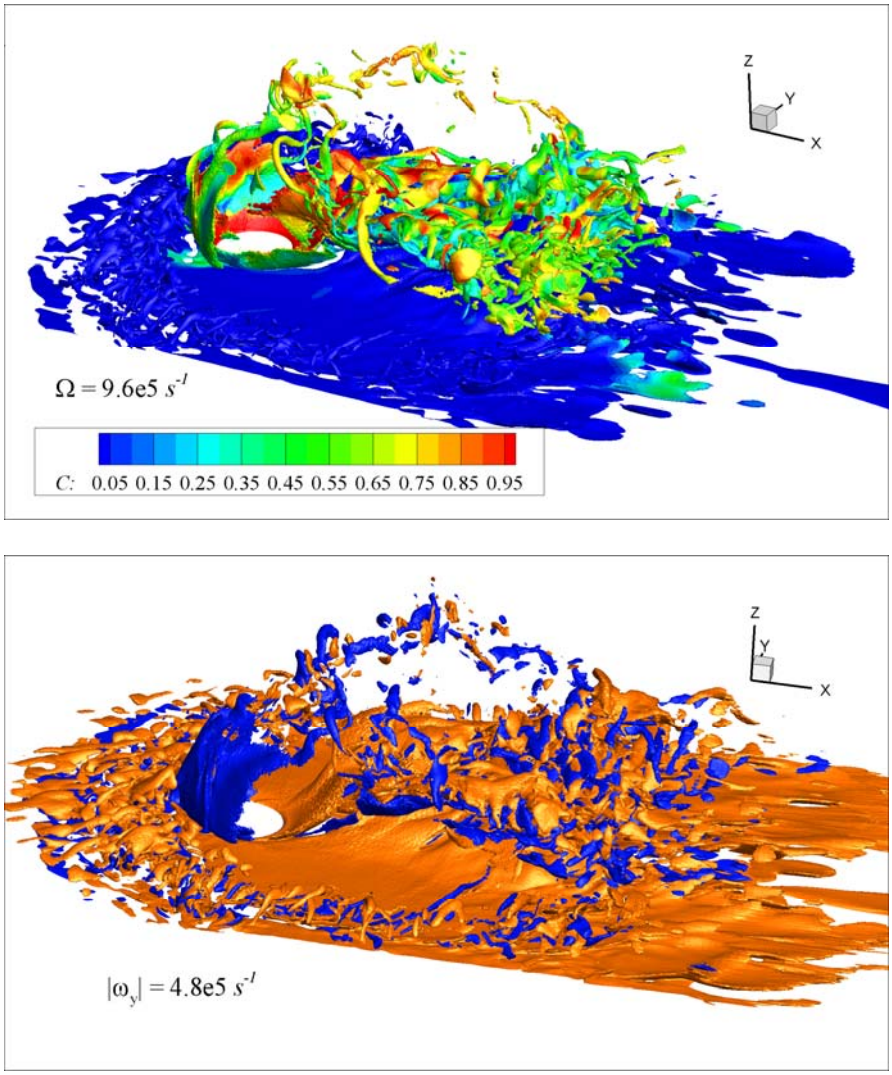

Figure 6.14 Iso-surfaces of instantaneous (a) vorticity magnitude $\Omega = 9.6\times10^{5} s^{-1}$, and (b) y-component vorticity $\left|\omega_y\right| = 4.8\times10^{5} s^{-1}$

This page intentionally left blank

Chapter 7

Summary and Future Work

7.1 Summary

The research work conducted for this thesis has explored the physical mechanisms governing the flow dynamics and mixing process of a jet into crossflow, a central component of fuel injection systems with a wide range of industrial and environmental applications. The scenarios under realistic gas turbine conditions—those being relatively high injection speeds with moderate velocity ratios—are examined through a series of simulations, covering the regimes of both subsonic and supersonic flows. A unique aspect of this work is its comprehensive investigation of the response of the flow field and mixing details to external excitations in the crossflow, on which limited work has been devoted to date.

A density-based in-house code is adapted to time-accurately resolve the complex vortical structures (and shock waves, in the supersonic case). The theoretical formulation includes the complete conservation equations of mass, momentum, energy and species in three dimensions. The finite-volume approach and a domain decomposition method are employed to time-accurately solve the governing equations. Turbulence closure is achieved by applying the large-eddy-simulation technique. The numerical framework is first validated against the experimental data for a low-speed case in terms of mean flow

quantities and is then further confirmed by reproducing the scalar field in a supersonic environment.

After validation and grid-convergence testing, the flow physics of a jet into stationary crossflow are revisited and further examined by simulating two cases with different velocity ratios. The typical vortical structures are identified: the horseshoe vortices appear to be relatively weak compared to other vortices; spanwise rollers (jet shear-layer vortices) form on the windward and leeward sides of the jet and play important roles in defining the boundary of the jet plume and engulfing the crossflow in the near field; the crossflow boundary layer separates in the wake of the jet and induces tornado-like upright vortices; the hanging vortices are generated in the skewed mixing layer and break down as they travel in a mean velocity, contributing to the formation of the counter-rotating vertex pair (CVP); the CVP collects more vorticity from the wake vortices as it evolves downstream and becomes the dominant structure in the far field, and its topology structure can be manifested by the mean flow properties. The strength and structures of vortices vary for different velocity ratios, with more apparent visualizations in the case of a higher velocity ratio. Aside from the engulfing in the gaps between the shear-layer vortices, the upright wake vortices have a high intermittency in transporting the crossflow fluid into the jet body, especially in the lower velocity ratio cases where the instantaneous jet plume is not actually separated from the crossflow boundary wall. The temporal mixing deficiency (TMD) and the spatial mixing deficiency (SMD) as well as the probability density functions (PDF) are calculated to quantify the mixing efficiency, showing a strong dependency on the velocity ratio and exhibiting less heterogeneity in the temporal evolutions of a high velocity case.

Previous work has analyzed the stability of transverse jets either through experimental observations or theoretical modeling. In this work, both spectral analysis and proper orthogonal decomposition (POD) are used to detect the intrinsic flow instability from the fluctuating pressure and scalar fields for a case with velocity ratio 4. The dominant shear-layer instability and relatively weak transverse and spanwise motions are extracted and found to be closely related to the flow structures. The transverse jet appears to be globally (absolutely) unstable, and therefore high velocity oscillations are imposed to the crossflow at various frequencies in order to investigate the behaviors of transverse jets in oscillating environments. Analysis indicates that low-level excitations have little influence on the jet penetration and evolution, while moderate/high velocity excitations induce strong vorticity generation and subsequent breakdown, yielding a much shorter jet-core and significant loss in plume contiguity. POD analysis reveals that flapping and detaching motions at the forcing frequencies (and their subharmonics) play predominant roles in the jet evolution, creating a lower "center of gravity" in the scalar field and an elongated and narrowed jet plume in any transverse planes. The mixing indices, i.e. SMD and TMD, show marginal variations among the cases with different forcing frequencies at low-level amplitudes, while for a fixed forcing frequency, the SMD decreases and the TMD increases as the excitation magnitude increases, resulting from the enlarged jet plume size and weakened plume contiguity.

The thesis subsequently presents the flow dynamics and mixing process of a sonic ethylene jet into supersonic air crossflow. The salient shock structures are captured in the time-averaged flow field: the bow shock, the separation shock, the Prandtl-Meyer expansion wave, the barrel shock, the Mach disk and the weak reflected shocks. Time-accurate realizations of the Mach number, pressure gradient, density gradient, vorticity, and ethylene concentration are explored to examine the unsteady features of this

supersonic mixing. The size of the Mach disk varies temporally but its distance from the injection orifice changes marginally and is consistent with the empirical estimation. The unsteady separation shock yields a varying shock front in the lower part of the bow shock. The periodic shedding of shear-layer vortices creates kinks at the windward barrel shock and accounts significantly for the crossflow entrainment through a stretching-tilting-tearing mechanism. The current simulation under-predicts the mixing by showing a larger maximum in ethylene concentration than the experimental data, mostly due to the mismatch of flow unsteadiness in the incoming flows. A large, low-speed, high-temperature zone is formed ahead of the jet, providing a site for the flame to be stabilized in the scramjet combustors. In the wake region, a subsonic region is also observed, suggesting the disturbances downstream are capable of traveling back to the near field and impacting the fuel injection processes.

7.2 Recommendation for Future Work

Since the flow field in a turbulent jet into crossflow involves a broad range of length scales, fine grid resolution is needed to capture the flow details; thus, more efficient temporal integration and more effective spatial discretization schemes should be considered in the future, together with better grid distributions.

The response of flow dynamics and mixing to external excitations has been examined in the subsonic case, yet the scenarios for a sonic jet into supersonic crossflow have not been clarified. Therefore, analyses can be carried out to explore the influences

of oscillations in crossflow downstream on the shock systems, vortex structures and mixing details in the near field.

The unsteady fuel/air mixing process has great potential to create combustion instabilities, as observed in Chapter 1. The current work has resolved the mixing field and quantified the mixing efficiency based on the mean data, yet its influences on combustion dynamics cannot be elucidated without the engagement of reaction details. Thus the addition of chemical reactions could be very useful and significant when exploring the physical and chemical processes in an actual combustor.

This page intentionally left blank

Bibliography

Adams, N. A. and Franz, S. (2004), "Implicit subgrid-scale modeling by adaptive deconvolution," *Journal of Computational Physics*, Vol. 200, pp. 412-431.

Alves, L. S., Kelly R. E., and Karagozian, A. R. (2007), "Local stability analysis of an inviscid transverse jet," *Journal of Fluid Mechanics*, Vol. 581, pp. 401-418.

Andreopoulos, J. (1983). "Heat transfer measurements in a heated jet-pipe flow issuing into a cold cross stream," *Physics of Fluids*, Vol. 26.

Apte, S. V. and Yang, V. (2002),"Unsteady flow evolution in a porous chamber with surface mass injection II: Forced oscillations," *AIAA Journal*, Vol. 40, pp. 244-253.

Arienti, M. and Soteriou, M. C. (2009), "Time-resolved proper orthogonal decomposition of liquid jet dynamics," *Physics of Fluids*, Vol. 21.

Ashkenas, H. and Sherman, F. S. (1966), "The structure and utilization of supersonic free jets in low density wind tunnels," In *Rarefied Gas Dynamics Volume II*, pp. 84-105. Academic Press, New York.

Bagheri, S., Schlatter, P., Schmid, P. J., and Henningson, D. S. (2009), "Global stability of a jet in crossflow," *Journal of Fluid Mechanics*, Vol. 624, pp. 33-44.

Bardina J., Ferziger, J. H. and Reynolds, W. C. (1980), "Improved subgrid scale models for Large Eddy Simulation," AIAA Paper 1980-1357.

Ben-Yaker, A. (2000), "Experimental investigation of mixing and ignition of transverse jets in supersonic crossflows," Ph.D. Thesis, Stanford University.

Ben-Yaker, A., Mungal, G. M., and Hanson, R. K. (2006), "Time evolution and mixing characteristics of hydrogen and ethylene transverse jets in supersonic crossflows," *Physics of Fluids*, Vol. 18: 026101.

Bernal, L. P. and Roshko, A. (1986), "Streamwise vortex structure in plane mixing layers," *Journal of Fluid Mechanics*, Vol. 170, pp. 499-525.

Billig, F. S., Orth, R. C., and Lasky, M. (1971), "A unified analysis of gaseous jet penetration," *AIAA Journal*, Vol. 9, pp. 1048-1058.

Boles, J. A., and Edwards, J. R., (2008), "Hybrid LES/RANS Simulation of Normal Injection into a Supersonic Cross-Stream," AIAA Paper 2008-0622.

Boles, J. A., Edwards, J. R., and Baurle, R. A. (2010), "Large-Eddy/Reynolds-Averaged Navier–Stokes Simulations of Sonic Injection into Mach 2 Crossflow," *AIAA Journal*, Vol. 48, No. 7.

Borges, R., Carmona, M., Costa, B., and Don, W. S. (2008), "An improved weighted essentially non-oscillatory scheme for hyperbolic conservation laws," *Journal of Computational Physics*, Vol. 227, pp. 3191-3211.

Brown, G. L. and Roshko, A. (1974), "On density effects and large structure in turbulent mixing layers," *Journal of Fluid Mechanics*, Vol. 64, pp. 775-816.

Calhoon, W. and Menon. S. (1996), "Subgrid Modeling for Reacting Large Eddy Simulations," AIAA Paper 1996-0561.

Camussi, R., Gui, G., and Stella, A. (2002), "Experimental study of a jet in a crossflow at very low Reynolds number," *Journal of Fluid Mechanics*, Vol. 454, pp. 113-144.

Cho, J. H. and Lieuwen, T. (2005), "Laminar premixed flame response to equivalence ratio oscillations," *Combustion and Flame*, Vol. 140, pp. 116-129.

Crocco, L. and Cheng, S. I. (1956), "Theory of Combustion Instability in Liquid Propellant Rocket Motors," AGARDograph No.8, Butterworths Scientific Publications, London.

Dandois, J., Garnier, E., and Sagaut , P. (2006), "Unsteady Simulation of Synthetic Jet in a Crossflow," *AIAA Journal*, Vol. 44, pp. 225-238

Denev, J. A., Fröhlich, J., and Bockhorn, H. (2009), "Large eddy simulation of a swirling transverse jet into a crossflow with investigation of scalar transport," *Physics of Fluids*, Vol. 21.

Dimotakis P. E. (1991), "On the convection velocity of turbulent structures in supersonic shear layers," AIAA Paper 1991-1724.

Dimotakis P. E. and Brown G. L. (1976), "The mixing layer at high Reynolds number: large structure dynamics and entrainment," *Journal of Fluid Mechanics*, Vol. 78, pp. 535-560

Eggels, J. G. M., Unger, F., Weiss, M. H., Westerweel, J., Adrian, R. J., Friedrich, R., and Nieuwstadt, F. T. M. (1994), "Fully developed turbulent pipe flow: a comparison between direct numerical simulation and experiment," *Journal of Fluid Mechanics*, Vol. 268, pp. 175-209.

Erlebacher, G., Hussaini, M. Y., Speziale, C. G., and Zang, T. A. (1992), "Toward The Large-Eddy Simulation of Compressible Turbulent Flows," *Journal of Fluid Mechanics*, Vol. 238, pp. 155-185.

Eroglu, A. and Breidenthal, R. E. (2001), "Structure, penetration, and mixing of pulsed jets in crossflow," *AIAA Journal*, Vol. 39, pp. 417-423.

Everett, D. E., Woodmansee, M. A., Dutton, J. C., and Morris, M. J. (1998), "Wall pressure measurements for a sonic jet injected transversely into a supersonic crossflow," *Journal of Propulsion and Power*, Vol. 14, pp. 861-868.

Fearn, R. and Weston, R. P. (1974), "Vorticity associated with a jet in a cross flow," *AIAA Journal*, Vol. 12, pp. 1666-1671.

Ferrante, A., Pantano, C., Matheou, G., and Dimotakis, P. E. (2009), "On the Effects of the Upstream Conditions on the Transition of an Inclined Jet into a Supersonic Cross-Flow," AIAA Paper 2009-1511.

Ferrante, A., Matheou, G., and Dimotakis, P. E. (2010), "LES of an Inclined Jet into a Supersonic Turbulent Crossflow: Synthetic Inflow Conditions," AIAA Paper 2010-1287.

Fric, T. F. and Roshko, A. (1994), "Vortical structure in the wake of a transverse jet," *Journal of Fluid Mechanics*, Vol. 279, pp. 1-47.

Fureby, C. (1996), "On Subgrid Scale Modeling in Large Eddy Simulations of Compressible Fluid Flow, " *Physics of Fluids*, Vol. 8, pp. 1301-1311.

Génin, F. and Menon, S. (2010), "Dynamics of sonic jet injection into supersonic crossflow," *Journal of Turbulence*, Vol. 11, pp. 1-30.

Germano, M., Piomelli, U., Moin, P., and Cabot, W. H. (1991), "A Dynamic Subgrid-scale Eddy Viscosity Model," *Physics of Fluids* A, Vol. 3, pp.1760-1765.

Ghosal, S. (1996), "An Analysis of Numerical Errors in Large Eddy Simulation of Turbulence," *Journal of Computational Physics*, Vol. 125, pp. 187-206.

Grinstein, F. F. and Fureby, C. (2007), "On Flux-Limiting-Based Implicit Large Eddy Simulation," *Journal of Fluids Engineering*, Vol. 129, Issue 12, 1483 (10 pages).

Gruber, M. R., Nejad, A. S., Chen, T. H., and Dutton, J. C. (1995), "Mixing and penetration studies of sonic jets in a Mach 2 freestream," *Journal of Propulsion and Power*, Vol. 11, pp. 315-323.

Guan, H. (2005), "Large-eddy simulation and the dynamical property of turbulent jets," Ph.D. Thesis, HoHai University, Nanjing, China.

Gutmark, E. J., Schado, K. C., and Yu, K. H. (1995), "Mixing Enhancement in Supersonic Free Shear Flows," *Annual Review of Fluid Mechanics*, Vol. 27, pp. 375-417.

Hasselbrink, E. F. and Mungal, M. G. (2001), "Transverse jets and jet flames. Part 2. Velocity and oil field imaging," *Journal of Fluid Mechanics*, Vol. 443, pp. 27-68.

Haven B. A. and Kurosaka M. (1997), "Kidney and anti-kidney vortices in crossflow jets," *Journal of Fluid Mechanics*, Vol. 352, pp. 27-64.

Hickel, S., Adams, N. A., Andrzej, J., and Domaradzki, J. A. (2006), "An adaptive local deconvolution method for implicit LES," *Journal of Computational Physics*, Vol. 213, pp. 413-436.

Ho, C. M. and Huerre, P. (1984), "Perturbed Free Shear Layers," *Journal of Fluid Mechanics*, Vol. 16, pp. 365-424.

Holdeman, J. D., Liscinsky, D. S., and Oechsle, V. L. (1997), "Mixing of Multiple Jets With a Confined Subsonic Crossflow: Part I—Cylindrical Duct," *Journal of Engineering for Gas Turbines and Power Volume*, Vol. 119, 852 (11 pages).

Holmes, P., Lumley, J. L., and Berkooz, G. (1998), "The Proper Orthogonal Decomposition in the Analysis of Turbulent Flows," *Annual Review of Fluid Mechanics*, Vol. 25, pp. 539-575.

Huang R. F. and Lan, J. (2005), "Characteristic modes and evolution processes of shear-layer vortices in an elevated jet," *Physics of Fluids*, Vol. 17, pp. 1-13.

Huber, P., Schexnayder, C., and McClinton, C. (1979), "Criteria for self-ignition of supersonic hydrogen-air mixtures," NASA Technical Paper 1457.

Jameson, A. (1983), "The Evolution of Computational Methods in Aerodynamics," *Journal of Applied Mathematics*, Vol. 50, pp.1052-1070.

Jameson, A., Schmidt, W., and Turkel, E. (1981), "Numerical solution of the Euler equations by the finite volume method using Runge-Kutta time-stepping schemes," AIAA Paper 1981-1259.

Jiang, G. S. and Shu, C. W. (1996), "Efficient implementation of weighted ENO schemes," *Journal of Computational Physics*, Vol. 126, pp. 202-228.

Johari H., Pacheco-Tougas, M., and Hermanson J. C. (1999), "Penetration and mixing of fully modulated turbulent jets in crossflow," *AIAA Journal*, Vol. 37, pp. 842-850.

Jorgenson, P. and Turkel, E. (1993), "Central Difference TVD Schemes for Time Dependent and Steady State Problems," *Journal of Computational Physics*, Vol. 107, pp. 197-308.

Kamotani, Y. and Greber, I. (1972), "Experiments on a turbulent jet in a cross flow," *AIAA Journal*, Vol. 10, pp. 1425-1429.

Karagozian, A. R. (1986), "An analytical model for the vorticity associated with a transverse jet," *AIAA Journal*, Vol. 24, pp. 429-436.

Karagozian, A. R. (2010), "Transverse jets and their control," *Progress in Energy and Combustion Science* xxx (2010) 1-23.

Kelso, R. M. and Smits, A. J. (1995), "Horseshoe vortex systems resulting from the interaction between a laminar boundary layer and a transverse jet," *Physics of Fluids*, Vol. 7, pp. 153-158.

Kelso R. M., Lim T. T., and Perry, A. E. (1996), "An experimental study of round jets in cross-flow," *Journal of Fluid Mechanics*, Vol. 306, pp. 111-144.

Kim, S. D., Lee, B. J., Lee, H. J., Jeung, I. S., and Choi, J. Y. (2010), "Realization of contact resolving approximate Riemann solvers for strong shock and expansion flows," *International Journal for Numerical Methods In Fluids*, Vol. 62, pp. 1107–1133.

Kordulla, W. and Vinokur, M. (1983), "Efficient Computation of Volume in Flow Predictions," *AIAA Journal*, Vol. 21, pp. 917-918.

Kravenchko, A. G. and Moin, P. (1997), "On the effect of numerical errors in large eddy simulations," *Journal of Computational Physics*, Vol. 131, pp. 310-322.

Kremer, D. M., am Ende, M. T., Mustakis, J. G., and am Ende, D. J. (2007), "A numerical investigation of a jet in an oscillating crossflow," *Physics of Fluids*, Vol. 19.

Lam, K. M. and Xia, L. P. (2001), "EXPERIMENTAL SIMULATION OF A VERTICAL ROUND JET ISSUING INTO AN UNSTEADY CROSS-FLOW," *Journal of Hydraulic Engineering*, Vol. 127, pp. 369-379.

Lee, S. Y., Seo, S., Broda, J. C., Pal, S., and Santoro R. J. (2000), "An Experimental Estimation of Mean Reaction Rate and Flame Structure During Combustion Instability in a Lean Premixed Gas Turbine Combustor," *Proceeding of Combustion Institute*, The Combustion Institute, Vol. 28, pp. 775-782.

Leonard, A. (1974), "Energy Cascade in Large-Eddy Simulation of Turbulence," *Advances in Geophysics*, Vol. 18a.

Lieuwen, T. and Zinn, B. T. (1998), "The Role of Equivalence Ratio Oscillation in Driving Combustion Instabilities in Low Nox Gas Turbines," *Proceeding of Combustion Institute*, The Combustion Institute.

Lilly, D. K. (1992), "A Proposed Modification of the Germano-Subgrid-Scale Closure Method," *Physics of Fluids* A-Fluid Dynamics, Vol. 4, pp. 633-635.

Lin, H. C. (1991), "Dissipation additions to flux-difference splitting," AIAA Paper 1991-1544.

Lin, K. C., Ryan, M., Carter, C., Gruber, M., and Raffoul, C. (2010), "Raman Scattering Measurements of Gaseous Ethylene Jets in Mach 2 Supersonic Crossflow," *Journal of Propulsion and Power*, Vol. 26, No. 3.

Liscinsky, D. S., True, B., and Holdeman, J. D. (1993), "Experimental Investigation of Crossflow Jet Mixing in a Rectanglular Duct," NASA Technical Memorandum 1061152, AIAA-93-2037.

Liu, X. D., Osher, S., and Chan, T. (1994), "Weighted essentially non-oscillatory schemes," *Journal of Computational Physics*, Vol. 115, pp. 200–212.

Lu, G. (1995), "A numerical investigation of skewed mixing layers," Ph.D. Thesis, Stanford University.

M'Closkey, R. T., King, J. M., Cortelezzi, L., and Karagozian, A. R. (2002), "The actively controlled jet in crossflow," *Journal of Fluid Mechanics*, Vol. 452, pp. 325-335.

Maddalena, L., Campioli, T. L., and Schetz, J. A. (2006), "Experimental and Computational Investigation of Light-Gas Injectors in Mach 4.0 Crossflow," *Journal of Propulsion and Power*, Vol. 22.

Margason, R. J. (1993), "Fifty years of jet in crossflow research," *Computational and Experimental Assessment of Jets in Cross Flow* 1993 (No. CP 534, AGARD).

Megerian, S. and Karagozian, A. R. (2005), "Evolution of shear layer instabilities in the transverse jet," AIAA Paper 2005-0142.

Megerian, S., Davitan, J., Alves, B., and Karagozian, A. R. (2007), "Transverse-jet shear layer instabilities, Part 1. Experimental Studies," *Journal of Fluid Mechanics*, Vol. 593, pp. 93-129.

Meyer, K., Pedersen, J., and Özcan, O. (2007), "A turbulent jet in crossflow analysed with proper orthogonal decomposition," *Journal of Fluid Mechanics*, Vol. 583, pp. 199–227.

Moin, P. and Kim, J. (1982), "Numerical Investigation of Turbulent Channel Flow," *Journal of Fluid Mechanics*, Vol. 118, pp. 341-377.

Moin, P., Squires, K., Cabot, W., and Lee, S. (1991), "A Dynamic Subgrid-Scale Model for Compressible Turbulence and Scalar Transport," *Physics of Fluids* A, Vol. 3, pp. 2746-2757.

Morkovin, M. V. (1987), "Transition at hypersonic speeds," NASA CR 178315, Washington D. C.

Muppidi, S. and Mahesh, K. (2005), "Study of trajectories of jets in crossflow using direct numerical simulations," *Journal of Fluid Mechanics*, Vol. 530, pp. 81-100.

Muppidi, S. and Mahesh, K. (2006), "A two-dimensional model problem to explain CVP formation in a transverse jet," *Physics of Fluids*, Vol. 18: 085103.

Muppidi, S. and Mahesh, K. (2008), "Direct numerical simulation of passive scalar transport in transverse jets," *Journal of Fluid Mechanics*, Vol. 598, pp. 335-360.

Muruganandam, T. M., Lakshmi, S., Ramesh, A. A., Viswamurthy, S. R., Sujith, R. I., and Sivaram, B. M. (2002), "Mixing of Transversely Injected Jets into a Crossflow Under Low-Density Conditions," *AIAA Journal*, Vol. 40, pp. 1388-1394.

Narayanan, S., Barooah, P., and Cohen, J. M. (2003), "Dynamics and control of an isolated jet in crossflow," *AIAA Journal*, Vol. 41, pp. 2316-2330.

New, T. H., Lim, T. T., and Luo, S. C. (2003), "Elliptic jets in cross-flow," *Journal of Fluid Mechanics*, Vol. 494, pp. 119-140.

Nicoud, F. and Ducros, F. (1999), "Subgrid-scale stress modeling based on the square of the velocity gradient tensor," *Flow, Turburlence and Combustion*, Vol. 62, pp. 183-200.

Norma, M. L. and Winkler, K-H. A., Spring/Summer 1985, Los Alamos Science.

Papamoschou, D. (1990), "Communication paths in the compressible shear layer," AIAA Paper 1990-0155.

Parker, T. E., Allen, M. G., Foutter, R. R., Sonnenfroh, D. M., and Rawlins, W. T. (1995), "Measurements of OH and H2O for reacting flow in a supersonic combusting ramjet combustor," *Journal of Propulsion and Power*, Vol. 11, pp. 1154-1161.

Peterson, D. M., Subbareddy, P. K., and Candler, G. V. (2006), "Detached Eddy Simulations of Flush Wall Injection into a Supersonic Freestream," AIAA Paper 2006-4576.

Peterson, D. M. and Candler, G. V. (2010), "Supersonic Combustor Fuel Injection Simulations Using a Hybrid RANS/LES Approach," AIAA Paper 2010-411.

Poling, B. E., Prausnitz, J. M., and O'Connell, J. P., "The Properties of Gases and Liquids," McGraw-Hill Companies, Inc., 2000.

Pope, S. B., "Turbulent Flows," Cambridge University Press, 2000.

Prière, C., Gicquel, L. Y. M., Kaufmann, P., Krebs, W., and Poinsot, T. (2004), "Large Eddy Simulation Predictions of Mixing Enhancement for Jets in Cross-Flows," *Journal of Turbulence*, Vol. 5, pp.1-24.

Quirk J. J. (1994), "A contribution to the great Riemann solver debate," *International Journal for Numerical Methods in Fluids*, Vol.18, pp. 555–574.

Rai, M. M., and Chakravarthy, S. (1993), "Conservative High-order Accurate Finite Difference Method for Curvilinear Grids," AIAA Paper 1993-3380.

Richards, G. A. and Janus, M. C. (1998), "Characterization of Oscillations during Premix Gas Turbine Combustion," *ASME Journal of Engineering for Gas Turbines and Power*, Vol. 120, pp. 294-302.

Rayleigh, J. W. S., The Theory of Sound, Vol. II, Dover, New York, 1945.

Rowley, C. W., Colonius, T., and Murray, R. (2000), "POD Based Models of Self-Sustained Oscillations in the Flow Past an Open Cavity," AIAA Paper 2000-969.

Rudman, M. (1996), "Simulation of the near field of a jet in cross flow," *Experimental Thermal and Fluid Science*, Vol. 12, pp. 134-141.

Sanders, R., Morano, E., and Druguet, M. (1998), "Multidimensional dissipation for upwind schemes; stability and applications to gas dynamics," *Journal of Computational Physics*, Vol. 145, pp. 511–537.

Santiago, J. G. and Dutton, J. C. (1997), "Velocity measurements of a jet injected into a supersonic crossflow," *Journal of Propulsion and Power*, Vol. 13, pp. 264-273.

Schetz, J. A. and Billig, F. S. (1966), "Penetration of gaseous jets injected into a supersonic stream," *Journal of Spacecraft and Rockets* 3, Vol. 3, pp. 1658-1665.

Schlüter, J. U. and Schönfeld, T. (2000), "LES of jets in cross flow and its application to a gas turbine burner", *Flow, Turbulence and Combustion*, Vol. 65, pp. 177-203.

Seo, S. (1999), "Parametric Study of Lean Premixed Combustion Instability in a Pressured Model Gas Turbine Combostor," Ph.D. Thesis, The Pennsylvania State University.

Shapiro, S., King, J., M'Closkey, R. T., and Karagozian, A. R. (2006), "Optimization of controlled jets in crossflow," *AIAA Journal*, Vol. 44, pp. 1292-1298.

Smagorinsky, J. (1963), "General circulation experiments with the primitive equations," *Monthly Weather Review*, Vol. 91, pp. 99-164.

Smith, S. H. and Mungal, M. G. (1998), "Mixing, structure and scaling of the jet in crossflow," *Journal of Fluid Mechanics*, Vol. 357, pp. 83-122.

Speziale, C. G., Erlebacher, G., Zang, T. A., and Hussaini, M. Y. (1988), "The Subgrid-Scale Modeling of Compressible Turbulence," *Physics of Fluids*, Vol. 31, pp. 940-942.

Su, L. K. and Mungal, M. G. (2004), "Simultaneous measurement of scalar and velocity field evolution in turbulent crossflowing jets," *Journal of Fluid Mechanics*, Vol. 513, pp. 1-45.

Sun, O. S. and Su, L. K. (2004), "Experimental assessment of scalar mixing models for large-eddy simulation," AIAA Paper 2004-2550.

Sutton, G. P. and Biblarz, O. (2000), "Rocket Propulsion Elements," 7th Edition, John Wiley and Sons.

Swanson, R. C. and Turkel, E. (1992), "On Central-difference and Upwind Schemes," *Journal of Computational Physics*, Vol. 101, pp. 292-306.

Turns, S. R., "An Introduction to Combustion: Concepts and Applications," McGraw-Hill Book Co., 2000.

Vermeulen, P. J., Chin, C. F., and Yu, W. K. (1990), "Mixing of an acoustically pulsed air jet with a confined crossflow," *Journal of Propulsion and Power*, Vol. 6, pp. 777-783.

Wang, S. (2002), "Vortical flow dynamics and acoustic response of gas-turbine swirl-stabilized injectors," Ph.D. Thesis, The Pennsylvania State University.

Wang, S. and Yang, V. (2005), "Unsteady flow evolution in swirl injectors with radial entry. II. External excitations," *Physics of Fluids*, Vol. 17.

Weiss, R. R. (1966), "An Introduction to Combustion Instability in Liquid Propellant Rocket Engines," AFRPL-TR-66-150, Edwards, CA.

Won, S. H., Jeung, I. S., Parent, B., and Choi, J. Y. (2010), "Numerical Investigation of Transverse Hydrogen Jet into Supersonic Crossflow Using Detached-Eddy Simulation," *AIAA Journal*, Vol. 48.

Xia, L. P. and Lam, K. M. (2004), "Unsteady Effluent Dispersion in a Round Jet Interacting with an Oscillating Cross-Flow," *Journal of Hydraulic Engineering*, Vol. 130, pp. 667-677.

Yuan, L. L. (1997), "Large Eddy Simulations of a Jet in Crossflow," Ph.D. Thesis, Stanford University.

Yuan, L. L. and Street, R. L. (1998), "Trajectory and entrainment of a round jet in crossflow," *Physics of Fluids*, Vol. 10, pp. 2323-2335.

Yuan, L. L., Street, R. L., and Ferziger, J. H. (1999), "Large-eddy simulations of a round jet in crossflow," *Journal of Fluid Mechanics*, Vol. 379, pp. 71-104.

Yoshizawa, A. (1986), "Statistical Theory for Compressible Turbulent Shear Flows, with the Applications to Subgrid Modeling," *Physics of Fluids*, Vol. 29, pp. 2152-2164.

Zingg, D. W., De Rango, S., Nemec, M., and Pullian, T. H. (2000), "Comparison of Several Spatial Discretization for Navier-Stokes Equations," *Journal of Computational Physics*, Vol. 160, pp. 683-704.

VITA

Liwei Zhang

Liwei Zhang was born in Xiangfan, Hubei, China, on October 20th, 1983 (September 15th, 1983 in Lunar Calendar). She received her B.S. in Theoretical and Applied Mechanics from Department of Mechanics and Mechanical Engineering, the University of Science and Technology of China (USTC) in July 2006. She moved to the United States in August 2006 to pursue a doctoral degree in Mechanical Engineering at the Pennsylvania State University and has since been working in the areas of theoretical and computational fluid dynamics.